RUB

Constitutive modelling and numerical simulation of localization phenomena in solid materials with application to soils and geomaterials

Trinh Bach Tuyet
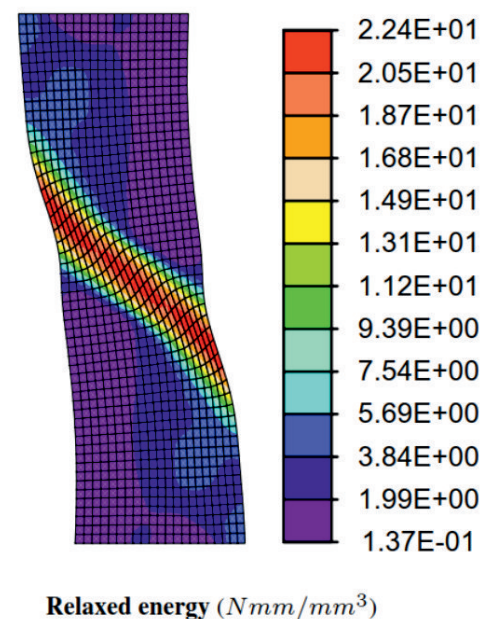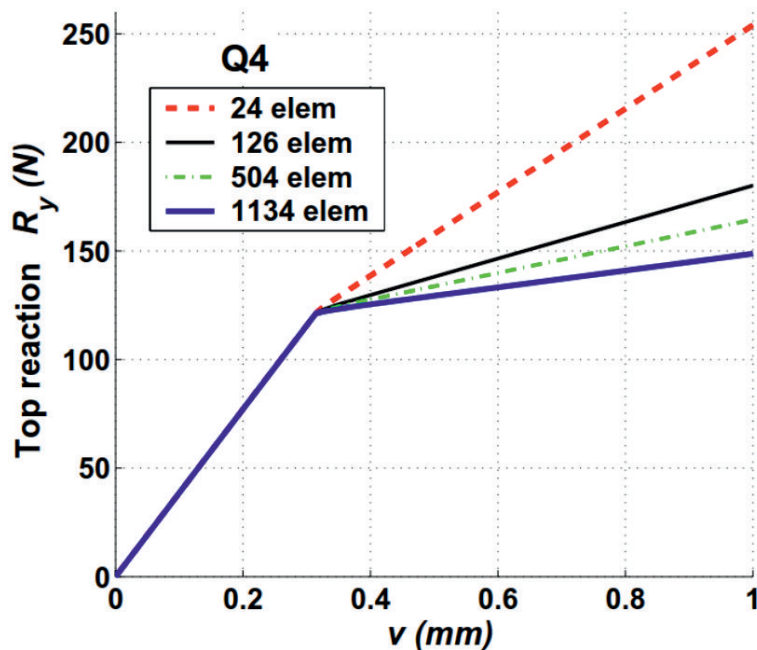
RUHR-UNIVERSITÄT BOCHUM
Institut für Mechanik

Constitutive Modelling and Numerical Simulation of Localization Phenomena in Solid Materials with Application to Soils and Geomaterials

Mitteilungen aus dem Institut für Mechanik Nr. 153

Acknowledgements

Summary

Strain localization is observed in various materials as narrow zones of intense shearing, known as shear bands. The formation of shear bands is accompanied by a softening response, characterized by a decrease in stress or strength of the material with accumulated inelastic strain, usually leading to complete collapse of the structure. This thesis is devoted to the treatment of localization phenomena in solids and is composed of three parts.

Firstly, displacement and mixed finite element formulations of shear localization in materials are introduced to decrease mesh dependence for shear bands's simulation. The formulations are based on hypoplastic constitutive laws for soils and the mixed-enhanced treatment involving displacement, strain and stress rates as independently varied fields. The numerical results are compared with available experimental data of Hostun RF sand and numerical results of Karlsruhe sand on biaxial tests.

Secondly, a strong discontinuity analysis for hypoplastic models, known as an alternative way to simulate strain localization without the introduction of characteristic lengths, is presented in order to eliminate mesh dependence. It examines the hypoplastic models compatible with unbounded strains under certain conditions in order that the displacement jump, the stress field at the discontinuity path and the normal vector can be determined.

Finally, a theoretical framework for the treatment of shear localizations in inelastic materials and porous media is developed. The theory is based on energy minimization principles associated with micro-structure developments under the assumption of a zero thickness shear band. Shear bands are treated as laminates of first order. The problem of the non-convex energy arising due to the formation of shear bands is solved by energy relaxation in order to ensure that the corresponding problem is well-posed. Numerical results are shown in order to evaluate the performance of the proposed concept.

Kurzfassung

Lokalisierungsphänomene können bei unterschiedlichen Materialien beobachtet werden. Sie entstehen meist durch einen Entfestigungsprozess, bei dem sich die Dehnungen in schmalbandigen Bereichen hoher Scherung konzentrieren. Solche Bereiche bezeichnet man als Scherbänder. Das Entstehen von Scherbändern ist oft durch einen Abfall der im Material wirkenden Spannung sowie einer Akkumulation von plastischer Dehnung begleitet und führt letztendlich zum Materialversagen. Die vorliegende Dissertation befasst sich mit der Beschreibung und Berechnung von Lokalisierungsphänomenen und gliedert sich in drei Teile:

Der erste Teil ist der Beschreibung von Scherbändern auf der Basis eines hypoplastischen Gesetzes für Materialien gewidmet. Die problematische Netzabhängigkeit der Lösungen wird durch Verwendung von gemischten Finite-Elemente-Ansätzen verringert. Die gemischten Ansätze verwenden neben dem Verschiebungsfeld auch das Spannungs- und Dehnungsfeld als unabhängige Variablen. Die erzielten Ergebnisse werden anhand von experimentellen Daten für Hostun RF und numerischen Ergebnissen für Karlsruher Sand an Biaxialtests validiert.

Der zweite Teil befasst sich mit der Beschreibung von Scherbändern durch starke Diskontinuitäten. Dieser Ansatz vermag die Netzabhängigkeit der hypoplastischen Modelle zu vermeiden, ohne dass eine charakteristische Länge in die konstitutive Beschreibung eingeführt werden muss. Es wird untersucht, wie die Verschiebungs- und Spannungssprünge sowie deren Orientierung eindeutig bestimmt werden kann.

Im dritten Teil wird schließlich ein theoretisches Gerüst für die Behandlung von Scherlokalisierungen bei unelastischen und porösen Materialien aufgestellt. Das Gerüst basiert auf dem Prinzip der Energieminimierung und behandelt Scherbänder als Laminate erster Ordnung mit verschwindender Dicke. Das Auftreten von Scherbändern führt hierbei auf ein schlecht gestelltes Problem, das keine regulären Lösungen besitzt. Mithilfe der sogenannte Relaxierungsmethoden der Variationsrechnung lassen sich jedoch verallgemeinerte Lösungen angeben, die darüber hinaus auch die Orientierung der Scherbänder adäquat beschreiben. Anhand numerischer Beispiele wird die Brauchbarkeit des hier gezeigten Ansatzes demonstriert.

Contents

Nomenclature

Symbols	Meaning
Ω	Reference configuration
$\Omega(t)$	Current configuration
Ω^+, Ω^-	Subdomain of Ω
Ω^h	Localized zone
$\partial\Omega$	Boundary of Ω
$\partial\Omega_u$	Part of boundary where the displacement $\bar{u}$ is prescribed
$\partial\Omega_\sigma$	Part of boundary on which the traction $\bar{t}$ is specified
$\partial\Omega_p$	Part of boundary on which the values of p are specified
$\partial\Omega_w$	Part of boundary where the normal outflow w_n is prescribed
$\boldsymbol{\Phi}_p$	Shape function vector of pressure
$\boldsymbol{\Phi}_v$	Shape function vector of volume change
Π	Total potential energy
$\boldsymbol{\Sigma}$	Stress in the isoparametric space
$\boldsymbol{\alpha}, \boldsymbol{\beta}$	Enhanced modes
α	Biot's constant
$\bar{\boldsymbol{\alpha}}$	Internal variable
$\bar{\alpha}$	Material parameter
α_0, β_0	Constitutive constants
δ_S^h	Dirac delta distribution
δ_{ij}	Kronecker delta
$\epsilon_{ij}, \boldsymbol{\epsilon}$	Infinitesimal strain tensor
ϵ_{ii}	Volumetric strain
$\boldsymbol{\epsilon}_{en}$	Enhanced mode
ϵ_m	Average strain
ϵ_v	Volume change
$\tilde{\boldsymbol{\epsilon}}_v$	Volume change vector
$\bar{\bar{\boldsymbol{\epsilon}}}$	Continuous part of $\boldsymbol{\epsilon}$
$\boldsymbol{\gamma}$	$(\boldsymbol{m} \otimes \boldsymbol{n})^{\mathrm{s}}$
λ, μ	Lamé constants
λ_0	$\left\|\boldsymbol{D}_S\right\| - \left\|\boldsymbol{D}_{\Omega\backslash S}\right\|$
$\bar{\lambda}_c, \bar{\mu}$	Material parameters
μ_S	Collocation function
$\boldsymbol{\nu}$	Outward normal unit vector on $\partial\Omega_\sigma$
$\boldsymbol{\nu}'$	Outward normal unit vector on $\partial\Omega_w$

Symbols	Meaning
ρ	Total density of the mixture
ρ_s	Intrinsic density of the solid phase
ρ_w	Intrinsic density of the water phase
$\boldsymbol{\sigma}$	Cauchy stress tensor
$\overset{\oplus}{\boldsymbol{\sigma}}$	Objective stress rate
$\overset{\circ}{\boldsymbol{\sigma}}$	Zaremba or Jaumann stress rate
$\mathcal{L}\boldsymbol{\sigma}$	Lie or Oldroyd stress rate
$\overset{\triangle}{\boldsymbol{\sigma}}$	Convected stress rate
$\overset{\Xi}{\boldsymbol{\sigma}}$	Green-Mclnnis-Naghdi stress rate
$\overset{\otimes}{\boldsymbol{\sigma}}$	Truesdell stress rate
$\overset{\triangledown}{\boldsymbol{\sigma}}$	Stress rate
$\hat{\boldsymbol{\sigma}}$	Normalized Cauchy stress tensor
$\hat{\boldsymbol{\sigma}}^*$	Deviatoric part of $\hat{\boldsymbol{\sigma}}$
$\boldsymbol{\sigma}''$	Effective Cauchy stress tensor
$\boldsymbol{\tau}$	Traction vector
θ	Lode-angle
$\boldsymbol{\xi} = (\xi,\,\eta)$	Natural coordinates in Chapter 4
$\xi,\,\eta$	Curvilinear coordinates in Chapter 6
ξ	Volume fraction in Chapter 2 and Part II of this thesis
$\boldsymbol{\varphi}$	Fluctuation field
φ_c	Critical friction angle
ζ	Variation in water content
$\bar{\zeta}$	Magnitude of the jump of the strain rate
$\mathcal{A}_{ijkl},\,\boldsymbol{\mathcal{A}}$	Material tangent operator
$\bar{\mathcal{D}}_{ijkl},\,\bar{\boldsymbol{\mathcal{D}}}$	Material tangent operator
$\boldsymbol{\mathcal{C}},\,\boldsymbol{\mathcal{D}}$	Symmetric fourth-order, positive definite tensors
$\boldsymbol{\mathcal{E}}$	Strain in the isoparametric space
$\mathcal{E}_1$	Major principal strain
$\mathcal{E}_2$	Minor principal strain
$\bar{\boldsymbol{\mathcal{E}}}$	Constitutive fourth-order tensor
$\boldsymbol{\mathcal{I}}$	Fourth-order unit tensor
$\mathcal{L}_{ijkl},\,\boldsymbol{\mathcal{L}}$	Constitutive fourth-order tensor
$\mathcal{Q}_{ijkl},\,\boldsymbol{\mathcal{Q}}$	Constitutive fourth-order tensor
$a_{ijkl},\,\boldsymbol{a}$	Spatial tangent operator
$\boldsymbol{c}$	Vector defined by eq. (6.52)
d	Intensity of shear mode bifurcation on a micro-scale

Symbols	Meaning
e	Current void ratio
e_i	Maximum void ratio
e_d	Minimum void ratio
e_c	Critical void ratio
$\boldsymbol{e}_1$, $\boldsymbol{e}_2$	Eigenvectors
f_d, f_e	Density factor
f_b	Barotropy function
f_s	Stiffness factor
$\boldsymbol{f}$	Body force (per unit volume) in Ω
$\boldsymbol{f}_{ext}$	External load
$\boldsymbol{f}_1$, $\boldsymbol{f}_2$	Residual forces
h_s	Granulate hardness
j	Determinant of the jacobian matrix
j_0	Determinant of the jacobian matrix $\boldsymbol{A}$
$\boldsymbol{k}$	Permeability has the dimension of [length]^3[time]/[mass]
$\boldsymbol{k}'$	Permeability has the dimension of [length]/[time]
$\boldsymbol{l}$	Spatial velocity gradient
$\boldsymbol{m}$, $\boldsymbol{n}$	Unit oriented vectors of the shear band evolution
$\bar{\boldsymbol{m}}$	Mean matrix operator
n	Porosity
$\bar{n}$	Constitutive constant
p	Mean pressure in Chapters 3-4
p	Pore pressure in Chapter 9
$\bar{p}$	Prescribed pore pressure on Ω_w
$\tilde{\boldsymbol{p}}$	Pressure vector
r	Scalar defined by eq. (7.19) in Chapter 6
s	Scalar defined by eq. (7.19) for 1D problem
	and eq. (7.40) for 2D problem in Chapter 7
s	Scalar defined by eq. (8.9) in Chapter 8
sign	Sign function
t	Time
$\bar{\boldsymbol{t}}$	Prescribed surface load on Ω_σ
$\bar{t}$	Prescribed surface load in x-direction
$\boldsymbol{u}$	Displacement vector
u, v	Displacement components in x- and y-direction
$\bar{\boldsymbol{u}}$	Prescribed displacement on Ω_u
$\bar{\bar{\boldsymbol{u}}}$	Continuous part of $\boldsymbol{u}$
$\tilde{\boldsymbol{u}}$	Displacement vector at nodal nodes

Symbols	Meaning
$\boldsymbol{v}$	Velocity vector
$\boldsymbol{w}$	Displacement of the pore fluid relative to the solid skeleton
w_n	Normal outflow on Ω_w
$\boldsymbol{x}$	Reference position vector
$\boldsymbol{y}$	Current position vector
A	Material parameter
$\boldsymbol{A}$	Jacobian matrix at the center of element
$\bar{\boldsymbol{A}}$	Second-order tensor defined by eq. (6.49)
$\boldsymbol{B}$	Strain-displacement interpolation defined by eq.(4.78))
$\boldsymbol{B}_u$	Standard strain-displacement interpolation
$\boldsymbol{B}_\alpha$	Shape function of enhanced strain
$\boldsymbol{B}_\sigma$	Shape function of enhanced stress
$\boldsymbol{C}$	Right-Green deformation tensor
$\boldsymbol{D}$	Stretching tensor
$\bar{\boldsymbol{D}}$	Direction of stretching tensor
$\breve{\boldsymbol{D}}_T$	Tangent operator
$\boldsymbol{D}^*$	Deviatoric stretching tensor
$\Delta\boldsymbol{D}$	$(\boldsymbol{c}\otimes\boldsymbol{n})^s = \Delta\boldsymbol{D}$
$\boldsymbol{F}$	Deformation gradient tensor
$\boldsymbol{F}_R$	Viscous drag forces
$\boldsymbol{G}$	Constitutive second-order tensor
$\boldsymbol{H}$	Constitutive second-order tensor
H_S	Unit ramp function
J	Determinant of deformation gradient
$\boldsymbol{I}$	Second-order unit tensor
$\boldsymbol{I}_d$	Deviatoric operator
I	Functional
$I_Q,\ I_R$	Relaxed functional
$\boldsymbol{K}_T,\ \boldsymbol{K}_{uu}, \boldsymbol{K}_{\alpha u},\ \boldsymbol{K}_{u\alpha},\ \boldsymbol{K}_{\alpha\alpha}$	Stiffness matrix
K_T	Bulk modulus of the solid skeleton
K_s	Bulk modulus of the grain material
K_w	Bulk modulus of the water
$\boldsymbol{L}$	Constitutive second-order tensor
$\boldsymbol{N}$	Constitutive second-order tensor
$\boldsymbol{N}_u$	Shape function vector of displacement
$\boldsymbol{P}$	First Piola Kirchhoff stress tensor
$\boldsymbol{Q}$	Orthogonal tensor

Symbols	Meaning
Q	Biot's constant
$\bar{Q}$	Material parameter
QW	Quasiconvexified functional
$\bar{\boldsymbol{Q}}$	Acoustic tensor
$\boldsymbol{R}$	Rotation tensor
R	Maximum shear strain
$\boldsymbol{S}$	Second Piola Kirchhoff stress tensor
S	Discontinuous plane
$\bar{\boldsymbol{T}}$	Prescribed surface load on $\partial\Omega_\sigma$
$\boldsymbol{U}$	Material stretching tensor
$\boldsymbol{V}$	Spatial stretching tensor
$\boldsymbol{W}$	Spin tensor
W	Strain energy density
W_R	Relaxed energy
W^{mix}	Mixed energy
$\delta\left(\bullet\right)$	Variation of $(\bullet)$
$\nabla\left(\bullet\right)$	Nabla operator
$\dot{(\bullet)}$	Rate of $(\bullet)$
$(\bullet)^s$	Symmetric part of $(\bullet)$
$(\bullet)^{skew}$	Skew-symmetric part of $(\bullet)$
$(\bullet)_S$	$(\bullet)$ at a given material point of S
$(\bullet)_{\Omega\backslash S}$	$(\bullet)$ at neighbouring point on the continuum part of $\Omega\backslash S$
$(\bullet)_1$	$(\bullet)$ corresponding to the low-strain domain
$(\bullet)_2$	$(\bullet)$ corresponding to the high-strain domain
$[[\bullet]]$	Jump of $(\bullet)$
$\|\bullet\|$	Euclidean norm of $(\bullet)$

1. Introduction

Regions of high strain localization by intense shearing are referred to as shear bands. The emergence of shear bands in a deforming body is accompanied by a softening response, characterized by a decrease in stress or strength of the material with accumulated plastic strain. Although the formation of shear bands is one of many possible deformation modes, it is usually a precursor to failure. Predictions of the onset and evolution of shear bands play an important role in determining the safety of structures, improving mechanical properties of material and designing material microstructure. This is due to the fact that shear banding provides failure mechanisms and thereby determines the pattern of failure.

Attempts in classical continuum theory to capture shear bands fail, in the sense that the solution yelled by the continuum theory appeared to be determined fully by the fineness of the discretization. At the onset of localization, the boundary value problem ceases to be well posed because the elliptic character of the governing equations is lost. Consequently, it gives rise to non-unique solutions. After discretization, numerical solutions depend strongly on the mesh size, which explains the observed mesh sensitivity [21].

There exists three enhanced continuum approaches

- Cosserat theory [24, 49, 79, 108]

- Non-local theory [4, 110, 101, 106]

- Gradient-enhanced theory [22, 92, 93, 107]

The above approaches are known as generalized continuum theories and have successfully demonstrated mesh independence. In the corresponding numerical models, however, the element size needed to accurately resolve the failure process must be at least an order of magnitude smaller than the width of shear bands, which is normally a very small relative to the dimension of the structure [64]. A detailed summary of previous work is presented in Section 2.3.

Therefore, the development and computational evaluation of suitable mathematical descriptions of strain localization in solids is a challenging endeavor. Consequently, it is necessary to develop renewal constitutive models and computational methods to simulate strain localization.

1.1. Scopes and Objectives

The objectives of this work are

1. Variational formulation of hypoplastic models including the standard displacement formulation as well as the multi-field formulations in which displacement, strain and stress rates are regarded as independent variables;

2. An analysis of strong discontinuities in hypoplasticity;

3. Development of a theoretical framework for the analysis of localized failure in inelastic materials as well as porous media. The theory is based on the energy minimization principles associated with micro-structure developments.

The presented numerical simulation of strain localization in this thesis is restricted in two dimensions and rate-independent solids.

1.2. Outline

The outline of the thesis is as follows:

- **Chapter 2** begins with the presenting strain localization phenomena. Then, some basic concepts related to material instability are briefly summarized. The different numerical approaches to simulation of shear localization in literature are then introduced.

The remainder of this thesis is divided into two parts. The first part, called "Simulation of strain localization in hypoplasticity", is composed of four chapters:

- **Chapter 3** Mathematical struture of hypoplastic constitutive models and Wolffersdorff hypoplastic model are reviewed.

- **Chapter 4** The mixed-enhanced finite element simulation of strain localization is introduced. First, the variational formulation is established. Then, its applications in the standard displacement method, the three-field mixed formulation, the enhanced assumed strain method and the mixed enhanced strain method are presented. Finally, time integration scheme and flowchart for the enhanced assumed strain method are introduced.

- **Chapter 5** Numerical examples demonstrating the performance of different finite element formulations in Chapter 4 are discussed in details and compared with available experimental data for Hostun RF sand and numerical results for Karlsruhe sand on biaxial tests.

- **Chapter 6** Strong discontinuity analysis incorporating hypoplastic models is extended.

The second part of the thesis is dedicated to strain localization analysis with the relaxation theory, and is presented in the three following chapters:

- **Chapter 7** A new approach to the problem of shear localization is proposed at small deformations. It is based on energy minimization principles associated with micro-structure developments and the micro-shearing of a rank-one laminate which is aligned to a shear band. This approach is first explained in detail in a one-dimensional problem, then extended to two-dimensional problems. Next, an application of the proposed formulation to isotropic materials is presented. The capability of the proposed concept is demonstrated through numerical simulations of a shear test and a tension test under plane strain condition.

- **Chapter 8** This chapter is concerned with the extension of geometric and material non-linearities. The theory is predicated upon Chapter 7. An application of the proposed formulation to Neo-Hookean materials and numerical simulation are shown.

- **Chapter 9** The relaxed energy for the problem of shear localization in fluid-saturated inelastic porous media is proposed at small deformations. Herein not only the strain field but also a variation in water content inside the shear band are assumed to tend to infinity.

Finally, **Chapter 10** applies conclusions and outlook.

2. Softening and strain localization

2.1. Strain localization phenomena

Strain localization phenomena are observed at the macro-level in various materials, when intense shearing in narrow zones occurs. The narrow zones within the materials, where intensive inhomogeneous deformation occurs due to shearing, are called *shear bands*. The formation of shear bands as depicted in Fig. 2.1 is accompanied by a softening response usually leading to complete collapse of the structure.
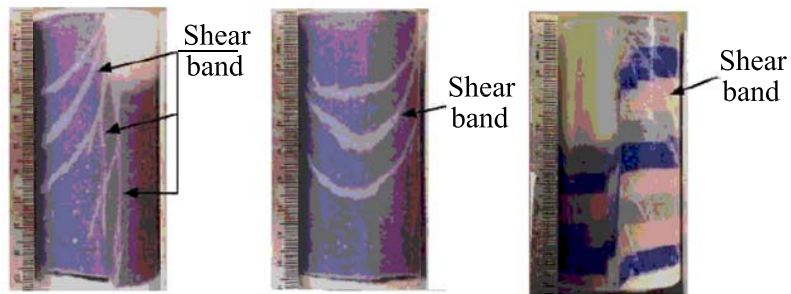
a. Digitized Image for sand (dyed pink, gray and blue) and clay (white)[53].
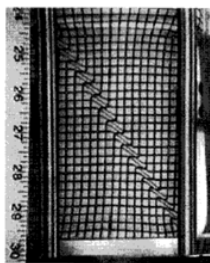
b. Fine-grained sand [1].   c. Metallite glasses [67].   d. 7039 aluminum alloy [65].
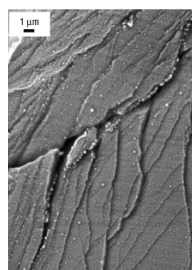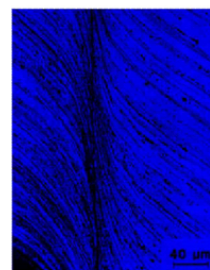
Figure 2.1.: Formation of shear bands in various materials.

Inhomogeneous deformations in general may be caused by either geometrical or materials effects. To understand the inhomogeneous deformation of materials and behaviour of shear bands, we investigate, for example, a biaxial test of loose, fined-grained sand under undrained conditions (see *Finno et al., 1996*[35]). The difference $|W_u - W_l|$ between upper

and lower widths of a specimen (Fig. 2.2) represents the inhomogeneous deformation.
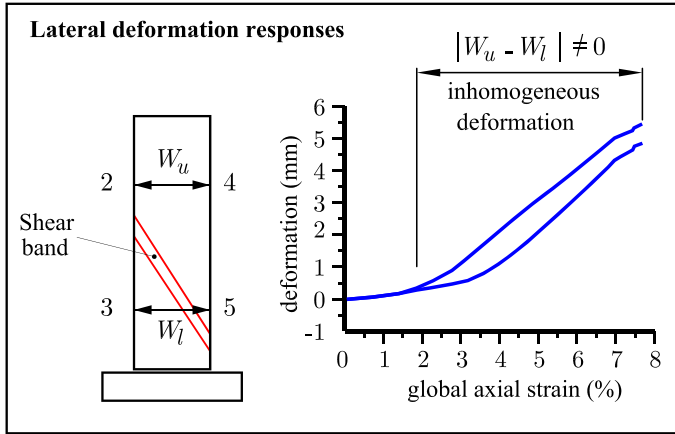
global axial strain = 2.1% → the onset of localization.

global axial strain = 2.8% → the shear band completely forms and the upper portion behaves
                                              as a mass sliding over the lower portion of the specimen.

Figure 2.2.: Lateral deformation response during undrained shear [35]

The global measured response in Fig. 2.2 is not representative of the local behaviour inside the shear band. Fig. 2.3 shows that the shear strains in the bands reach levels as high as 50-60%; outside the shear band shear strains reach no higher than 3% and the volume change outside the band is close to zero [35].
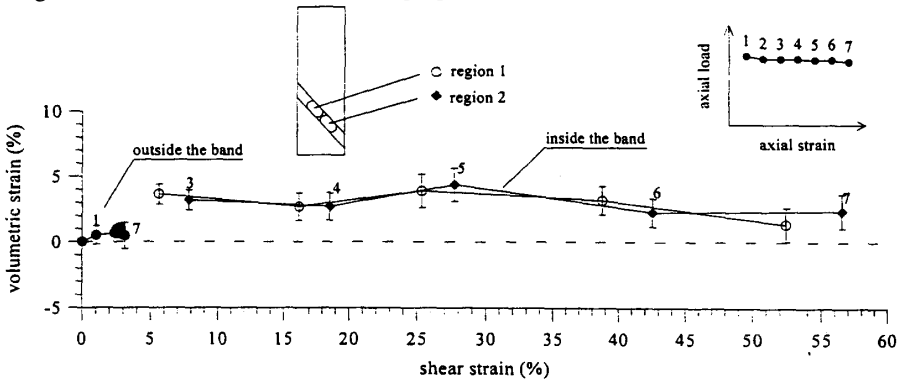
Figure 2.3.: Stereophotogrammetry-based volumetric verus shear strains [35].

The following observations of the shear band formation are reported on biaxial tests

- Most of the deformation is concentrated parallel to the band (Fig. 2.4, [35]).

- The normal movements are much smaller than those in the tangent direction and vary erratically (Fig. 2.4, [35]).

- The thickness and orientation of shear bands depend on a number of factors including (*Desrues et al., 2004*[27]):

  – the initial state of the material (mean effective stress and void ratio)

  – its grading (grain size, uniformity, etc.)

  – the size and slenderness of the specimen.
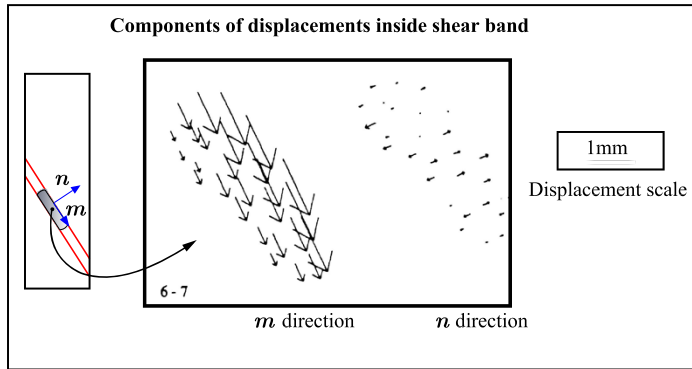
Figure 2.4.: Components of displacement inside the shear band [35].

From microscopic observations, the origin of strain localization phenomena lies generally in the material microstructure. Since most of materials are observed as inhomogeneous and discontinous ones at meso-level, the microstructures evolve in the materials during an increasing deformation [92]. Grains rotate and slide, microvoids nucleate and grow, microcracks propagate and get arrested by encountered aggregate, new microcracks initiate from existing weak spots.

The evolution and structure of shear bands in solids depends on various microstructural processes and factors including, for example, misorientation between shear band planes and slip planes, grain size, tangled and cell structures of dislocations [29, 30]. Such microstructural inhomogeneities result in the development of strain heterogeneities which, in turn, lead to the initiation of localized deformation bands. The local interaction between the various microprocesses determines the structure (width and spacing) of these shear bands [123].

It should be noted that in higher dimensions strain localization is not always due to inhomogeneities [92]. For example, in a homogeneous material, strain localization may occur because of high gradient deformation when a ductile metal is deformed sufficiently far into the plastic range (*Lemonds et al., 1985*[66]). Moreover, *Lisiecki et al., 1982* [69] demonstrated that shear bands showed no evidence for void or microcrack initiation, instead, the nonuniform crystal lattice rotations occuring during necking cause a geometrical softening which promotes localized shearing as depicted in Fig. 2.5 [3].
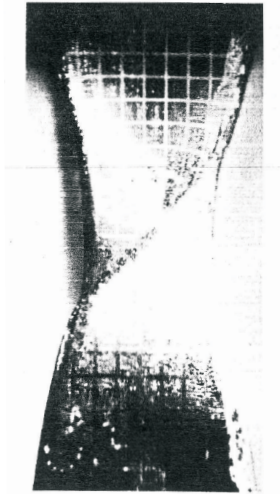
Figure 2.5.: Localized shearing and the inception of shear failure during uniaxial tension of a single crystal of pure copper (*Lisiecki et al., 1982*[3, 69]).

2.2. Some basic concepts related to material instability

The governing equations include the equilibrium equations, kinematics equations and constitutive equations. As a shear band occurs, the governing equations of the classical continuum theory result in an infinite number of possible solutions due to the ill-posed boundary value problem. As a result of this, numerical solutions suffer from a discretization sensitivity [21]. By discretization with coarse or fine mesh the phenomena of mesh sensitivity or mesh dependence are recognized and start to appear if loss of ellipticity, which is accompanied with loss of material stability, is met or if the potential energy is nonquasiconvex.

Because the mesh dependence is caused by a fundamental problem from a mechanical and mathematical nature, in the following sections we will first glance through kinematic description and then discuss some basic concepts regarding loss of material stability, loss of ellipticity and nonquasiconvexity.

2.2.1. Kinematic description

Let us consider the solution of the displacement boundary value problem. Four types of kinematic descriptions are distinguished based upon the regularity of the displacement field

- *No discontinuity* (Fig. 2.6a): The displacement field is once continuously differentiable and the strain field remains continuous. There exists no concentration of high

strains in a narrow band. Thus, the well-posed boundary value problem is assured and interpreted as a unique solution with continuous dependence on the given data as depicted in Fig. 2.7a: one force F corresponds to one displacement.
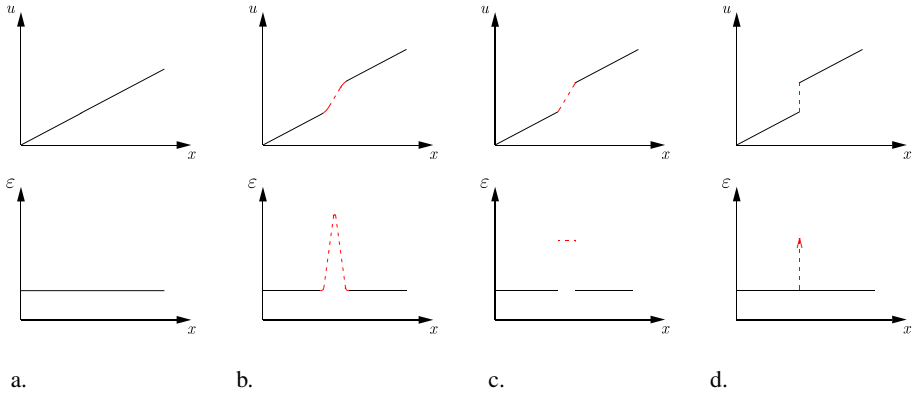
Figure 2.6.: Kinematics description with (a) and (b) no discontinuity, (c) two weak discontinuities, (d) one strong discontinuity in one-dimensional problem.
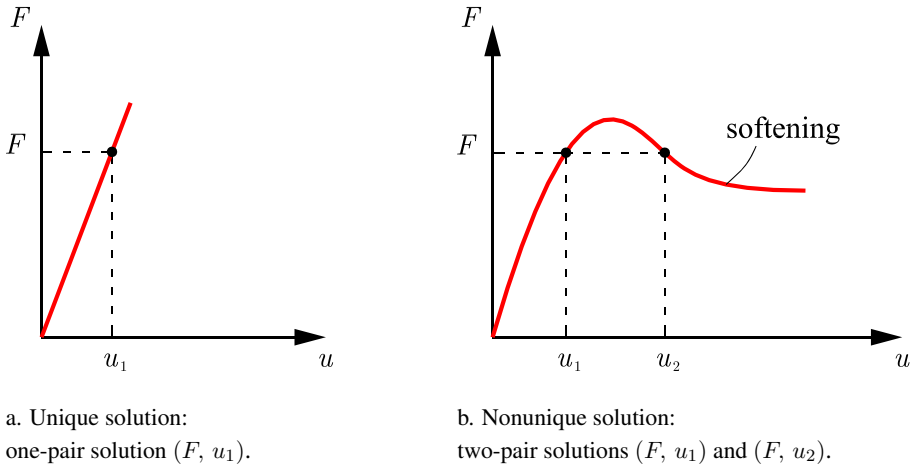
a. Unique solution:
one-pair solution (F, u_1).

b. Nonunique solution:
two-pair solutions (F, u_1) and (F, u_2).

Figure 2.7.: Uniqueness and nonuniqueness.

- *No discontinuity-high strains in a narrow band* (Fig. 2.6b): The displacement field is once continuously differentiable and the strain field remains continuous. However, strain localization is manifested by high strains in a narrow band, with a continuous transition to much lower strains in the surrounding parts of the body. In physical terms, this corresponds to a damage process zone with a continuously varying concentration of defects [52].

- *Weak discontinuity* (Fig. 2.6c): Displacement field remains continuous, but deformation gradient is discontinuous, i.e., strain components have a jump. The region of

localized deformation is characterized by a band of a small but finite thickness, separated from the remaining part of the body by weak discontinuities. In physical terms, the band between the weak discontinuities corresponds to a damage process zone with an almost constant density of microdefects [52].

- *Strong discontinuity* (Fig. 2.6d): The displacement field is discontinuous. That is the displacement jump across a discontinuity curve (in two dimensions) or discontinuity surface (in three dimensions). The corresponding strain field consists of a regular part and a singular one. In physical terms, the strong discontinuity corresponds to a crack [52]. The idea of strong discontinuity is equivalent to the assumption of a zero band thickness so that the constitutive model is no longer required to provide a characteristic length scale [14].

In the three latter types, the boundary value problem becomes ill-posed, that is, it does not have a unique solution with continuous dependence on the given data: one force F corresponds to two or multiple displacements as shown in Fig. 2.7b. The nonuniqueness is the source of instability of a solution.

2.2.2. Material stability and loss of material stability

2.2.2.1. Material stability in small

Stable material is usually defined by the following condition (*Hill, 1958*[47], *Maier et al.*, 1979[70]):

$$\dot{\boldsymbol{\sigma}} : \dot{\boldsymbol{\epsilon}} > 0. \tag{2.1}$$

This condition means that the inner product of the stress rate $\dot{\boldsymbol{\sigma}}$ and the strain rate $\dot{\boldsymbol{\epsilon}}$ is positive.

In an uniaxial tension or compression test, this inner product becomes obviously negative when the slope of the *homogenized* axial stress-axial strain curve is negative. This phenomenon is called *strain softening* (*Borst* [21, 23]). The term "homogenized" is referred to the fact that the initial flaws and boundary conditions necessarily induce a inhomogeneous stress state in a specimen [23].

In this section, we limit our discussion to incrementally linear constitutive equations:

$$\dot{\boldsymbol{\sigma}} = \bar{\boldsymbol{\mathcal{D}}} : \dot{\boldsymbol{\epsilon}}, \tag{2.2}$$

where $\bar{\boldsymbol{\mathcal{D}}}$ is the material tangent stiffness tensor.

Substituting eq. (2.2) into eq. (2.1) we obtain

$$\dot{\boldsymbol{\epsilon}} : \bar{\boldsymbol{\mathcal{D}}} : \dot{\boldsymbol{\epsilon}} > 0. \tag{2.3}$$

Stability of a body that occupies a volume V is guaranteed if

$$\int_\Omega \dot{\boldsymbol{\sigma}} : \dot{\boldsymbol{\epsilon}}\, d\Omega > 0 \tag{2.4}$$

for all kinematically admissible $\dot{\boldsymbol{\epsilon}}$.

2.2.2.2. Loss of material stability

A necessary condition for *loss of material stability* is the violation of the inequality (2.1) (*Neilsen, 1993*[81]). The limitting case which the inequality of (2.1) is replaced by an equality

$$\dot{\boldsymbol{\sigma}} : \dot{\boldsymbol{\epsilon}} = 0 \tag{2.5}$$

indicates the onset of unstable material behaviour. Here $\dot{\boldsymbol{\sigma}}$ and $\dot{\boldsymbol{\epsilon}}$ are the stress and strain rates at some points or region in the body.

Loss of material stability may lead to material instability, which implies the violation of the inequality (2.4).

Substituting eq. (2.2) into eq. (2.5) we obtain *loss of positive definiteness of the material tangent stiffness tensor* $\bar{\boldsymbol{\mathcal{D}}}$ [21, 23]

$$\dot{\boldsymbol{\epsilon}} : \bar{\boldsymbol{\mathcal{D}}} : \dot{\boldsymbol{\epsilon}} = 0 \tag{2.6}$$

which implies the singularity of the symmetric part of $\bar{\boldsymbol{\mathcal{D}}}$

$$\det(\bar{\boldsymbol{\mathcal{D}}}^s) = 0. \tag{2.7}$$

2.2.3. Ellipticity and loss of ellipticity

2.2.3.1. Ellipticity

The rate boundary value problem is well-posed if the following conditions are satisfied [21, 23]:

- the boundary complementing condition, which excludes the emergence of stationary surface waves (Rayleigh waves),

- the interfacial complementing condition, which excludes the emergence of stationary interfacial waves (Stonely waves),

- *ellipticity*, which is a local condition and implies that a finite number of linearly independent solutions are admitted, continuously depending on the data and not involving discontinuties (*Benallal et al., 1991*[11], see also [21, 23]).

2.2.3.2. Loss of ellipticity

Loss of ellipticity allows an infinite number of solutions to occur, including those which involve discontinuities [21].

Let us consider a homogeneous solid subjected to monotonic, proportional loading. We suppose that within the process of deformation, a plane S emerges and seperates a zone of localized deformation from the rest of the body. The discontinuous solution can occur such that subsequent strain rates become discontinuous across parallel plane. Maxwell's compatibility conditions require that [21, 23]

$$[[\dot{\boldsymbol{\epsilon}}]] = \dot{\boldsymbol{\epsilon}}_S - \dot{\boldsymbol{\epsilon}}_{\Omega \setminus S} = \bar{\zeta}(\boldsymbol{m} \otimes \boldsymbol{n})^s, \tag{2.8}$$

where $[[\dot{\boldsymbol{\epsilon}}]]$ is the jump of strain rate in the localized zone; $\bar{\zeta}$ is the magnitude of the jump of strain rate; $\dot{\boldsymbol{\epsilon}}_S$ and $\dot{\boldsymbol{\epsilon}}_{\Omega \setminus S}$ are strain rates inside and outside the localized zone, respectively; $\boldsymbol{n}$ is a unit normal vector to the discontinuous plane S (Fig. 2.8); $\boldsymbol{m}$ is a unit vector describing the orientation of relative velocity of regions on opposite sides of the localized deformation zone (Fig. 2.8).
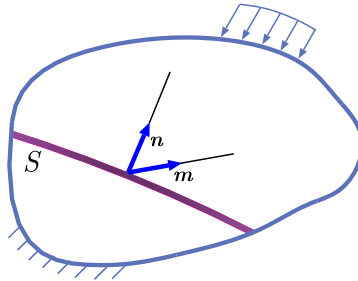
Figure 2.8.: Definition of unit vectors $\boldsymbol{n}$ and $\boldsymbol{m}$ at the surface S.

From eq. (2.2), the stress rates inside and outside the localized zone are given by

$$\dot{\boldsymbol{\sigma}}_S = \bar{\boldsymbol{D}} : \boldsymbol{\epsilon}_S, \tag{2.9}$$

$$\dot{\boldsymbol{\sigma}}_{\Omega \backslash S} = \bar{\boldsymbol{D}} : \boldsymbol{\epsilon}_{\Omega \backslash S}. \tag{2.10}$$

Thus, the jump of stress rates $[[\dot{\boldsymbol{\sigma}}]]$ in the localized zone reads

$$[[\dot{\boldsymbol{\sigma}}]] = \dot{\boldsymbol{\sigma}}_S - \dot{\boldsymbol{\sigma}}_{\Omega \backslash S} = \bar{\boldsymbol{D}} : [[\dot{\boldsymbol{\epsilon}}]], \tag{2.11}$$

where $[[\dot{\boldsymbol{\epsilon}}]]$ is defined by eq. (2.8).

For continuing equilibrium, the jump of traction rate $[[\dot{\boldsymbol{t}}]]$ across the boundaries of the localized zone must be zero [81]

$$[[\dot{\boldsymbol{t}}]] = \boldsymbol{n}\dot{\boldsymbol{\sigma}}_S - \boldsymbol{n}\dot{\boldsymbol{\sigma}}_{\Omega \backslash S} = \boldsymbol{n}[[\dot{\boldsymbol{\sigma}}]] = 0. \tag{2.12}$$

Subsituting eqs. (2.11) and (2.8) into eq.(2.12) leads to

$$[[\dot{\boldsymbol{t}}]] = \bar{\zeta}(\boldsymbol{n}.\bar{\boldsymbol{D}}.\boldsymbol{n})\boldsymbol{m} = \bar{\zeta}\bar{\boldsymbol{Q}}\boldsymbol{m} = 0, \tag{2.13}$$

where $\bar{\boldsymbol{Q}}$ is denoted as the acoustic tensor:

$$\bar{\boldsymbol{Q}} = \boldsymbol{n}.\bar{\boldsymbol{D}}.\boldsymbol{n}. \tag{2.14}$$

A non-trivial solution $(\bar{\zeta} \neq 0)$ exists if only if the acoustic tensor $\bar{\boldsymbol{Q}}$ is singular, i.e.

$$\det(\bar{\boldsymbol{Q}}) = \det(\boldsymbol{n}.\bar{\boldsymbol{D}}.\boldsymbol{n}) = 0. \tag{2.15}$$

If the condition of the discontinuous bifurcation (2.15) in a material point is met, the *loss of ellipticity* of the governing equations *for static problems* or the *loss of hyperbolicity for dynamic problems* occurs. Thereafter, the strain field at this material point can change suddenly from a homogeneous state to a localized state, consequently, discontinuous solutions characterized by a strain discontinuity can emerge.

It should be noted that the loss of material stability (2.7) is a necessary condition for the loss of ellipticity. To prove it, let us first express the material stability (2.3) in term of kinematically compatible mode $[[\dot{\boldsymbol{\epsilon}}]]$ by inserting eq. (2.8) into eq. (2.3) [21, 23]:

$$(\boldsymbol{m} \otimes \boldsymbol{n})^s : \bar{\boldsymbol{D}} : (\boldsymbol{m} \otimes \boldsymbol{n})^s > 0. \tag{2.16}$$

The limiting case that the inequality (2.16) is replaced by an equality reads

$$\boldsymbol{m}(\boldsymbol{n}.\bar{\boldsymbol{\mathcal{D}}}^s.\boldsymbol{n})\boldsymbol{m} = 0. \tag{2.17}$$

This condition refers to as the *loss of strong ellipticity* in *Neilsen and Schreyer, 1993*[81] and will first occur when

$$\det(\boldsymbol{n}.\bar{\boldsymbol{\mathcal{D}}}^s.\boldsymbol{n}) = 0, \tag{2.18}$$

where $D^s_{ijkl} = \frac{1}{2}(D_{ijkl} + D_{klij})$.

The loss of material stabilty and the loss of ellipticity identify the same first bifurcation point as shown in eqs. (2.18) and (2.15) for materials with associated flow rules due to the symmetry property of the material tangent stiffness tensor $\bar{\boldsymbol{\mathcal{D}}}$. For materials with non-associated flow rules, eq. (2.18) is always met prior to satisfaction of eq. (2.15). More discussion can be found in *Borst* [21, 23], *Neilsen and Schreyer, 1993*[81].

2.2.4. Quasiconvexity, rank-one convexity and nonquasiconvexity

The existence of equilibrium solutions of the non-linear boundary value problems can be proved based on the direct methods of calculus of variations. The basic idea of this method is the minimization of a energy functional.

For simplicity, we limit our discussion to non-linear elastic material. The total potential energy may be expressed in the following form

$$\Pi(\boldsymbol{u}) = \int_\Omega W(\nabla^s \boldsymbol{u}) \, d\Omega - \int_\Omega \boldsymbol{u}^{\mathrm{T}} \boldsymbol{f} \, d\Omega - \int_{\partial\Omega_\sigma} \boldsymbol{u}^{\mathrm{T}} \bar{\boldsymbol{t}} \, dA, \tag{2.19}$$

where $\boldsymbol{u}$ is the displacement, $\boldsymbol{f}$ is the body force per unit volume, $\bar{\boldsymbol{t}}$ is the distributed load acting on the part $\partial\Omega_\sigma$ of the surface and W is the elastic strain energy.

Now we interest in minimization problems of functionals

$$(\mathcal{P}) \quad \inf_{\boldsymbol{u}} \left\{ \Pi(\boldsymbol{u}) | \, \boldsymbol{u} = \bar{\boldsymbol{u}} \text{ on } \partial\Omega_u \right\}. \tag{2.20}$$

2.2.4.1. Quasiconvexity

It is observed that the first derivative of the displacement appears in the first term of (7.1) while the second and third terms of (7.1) are linear functionals of $\boldsymbol{u}$. Thus, the existence of minimizers for $(\mathcal{P})$ (7.3) depends on the property of W. It is well known that the mathematically simple hypothesis that W be convex with respect to $\nabla^s \boldsymbol{u}$ ensures the existence

of minimizers for $(\mathcal{P})$ (7.3). Unfortunately, as pointed out by *Ball, 1977*[5], this fact is only of mathematical interest because convexity of W with respect to $\nabla^s \boldsymbol{u}$ is unacceptable physically. Firstly, such convexity conflicts with the requirement that W is objective [5]. Secondly, strict convexity with respect to $\nabla^s \boldsymbol{u}$ implies uniqueness (*Hill, 1958*[47]). However, the minimizers for $(\mathcal{P})$ (7.3) can still exist if some less restriction condition on W is introduced.

Morrey, 1952[77] proposed a suitable condition regarded as a constitutive restriction on W [5], termed *quasiconvexity*. W is said to be *quasiconvex* if (*Ball, 1977*[5])

$$W(\boldsymbol{\epsilon}) \leq \frac{1}{\omega} \int_\omega W\left(\boldsymbol{\epsilon} + \nabla^s \boldsymbol{\varphi}\right) d\Omega \tag{2.21}$$

holds for every bounded domain ω and every vector-field $\boldsymbol{\varphi}$ with $\boldsymbol{\varphi} = \boldsymbol{0}$ on $\partial\omega$. Herein $\boldsymbol{\varphi}$ is denoted as the fluctuation field.

Let us consider the existence of minimizers for $(\mathcal{P})$ in (7.3). It may be proved that if the following conditions are satisfied

- W is bounded,

- W is coercive,

- W is quasi-convex,

there exists at least one solution for $(\mathcal{P})$ (*Dacorogna, 1989*[20] p.180).

For specific functions it is very difficult to verify the quasiconvexity condition (2.21) since we have to check a nonlocal integral condition. Therefore, the modern mathematical theory of elasticity deals with various concepts of convexity which are related as follows:

$$W \text{ convex} \Rightarrow W \text{ polyconvex} \Rightarrow W \text{ quasiconvex} \Rightarrow W \text{ rank-one convex.} \tag{2.22}$$

However it must be kept in mind that the converse theorem does not hold in general.

The condition (2.22) implies that polyconvexity and rank-one convexity is a sufficient condition and a necessary condition for quaxiconvexity, respectively.

2.2.4.2. Rank-one convexity

In practice we use a simple consequence of quasiconvexity: *rank-one convexity* [20], which is a local condition.

W is said to be *rank-one convex* at $\boldsymbol{\epsilon}$ if

$$\xi W(\boldsymbol{\epsilon}_2) + (1 - \xi)W(\boldsymbol{\epsilon}_1) \geq W(\boldsymbol{\epsilon}) \tag{2.23}$$

holds for every $0 \leq \xi \leq 1$, for all the laminate strains ϵ_1 and ϵ_2 which satisfy the conditions

$$\epsilon = \xi \epsilon_2 + (1 - \xi) \epsilon_1 \tag{2.24}$$

and

$$\text{rank}(\epsilon_2 - \epsilon_1) \leq 1. \tag{2.25}$$

For unit vectors $\boldsymbol{m}$, $\boldsymbol{n}$ and scalar $\bar{\zeta}$, the condition (2.25) means

$$\epsilon_2 - \epsilon_1 = \bar{\zeta} \, (\boldsymbol{m} \otimes \boldsymbol{n})^s. \tag{2.26}$$

ϵ_1 and ϵ_2 which satisfy (2.26) are said to be *rank-one-connected* [6, 39].

Legrendre-Hadamard condition

Based on the definition of the rank-one convexity, the *ellipticity* or *Legrendre-Hadamard* condition (2.27) [5] can be obtained by differentiating (2.23) twice if W is quasiconvex and twice continuously differentiable

$$(\boldsymbol{m} \otimes \boldsymbol{n})^s : \frac{\partial W^2(\epsilon)}{\partial \epsilon^2} : (\boldsymbol{m} \otimes \boldsymbol{n})^s \geq 0. \tag{2.27}$$

Let us denote by $\bar{\mathcal{D}}$ the material tangent stiffness tensor

$$\bar{\mathcal{D}} = \frac{\partial W^2(\epsilon)}{\partial \epsilon^2}. \tag{2.28}$$

As can be easily seen in (2.28), the four-order tensor $\bar{\mathcal{D}}$ satisfies the following symmetry conditions (ϵ is symmetric) such as $\mathcal{D}_{ijkl} = \mathcal{D}_{jikl} = \mathcal{D}_{ijlk} = \mathcal{D}_{klij}$. Thus, the inequality (2.27) can be expressed as

$$\boldsymbol{m}.\bar{\boldsymbol{Q}}.\boldsymbol{m} \geq 0 \tag{2.29}$$

where $\bar{\boldsymbol{Q}}$ is the acoustic tensor defined by eq. (2.14).

Because $\bar{\mathcal{D}}$ is symmetric, the loss of material stability (2.18) or the violation condition (2.29) and the loss of ellipticity (2.15) result in the same bifurcation point. If the condition (2.29) does not hold, it indicates a loss of smoothness and induces the development of a strain discontinuity across the discontinuous surface S.

2.2.4.3. Non-rank-one convexity and nonquasiconvexity

W is said to be *non-rank-one convex* at $\boldsymbol{\epsilon}$ if the inequality (2.23) is violated (*Bartel et al., 2004*[6]):

$$\xi W(\boldsymbol{\epsilon}_2) + (1 - \xi)W(\boldsymbol{\epsilon}_1) < W(\boldsymbol{\epsilon}) \tag{2.30}$$

holds for every $0 \leq \xi \leq 1$, for all rank-one connected $\boldsymbol{\epsilon}_1$ and $\boldsymbol{\epsilon}_2$.

The present condition is sufficient for *nonquasiconvexity* according to (2.22). Thus, the minimum of $(\mathcal{P})$ (7.3) may be unattained. In this case, the ellipticity of the governing equations is lost due to the violation of the Legrendre-Hadamard condition (2.27).

The problems of optimal design, composites, natural polymorphic materials (martensites), polycrystals, smart materials, biomaterials, etc. yield to variational problems with locally unstable solutions (or oscillatory solutions) [19] due to internal buckling, development of local fine-scale micro-structures or phase decomposition. These problems are called nonquasiconvex. The problems of nonlinear elasticity are also generally nonquasiconvex [19, 25]. Such nonquasiconvex problems give rise to the micro-structures.

By means of the relaxation theory (*Hackl and Hoppe, 2001*[42], *Carstensen et al., 2002*[15]), W is replaced by *quasiconvex envelop* of W (see Section 7.1), in order that the minimum of $(\mathcal{P})$ may be attained a solution. Futhermore, if the quasiconvex envelop of W (7.6) in some region of the solid is smaller than the value of function W, the solution is unstable. *This oscillatory solution indicates that composite is optimal, while the smooth solution means that pure phase is optimal* [19].

2.3. Related work

In simulation of strain localization, to avoid mathematical ill-posedness of the boundary value problem, consequently mesh-dependence, some enhanced continuum approaches can be found in literatures such as the *Cosserat theory*, the *nonlocal approach*, and the *gradient-enhanced approach*.

In the *Cosserat theory* (or so-called *micropolar theory*) [33], stresses and strains are computed in the micropolar continuum: the couple stresses and curvatures supplemeting with stress and strain of a standard continuum. Additional rotation degrees of freedom related to curvatures and couple stresses are introduced and lead to non-symmetry of the stress tensors. Via micropolar quantities (the couple stresses and curvatures) an internal length scale is treated as an additional material parameter, thus, the width of a shear band can be properly determined (*Mühlhaus and Vardoulakis, 1987*[79], *de Borst and Sluys, 1991*[24], *Huang and Bauer, 2003*[49]).

The *nonlocal approach* (*Strömberg and Ristinmaa, 1996*[101], *Bažant et al.,1984*[4]) incorporates a nonlocal quantity replacing a certain variable, such as strain. This nonlocal quantity computed with an integral format is defined as weighted averaging over a spatial neighborhood of each point under consideration [52]. The associated internal length scale influences the weight amplitude in the vicinity of a material point in the integral format (*Engelen et al., 2003*[32]).

The *gradient-enhanced approach* (*Borst and Mühlhaus, 1992*[22], *Pamin, 1994*[92]) avoids the integral format by approximating the nonlocal kernel with a Taylor series expansion, which yields a differential format (*Engelen et al., 2003*[32], *Jirásek, 2002*[52]). This approach can be classified into two categories: explicit and implicit gradient types. The *explicit gradient formulations* involve the higher-order gradient terms of a local quantity in the constitutive relations (*Mühlhaus and Aifantis, 1991*[78], *Borst and Mühlhaus, 1992*[22]). The *implicit gradient methods* (*Peerlings et al., 1996*[93], *Pamin, 1994*[92]) take into account the higher-order derivatives of a nonlocal variable. Both of them can be considered as higher-order extensions of the local plasticity theory and result in a finite band width.

In the above approaches an internal length scale, which is known to reflect certain changes in the microstructures in a shear bands, is needed. The models corresponding to these approaches suffer from the drawback that the element size needed to accurately resolve the failure process must be at least an order of magnitude smaller than the width of shear zones to obtain results independent of the mesh size [64]. The *strong discontinuity approach*, known as an alternative way to simulate strain localization without the introduction of characteristic lengths, is predicated upon the assumption that the displacement field is discontinuous (*Simo et al., 1993*[98], *Oliver, 1995*[88], *Armero and Garikipati, 1996*[2]). This approach can be categorized into unregularized and regularized strong discontinuities. For *unregularized strong discontinuities* the discontinuous displacement field induces an unbounded strain field having the character of a Dirac-delta distribution [2]. For *regularized strong discontinuity* [100] one considers a transition from continuous to discontinuous response by using an approximation of the Dirac-delta distribution. The term "*strong discontinuity*" refers to a particular procedure in which the shear band thickness is assumed to be zero, thus circumventing the issue of length scale in finite element analysis (*Lai et al., 2003* [62]). In this approach, however, it is necessary to determine the position of a shear band by tracking strong discontinuities.

In recent years a new methodology problem based on *energy relaxation* has been developed to simulate strain localization (*Hackl, 2005*[39], *Hackl and Hoppe, 2001*[42], *Miehe and Lambrecht,2003*[74, 73], *Lambrecht et al., 2003*[63]. The advantage of this theory is the natural formation of shear bands based on the energy minimization principles associated with micro-structure developments. The theory has been applied also to phase transformation (*Müller, 1999*[80], *Hackl and Heinen, 2008*[41]; *Bartel and Hackl, 2008*[7]) and inelastic materials by constructing an incremental variational formulation of inelasticity (*Hackl and Fischer, 2008*[40], *Carstensen, Hackl, and Mielke, 2002*[15], *Miehe, 2002*[72]). The general

internal variable formulation of inelasticity is governed by the stored energy function and the dissipation function and can be applied to viscoelasticity, plasticity and damage mechanics.

In this thesis, the two latter approaches are considered. First, the strong discontinuity approach incorporating hypoplastic models is developed in Chapter 6. Second, based on general concepts of relaxation, a new approach is established to the treatment of localization problems in inelastic materials and porous media in Chapter 7-9.

Part I.

Simulation of strain localization in hypoplasticity

3. Hypoplastic constitutive equations

Many materials such as soils, metals, polymers behave in an inelastic e.g. plastic way. The elasto-plastic constitutive equations of these materials may be expressed by assuming that the total deformation may be decomposed into elastic and plastic components [88]. In contrast to elasto-plastic models, hypolasticity is a class of incrementally nonlinear, rate type models, developed without the decomposition of deformation into elastic and plastic parts. These models can be classified into two categories: the CLoe models proposed first by *Chambon and Desrues, 1994* [18] and the K-hypoplastic models pioneered by *Kolymbas et al. (1991, 1994, 1997)*[58, 59, 60]. The K-hypoplastic models are expressed as a single constitutive equation of the rate type which can model the behaviour of non-linear material from initial state to failure state (*Bauer, 2000*[10]). In the following considerations, mathematical basis of K-hypoplastic constitutive equations is briefly summarized. Then the special case of K-hypoplastic model which is Wolffersdorff hypoplastic model proposed by Wolffersdorff [113] is shortly introduced.

3.1. Hypoplastic constitutive equations: Mathematical structure

3.1.1. Kinematics of deforming bodies

Let $y = y(x, t)$ denote the motion of a body from its reference configuration Ω to the current configuration $\Omega(t)$ at time t , $F(x, t) = \nabla y(x, t)$ the corresponding deformation gradient, and $v(x, t) = \dot{y}(x, t)$ the velocity vector. The spatial velocity gradient $l(y, t)$ is given by [48]

$$l = Dv = \dot{F}F^{-1}.\tag{3.1}$$

The multiplicative decomposition of the deformation gradient F can be expressed as

$$F = RU = VR,\tag{3.2}$$

where R, U and V are the rotation tensor, the material stretch tensor and the spatial stretch tensor, respectively.

The additive decomposition of the spatial velocity gradient l is

$$l = D + W\tag{3.3}$$

where the stretching tensor D and the spin tensor W are the symmetric and antisymmetric parts of l, respectively, i.e.

$$D = \frac{1}{2}\left(l + l^T\right) \quad ; \quad W = \frac{1}{2}\left(l - l^T\right).$$

(3.4)

3.1.2. Functional constitutive equations

According to the general theory of constitutive equations, the Cauchy stress tensor $\sigma(y, t)$ is a functional of the deformation history (*Kolymbas, 2000*[56], *Tamagnini et al., 2000*[102])

$$\sigma\left(y\left(x, t\right)\right) = \overset{\infty}{\underset{s=0}{\mathcal{G}}}\left(F^{(t)}\left(x\right), s\right),$$

(3.5)

where the history of the deformation gradient up to time t at material point x is defined by

$$F^{(t)}\left(x, s\right) \equiv F\left(x, t - s\right), \quad s \in [t, +\infty).$$

(3.6)

3.1.3. Rate type constitutive equations

In general, the constitutive equation (3.5) is very complex. There are many simplified forms of this constitutive law in literature. One of the special forms of (3.5) is a so-called rate type constitutive equation.

Let us assume that for every process compatible with the constitutive equation (3.5) the functions $\sigma = \sigma(t)$ and $F = F(t)$ satisfy a differential equation

$$\dot{\sigma} = G\left(\sigma, F, \dot{F}\right).$$

(3.7)

The differential equation (3.7) is called the rate type constitutive equation and is used frequently in soil mechanics. Materials whose constitutive equations have this form are called materials of the rate type.

The general constitutive equation (3.5) or the special form (3.7) must be satisfied certain general conditions such as e.g. objectivity. That is, material properties must be invariant under changes of observers. In order to fulfill this objective requirement we must introduce the objective stress rates and the objectivity of constitutive equations.

3.1.4. Objective stress rates

It is important to introduce the objective stress rate in order to formulate the constitutive equation of rate type. There are infinitively many possible objective stress rates. Some of them are meationed here (*Kolymbas, 2000*[56], *Kolymbas and Herle, 2003*[61]):

- Zaremba or Jaumann stress rate

$$\overset{\circ}{\boldsymbol{\sigma}} = \dot{\boldsymbol{\sigma}} + \boldsymbol{\sigma}\boldsymbol{W} - \boldsymbol{W}\boldsymbol{\sigma}, \tag{3.8}$$

- Lie or Oldroyd stress rate

$$\mathcal{L}\boldsymbol{\sigma} = \dot{\boldsymbol{\sigma}} - \left(\boldsymbol{\sigma}\boldsymbol{l}^T + \boldsymbol{l}\boldsymbol{\sigma}\right) = \overset{\circ}{\boldsymbol{\sigma}} - \left(\boldsymbol{\sigma}\boldsymbol{D} + \boldsymbol{D}\boldsymbol{\sigma}\right), \tag{3.9}$$

- Convected stress rate

$$\overset{\triangle}{\boldsymbol{\sigma}} = \dot{\boldsymbol{\sigma}} - \left(\boldsymbol{\sigma}\boldsymbol{l} + \boldsymbol{l}^T\boldsymbol{\sigma}\right) = \overset{\circ}{\boldsymbol{\sigma}} + \left(\boldsymbol{\sigma}\boldsymbol{D} + \boldsymbol{D}\boldsymbol{\sigma}\right), \tag{3.10}$$

- Green-Mclnnis-Naghdi stress rate

$$\overset{\Xi}{\boldsymbol{\sigma}} = \dot{\boldsymbol{\sigma}} + \boldsymbol{\sigma}\boldsymbol{\Omega} - \boldsymbol{\Omega}\boldsymbol{\sigma}, \tag{3.11}$$

- Truesdell stress rate

$$\overset{\otimes}{\boldsymbol{\sigma}} = \mathcal{L}\boldsymbol{\sigma} + (\mathrm{tr}\boldsymbol{D})\,\boldsymbol{\sigma}, \tag{3.12}$$

where $\boldsymbol{\Omega} = \dot{\boldsymbol{R}}\boldsymbol{R}^{\mathrm{T}}$.

3.1.5. Hypoplasticity constitutive equations

Hypoplastic constitutive equations belong to a sub-class of (3.7) and represent the objective stress rate as an explicit function of stress, stretching (and other internal variables). There are two special cases distinguished here: amorphous and endomorphous (*Kolymbas, 1991*[58], *Tamagnini et al., 2000*[102]).

In the amorphous hypoplastic material, there exists only stress as state variable

$$\overset{\oplus}{\boldsymbol{\sigma}} = \boldsymbol{H}\left(\boldsymbol{\sigma}, \boldsymbol{D}\right), \tag{3.13}$$

where $\overset{\oplus}{\boldsymbol{\sigma}}$ denotes any objective stress rate defined in Section 3.1.4. Because the Zaremba or Jaumann stress rate $\overset{\circ}{\boldsymbol{\sigma}}$ defined by eq. (3.8) is used frequently in hypoplastic constitutive equations, in the following, we will consider this stress rate in the framework of hypoplasticity.

In real materials the mechanical properties at any material point depend not only on stress and strain but also on some additional state variables. The endomorphous hypoplastic material which depends on $\boldsymbol{\sigma}$ and the so-called internal variable $\bar{\boldsymbol{\alpha}}$ has the following form

$$\overset{\circ}{\boldsymbol{\sigma}} = \boldsymbol{H}\left(\boldsymbol{\sigma}, \boldsymbol{D}, \bar{\boldsymbol{\alpha}}\right). \tag{3.14}$$

The change of $\bar{\alpha}$ is specified by an evolution equation.

3.1.6. Objectivity of constitutive equations

The constitutive equation (3.13) has to satisfy the following principle of material objectivity (*Wu and Kolymbas, 1990*[119],*Tamagnini et al., 2000*[102])

$$H\left(Q\sigma Q^T, QDQ^T\right) = QH\left(\sigma, D\right)Q^T, \tag{3.15}$$

for any arbitrary orthogonal tensor Q. This implies that $H(\sigma, D)$ is an isotropic function of both σ and D. In the most general case, the representation theorem for an isotropic tensor-valued function of two symmetric tensors can be written as (*Wu and Kolymbas, 1990*[119], *Kolymbas and Herle, 2005*[57])

$$\begin{aligned}
H\left(\sigma, D\right) &= \varphi_0 1 + \varphi_1 \sigma + \varphi_2 D + \varphi_3 \sigma^2 + \varphi_4 D^2 + \varphi_5 \left(\sigma D + D\sigma\right) \\
&+ \varphi_6 \left(\sigma^2 D + D\sigma^2\right) + \varphi_7 \left(\sigma D^2\right. \\
&+ \left. D^2 \sigma\right) + \varphi_8 \left(\sigma^2 D^2 + D^2 \sigma^2\right),
\end{aligned} \tag{3.16}$$

where the coefficients φ_α are functions of the invariants and joint invariants of σ and D (*Wu, 1998*[116]).

3.1.7. Rate independent materials

We may consider the formulation of constitutive equations for rate independent materials, which is a specific case of eq. (3.13). According to *Wu and Kolymbas, 1990*[119], this restriction implies that the function $H(\sigma, D)$ is positively homogeneous of degree one in D

$$H(\sigma, \bar{\lambda}D) = \bar{\lambda}H(\sigma, D) \text{ for } \bar{\lambda} > 0. \tag{3.17}$$

Let us define the direction $\bar{D}$ of the tensor D as

$$\bar{D} = \frac{D}{\|D\|}, \ D \neq 0, \tag{3.18}$$

where the Euclidean norm of D is given by

$$\|D\| = \sqrt{D : D} = \sqrt{\operatorname{tr}\left(D^2\right)}. \tag{3.19}$$

Note that $\bar{D}$ has a unit Euclidean norm, that is

$$\left\|\bar{D}\right\| = \sqrt{\bar{D} \bullet \bar{D}} = 1. \tag{3.20}$$

With the restriction (3.17) eq. (3.13) implies (*Kolymbas, 2000*[56])

$$\overset{\circ}{\boldsymbol{\sigma}} = \boldsymbol{H}(\boldsymbol{\sigma}, \boldsymbol{D}) = \boldsymbol{H}\left(\boldsymbol{\sigma}, \|\boldsymbol{D}\| \, \bar{\boldsymbol{D}}\right) = \boldsymbol{H}(\boldsymbol{\sigma}, \bar{\boldsymbol{D}}) \, \|\boldsymbol{D}\| = \boldsymbol{\mathcal{H}}\left(\boldsymbol{\sigma}, \bar{\boldsymbol{D}}\right) : \boldsymbol{D}. \qquad (3.21)$$

Clearly the function $\boldsymbol{H}(\boldsymbol{\sigma}, \bar{\boldsymbol{D}})$ is an isotropic function of its arguments.

3.1.8. Incrementally linear and non-linear constitutive models

If the function $\boldsymbol{H}(\boldsymbol{\sigma}, \boldsymbol{D})$ in the constitutive equation (3.21) is linear with respect to $\boldsymbol{D}$, then there exists a fourth-order tensor $\bar{\boldsymbol{\mathcal{E}}}$ depending upon only stress state $\boldsymbol{\sigma}$ and such that

$$\overset{\circ}{\boldsymbol{\sigma}} = \boldsymbol{H}\left(\boldsymbol{\sigma}, \boldsymbol{D}\right) = \bar{\boldsymbol{\mathcal{E}}}\left(\boldsymbol{\sigma}\right) : \boldsymbol{D}. \qquad (3.22)$$

The particular form of the constitutive equation (3.22) was developed by *Drăguşin, 1981*[31] for soils and is a sub-class of hypoelastic constitutive equations. It must be stressed that incremental linearity does not imply linearity of the stress-strain response over a finite stress increment.

For an incrementally non-linear material $\boldsymbol{H}\left(\boldsymbol{\sigma}, \boldsymbol{D}\right)$ is non-linear in $\boldsymbol{D}$ (*Wu, 1992*[115], *Gudehus, 1996*[38]), thus, in particular

$$\boldsymbol{H}\left(\boldsymbol{\sigma}, \boldsymbol{D}\right) \neq -\boldsymbol{H}\left(\boldsymbol{\sigma}, -\boldsymbol{D}\right), \qquad (3.23)$$

which, in turn, implies that

$$\boldsymbol{\mathcal{H}}\left(\boldsymbol{\sigma}, \bar{\boldsymbol{D}}\right) \neq -\boldsymbol{\mathcal{H}}\left(\boldsymbol{\sigma}, -\bar{\boldsymbol{D}}\right), \qquad (3.24)$$

where $\boldsymbol{\mathcal{H}}$ is the constitutive tensor of fourth order defined by eq. (3.21). An particular incrementally non-linear constitutive equation is proposed by *Wu, 1992*[115]. He assumed that the constitutive equation (3.21) can be decomposed into two parts representing the reversible and irreversible behaviour of the material. The equation (3.21) may be taken one of the following forms

$$\overset{\circ}{\boldsymbol{\sigma}} = \boldsymbol{L}\left(\boldsymbol{\sigma}, \boldsymbol{D}\right) + \boldsymbol{N}\left(\boldsymbol{\sigma}\right) \|\boldsymbol{D}\|, \qquad (3.25)$$

$$\overset{\circ}{\boldsymbol{\sigma}} = \boldsymbol{L}\left(\boldsymbol{\sigma}, \boldsymbol{D}\right) + \boldsymbol{N}\left(\boldsymbol{\sigma}\right) \frac{\boldsymbol{D}^2}{\|\boldsymbol{D}\|}, \qquad (3.26)$$

$$\overset{\circ}{\boldsymbol{\sigma}} = \boldsymbol{L}\left(\boldsymbol{\sigma}, \boldsymbol{D}\right) + \boldsymbol{N}\left(\boldsymbol{\sigma}\right) \|\boldsymbol{D}^*\|, \qquad (3.27)$$

where $\boldsymbol{D}^*$ is the deviatoric stretching tensor, $\boldsymbol{L}\left(\boldsymbol{\sigma}, \boldsymbol{D}\right)$ and $\boldsymbol{N}\left(\boldsymbol{\sigma}\right)$ are the second-order tensors.

In order to investigate properties of constitutive equations, *Gudehus, 1979*[37] introduced the concept of response envelope. Using the response envelope, *Wu* proved that the constitutive equations (3.26-3.27) are ruled out because they may lead to the unacceptable form of the 'heart'-shaped or '8'-shaped contours (*Wu, 2000*[120], *Niemusnis, 2003* p.25[82]). Thus, the constitutive equation (3.25) incorporating eq. (3.21) reads

$$\overset{\circ}{\boldsymbol{\sigma}} = \left(\boldsymbol{\mathcal{L}}\left(\boldsymbol{\sigma}\right) : \bar{\boldsymbol{D}} + \boldsymbol{N}\left(\boldsymbol{\sigma}\right) \right) \|\boldsymbol{D}\| = \boldsymbol{\mathcal{L}}\left(\boldsymbol{\sigma}\right) : \boldsymbol{D} + \boldsymbol{N}\left(\boldsymbol{\sigma}\right) \|\boldsymbol{D}\|, \tag{3.28}$$

where the fourth-order tensor $\boldsymbol{\mathcal{L}}\left(\boldsymbol{\sigma}\right)$ and the second-order tensor $\boldsymbol{N}\left(\boldsymbol{\sigma}\right)$ depend only on the stress tensor $\boldsymbol{\sigma}$.

The constitutive equation (3.25) can be recast in a more convenient form (*Wu and Bauer, 1996*[118])

$$\overset{\circ}{\boldsymbol{\sigma}} = \left(\boldsymbol{\mathcal{L}}\left(\boldsymbol{\sigma}\right) + \boldsymbol{N}(\boldsymbol{\sigma}) \otimes \bar{\boldsymbol{D}} \right) : \boldsymbol{D}, \tag{3.29}$$

where $\bar{\boldsymbol{D}}$ stands for the direction of stretching defined by (3.18), and the symbol $\otimes$ is denoted as an outer product between two tensors.

According to *Wu and Bauer, 1994*[117] (see also *Tamagnini et al., 2000*[102]), the function $\boldsymbol{H}\left(\boldsymbol{\sigma}, \boldsymbol{D}\right)$ should be positively homogeneous with respect to $\boldsymbol{\sigma}$

$$\boldsymbol{H}(\bar{\lambda}\boldsymbol{\sigma}, \boldsymbol{D}) = \bar{\lambda}^{\bar{m}} \boldsymbol{H}(\boldsymbol{\sigma}, \boldsymbol{D}), \quad \forall \bar{\lambda} > 0, \tag{3.30}$$

where $\bar{m}$ is the degree of homogeneity. This property, defined barotropy, implies that the behavior of the material can be normalized with respect to $(\mathrm{tr}\boldsymbol{\sigma})^{\bar{m}}$. *Tamagnini et al., 2000* (p.111 [102]) remarked that :
"The experimental observation that a proportional strain path starting from a nearly stress-free and undistorted state yields a proportional stress path poses some additional restrictions on the function $\boldsymbol{H}\left(\boldsymbol{\sigma}, \boldsymbol{D}\right)$. In the particular case of amorphous hypoplastic materials, it can be shown that a sufficient condition to satisfy this requirement is that $\boldsymbol{H}\left(\boldsymbol{\sigma}, \boldsymbol{D}\right)$ be positively homogeneous with respect to $\boldsymbol{\sigma}$."

3.2. Reference hypoplastic constitutive model

The Wolffersdorff hypoplastic model [113], a particular case of the K-hypoplastic model, is an incrementally non-linear constitutive equation which has the form (3.28):

$$\overset{\circ}{\boldsymbol{\sigma}} = \boldsymbol{\mathcal{L}} : \boldsymbol{D} + \boldsymbol{N} \|\boldsymbol{D}\|, \tag{3.31}$$

where the objective co-rotational (Jaumann) stress rate $\overset{\circ}{\boldsymbol{\sigma}}$ of the Cauchy stress tensor $\boldsymbol{\sigma}$ is defined by (3.8)

$$\overset{\circ}{\boldsymbol{\sigma}} = \dot{\boldsymbol{\sigma}} - \boldsymbol{W}\boldsymbol{\sigma} + \boldsymbol{\sigma}\boldsymbol{W}. \tag{3.32}$$

Herein $\mathcal{L}$ is the constitutive tensor of fourth order and $\boldsymbol{N}$ is the one of second order. It is noted that the tensorial functions $\mathcal{L} : \boldsymbol{D}$ and $\boldsymbol{N}\|\boldsymbol{D}\|$ are linear and non-linear in $\boldsymbol{D}$, respectively. The specific form of the constitutive tensors $\mathcal{L}$ and $\boldsymbol{N}$ determines the particular model of the hypoplastic law.

In the theory proposed by von Wolffersdorff [113] two tensors are given by

$$\mathcal{L} = f_b f_e \frac{1}{\mathrm{tr}\left(\hat{\boldsymbol{\sigma}}^2\right)} \left(F^2 \mathcal{I} + a^2 \hat{\boldsymbol{\sigma}} \otimes \hat{\boldsymbol{\sigma}}\right), \tag{3.33}$$

$$\boldsymbol{N} = f_d f_b f_e \frac{aF}{\mathrm{tr}\left(\hat{\boldsymbol{\sigma}}^2\right)} \left(\hat{\boldsymbol{\sigma}} + \hat{\boldsymbol{\sigma}}^*\right), \tag{3.34}$$

where $\mathcal{I}$ is the fourth-order unit tensor given by

$$\mathcal{I}_{ijkl} = \frac{1}{2}\left(\delta_{ik}\delta_{jl} + \delta_{il}\delta_{jk}\right). \tag{3.35}$$

The normalized stress tensor $\hat{\boldsymbol{\sigma}}$ and its deviatoric part $\hat{\boldsymbol{\sigma}}^*$ are defined by

$$\hat{\boldsymbol{\sigma}} = \frac{\boldsymbol{\sigma}}{\mathrm{tr}\left(\boldsymbol{\sigma}\right)}, \tag{3.36}$$

$$\hat{\boldsymbol{\sigma}}^* = \hat{\boldsymbol{\sigma}} - \frac{1}{3}\boldsymbol{I}. \tag{3.37}$$

The factor a in eqs. (3.33) and (3.34) depends on the critical friction angle φ_c through the relation

$$a = \frac{\sqrt{3}\left(3 - \sin\varphi_c\right)}{2\sqrt{2}\sin\varphi_c}. \tag{3.38}$$

The effect of the mean pressure $-\dfrac{\mathrm{tr}\boldsymbol{\sigma}}{3}$ and the current void ratio e taken into account in the constitutive law (3.31) are specified by the density f_d and the stiffness factor f_s

$$f_d = \left(\frac{e - e_d}{e_c - e_d}\right)^{\alpha_0}, \tag{3.39}$$

$$f_s = f_b f_e, \tag{3.40}$$

with the density factor f_e and the barotropy function f_b being given by

$$f_e = \left(\frac{e_c}{e}\right)^{\beta_0}, \tag{3.41}$$

$$f_b = \frac{h_s}{\bar{n}} \left(\frac{e_{i0}}{e_{c0}}\right)^{\beta_0} \frac{1 + e_i}{e_i} \left(-\frac{tr\boldsymbol{\sigma}}{h_s}\right)^{1-\bar{n}} \left[1 + a^2 - a\sqrt{3}\left(\frac{e_{i0} - e_{d0}}{e_{c0} - e_{d0}}\right)^{\alpha_0}\right]^{-1}, \tag{3.42}$$

where $0.1 < \alpha_0 < 0.3$ and $0 \le \beta_0 \le 2.5$ [8, 46] are constitutive constants.

It should be noted that a wide range of densities, pressures and deformations is included in the material parameters by considering the barotropy and pyknotropy effects in this model. These effects take into account pressure and density dependence, respectively (*Tamagnini et al., 2000*[102]).

The dependence of void ratio on pressure in eqs. (3.39), (3.41) and (3.42) is taken into account by the following relation

$$\frac{e_i}{e_{i0}} = \frac{e_d}{e_{d0}} = \frac{e_c}{e_{c0}} = \exp\left[-\left(-\frac{tr\boldsymbol{\sigma}}{h_s}\right)^{\bar{n}}\right], \tag{3.43}$$

where e_i, e_d and e_c are the maximum, minimum and critical void ratios, respectively; e_{i0}, e_{d0} and e_{c0} are the corresponding values for $tr\boldsymbol{\sigma} \approx 0$; h_s having the dimension of stress is the granulate hardness representing a reference pressure; the exponent n reflects the pressure-sensitivity of a grain skeleton.
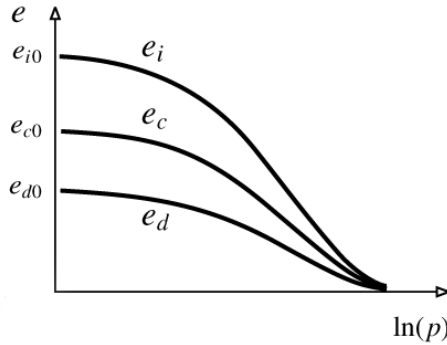
Figure 3.1.: Decrease of the maximum void ratio e_i, the critical void ratio e_c and the minimum void ratio e_d with increasing mean pressure p ($3p = -tr\boldsymbol{\sigma}$)[10].

The function $F(\hat{\boldsymbol{\sigma}})$ determined by fitting the yield condition by Matsuoka-Nakai has the form

$$F = \sqrt{\frac{1}{8}\tan^2\psi + \frac{2 - \tan^2\psi}{2 + \sqrt{2}\tan\psi\cos 3\theta}} - \frac{1}{2\sqrt{2}}\tan\psi, \tag{3.44}$$

where the Lode-angle θ is expressed as

$$\cos 3\theta = -\sqrt{6}\frac{tr\hat{\boldsymbol{\sigma}}^{*3}}{\left(tr\hat{\boldsymbol{\sigma}}^{*2}\right)^{3/2}}, \tag{3.45}$$

and

$$\tan \psi = \sqrt{3}\,\|\hat{\boldsymbol{\sigma}}^*\|\,. \tag{3.46}$$

It is generally assumed that the volume of grains remains constant. Therefore the rate of the void ratio can be expressed by the following evolution equation

$$\dot{e} = (1+e)\mathrm{tr}\boldsymbol{D}. \tag{3.47}$$

It is seen that there are eight constants in Wolffersdorff hypoplastic model: the critical friction angle φ_c; the granular hardness h_s; the void ratios e_{i0}, e_{c0} and e_{d0}; and the exponents $\bar{n}$, α_0 and β_0. The material parameters may be determined in simple index and element tests (*Bauer, 1996*[8], *Herle, 1999*[46]).

The Wolffersdorff hypoplastic model [113] will be used in the rest of the first part of this thesis.

4. Finite element simulation of strain localization in hypoplasticity

Finite element simulation of strain localization in non-polar hypoplastic models developed by *Hügel, 1995*[51], *Tejchman,1996*[109] and *Fellin et al., 2002*[34] exhibits mesh dependence. Enrichment of these models via e.g. polar hypoplasticity [107, 71, 49, 84] and non-local hypoplasticity [110, 71, 106] has been considered as some of techniques in order to remove mesh sensitivity. Although many numerical investigations using the above enhanced continuum models have been published, none of the publications deals with mixed-enhanced treatment involving displacement, strain and stress rates as independently varied fields in hypoplasticity.

In this chapter the multi-field finite element formulations of shear localization in granular materials are presented. The formulations are based on hypoplastic models and the variational formulation in terms of displacement, strain and stress rates as primary variables. Applications of the variational formulation in the standard displacement method, the three-field mixed formulation, the enhanced assumed strain method and the mixed enhanced strain method are introduced. Time integration schemes for updating stress, void ratio and tangent operator proposed by *Nübel et al., 1998*[83] and a flowchart for the enhanced assumed strain method are also presented.

4.1. Variational formulation

The finite element solutions of problems in mechanics require the variational formulation of the respective boundary value problems. Accordingly, in this section the variational formulation of the hypoplastic problems is first introduced. The presented formulation includes the standard displacement formulation as well as the multi-field formulations involving strain and stress rates as independent variables besides displacement rate. For simplicity, this formulation will be based on the amorphous hypoplastic constitutive law in which Cauchy stress is the only state variable. The formulation based on pyknotropic hypoplasticity regarding the void ratio as the additional state variable is similar and will not be presented in details.

In typical problems of soil mechanics it may be assumed that strains are infinitesimal. Under this assumption, no distinction between the stress and strain tensors defined with respect to the reference and deformed configuration of the body needs to be made. Consequently, the stretching tensor D is equal to the strain rate tensor $\dot{\epsilon}$ being the time derivative of the

infinitesimal strain tensor ϵ. As a result, the governing equations consist of:

1. The equilibrium equation which may be written in the rate form

$$\mathrm{div}\dot{\boldsymbol{\sigma}} + \dot{\boldsymbol{f}} = \boldsymbol{0}, \tag{4.1}$$

   where $\boldsymbol{f}$ is the body force (per unit volume) and $\dot{\boldsymbol{\sigma}}$ is the time derivative of $\boldsymbol{\sigma}$,

2. The constitutive equation of hypoplasticity in the form of the objective stress rate

$$\overset{\circ}{\boldsymbol{\sigma}} = \boldsymbol{H}(\boldsymbol{\sigma}, \dot{\boldsymbol{\epsilon}}) = \boldsymbol{\mathcal{L}}(\boldsymbol{\sigma}) : \dot{\boldsymbol{\epsilon}} + \boldsymbol{N}(\boldsymbol{\sigma}) \left\| \dot{\boldsymbol{\epsilon}} \right\|, \tag{4.2}$$

   or in the form [102, 16]

$$\dot{\boldsymbol{\sigma}} = \boldsymbol{G}(\boldsymbol{\sigma}, \dot{\boldsymbol{\epsilon}}) = \boldsymbol{\mathcal{Q}}(\boldsymbol{\sigma}) : \dot{\boldsymbol{\epsilon}} + \boldsymbol{N}(\boldsymbol{\sigma}) \left\| \dot{\boldsymbol{\epsilon}} \right\|, \tag{4.3}$$

   where

$$\mathcal{Q}_{ijkl} = \mathcal{L}_{ijkl} + \frac{1}{2} \left(\sigma_{il}\delta_{jk} - \sigma_{ik}\delta_{jl} + \sigma_{jl}\delta_{ik} - \sigma_{jk}\delta_{il} \right), \tag{4.4}$$

   $\boldsymbol{\mathcal{L}}$ and $\boldsymbol{N}$ are defined by (3.33) and (3.34), respectively,

3. The kinematic relation written in the rate form

$$\dot{\boldsymbol{\epsilon}} = \nabla^s \dot{\boldsymbol{u}}, \tag{4.5}$$

   where $\boldsymbol{u}$ is the displacement.

The above field equations are supplemented by the boundary conditions having the form

$$\dot{\boldsymbol{u}} = \dot{\bar{\boldsymbol{u}}} \quad \text{on } \partial\Omega_u, \tag{4.6}$$

$$\dot{\bar{\boldsymbol{t}}} = \dot{\boldsymbol{\sigma}}\boldsymbol{\nu} \quad \text{on } \partial\Omega_\sigma, \tag{4.7}$$

where $\bar{\boldsymbol{u}}$ and $\bar{\boldsymbol{t}}$ are the imposed displacement and traction force on boundaries $\partial\Omega_u$ and $\partial\Omega_\sigma$, respectively; $\boldsymbol{\nu}$ is the outward normal unit vector on the boundary $\partial\Omega_\sigma$; $\dot{(\,)}$ is the time derivative.

The equations (4.1), (4.2) and (4.5) are defined locally at every point in the reference configuration of the body under consideration. Based upon these equations the respective global relations which are valid for the whole body may be derived in the standard manner. Consequently, three integral identities as variational formulation are derived as the following.

First, taking the inner product of the local equilibrium equation (4.1) with the virtual velocity (rate of displacement) $\delta\dot{\boldsymbol{u}}$, integrating over the domain occupied by the body and applying the standard divergence theorem one gets

$$\int_\Omega \delta\left(\nabla^s \dot{\boldsymbol{u}}\right)^{\mathrm{T}} \dot{\boldsymbol{\sigma}} \, d\Omega = \int_\Omega \delta\dot{\boldsymbol{u}}^{\mathrm{T}} \dot{\boldsymbol{f}} d\Omega + \int_{\partial\Omega_\sigma} \delta\dot{\boldsymbol{u}}^{\mathrm{T}} \dot{\bar{\boldsymbol{t}}} \, dA. \tag{4.8}$$

This variational equation expressing the principle of virtual velocities (principle of virtual displacements in the rate form) provides the theoretical basis for the displacement-based finite element formulations of the problem.

The second variational equation is obtained by taking the inner product of the constitutive law of hypoplasticity (4.3) with the virtual strain rate $\delta\dot{\boldsymbol{\epsilon}}$ and integrating over the domain, thus one has

$$\int_\Omega \delta\dot{\boldsymbol{\epsilon}}^{\mathrm{T}}\left[\boldsymbol{G}\left(\boldsymbol{\sigma},\dot{\boldsymbol{\epsilon}}\right)-\dot{\boldsymbol{\sigma}}\right]d\Omega = 0. \tag{4.9}$$

Finally, the third variational equation which follows from the kinematical relation (4.5) yields

$$\int_\Omega \delta\dot{\boldsymbol{\sigma}}^{\mathrm{T}}\left[\nabla^s\dot{\boldsymbol{u}}-\dot{\boldsymbol{\epsilon}}\right]d\Omega = 0, \tag{4.10}$$

where $\delta\dot{\boldsymbol{\sigma}}$ denotes the virtual stress rate.

The integral identities (4.9) and (4.10) express the respective field equations in the global (integral) form and they provide, together with the equation (4.8), the variational basis for the multi-field finite element formulations of the problem.

4.2. Displacement-based finite element formulation

The classical single-field finite element formulations are based on the assumption according to which the kinematic relation (4.5) is satisfied at every point in the body and the stress rate is determined by the constitutive law (4.2), or equivalently (4.3). As a result, the variational equations (4.9) and (4.10) are satisfied identically, and the principle of virtual velocities (4.8) provides the complete formulation of the problem with the displacement rate as the only independent variable.

In this paper we restrict our attention to plane strain problems, thus, the kinematic relations (4.5) reduce to

$$\boldsymbol{\epsilon}_u = \nabla^s\boldsymbol{u} = \left\{ \begin{array}{c} \frac{\partial u}{\partial x} \\ \frac{\partial v}{\partial y} \\ \frac{\partial u}{\partial y}+\frac{\partial v}{\partial x} \end{array} \right\} = \left[\begin{array}{cc} \frac{\partial}{\partial x} & 0 \\ 0 & \frac{\partial}{\partial y} \\ \frac{\partial}{\partial y} & \frac{\partial}{\partial x} \end{array} \right] \left\{ \begin{array}{c} \tilde{u} \\ \tilde{v} \end{array} \right\}, \tag{4.11}$$

where $\tilde{u}$ and $\tilde{v}$ are the two components of nodal displacement. Moreover, the stress tensor $\boldsymbol{\sigma}$ has only three non-zero components and it may be written in the vector form

$$\boldsymbol{\sigma} = [\sigma_x, \sigma_y, \sigma_{xy}]. \tag{4.12}$$

In finite element analysis the displacements are assumed to be a function of the displacements at the nodes:

$$\boldsymbol{u} \approx \boldsymbol{N}_u(\boldsymbol{\xi})\tilde{\boldsymbol{u}}(t), \tag{4.13}$$

where $\boldsymbol{N}_u$ is the standard displacement interpolation matrix containing the Lagrange shape functions [126], $\tilde{\boldsymbol{u}}$ represents a listing of nodal displacements, $\dot{()}$ is time derivative.

Taking the time derivative of the approximation (4.13) we have

$$\dot{\boldsymbol{u}} \approx \boldsymbol{N}_u(\boldsymbol{\xi})\dot{\tilde{\boldsymbol{u}}}(t). \tag{4.14}$$

Substituting the approximations (4.13) and (4.14) into eq. (4.8) yields the discrete equation system

$$\int_{\Omega} \boldsymbol{B}_u^{\mathrm{T}} \dot{\boldsymbol{\sigma}} \, d\Omega \;\; = \;\; \dot{\boldsymbol{f}}_{ext}, \tag{4.15}$$

where $\boldsymbol{B}_u$ is the standard strain-displacement interpolation and $\dot{\boldsymbol{f}}_{ext}$ is the rate of the external load

$$\dot{\boldsymbol{f}}_{ext} = \int_{\Omega} \boldsymbol{N}_u^{\mathrm{T}} \dot{\boldsymbol{f}} \, d\Omega + \int_{\partial\Omega_\sigma} \boldsymbol{N}_u^{\mathrm{T}} \dot{\boldsymbol{t}} \, dA. \tag{4.16}$$

Based on this formulation the eight-node (Q8) and four-node (Q4) quadrilateral elements as well as the three-node triangular element (CST) will be considered in Chapter 5.

In practice, the displacement-based finite element formulation is often used. In certain problems when constraints such as incompressibility arise, it is necessary to employ some other techniques. Some of the techniques introduced here are the three-field mixed formulation, the enhanced assumed strain method, and the mixed enhanced strain method.

4.3. Three-field mixed formulation

The three-field mixed formulation proposed by *Zienkiewicz and Taylor* [104, 127] is used within hypoplastic model in this section. This formulation is based on three primary variables: the displacement field $\boldsymbol{u}$, the pressure p and the volume change ϵ_v.

Let use denote the mean and deviatoric matrix operators in two-dimensional problem as

$$\bar{m} = \begin{bmatrix} 1 & 1 & 1 & 0 \end{bmatrix}^T, \tag{4.17}$$

$$I_d = I - \frac{1}{3}\bar{m}\bar{m}^T = \begin{bmatrix} \frac{2}{3} & -\frac{1}{3} & -\frac{1}{3} & 0 \\ -\frac{1}{3} & \frac{2}{3} & -\frac{1}{3} & 0 \\ -\frac{1}{3} & -\frac{1}{3} & \frac{2}{3} & 0 \\ 0 & 0 & 0 & 1 \end{bmatrix} \tag{4.18}$$

where I is the second-order unit tensor.

The strain rate and stress rate can be written in a mixed form as

$$\dot{\epsilon} = I_d\nabla^s\dot{u} + \frac{1}{3}\bar{m}\dot{\epsilon}_v, \tag{4.19}$$

$$\dot{\sigma} = I_d\overset{\circ}{\sigma} + \bar{m}\dot{p}, \tag{4.20}$$

where $\dot{u}$, $\dot{p}$ and $\dot{\epsilon}_v$ are displacement, pressure and volume change rates, respectively; $\overset{\circ}{\sigma}$ is the stress rate obtained from the hypoplastic constitutive equation (4.3)

$$\overset{\circ}{\sigma} = G(\sigma, D). \tag{4.21}$$

By using eqs. (4.8)-(4.10) the weak equations with three fields $(\dot{u}, \dot{p}, \dot{\epsilon}_v)$ may be expressed as

$$\int_\Omega \delta\left(\nabla^s\dot{u}\right)^T \sigma d\Omega = \int_\Omega \delta\dot{u}^T f d\Omega + \int_{\partial\Omega_\sigma} \delta\dot{u}^T\bar{t}\, dA, \tag{4.22}$$

$$\int_\Omega \delta\dot{\epsilon}_v \left[\frac{1}{3}\bar{m}^T\overset{\circ}{\sigma} - \dot{p}\right] d\Omega = 0, \tag{4.23}$$

$$\int_\Omega \delta\dot{p}\left[\bar{m}^T\nabla^s\dot{u} - \dot{\epsilon}_v\right] d\Omega = 0. \tag{4.24}$$

Introducing finite element approximations to the variable as

$$u \approx N(\xi)\tilde{u}(t); \quad p \approx \Phi_p(\xi)\tilde{p}; \quad \epsilon_v \approx \Phi_v(\xi)\tilde{\epsilon}_v, \tag{4.25}$$

$$\dot{u} \approx N(\xi)\dot{\tilde{u}}(t); \quad \dot{p} \approx \Phi_p(\xi)\dot{\tilde{p}}(t); \quad \dot{\epsilon}_v \approx \Phi_v(\xi)\dot{\tilde{\epsilon}}_v(t), \tag{4.26}$$

and inserting into eqs. (4.22), (4.23) and (4.24) we have

$$\underline{Q(\dot{\sigma}) = \dot{f}_{ext}}, \tag{4.27}$$

$$\underline{Q_p - C\dot{\tilde{p}} = 0}, \tag{4.28}$$

$$\underline{g\dot{\tilde{u}} - C^T\dot{\tilde{\epsilon}}_v = 0}, \tag{4.29}$$

where

$$Q = \int_{\Omega} B_u^T \dot{\sigma} d\Omega, \tag{4.30}$$

$$\dot{f}_{ext} = \int_{\Omega} N^T \dot{f} d\Omega + \int_{\partial\Omega_{\sigma}} N^T \dot{t} dA, \tag{4.31}$$

$$Q_p = \int_{\Omega} \Phi_v^T \frac{1}{3} \bar{m}^T \dot{\sigma} d\Omega, \tag{4.32}$$

$$C = \int_{\Omega} \Phi_v^T \Phi_p d\Omega, \tag{4.33}$$

$$g = \int_{\Omega} \Phi_p^T \bar{m}^T B d\Omega. \tag{4.34}$$

Following *Zienkiewicz and Taylor, 2000*[127] we choose $\Phi_v = \Phi_p$ as well as assume that the pressure vector $\tilde{p}$ and volume change vector $\tilde{\epsilon}_v$ are taken locally in each element. Then, we have

$$\dot{\tilde{p}} = C^{-1} Q_p, \tag{4.35}$$

$$\dot{\tilde{\epsilon}}_v = \overline{W} \dot{u}, \tag{4.36}$$

where

$$\overline{W} = C^{-1} g \dot{u}. \tag{4.37}$$

Substituting (4.36) and (4.26) into (4.19) we have the rate of the mixed strain in each element

$$\dot{\epsilon} = I_d B_u \dot{u} + \frac{1}{3} \bar{m} \Phi_v \overline{W} \dot{u} = \begin{bmatrix} I_d & \frac{1}{3}\bar{m} \end{bmatrix} \begin{bmatrix} B_u \\ B_v \end{bmatrix} \dot{u}, \tag{4.38}$$

where

$$B_v = \Phi_v \overline{W}. \tag{4.39}$$

Let us recall eqs. (4.20) and (4.30)

$$\dot{\sigma} = I_d \dot{\sigma} + \bar{m} \dot{p}, \tag{4.40}$$

$$Q = \int_{\Omega} B_u^T \dot{\sigma} d\Omega. \tag{4.41}$$

By use of equs. (4.40) and (4.41), in addition to eqs. (4.32), (4.34), (4.35), (4.37) and (4.39), we can rewrite $\boldsymbol{Q}$ in the alternative form

$$\boldsymbol{Q} = \int_{\Omega} \boldsymbol{B}_u^T \dot{\boldsymbol{\sigma}} d\Omega = \int_{\Omega} \left[\begin{array}{cc} \boldsymbol{B}_u^T & \boldsymbol{B}_v^T \end{array} \right] \left[\begin{array}{c} \boldsymbol{I}_d \\ \frac{1}{3}\bar{\boldsymbol{m}}^T \end{array} \right] \dot{\breve{\boldsymbol{\sigma}}} d\Omega. \tag{4.42}$$

It is observed that it is not necessary to compute the true mixed stress $\boldsymbol{\sigma}$ except when reporting final results [127].

Let us denote $\breve{\boldsymbol{D}}_T$ as the tangent operator of constitutive law. By considering eq. (4.38) the tangent stiffness matrix can be written as

$$\begin{aligned} \mathbf{K}_T &= \int_{\Omega} \left[\begin{array}{cc} \boldsymbol{B}_u^T & \boldsymbol{B}_v^T \end{array} \right] \left[\begin{array}{c} \boldsymbol{I}_d \\ \frac{1}{3}\bar{\boldsymbol{m}}^T \end{array} \right] \breve{\boldsymbol{D}}_T \left[\begin{array}{cc} \boldsymbol{I}_d & \frac{1}{3}\bar{\boldsymbol{m}} \end{array} \right] \left[\begin{array}{c} \boldsymbol{B}_u \\ \boldsymbol{B}_v \end{array} \right] d\Omega \\ &= \int_{\Omega} \left[\begin{array}{cc} \boldsymbol{B}_u^T & \boldsymbol{B}_v^T \end{array} \right] \bar{\boldsymbol{D}}_T \left[\begin{array}{c} \boldsymbol{B}_u \\ \boldsymbol{B}_v \end{array} \right] d\Omega, \end{aligned} \tag{4.43}$$

where

$$\bar{\boldsymbol{D}}_T = \left[\begin{array}{c} \boldsymbol{I}_d \\ \frac{1}{3}\bar{\boldsymbol{m}}^T \end{array} \right] \breve{\boldsymbol{D}}_T \left[\begin{array}{cc} \boldsymbol{I}_d & \frac{1}{3}\bar{\boldsymbol{m}} \end{array} \right] = \left[\begin{array}{cc} \boldsymbol{I}_d\breve{\boldsymbol{D}}_T\boldsymbol{I}_d & \frac{1}{3}\boldsymbol{I}_d\breve{\boldsymbol{D}}_T\bar{\boldsymbol{m}} \\ \frac{1}{3}\bar{\boldsymbol{m}}^T\breve{\boldsymbol{D}}_T\boldsymbol{I}_d & \frac{1}{9}\bar{\boldsymbol{m}}^T\breve{\boldsymbol{D}}_T\bar{\boldsymbol{m}} \end{array} \right]. \tag{4.44}$$

Based on the three-field mixed formulation the eight-node (Q8) and four-node (Q4) quadrilateral elements and the three-node triangular element (CST) will be considered in Chapter 5.

4.4. Enhanced assumed strain method

Low-order quadrilaterals employing the enhanced assumed strain method (EAS) were developed by *Simo and Rifai* [99]. In their approach the strain field $\boldsymbol{\epsilon}$ is assumed in the form

$$\boldsymbol{\epsilon}(\boldsymbol{u}, \boldsymbol{\epsilon}_{en}) = \nabla^s \boldsymbol{u} + \boldsymbol{\epsilon}_{en}, \tag{4.45}$$

where $\boldsymbol{\epsilon}_{en}$ is the enhanced mode defined below.

By considering eqs. (4.8)-(4.10) the following equations

$$\int_{\Omega} \delta \left(\nabla^s \dot{\boldsymbol{u}} \right)^T \boldsymbol{\sigma} \, d\Omega = \int_{\Omega} \delta \dot{\boldsymbol{u}}^T \boldsymbol{f} \, d\Omega + \int_{\partial\Omega_\sigma} \delta \dot{\boldsymbol{u}}^T \dot{\bar{\boldsymbol{t}}} \, dA, \tag{4.46}$$

$$\int_{\Omega} \delta \dot{\boldsymbol{\epsilon}}_{en}^T \left[\boldsymbol{G} \left(\boldsymbol{\sigma}, \dot{\boldsymbol{\epsilon}} \right) - \dot{\boldsymbol{\sigma}} \right] \, d\Omega = 0, \tag{4.47}$$

$$\int_{\Omega} \delta \dot{\boldsymbol{\sigma}}^T \left[\nabla^s \dot{\boldsymbol{u}} - \dot{\boldsymbol{\epsilon}} \right] \, d\Omega = 0, \tag{4.48}$$

provide the variational formulation of the EAS method in the framework of hypoplastic models with the displacement rate $\dot{\boldsymbol{u}}$, the stress rate $\dot{\boldsymbol{\sigma}}$ and the strain rate $\dot{\boldsymbol{\epsilon}}_{en}$ referred to as independent variables.

Let us consider the following approximations

$$\boldsymbol{u} \approx \boldsymbol{N}_u(\boldsymbol{\xi})\,\tilde{\boldsymbol{u}}(t) \quad ; \quad \boldsymbol{\sigma} \approx \boldsymbol{B}_\sigma(\boldsymbol{\xi})\,\boldsymbol{\beta}(t) \quad ; \quad \boldsymbol{\epsilon}_{en} \approx \boldsymbol{B}_\alpha(\boldsymbol{\xi})\,\boldsymbol{\alpha}(t), \tag{4.49}$$

$$\dot{\boldsymbol{u}} \approx \boldsymbol{N}_u(\boldsymbol{\xi})\,\dot{\tilde{\boldsymbol{u}}}(t) \quad ; \quad \dot{\boldsymbol{\sigma}} \approx \boldsymbol{B}_\sigma(\boldsymbol{\xi})\,\dot{\boldsymbol{\beta}}(t) \quad ; \quad \dot{\boldsymbol{\epsilon}}_{en} \approx \boldsymbol{B}_\alpha(\boldsymbol{\xi})\,\dot{\boldsymbol{\alpha}}(t), \tag{4.50}$$

where $\boldsymbol{N}_u$, $\boldsymbol{B}_\epsilon$, $\boldsymbol{B}_\sigma$ are the shape function of the displacement, the enhanced strain and the stress, respectively.

Substituting the approximations (4.50) into eqs. (4.46)-(4.48) leads to the discrete system of equations

$$\begin{cases} \int_\Omega \boldsymbol{B}_u^{\mathrm{T}} \dot{\boldsymbol{\sigma}}\, d\Omega & = \quad \dot{\boldsymbol{f}}_{ext}. \\ \int_\Omega \boldsymbol{B}_\sigma^{\mathrm{T}} \boldsymbol{B}_\alpha\, d\Omega\, \dot{\boldsymbol{\alpha}} & = \quad \boldsymbol{0}. \\ \int_\Omega \boldsymbol{B}_\alpha^{\mathrm{T}} \boldsymbol{G}\,(\boldsymbol{\sigma}, \dot{\boldsymbol{\epsilon}})\, d\Omega - \int_\Omega \boldsymbol{B}_\alpha^{\mathrm{T}} \boldsymbol{B}_\sigma\, d\Omega\, \dot{\boldsymbol{\beta}} & = \quad \boldsymbol{0}. \end{cases} \tag{4.51}$$

The enhanced strain and stress are computed in tensor notation as follows [126]

$$\boldsymbol{\epsilon}_{en} = \frac{j_0}{j(\xi, \eta)} \boldsymbol{A}^{\mathrm{T}} \boldsymbol{E}(\boldsymbol{\xi}, \boldsymbol{\alpha}) \boldsymbol{A}, \tag{4.52}$$

$$\boldsymbol{\sigma} = \boldsymbol{A}^{-1} \boldsymbol{\Sigma}(\boldsymbol{\xi}, \boldsymbol{\beta}) \boldsymbol{A}^{-\mathrm{T}}, \tag{4.53}$$

where $\boldsymbol{E}$ and $\boldsymbol{\Sigma}$ are the strain and stress in the isoparametric space, respectively; j is the determinant of the jacobian matrix, $\boldsymbol{A}$ and j_0 are the jacobian matrix and its determinant, respectively, at the center of element corresponding to $\xi = 0$ and $\eta = 0$.

These transformations (4.52) and (4.53) have the property that [104]

$$\mathrm{tr}(\boldsymbol{\sigma}\boldsymbol{\epsilon}_{en}) = \frac{j_0}{j(\boldsymbol{\xi})} \mathrm{tr}\,(\boldsymbol{\Sigma}\boldsymbol{E})\,. \tag{4.54}$$

Eqs. (4.52) and (4.53) may be written in matrix form as follows

$$\boldsymbol{\epsilon}_{en} = \frac{j_0}{j(\boldsymbol{\xi})} \boldsymbol{F}_0^{\mathrm{T}} \boldsymbol{E}(\boldsymbol{\xi}, \boldsymbol{\alpha}), \tag{4.55}$$

$$\boldsymbol{\sigma} = \boldsymbol{F}_0^{-1} \boldsymbol{\Sigma}(\boldsymbol{\xi}, \boldsymbol{\beta}), \tag{4.56}$$

where

$$
\boldsymbol{F}_0^{\mathrm{T}} =
\begin{bmatrix}
A_{11}^2 & A_{21}^2 & 0 & A_{11}A_{21} \\
A_{12}^2 & A_{22}^2 & 0 & A_{12}A_{22} \\
0 & 0 & 1 & 0 \\
2A_{11}A_{12} & 2A_{21}A_{22} & 0 & A_{11}A_{22} + A_{12}A_{21}
\end{bmatrix},
\tag{4.57}
$$

and A_{ij} are the components of the tensor $\boldsymbol{A}$.

The interpolation formulas of the enhanced strain and stress fields, respectively, are assumed in the following form

$$
\boldsymbol{E}(\boldsymbol{\xi}, \boldsymbol{\alpha}) =
\begin{pmatrix}
\mathcal{E}_{\xi\xi} \\
\mathcal{E}_{\eta\eta} \\
0 \\
2\mathcal{E}_{\xi\eta}
\end{pmatrix}
=
\begin{bmatrix}
\xi & 0 & 0 & 0 \\
0 & \eta & 0 & 0 \\
0 & 0 & 0 & 0 \\
0 & 0 & \xi & \eta
\end{bmatrix}
\begin{pmatrix}
\alpha_1 \\
\alpha_2 \\
\alpha_3 \\
\alpha_4
\end{pmatrix},
\tag{4.58}
$$

$$
\boldsymbol{\Sigma}(\boldsymbol{\xi}, \boldsymbol{\beta}) =
\begin{bmatrix}
1 & 0 & 0 & 0 \\
0 & 1 & 0 & 0 \\
0 & 0 & 1 & 0 \\
0 & 0 & 0 & 1
\end{bmatrix}
\begin{pmatrix}
\beta_1 \\
\beta_2 \\
\beta_3 \\
\beta_4
\end{pmatrix}.
\tag{4.59}
$$

The interpolation of the enhanced strain (4.58) results in the equivalence between the EAS element and the incompatible mode element [111].

By use of the interpolations (4.58) and (4.59), the integral over element of eq. (4.54) written in matrix form yields

$$
\int_{\Omega_e} \boldsymbol{\sigma}^{\mathrm{T}} \boldsymbol{\epsilon}_{en}\, d\Omega = j_0 \int_{\Omega_e} \boldsymbol{\Sigma}^{\mathrm{T}} \boldsymbol{E}\, d\Omega = 0.
\tag{4.60}
$$

Consequently, we obtain the orthogonality condition between the enhanced strain shape function and the stress shape function over element

$$
\int_{\Omega_e} \boldsymbol{B}_\sigma^{\mathrm{T}} \boldsymbol{B}_\alpha\, d\Omega = \int_{\Omega_e} \boldsymbol{B}_\alpha^{\mathrm{T}} \boldsymbol{B}_\sigma\, d\Omega = 0,
\tag{4.61}
$$

as well as in the whole domain as a sum of integration over the volume of all finite elements

$$
\int_{\Omega} \boldsymbol{B}_\sigma^{\mathrm{T}} \boldsymbol{B}_\alpha\, d\Omega = \int_{\Omega} \boldsymbol{B}_\alpha^{\mathrm{T}} \boldsymbol{B}_\sigma\, d\Omega = 0.
\tag{4.62}
$$

On inserting (4.62) into (4.51) we obtain

$$\begin{cases} \int_\Omega \boldsymbol{B}_u^{\mathrm{T}} \dot{\boldsymbol{\sigma}} \, d\Omega & = \dot{\boldsymbol{f}}_{ext}. \\ \int_\Omega \boldsymbol{B}_\alpha^{\mathrm{T}} \boldsymbol{G}(\boldsymbol{\sigma}, \dot{\boldsymbol{\epsilon}}) \, d\Omega & = 0. \end{cases} \tag{4.63}$$

It should be noted that the discrete stress field is undetermined due to the orthogonality condition (4.60). Therefore, *Simo and Rifai* [99] suggested a procedure for stress recovery based on a least-square optimization. The evaluation of the discrete stress field can be referred to [94, 97, 122] and has been debated. *Bischoff et al., 1999* [13] showed that the stress field calculated from an elastic constitutive law converges to the correct solution which satisfies the orthogonality assumption (4.60). Herein we consider the stress field derived from the material law

$$\dot{\boldsymbol{\sigma}} = \boldsymbol{G}(\boldsymbol{\sigma}, \dot{\boldsymbol{\epsilon}}). \tag{4.64}$$

Consequently, the unknown variables are now displacement and strain rates. The set of equations (4.63) to be solved becomes

$$\begin{cases} \int_\Omega \boldsymbol{B}_u^{\mathrm{T}} \dot{\boldsymbol{\sigma}} \, d\Omega & = \dot{\boldsymbol{f}}_{ext}. \\ \int_\Omega \boldsymbol{B}_\alpha^{\mathrm{T}} \dot{\boldsymbol{\sigma}} \, d\Omega & = 0. \end{cases} \quad \text{or} \quad \begin{cases} \int_\Omega \boldsymbol{B}_u^{\mathrm{T}} \boldsymbol{\sigma} \, d\Omega & = \boldsymbol{f}_{ext}. \\ \int_\Omega \boldsymbol{B}_\alpha^{\mathrm{T}} \boldsymbol{\sigma} \, d\Omega & = 0. \end{cases} \tag{4.65}$$

This method is studied through the use of the four-node quadrilateral element in Chapter 5.

4.5. Mixed enhanced strain method

In the EAS method, imposing the orthogonality assumption (4.60) between stress and strain leads to elimination of the discretized stress field. *Kasper and Taylor* [54] suggested the mixed interpolation of the stress as an unknown variable, together with the displacement and the enhanced strain. More details of this method can be found in [54].

Based on eqs. (4.8)-(4.10) the variational formulation of rate type for hypoplastic models takes the following form

$$\int_\Omega \delta \left(\nabla^s \dot{\boldsymbol{u}}\right)^{\mathrm{T}} \dot{\boldsymbol{\sigma}} \, d\Omega = \int_\Omega \delta \dot{\boldsymbol{u}}^{\mathrm{T}} \dot{\boldsymbol{f}} \, d\Omega + \int_{\partial \Omega_\sigma} \delta \dot{\boldsymbol{u}}^{\mathrm{T}} \dot{\bar{\boldsymbol{t}}} \, dA, \tag{4.66}$$

$$\int_\Omega \delta \dot{\boldsymbol{\epsilon}}^{\mathrm{T}} \left[\boldsymbol{G}(\boldsymbol{\sigma}, \dot{\boldsymbol{\epsilon}}) - \dot{\boldsymbol{\sigma}}\right] d\Omega = 0, \tag{4.67}$$

$$\int_\Omega \delta \dot{\boldsymbol{\sigma}}^{\mathrm{T}} \left[\nabla^s \dot{\boldsymbol{u}} - \dot{\boldsymbol{\epsilon}}\right] d\Omega = 0, \tag{4.68}$$

where the displacement rate $\dot{u}$, the stress rate $\dot{\sigma}$ and the strain rate $\dot{\epsilon}$ as independent variables.

The interpolation formulas of stress and strain in the isoparametric space read [54]

$$\sigma = \beta_0 + A\mathcal{E}_1(\xi, \beta)A^T, \tag{4.69}$$

$$\epsilon = \gamma_0 + \frac{1}{j}A^{-T}\left[\mathcal{E}_1(\xi, \gamma) + \mathcal{E}_2(\xi, \alpha)\right]A^{-1}, \tag{4.70}$$

where

$$\beta_0 = A\hat{\beta}_0 A^T \quad , \quad \gamma_0 = A^{-T}\hat{\gamma}_0 A^{-1} \quad ; \tag{4.71}$$

$\hat{\beta}_0$, β, $\hat{\gamma}_0$, γ_0 and α are parameters; $\mathcal{E}_1(\xi, .)$ and $\mathcal{E}_2(\xi, .)$ are chosen as the following, respectively

$$\mathcal{E}_1(\xi, \gamma) = \begin{bmatrix} \eta\gamma_1 & 0 \\ 0 & \xi\gamma_2 \end{bmatrix} = \begin{bmatrix} \eta & 0 \\ 0 & \xi \end{bmatrix} \begin{pmatrix} \gamma_1 \\ \gamma_2 \end{pmatrix}, \tag{4.72}$$

$$\mathcal{E}_2(\xi, \alpha) = \begin{bmatrix} \eta\alpha_1 & 0 \\ 0 & \xi\alpha_2 \end{bmatrix} = \begin{bmatrix} \eta & 0 \\ 0 & \xi \end{bmatrix} \begin{pmatrix} \alpha_1 \\ \alpha_2 \end{pmatrix}, \tag{4.73}$$

and satisfy the orthogonality conditions

$$\int_{-1}^{1}\int_{-1}^{1} \mathcal{E}_1(.) \, d\xi d\eta = 0 \, ; \int_{-1}^{1}\int_{-1}^{1} \mathcal{E}_2(.) \, d\xi d\eta = 0 \, ;$$

$$\int_{-1}^{1}\int_{-1}^{1} \mathcal{E}_1(.)\mathcal{E}_2(.) \, d\xi d\eta = 0. \tag{4.74}$$

The jacobian A is averaged over the element Ω_e

$$A = \frac{1}{\Omega_e}\int_{\Omega_e} J(\xi) \, d\Omega. \tag{4.75}$$

On inserting eqs. (4.69) and (4.70) into eq. (4.68) and using the orthogonality conditions (4.74), in addition to integrating with time we have

$$\gamma_0 = \frac{1}{\Omega_e}\int_{\Omega_e} \nabla^s u \, d\Omega = \frac{1}{4j_0}\int_{\Omega_e} \nabla^s u \, d\Omega, \tag{4.76}$$

as well as the mixed enhanced strain ϵ in terms of the nodal displacement parameters $\tilde{u}$ and the enhanced modes α

$$\epsilon = \gamma_0 + \frac{1}{j}A^{-T}\mathcal{E}_1(\xi)\overline{G}^{-1}g\tilde{u}A^{-1} + \frac{1}{j}A^{-T}\mathcal{E}_2(\xi)\alpha A^{-1}, \tag{4.77}$$

or in matrix notation

$$\boldsymbol{\epsilon} = \boldsymbol{B}\left(\xi\right)\tilde{\boldsymbol{u}} + \boldsymbol{B}_\alpha\left(\xi\right)\boldsymbol{\alpha}, \tag{4.78}$$

where $\boldsymbol{B}$ is the strain-displacement matrix, $\boldsymbol{B}_\alpha$ is the stress interpolation matrix, j is the determinant of the jacobian matrix $\boldsymbol{A}$, and j_0 is the value of j at the center of element corresponding to $\xi = 0$ and $\eta = 0$.

Herein, the mapping between tensors and matrices are expressed as

$$\boldsymbol{\mathcal{E}}_1\left(\boldsymbol{\xi}\right)\boldsymbol{\beta} \quad \to \quad \bar{\boldsymbol{E}}_1\boldsymbol{\beta}, \tag{4.79}$$

$$\boldsymbol{A}^{\mathrm{T}}(\nabla^s\boldsymbol{u} - \boldsymbol{\gamma}_0)\boldsymbol{A} \quad \to \quad \boldsymbol{E}_3\tilde{\boldsymbol{u}}, \tag{4.80}$$

$$\boldsymbol{\gamma}_0 + \frac{1}{j}\boldsymbol{A}^{-\mathrm{T}}\boldsymbol{\mathcal{E}}_1(\boldsymbol{\xi})\overline{\boldsymbol{G}}^{-1}\overline{\boldsymbol{g}}\tilde{\boldsymbol{u}}\boldsymbol{A}^{-1} \quad \to \quad \boldsymbol{B}\left(\xi\right)\tilde{\boldsymbol{u}}, \tag{4.81}$$

$$\frac{1}{j}\boldsymbol{A}^{-\mathrm{T}}\boldsymbol{\mathcal{E}}_2(\boldsymbol{\xi})\boldsymbol{\alpha}\boldsymbol{A}^{-1} \quad \to \quad \boldsymbol{B}_\alpha\left(\xi\right)\boldsymbol{\alpha}, \tag{4.82}$$

where

$$\bar{\boldsymbol{E}}_1 \;\; = \;\; \begin{bmatrix} \eta & 0 \\ 0 & \xi \\ 0 & 0 \end{bmatrix}, \tag{4.83}$$

$$\overline{\boldsymbol{g}} \;\; = \;\; \int_\Omega \bar{\boldsymbol{E}}_1^{\mathrm{T}}\boldsymbol{E}_3\,d\Omega, \tag{4.84}$$

$$\overline{\boldsymbol{G}} \;\; = \;\; \int_\Omega \frac{1}{j}\bar{\boldsymbol{E}}_1^{\mathrm{T}}\boldsymbol{E}_3\,d\Omega = \int_{-1}^{1}\int_{-1}^{1}\bar{\boldsymbol{E}}_1^{\mathrm{T}}\boldsymbol{E}_3\,d\xi d\eta. \tag{4.85}$$

Finite element approximations for displacements give

$$\boldsymbol{u} \approx \boldsymbol{N}_u\tilde{\boldsymbol{u}} \qquad \nabla^s\boldsymbol{u} \approx \boldsymbol{B}_u\tilde{\boldsymbol{u}}, \tag{4.86}$$

where $\boldsymbol{N}_u$ is the standard shape function of displacement and $\boldsymbol{B}_u$ is the standard strain-displacement matrix. It should be noted that $\boldsymbol{B}$ in eq. (4.78) and $\boldsymbol{B}_u$ in eq. (4.86) are different, however, they satisfy the following relation

$$\int_{\Omega_e}\boldsymbol{B}^{\mathrm{T}}\boldsymbol{\sigma}\,d\Omega = \int_{\Omega_e}\boldsymbol{B}_u^{\mathrm{T}}\boldsymbol{\sigma}\,d\Omega. \tag{4.87}$$

The discrete system of equations for the three fields $(\dot{\boldsymbol{u}}, \dot{\boldsymbol{\epsilon}}, \dot{\boldsymbol{\sigma}})$ can be obtained by substituting (4.86) and (4.78) into the remaining equations (4.66) and (4.67)

$$\begin{cases} \int_\Omega \boldsymbol{B}_u^{\mathrm{T}} \dot{\boldsymbol{\sigma}} \, d\Omega & = & \dot{\boldsymbol{f}}_{ext}. \\ \int_\Omega \boldsymbol{B}^{\mathrm{T}} \left[\boldsymbol{G}\left(\boldsymbol{\sigma}, \dot{\boldsymbol{\epsilon}}\right) - \dot{\boldsymbol{\sigma}} \right] d\Omega & = & \boldsymbol{0}. \\ \int_\Omega \boldsymbol{B}_\alpha^{\mathrm{T}} \boldsymbol{G}\left(\boldsymbol{\sigma}, \dot{\boldsymbol{\epsilon}}\right) d\Omega. & = & \boldsymbol{0}. \end{cases} \tag{4.88}$$

If $\dot{\boldsymbol{\sigma}} = \boldsymbol{G}\left(\boldsymbol{\sigma}, \dot{\boldsymbol{\epsilon}}\right)$ is satisfied, by use of the relation (4.87) the above equation system reduces to

$$\begin{cases} \int_\Omega \boldsymbol{B}^{\mathrm{T}} \dot{\boldsymbol{\sigma}} \, d\Omega & = & \dot{\boldsymbol{f}}_{ext} \\ \int_\Omega \boldsymbol{B}_\alpha^{\mathrm{T}} \dot{\boldsymbol{\sigma}} \, d\Omega & = & \boldsymbol{0} \end{cases} \quad \text{or} \quad \begin{cases} \int_\Omega \boldsymbol{B}^{\mathrm{T}} \boldsymbol{\sigma} \, d\Omega & = & \boldsymbol{f}_{ext} \\ \int_\Omega \boldsymbol{B}_\alpha^{\mathrm{T}} \boldsymbol{\sigma} \, d\Omega & = & \boldsymbol{0} \end{cases} \tag{4.89}$$

which would also result from the following modified variational formulation for two independent fields $(\dot{\boldsymbol{u}}, \dot{\boldsymbol{\epsilon}})$

$$\int_\Omega \delta \dot{\boldsymbol{\epsilon}}^{\mathrm{T}} \dot{\boldsymbol{\sigma}} d\Omega = \int_\Omega \delta \dot{\boldsymbol{u}}^{\mathrm{T}} \boldsymbol{f} d\Omega + \int_{\partial \Omega_\sigma} \delta \dot{\boldsymbol{u}}^{\mathrm{T}} \dot{\bar{\boldsymbol{t}}} dA. \tag{4.90}$$

Based on the mixed enhanced strain method the four-node quadrilateral element will be considered in Chapter 5.

4.6. Finite element equations

Linearization of the equation systems (4.65) and (4.89) for the EAS and MES methods yields

$$\begin{bmatrix} \boldsymbol{K}_{uu} & \boldsymbol{K}_{u\alpha} \\ \boldsymbol{K}_{\alpha u} & \boldsymbol{K}_{\alpha\alpha} \end{bmatrix} \begin{Bmatrix} d\tilde{\boldsymbol{u}} \\ d\boldsymbol{\alpha} \end{Bmatrix} = \begin{Bmatrix} -\boldsymbol{f}_1 \\ -\boldsymbol{f}_2 \end{Bmatrix}, \tag{4.91}$$

where

$$\boldsymbol{K}_{uu} = \int_\Omega \boldsymbol{B}_u^T \frac{\partial \boldsymbol{\sigma}}{\partial \boldsymbol{\epsilon}} \boldsymbol{B}_u d\Omega \quad ; \qquad \boldsymbol{K}_{u\alpha} = \int_\Omega \boldsymbol{B}_u^T \frac{\partial \boldsymbol{\sigma}}{\partial \boldsymbol{\epsilon}} \boldsymbol{B}_\alpha d\Omega \, ; \tag{4.92}$$

$$\boldsymbol{K}_{\alpha u} = \int_\Omega \boldsymbol{B}_\alpha^T \frac{\partial \boldsymbol{\sigma}}{\partial \boldsymbol{\epsilon}} \boldsymbol{B}_u d\Omega \quad ; \qquad \boldsymbol{K}_{\alpha\alpha} = \int_\Omega \boldsymbol{B}_\alpha^T \frac{\partial \boldsymbol{\sigma}}{\partial \boldsymbol{\epsilon}} \boldsymbol{B}_\alpha d\Omega \, ; \tag{4.93}$$

$$\boldsymbol{f}_2 = \int_\Omega \boldsymbol{B}_\alpha^T \boldsymbol{\sigma} d\Omega \quad ; \qquad \boldsymbol{f}_1 = \int_\Omega \boldsymbol{B}_u^T \boldsymbol{\sigma} d\Omega - \boldsymbol{f}_{ext}. \tag{4.94}$$

Invoking the second equation of (4.91) one gets

$$d\boldsymbol{\alpha} = -\boldsymbol{K}_{\alpha\alpha}^{-1}\left(\boldsymbol{f}_2 + \boldsymbol{K}_{\alpha u}d\tilde{\boldsymbol{u}}\right), \tag{4.95}$$

which can be solved at the element level. Thus, the global unknown variables are only the displacements. Substituting (4.95) into the first equation of (4.91) we obtain

$$\boldsymbol{K}d\tilde{\boldsymbol{u}} = \boldsymbol{R}, \tag{4.96}$$

where

$$\boldsymbol{K} = \left(\boldsymbol{K}_{uu} - \boldsymbol{K}_{u\alpha}\boldsymbol{K}_{\alpha\alpha}^{-1}\boldsymbol{K}_{\alpha u}\right), \tag{4.97}$$

$$\boldsymbol{R} = -\boldsymbol{f}_1 + \boldsymbol{K}_{u\alpha}\boldsymbol{K}_{\alpha\alpha}^{-1}\boldsymbol{f}_2. \tag{4.98}$$

A solution strategy for eq. (4.95) can be found in *Simo and Rifai, 1990*[99], *Kasper and Taylor, 1997*[54]. The nonlinear system of equations (4.96) is solved by the BFGS algorithm [127].

The tangent operator $\dfrac{\partial\boldsymbol{\sigma}}{\partial\boldsymbol{\epsilon}}$ in eqs. (4.92) and (4.93) can be expressed as

$$\frac{\partial\boldsymbol{\sigma}}{\partial\boldsymbol{\epsilon}} = \boldsymbol{\mathcal{L}} + \boldsymbol{N} \otimes \frac{\boldsymbol{D}}{\|\boldsymbol{D}\|}. \tag{4.99}$$

It is observed that the tangent operator (4.99) is non-symmetric.

There are various ways to calculate the tangent operator due to the complicated constitutive law (4.2). It may be directly computed by eq. (4.99) [71] or approximated by numerical differentiation [34, 96, 44]. Alternatively, one may use the linear term as an approximation of the tangent operator [107, 49, 83]. In this thesis, the tangent operator is approximated by $2\boldsymbol{\mathcal{L}}$ as proposed in [83].

Since the material behaviour is assumed to be rate-independent, the introduction of a fictitious time scale is necessary for a quasi-static loading process. During integration, the numerical errors are not controlled if the stress, void ratio and tangent operator are updated once in the time increment [49]. Thus, the various sub-time stepping algorithms are proposed to overcome this drawback in literature [96, 83, 34, 44, 49]. The sub-time stepping algorithm suggested by *Nübel et al.*[83] shown in Fig. 4.1 is used in the next chapter.

The flowchart for the EAS method is depicted in Fig. 4.2.
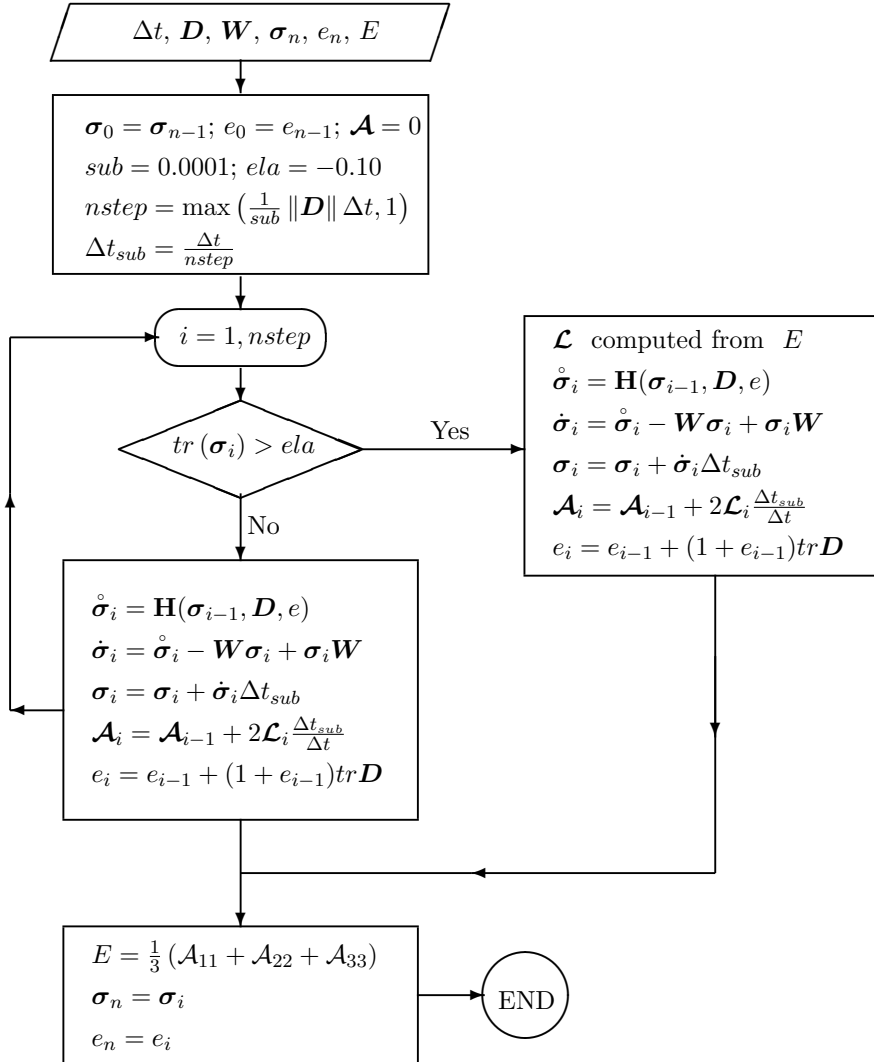
Figure 4.1.: Flow chart of the time integration scheme with the sub-time stepping algorithm proposed by *Nübel et al., 1998*[83].
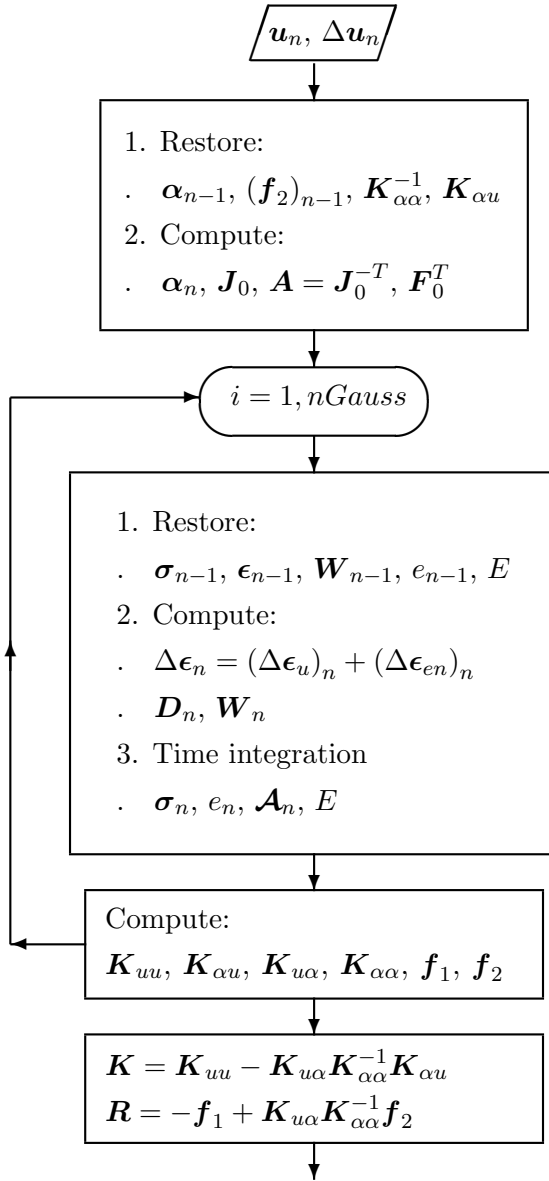
Figure 4.2.: Flow chart of the enhanced assumed strain method written in element level.

5. Numerical examples

In this chapter the different sub-time stepping algorithms are investigated firstly. Then several numerical examples demonstrating the capability and performance of the different finite element formulations mentioned in Chapter 4 are presented under plane strain condition. The numerical results are compared with the available experimental data for Hostun RF sand and the numerical results for Karlsruhe sand on biaxial tests. Finally, the tolerance value used for controlling the solution in biaxial test is examined. All simulations presented are implemented with the help of the non-linear finite element code FEAP[104, 105, 103].

5.1. The sub-time stepping

We investigate the sub-time stepping algorithms proposed by *Roddeman, 1997*[96], *Nübel et al., 1998*[83] and *Fellin and Ostermann, 2002*[34] in the examples of odeometer, biaxial and simple shearing tests of the soil specimen of $1\,m$ width and $1\,m$ height [34]. One four-node quadrilateral element based on the displacement method (Q4) is employed. The material parameters for Karlsruhe sand is given in Table 5.3.

$\varphi_c(^o)$	$h_s(MPa)$	$\bar{n}$	e_{d0}	e_{c0}	e_{i0}	α_0	β_0
30	190	0.45	0.40	0.80	1.189	0.15	1.00

Table 5.1.: Hypoplastic material parameters for Karlsruhe sand [8, 34, 51].

5.1.1. Example 1: One-dimensional compression test

In this test, a specimen has the initial conditions σ_y = -p_y = -100 N/m^2, $\sigma_x = -50\,N/m^2$ and the void ratio $e = 0.735$ at $t = 0$. It is compressed vertically by increasing the top pressure p_y to 1000 N/m^2 at $t = 1.0\,s$ and then decreasing to $600\,N/m^2$ at $t = 2\,s$. The time increment is $0.2\,s$. The geometry, boundary conditions, and numerical results are shown in Fig. 5.1.

5.1.2. Example 2: Biaxial test

A soil specimen is laterally compressed by a constant confined pressure $p_x = 100\,N/m^2$ with the initial conditions $\sigma_x = \sigma_y$ = -p_x = -100 N/m^2 and the void ratio $e = 0.735$ at $t = 0$.

a. Geometry and boundary conditions.   b. Stress-strain response.
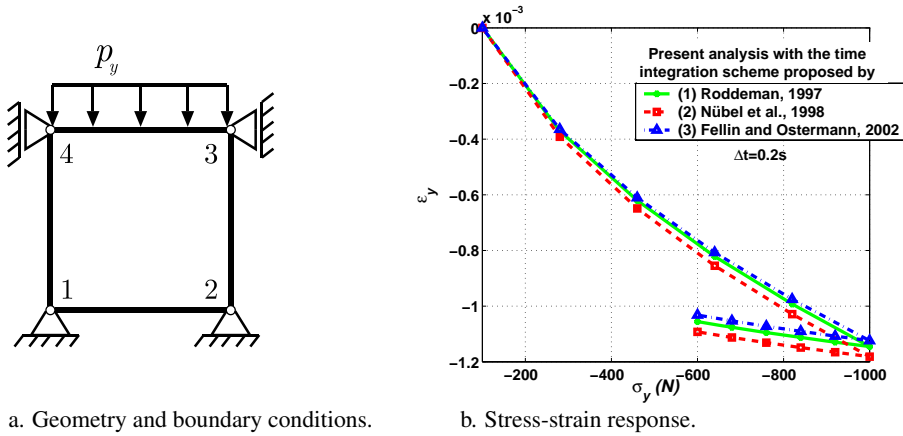
Figure 5.1.: Example 1: One-dimensional compression test.

The vertical prescribed displacement v of the top nodes is applied to $0.003\,m$ at $t = 1.0\,s$ after homogeneous consolidation. The starting and maximum time increments are $0.05\,s$ and $0.2\,s$, respectively. The geometry, boundary conditions, and numerical results are depicted in Fig. 5.2.

a. Geometry and
boundary conditions.   b. Stress-strain response.
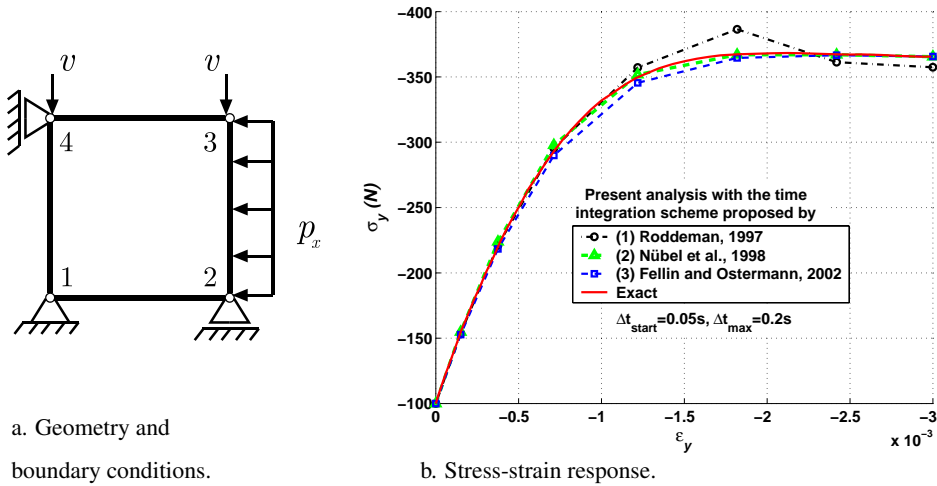
Figure 5.2.: Example 2: Biaxial test.

5.1.3. Example 3: Simple shearing

A soil specimen is vertically compressed by a constant confined pressure $p_y = 100\,N/m^2$ with the initial conditions $\sigma_x = \sigma_y = -100\,N/m^2$ and the void ratio $e = 0.735$ at $t = 0$. The horizontal prescribed displacement u of the top nodes is applied to $0.01\,m$ at $t = 1.0\,s$

after homogeneous consolidation. The starting and maximum time increments are $0.01\,s$ and $0.1\,s$, respectively. The geometry, boundary conditions, and numerical results are illustrated in Fig. 5.3.

a. Geometry and boundary conditions.   b. Stress-strain response.
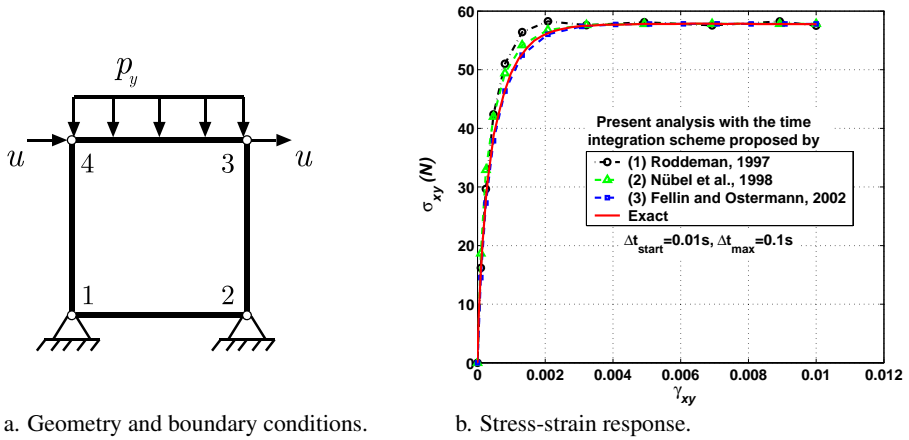
Figure 5.3.: Example 3: Simple shear test.

5.1.4. Remarks

Let (1), (2) and (3) denote the time integration schemes proposed by *Roddeman, 1997*[96], *Nübel et al., 1998*[83] and *Fellin and Ostermann, 2002*[34], respectively. As can be seen in Figs. 5.2 and 5.3, (2) and (3) give better results than (1). Some other examples such as biaxial tests presented in Section 5.2 confirm that (2) works well whereas the others interrupt as the limit-load-state reaches. Thus, (2) is used in this thesis.

For the time integration (2), *Nübel et al., 1998* used the forward Euler method. They further introduced an appropriate algorithm to handle the admissible states. If the void ratio e is larger than the maximum void ratio e_i or smaller than the minimum void ratio e_d, it is assigned e_i or e_d, respectively. In addition, if an inadmissible state such as $\mathrm{tr}\boldsymbol{\sigma} > 0$ is reached, the stress, the tangent operator and the void ratio are updated by tension cut. Herein the linear term $2\mathcal{L}$, which is symmetric, is considered as an approximation of the tangent operator (4.99).

The time integration (1) is based upon the forward Euler method while the second-order extrapolated Euler method is employed in (3). The admissible stress state is handled in both time integration schemes. If an inadmissible state such as $\mathrm{tr}\boldsymbol{\sigma} > 0$ or $e > e_d$ is reached at the end of the time step, the step is rejected and done again with half of the step size. While the unsymmetric tangent operator (4.99) is approximated by numerical differential at the end of time increment in (1), a super vector including the stress, the void ratio and the tangent operator is solved numerically in (2).

5.2. Types of elements

Different kinds of elements are used in the next examples. They are summarized in Fig. 5.4.

Element type	Method	Number of Gauss points	Notation
	MES[1]	2x2	MES
	EAS[2]	2x2	EAS
	Mix[3]	2x2	Mixed-Q4
	Disp[4]	2x2	Q4
	Mix	3x3	Mixed-Q8
	Disp	3x3	Q8
	Mix	1	Mixed-CST
	Disp	1	CST

MES[1]: Mixed enhanced strain
EAS[2]: Enhanced assumed strain
Mix[3]: Three-field mixed formulation
Disp[4]: Standard displacement

Figure 5.4.: Notation of element type.

5.2.1. Example 4

A specimen of $0.1025\,m$ width and $0.3395\,m$ height is laterally compressed by a constant confined pressure of $100\,kPa$. A prescribed vertical displacement v of the top nodes varies from 0 to $0.02\,m$ at $t = 2\,s$ after isotropical consolidation. The material in the indicated middle left part of the sample (size $0.0566\,m \times 0.0513\,m$) is equipped with an initially higher void ratio of 0.6424×1.1, whereas the void ratio is 0.6424 elsewhere as depicted in Fig. 5.5. The calculations were performed under gravity. The material parameters are given in Table 9.1 for Hostun RF sand. It should be noted that the material parameters presented here differs slightly from the material paramters originally calibrated by *Herle* [45, 46] in order to fit the experimentalal data in this example.

$\varphi_c(^o)$	$h_s(MPa)$	$\bar{n}$	e_{d0}	e_{c0}	e_{i0}	α_0	β_0
34	1000	0.29	0.63	1.00	1.15	0.134	1.35

Table 5.2.: Hypoplastic material parameters for Hostund RF sand [45, 46, 110].

The initial conditions are summarized as follows

$$\sigma_y = \sigma_c + \gamma_d\, y, \tag{5.1}$$

$$\sigma_x = \sigma_c + K_0 \sigma_y, \tag{5.2}$$

$$\sigma_{xy} = \sigma_{yx} = 0, \tag{5.3}$$

where the confined pressure $\sigma_c = -100\,kPa$; the pressure coefficient at rest $K_0 = 0.4408$; the vertical coordinate y is measured from the top of the specimen; the initial density $\gamma_d = 16.135\,KN/m^3$; σ_x and σ_y are the horizontal and vertical normal stresses, respectively; σ_{xy} is the horizontal shear stress.
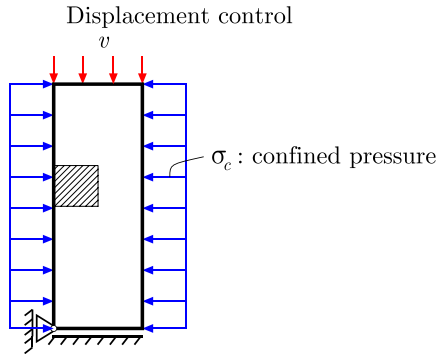
Figure 5.5.: Example 4: Biaxial test. Geometry and boundary conditions.

The test is performed with two different discretizations of the sample: 12 and 192 elements. As can be seen in Figs. 5.6a and 5.7a, the stress-strain curves behave identically for $v < 0.0097\,m$ ($\epsilon_y < 2.8645\,\%$). The localization is delayed until $v \approx 0.0097\,mm$ ($\epsilon_y \approx 2.8645\,\%$), then the performance of the diverse finite element methods starts to differ because the softening zone is now prone to element type. The smaller the number in the legends of Figs. 5.6a and 5.7a is, the closer to the experiment data of the shf40 sample (*Hammad, 1991*[43], *Desrues et al, 2000*[28]) the numerical solution is.

Q4, Mixed-Q4 and Mixed-Q8 elements face inherent limitations in the presence of localized deformations. Mesh-dependenced response for Q4 and Mixed-Q4 elements becomes evident. By considering post-peak behaviour the Q8 element behaves better than the Mixed-Q8 element.

The solutions by using MES, EAS, CST and Mixed-CST elements are in rather good agreement with the experiment [28, 43], thus showing the potential of the enhanced finite element methods and the quadrilateral finite elements composed of four diagonally crossed triangles in capturing localization. It is also observed that the numerical results obtained from CST and Mixed-CST elements are identical. Hence, CST element may be employed instead of

Mixed-CST element whose finite element formulation is more complicated than the CST element's finite element formulation.

a. Stress-strain curve.   b. Volumetric strain-axial strain.
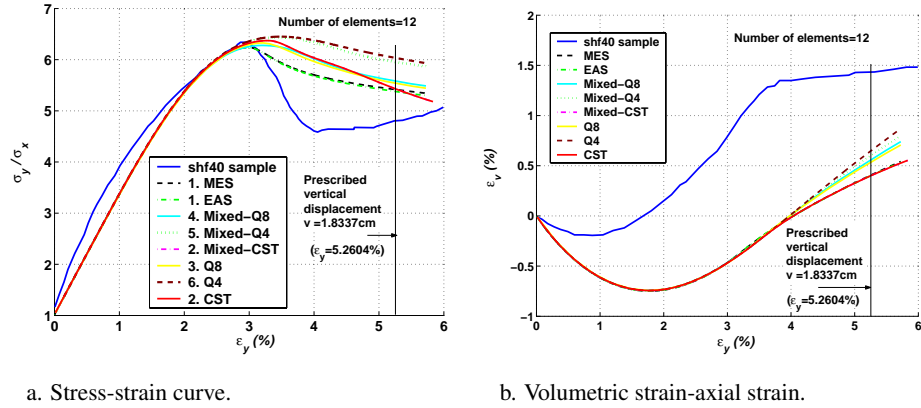
Figure 5.6.: Example 4: Biaxial test (12 elements).

a. Stress-strain curve.   b. Volumetric strain-axial strain.
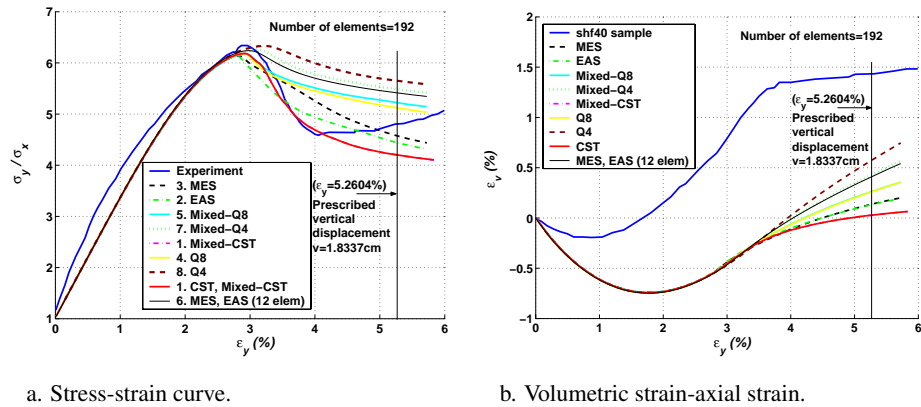
Figure 5.7.: Example 4: Biaxial test (192 elements).

The volumetric strain vs. axial strain curves are depicted in Figs. 5.6b and 5.7b. It is shown that the obtained numerical results do not match experimental results.

It is very interesting to see the performance of the different finite element formulations by considering the deformation shape of the sample (Figs. 5.8 and 5.9) in comparison with the experiment [43]. The deformation shapes prior to the bifurcation point are similar. After this point, the behaviour of every element type begins to differ. As can be seen, MES, EAS and QM6 elements are able to model shear bands whereas the Q4 element is not a good choice to capture effects of strain localization.
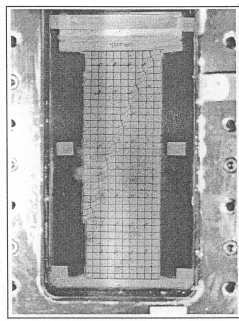
a. shf40 sample [43].   b. MES element.   c. EAS element.
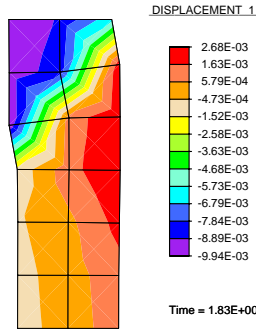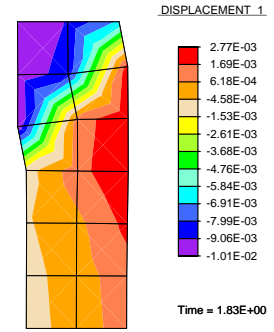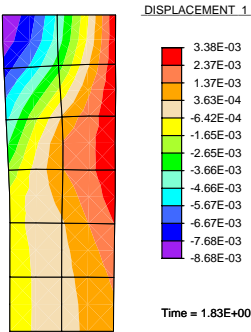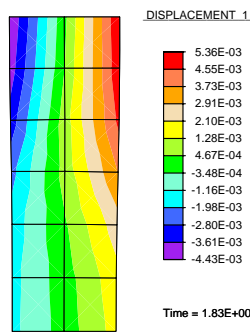
d. Mixed-Q8 element.   e. Mixed-Q4 element.   f. Mixed-CST element.
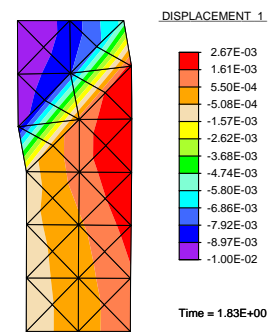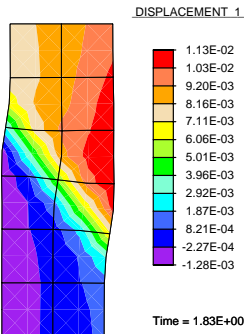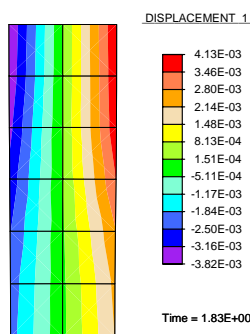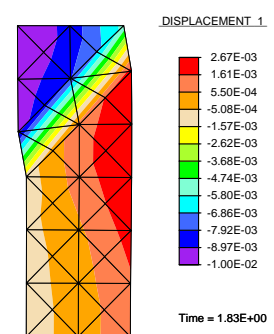
g. Q8 element.   h. Q4 element.   i. CST element.

Figure 5.8.: Example 4: Comparison of the different finite element methods: Distribution of the horizontal displacement at $v = 1.8337 cm$ (12 elements-tol=1.E-18).
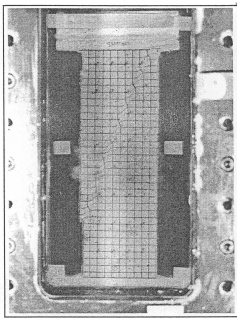
a. shf40 sample [43].
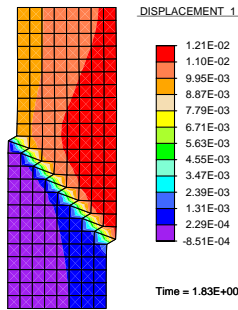
b. MES element.
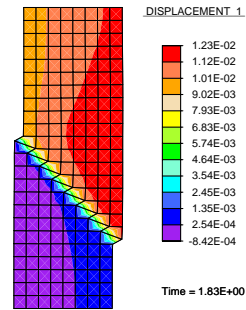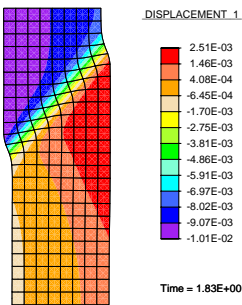
c. EAS element.
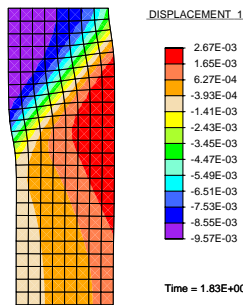
d. Mixed-Q8 element.
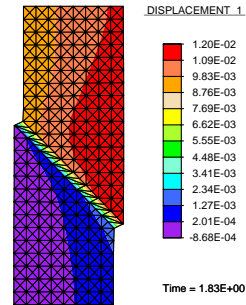
e. Mixed-Q4 element.

f. Mixed-CST element.
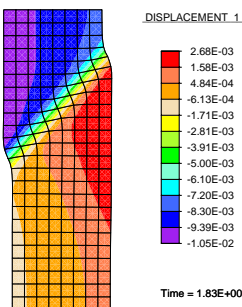
g. Q8 element.
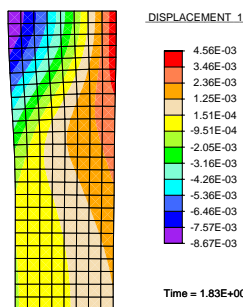
h. Q4 element.
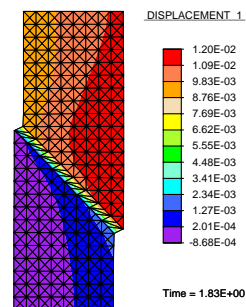
i. CST element.

Figure 5.9.: Example 4: Comparison of the different finite element methods: Distribution of the horizontal displacement at $v = 1.8337cm$ (192 elements-tol=1.E-18).

5.2.2. Example 5

A specimen of $0.04\,m$ width and $0.14\,m$ height is laterally compressed by a constant confined pressure of $400\,kPa$. A prescribed vertical displacement v of the top nodes varies from 0 to $0.01\,m$ at $t = 1\,s$ after isotropical consolidation. The material in the indicated middle left part of the sample (size $0.02\,m \times 0.02\,m$) is equipped with an initially higher void ratio of 0.45, whereas the void ratio is 0.40 elsewhere as depicted in Fig. 5.10. The calculations were performed without gravity. The material parameters given in Table 5.3 for Karsruhe sand is valid for higher pressures and proposed by *Bauer, 1996*[8]. The other set of material parameters suggested by *Herle, 1997*[45, 46] is valid for smaller pressures.
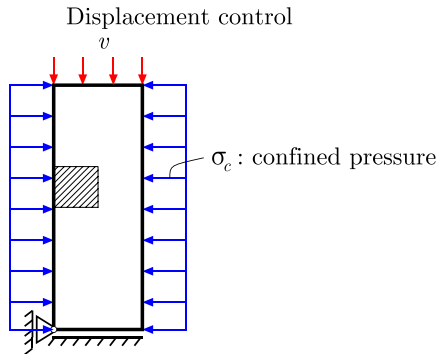
Figure 5.10.: Example 5: Biaxial test. Geometry and boundary conditions.

$\varphi_c(^o)$	$h_s(MPa)$	$\bar{n}$	e_{d0}	e_{c0}	e_{i0}	α_0	β_0
30	190	0.45	0.40	0.80	1.189	0.15	1.00

Table 5.3.: Hypoplastic material parameters for Karsruhe sand [8, 34, 51].

We consider first the discretization of the domain in 8×28 elements. As shown in Fig. 5.11, the responses are rather different to one another when considering the post-critical equilibrium branches. The softening region is prone to element type. It should be noted that the present results employing the time integration scheme suggested by *Nübel et al,1998*[83] are compared with the numerical results using the time integration schemes proposed by *Fellin and Ostermann, 2002*[34], *Roddeman, 1997*[96]. As expected, the enhanced finite element methods and the quadrilateral finite elements composed of four diagonally crossed triangles make the post-peak behaviour softer than the others.

The numerical results shown in Fig. 5.12 are obtained with four different discretizations of the sample: 2×7, 4×14, 8×21 Q8 and Mixed-Q8 elements, 8×28 Q4 and Mixed-Q4

a. Force-displacement curve.

b. Volumetric strain-axial strain.
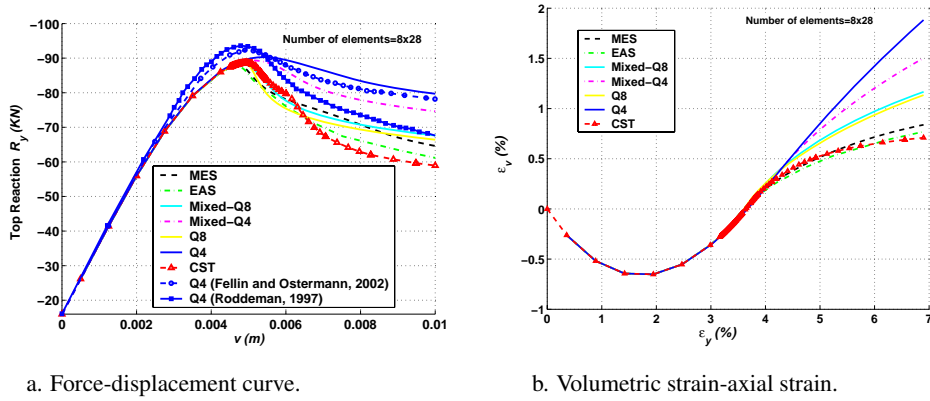
Figure 5.11.: Example 5: Biaxial test (8x28 elements).

elements, $8 \times 28 \times 4$ CST and Mixed-CST elements. The present results illustrate the mesh-dependent response due to the lack of an intrinsic characteristic length scale not allowing continuation of the analysis in post-localized behaviour.

a. Force-displacement curve.

b. Volumetric strain-axial strain.
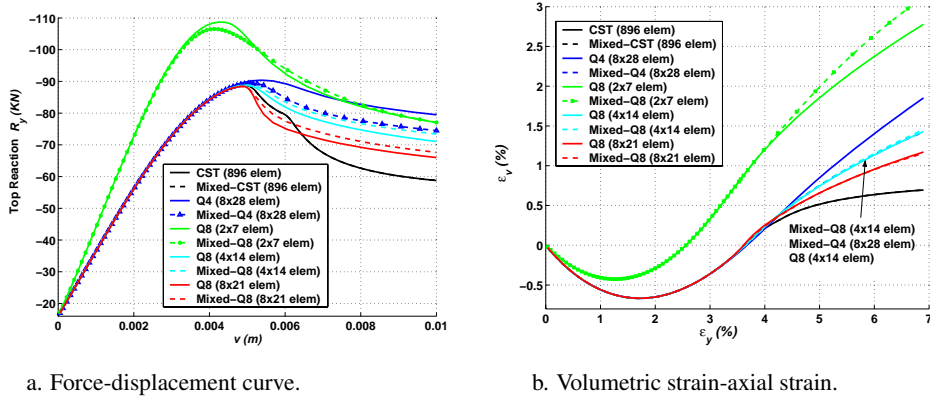
Figure 5.12.: Example 5: Biaxial test.

The distribution of the void ratio and the deformation shape are depicted in Figs. 5.13 and 5.14. As observed, a large void ratio is produced inside the shear band. Moreover there exist two shear bands simultaneously when using *Fellin and Ostermann*'s time integration scheme (Figs. 5.13a and 5.14a). The present results show that two shear bands appear simultaneously only when the tolerance value is chosen as $1.E^{-6}$ (see Section 5.3 and Fig. 5.16). If the tolerance value is smaller than $1.E^{-6}$, either only one shear band occurs or one is more dominant than the other. The emergence of the shear bands in the latter case is similar to *Roddeman*'s result (Figs. 5.13b and 5.14b).
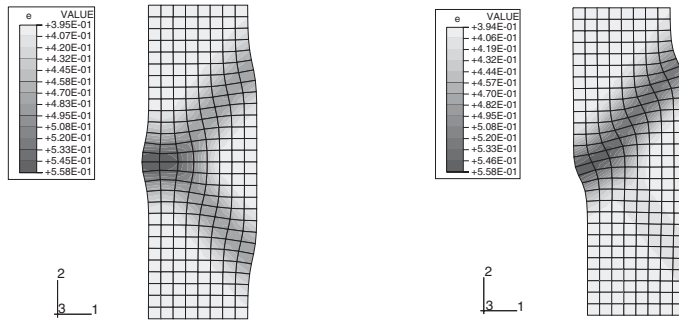
a. 8×28 Q4 elem
(*Fellin and Ostermann, 2002*[34]).

b. 8×28 Q4 elem
(*Roddeman, 1997*[34]).
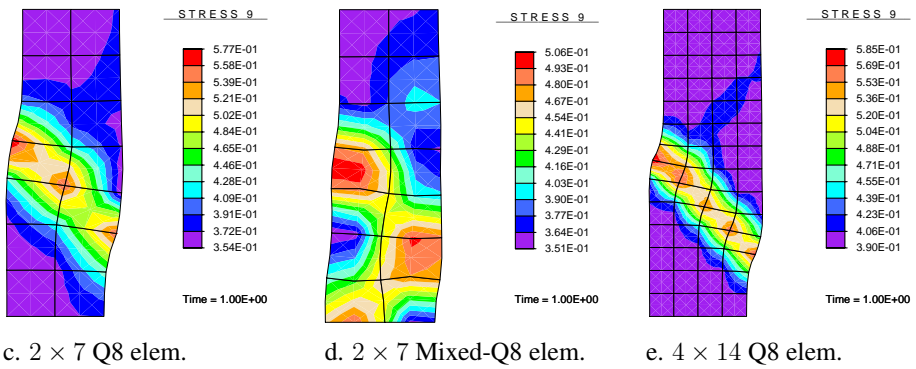
c. 2×7 Q8 elem.

d. 2×7 Mixed-Q8 elem.

e. 4×14 Q8 elem.
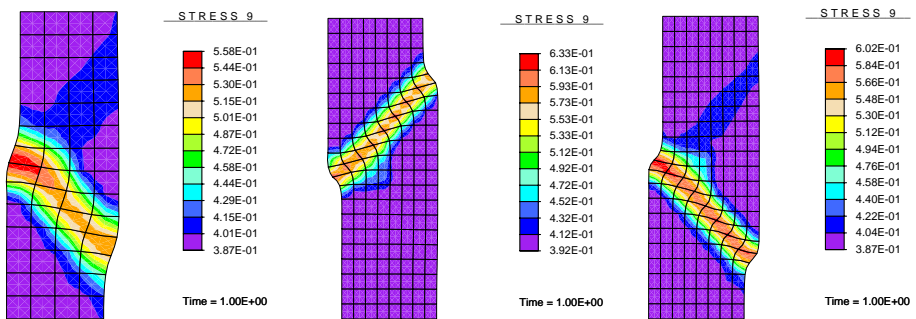
f. 4×14 Mixed-Q8 elem.

g. 8×21 Q8 elem.

h. 8×21 Mixed-Q8 elem.

Figure 5.13.: Example 5: Comparison of the different finite element methods: Distribution of the the void ratio at $v = 1.0 \, cm$ (tol=1.E-18).
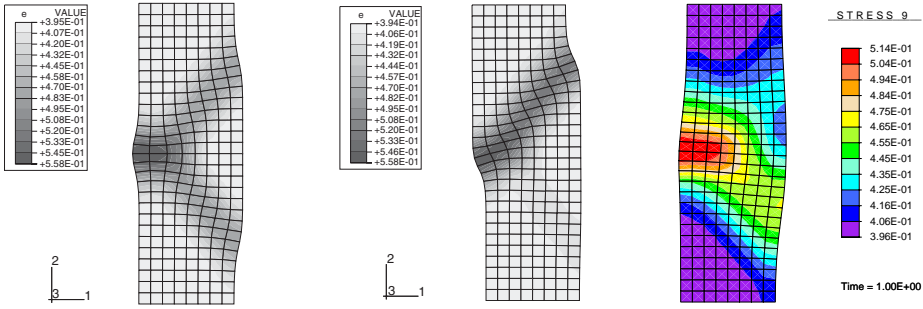
a. Q4 elem (*Fellin and Ostermann, 2002*[34]).

b. Q4 elem (*Roddeman, 1997*[34]).

c. Q4 elem.
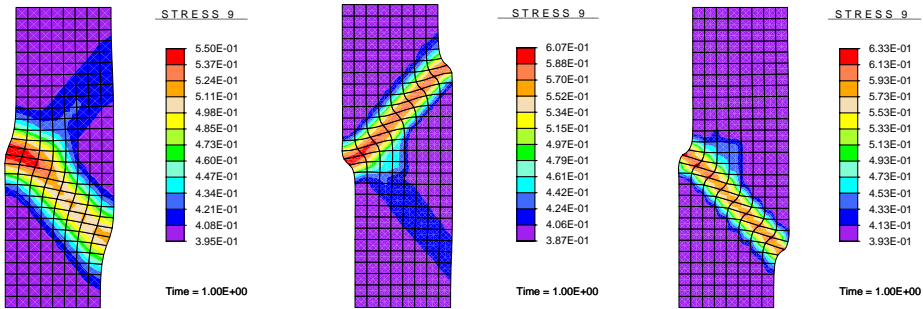
d. Mixed-Q4 elem.

e. Mixed-Q8 elem.

f. Q8 elem.
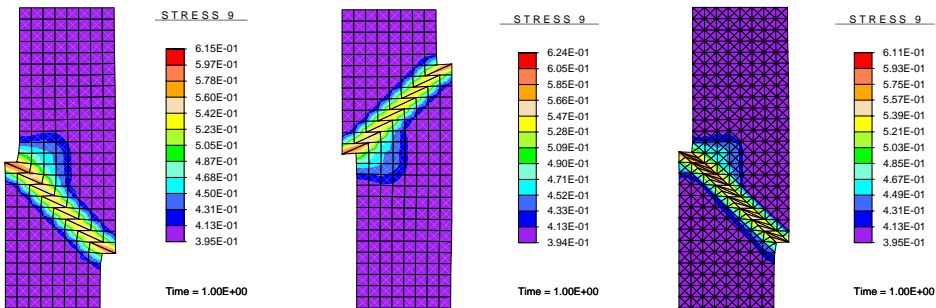
f. MES elem.

g. EAS elem.

h. CST and Mixed-CST elem.

Figure 5.14.: Example 5: Comparison of the different finite element methods: Distribution of the void ratio at $v = 1.0\,cm$ (8×28 elements-tol=1.E-18).

5.3. Tolerance

The non-linear system of equations (4.15), (4.65), and (4.89) is typically solved by Newton's method. Iterations are required and repeated until a norm of the solution is less than some tolerance. The tolerance used for controlling the solution in FEAP [105] is

$$E_i = d\tilde{u}_i.R_i, \tag{5.4}$$

with convergence assumed when

$$E_i < \text{tol}.E_0, \tag{5.5}$$

where tol is the input tolerance value, R_i is the residual force and $d\tilde{u}_i$ is the increment solution defined in eq. (4.91).

Now we investigate the tolerance value in the example 5 (see Section 5.2.2). As can be seen in Fig. 5.15, the tolerance has a minor effect not only in the post-peak behaviour of the global load-displacement curve but also in the volumetric strain-axial strain curve. However the distribution of the horizontal displacement as depicted in Fig. 5.16 depends on the tolerance value. When the tolerance value is smaller than 1.E-18, the distribution of the vertical displacement is exactly identical.
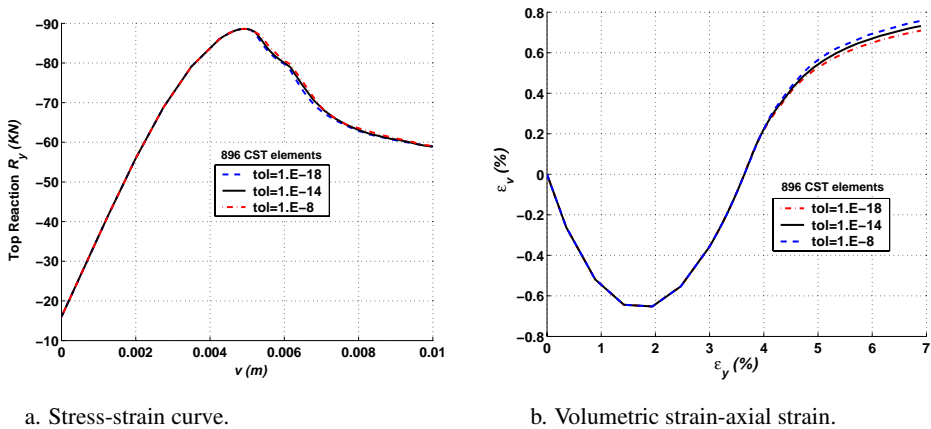
a. Stress-strain curve.

b. Volumetric strain-axial strain.

Figure 5.15.: Example 5: Biaxial test: Comparison of the different tolerance values of tol.

Table 5.4 depicts the change of the direction of shear bands with respect to the tolerance value.

Number of elements	Type of element	Tolerance	Shear band direction
8×28	Q4	1.E-8	Type 2
8×28	Q4	1.E-18	Type **1** + 2
8×28	Mixed-Q4	1.E-8	Type 1
8×28	Mixed-Q4	1.E-18	Type 1
2×7	Q8	1.E-8	Type 1
2×7	Q8	1.E-18	Type **1** + 2
4×14	Q8	1.E-20	Type **1** + 2
8×21	Q8	1.E-8	Type 1
8×21	Q8	1.E-18	Type 2
2×7	Mixed-Q8	1.E-18	-
4×14	Mixed-Q8	1.E-20	Type **1** + 2
8×21	Mixed-Q8	1.E-18	Type **1** + 2
896	CST	1.E-6	Type 1+2
896	CST	1.E-8	Type 1
896	CST	1.E-10	Type 1
896	CST	1.E-12	Type 2
896	CST	1.E-14	Type 1
896	CST	1.E-16	Type 1
896	CST	1.E-18	Type 1
896	CST	1.E-20	Type 1
896	Mixed-Q8	1.E-12	Type 2
896	Mixed-Q8	1.E-18	Type 1

Type 1: The left middle to the right down direction.
Type 2: The left middle to the right up direction.
The bold symbol means that the mentioned direction dominates.

Table 5.4.: Example 5: Orientation of shear bands.
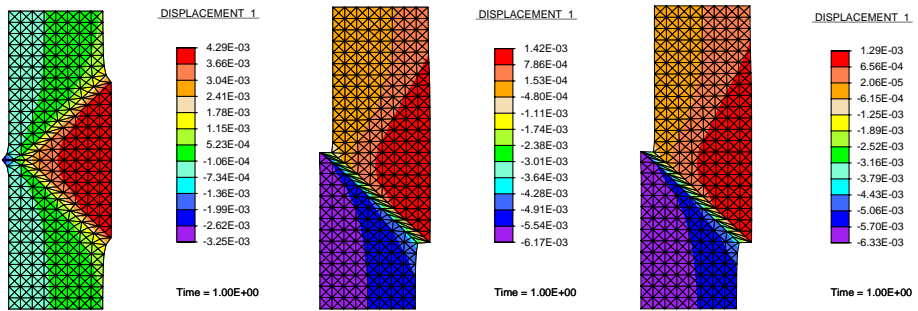
a. Tolerance = 1.E-6, 1.E-8 and 1.E-10, respectively.
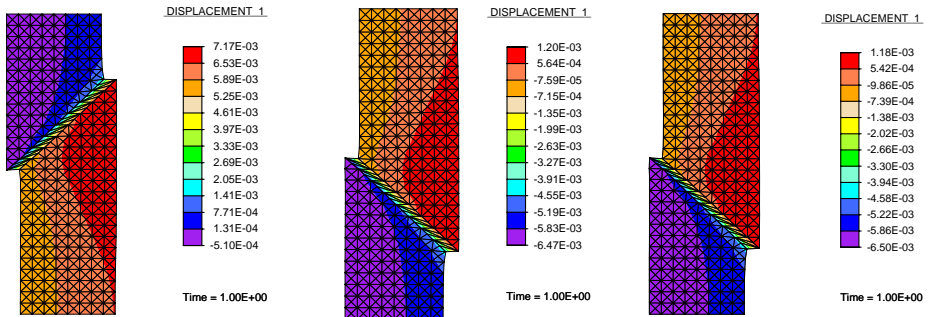
b. Tolerance = 1.E-12, 1.E-14 and 1.E-16, respectively.
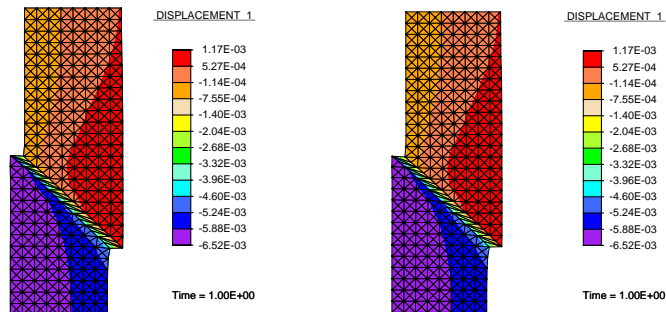
c. Tolerance = 1.E-18 and 1.E-20, respectively.

Figure 5.16.: Example 5: Biaxial test: Comparison of the different tolerance value tol: Distribution of the vertical displacement at $v = 1.0\,cm$ ($8 \times 28 \times 4$ CST elements).

6. Strong discontinuity analysis for hypoplastic models

Hypoplastic models (*Bauer, 1996*[8], *Gudehus,1996*[38], *Wolffersdorff, 1996*[113]) have been developed to describe the mechanical behaviour of granular materials and they are expressed as a single constitutive equation of the rate type. In contrast to elasto-plastic models, a decomposition of deformation into elastic and plastic parts is not required. Consequently, an explicit definition of yield surface, plastic potential, flow rule and consistency condition is not introduced. However, the displacement and mixed finite element formulations of shear localization based on these models presented in Chapter 4 exhibit mesh dependence through the numerical results as shown in Chapter 5. To remove mesh dependence, the non-local [106, 110, 71] and polar hypoplastic models [107, 71, 49, 84] as extensions of the classical models were suggested.

In recent years, a new methodological problem based on the concept of strong discontinuity has been developed (*Simo et al., 1993*[98], *Garikipati, 1996*[36], *Oliver, 2002*[87]). In this context, the displacements are jumps across discontinuity surface. The strain field, therefore, consists of a regular part which is continuous and a singular part which is unbounded due to the appearance of the Dirac delta distribution. The so-called strong discontinuity analysis examines the continuum constitutive models compatible with unbounded strains under certain conditions [88, 86].

In this part of this thesis, strong discontinuity analysis for hypoplastic models at small deformation is proposed. The theory is predicated upon the assumption that the normal movements are much smaller than those in the tangent direction within a shear band (see Section 2.1), thus, they can be neglected.

6.1. Kinematics

Let S be a discontinuity surface in a body Ω across which the displacement field $\boldsymbol{u}$ is discontinuous. The orientation of the discontinuity surface, or band, is defined by a unit normal vector $\boldsymbol{n}$ which could vary from point to point on S.

The displacement $\boldsymbol{u}$ is assumed in the following form [89]

$$\boldsymbol{u} = \bar{\boldsymbol{u}}(\boldsymbol{x}, t) + H_S(\boldsymbol{x}) \left[\!\left[\boldsymbol{u}\right]\!\right](\boldsymbol{x}, t), \tag{6.1}$$

where $\bar{\bar{u}}$ is the continuous part of u and $[[u]]$ is the jump discontinuity on the surface S separating the subdomains Ω^- and Ω^+ of Ω as shown in Fig. 6.1, H_S is the unit ramp function defined by

$$H_S = \begin{cases} 0 & x \in \Omega^-, \\ 1 & x \in \Omega^+, \\ \frac{\xi - \xi^-}{\xi^+ - \xi^-} & x \in \Omega^h \to S. \end{cases} \tag{6.2}$$
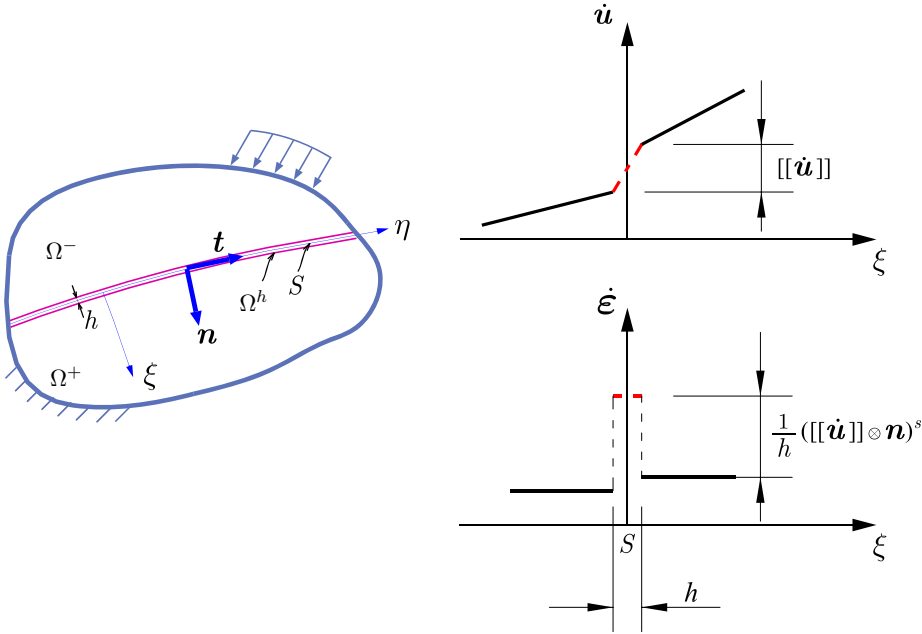
Figure 6.1.: Regularized strong discontinuity [87]

The displacement rate $\dot{u}$ reads

$$\dot{u} = \dot{\bar{\bar{u}}}(x, t) + H_S(x) [[\dot{u}]] (x, t). \tag{6.3}$$

The associated total strain rate tensor resulting from (6.3) consists of a regular part being continuous and a singular part being unbounded [89]:

$$\begin{aligned} \dot{\epsilon} &= \nabla^s \dot{\bar{\bar{u}}} + H_S \nabla^s [[\dot{u}]] + \mu_S \frac{1}{h} \left([[\dot{u}]] \otimes n \right)^s, \\ &= \underbrace{\dot{\bar{\epsilon}}}_{\text{bounded}} + \underbrace{\mu_S \frac{1}{h} \left([[\dot{u}]] \otimes n \right)^s}_{\text{unbounded when } h \to 0}, \end{aligned} \tag{6.4}$$

where μ_S is a collocation function on Ω^h

$$\mu_S(\boldsymbol{x}) = \begin{cases} 1 & \forall \boldsymbol{x} \in \Omega^h, \\ 0 & \forall \boldsymbol{x} \notin \Omega^h. \end{cases} \tag{6.5}$$

In infinitesimal strain theory, no distinction between the stress and strain tensors defined with respect to the reference and deformed configuration of the body needs to be made. Consequently, the stretching tensor $\boldsymbol{D}$ being the symmetric part of the spatial velocity gradient is equal to the strain rate tensor $\dot{\boldsymbol{\epsilon}}$:

$$\begin{aligned} \boldsymbol{D} = \dot{\boldsymbol{\epsilon}} &= \nabla^s \dot{\bar{\boldsymbol{u}}} + H_S \nabla^s [[\dot{\boldsymbol{u}}]] + \mu_S \frac{1}{h} \left([[\dot{\boldsymbol{u}}]] \otimes \boldsymbol{n} \right)^s, \\ &= \underbrace{\dot{\bar{\boldsymbol{\epsilon}}}}_{\text{bounded}} + \underbrace{\mu_S \frac{1}{h} \left([[\dot{\boldsymbol{u}}]] \otimes \boldsymbol{n} \right)^s}_{\text{unbounded when } h \to 0}. \end{aligned} \tag{6.6}$$

The spin tensor $\boldsymbol{W}$, the skew-symmetric part of the spatial velocity gradient defined by (3.4), is given by

$$\boldsymbol{W} = \underbrace{\left(\nabla \dot{\bar{\boldsymbol{u}}} \right)^{\text{skew}} + H_S \left(\nabla [[\dot{\boldsymbol{u}}]] \right)^{\text{skew}}}_{\text{bounded}} + \underbrace{\mu_S \frac{1}{h} \left([[\dot{\boldsymbol{u}}]] \otimes \boldsymbol{n} \right)^{\text{skew}}}_{\text{unbounded when } h \to 0}, \tag{6.7}$$

where $(\bullet)^{\text{skew}}$ is the skew-symmetric part of $(\bullet)$.

Let $\boldsymbol{D}_{\Omega \backslash S}$ and $\boldsymbol{W}_{\Omega \backslash S}$ denote the stretching tensor and the spin tensor, respectively, at the neighbouring point on the continuum part of the body $\Omega \backslash S$ corresponding to $\mu_S(\boldsymbol{x}) = 0$. From (6.6) and (6.7) we have

$$\boldsymbol{D}_{\Omega \backslash S} = \dot{\bar{\boldsymbol{\epsilon}}} = \nabla^s \dot{\bar{\boldsymbol{u}}} + H_S \nabla^s [[\dot{\boldsymbol{u}}]], \tag{6.8}$$

$$\boldsymbol{W}_{\Omega \backslash S} = \left(\nabla \dot{\bar{\boldsymbol{u}}} \right)^{\text{skew}} + H_S \left(\nabla [[\dot{\boldsymbol{u}}]] \right)^{\text{skew}}. \tag{6.9}$$

Similarly, the stretching tensor $\boldsymbol{D}_S$ and the spin tensor $\boldsymbol{W}_S$ at the given point of the discontinuity surface S corresponding to $\mu_S(\boldsymbol{x}) = 1$ are given by, respectively,

$$\boldsymbol{D}_S = \dot{\bar{\boldsymbol{\epsilon}}} + \frac{1}{h} \left([[\dot{\boldsymbol{u}}]] \otimes \boldsymbol{n} \right)^s, \tag{6.10}$$

$$\boldsymbol{W}_S = \left(\nabla \dot{\bar{\boldsymbol{u}}} \right)^{\text{skew}} + H_S \left(\nabla [[\dot{\boldsymbol{u}}]] \right)^{\text{skew}} + \frac{1}{h} \left([[\dot{\boldsymbol{u}}]] \otimes \boldsymbol{n} \right)^{\text{skew}}. \tag{6.11}$$

Thus, the jump of the stretching tensor $\boldsymbol{D}$ and the spin tensor $\boldsymbol{W}$ in the localized zone are presented as follows, respectively

$$[[\boldsymbol{D}]] = \boldsymbol{D}_S - \boldsymbol{D}_{\Omega \backslash S} = \frac{1}{h} \left([[\dot{\boldsymbol{u}}]] \otimes \boldsymbol{n} \right)^s, \tag{6.12}$$

$$[[\boldsymbol{W}]] = \boldsymbol{W}_S - \boldsymbol{W}_{\Omega \backslash S} = \frac{1}{h} \left([[\dot{\boldsymbol{u}}]] \otimes \boldsymbol{n} \right)^{\text{skew}}. \tag{6.13}$$

Based on eq. (6.6) the norm of the strain rate has the following form

$$
\begin{aligned}
\|\boldsymbol{D}\| = \|\dot{\boldsymbol{\epsilon}}\| &= \left(\dot{\boldsymbol{\epsilon}} : \dot{\boldsymbol{\epsilon}}\right)^{1/2}, \\
&= \left(\dot{\bar{\boldsymbol{\epsilon}}} : \dot{\bar{\boldsymbol{\epsilon}}} + 2\dot{\bar{\boldsymbol{\epsilon}}} : \mu_S \frac{1}{h}\left([[\dot{\boldsymbol{u}}]] \otimes \boldsymbol{n}\right)^s\right. \\
&\quad \left. + \; \mu_S \frac{1}{h^2}\left([[\dot{\boldsymbol{u}}]] \otimes \boldsymbol{n}\right)^s : \left([[\dot{\boldsymbol{u}}]] \otimes \boldsymbol{n}\right)^s\right)^{1/2}.
\end{aligned}
\tag{6.14}
$$

By substituting $\mu_S = 0$ into eq. (6.14) we obtain the norm of the strain rate $\left\|\boldsymbol{D}_{\Omega\backslash S}\right\|$ in $\Omega\backslash S$

$$
\left\|\boldsymbol{D}_{\Omega\backslash S}\right\| = \left(\dot{\bar{\boldsymbol{\epsilon}}} : \dot{\bar{\boldsymbol{\epsilon}}}\right)^{1/2}.
\tag{6.15}
$$

When the bandwidth h tends to 0, the concept of strong discontinuity is recovered [90]

$$
\lim_{h \to 0} \frac{1}{h} = \delta_S^h,
\tag{6.16}
$$

and the first and second terms in eq. (6.14) are rather small in comparison with the third one, hence, they can be neglected. On inserting $\mu_S = 1$ into eq. (6.14) we get the norm of the strain rate $\|\boldsymbol{D}_S\|$ in S:

$$
\|\boldsymbol{D}_S\| \approx \frac{1}{h} \left\|\left([[\dot{\boldsymbol{u}}]] \otimes \boldsymbol{n}\right)^s\right\|.
\tag{6.17}
$$

Let us define λ_0 by

$$
\lambda_0 = \|\boldsymbol{D}_S\| - \left\|\boldsymbol{D}_{\Omega\backslash S}\right\|.
\tag{6.18}
$$

Because $\left\|\boldsymbol{D}_{\Omega\backslash S}\right\|$ (6.15) is much smaller than $\|\boldsymbol{D}_S\|$ (6.17) as h tends to zero, we can obmit $\left\|\boldsymbol{D}_{\Omega\backslash S}\right\|$. Eq. (6.18) becomes

$$
\lambda_0 = \left\|\boldsymbol{D}_{\Omega\backslash S}\right\| - \|\boldsymbol{D}_S\| \approx \|\boldsymbol{D}_S\| \approx \frac{1}{h}\left\|\left([[\dot{\boldsymbol{u}}]] \otimes \boldsymbol{n}\right)^s\right\|.
\tag{6.19}
$$

6.2. Governing equations

Let $\partial\Omega_u \subset \partial\Omega$ and $\partial\Omega_\sigma \subset \partial\Omega$ be the boundaries subjected to the usual essential and natural boundary conditions, respectively. The governing equations can be written as

$$
\begin{aligned}
\text{div}\boldsymbol{\sigma} + \boldsymbol{f} &= \boldsymbol{0} \quad \text{in } \Omega\backslash S, & (6.20)\\
\boldsymbol{u} &= \bar{\boldsymbol{u}} \quad \text{in } \Omega_u, & (6.21)\\
\bar{\boldsymbol{t}} &= \boldsymbol{\sigma}\boldsymbol{\nu} \quad \text{in } \Omega_\sigma, & (6.22)\\
\boldsymbol{\sigma}_S\,\boldsymbol{n} &= \boldsymbol{\sigma}_{\Omega\backslash S}\,\boldsymbol{n} \quad \text{in } S, & (6.23)
\end{aligned}
$$

where $\boldsymbol{f}$ is the body force (per unit volume); $\boldsymbol{\sigma}$ is the Cauchy stress; $\boldsymbol{\sigma}_S$ is the Cauchy stress at a given material point of the discontinuity surface S and $\boldsymbol{\sigma}_{\Omega\backslash S}$ is the stress at a neighbouring point on the continuum part of the body $\Omega\backslash S$; $\bar{\boldsymbol{u}}$ and $\bar{\boldsymbol{t}}$ are the prescribed displacement and traction vectors, respectively; $\boldsymbol{\nu}$ is the outward normal unit vector to the boundary $\partial\Omega$; $\boldsymbol{n}$ is the unit normal to S pointing to Ω^+.

If the emergence of shear bands does not occur, that is, the displacement is continuous, then eq. (6.23) is satisfied identically, and the governing equations of the problems involving strong discontinuities reduce to the form in classical problems.

6.3. Strong discontinuity analysis

6.3.1. Traction continuity - Stress boundedness

Let $\boldsymbol{\tau}_S$ and $\boldsymbol{\tau}_{\Omega\backslash S}$ be the traction vectors in S and $\Omega\backslash S$, respectively. The traction continuity conditions across S read by recalling eq. (6.23)

$$
\begin{aligned}
\boldsymbol{\tau}_S &= \boldsymbol{\sigma}_S\,\boldsymbol{n}, & (6.24)\\
\boldsymbol{\tau}_{\Omega\backslash S} &= \boldsymbol{\sigma}_{\Omega\backslash S}\,\boldsymbol{n}, & (6.25)\\
\boldsymbol{\tau}_S &= \boldsymbol{\tau}_{\Omega\backslash S}. & (6.26)
\end{aligned}
$$

From eqs. (6.24-6.26) we obtain

$$
[[\boldsymbol{\tau}]] = \boldsymbol{\sigma}_S\,\boldsymbol{n} - \boldsymbol{\sigma}_{\Omega\backslash S}\,\boldsymbol{n} = [[\boldsymbol{\sigma}]]\,\boldsymbol{n} = \mathbf{0}, \tag{6.27}
$$

where

$$
[[\boldsymbol{\sigma}]] = \boldsymbol{\sigma}_S - \boldsymbol{\sigma}_{\Omega\backslash S}. \tag{6.28}
$$

At a neighbouring point on the continuum part of the body $\Omega\backslash S$, the strain, the strain rate and the void ratio are bounded. Thus, the stress $\boldsymbol{\sigma}_{\Omega\backslash S}$ and the stress rate $\dot{\boldsymbol{\sigma}}_{\Omega\backslash S}$ are bounded. The unit normal vector $\boldsymbol{n}$ is bounded. Following eqs. (6.24)-(6.26) the tractions $\boldsymbol{\tau}_{\Omega\backslash S}$ in $\Omega\backslash S$ and $\boldsymbol{\tau}_S$ in S are bounded. Consequently, the stress $\boldsymbol{\sigma}_S$, the stress rate $\dot{\boldsymbol{\sigma}}_S$ in S and the stress jump $[[\boldsymbol{\sigma}]]$ are bounded (see also in *Oliver, 2002*[87]).

$$
\begin{aligned}
\boldsymbol{n} &\to \text{bounded}, & (6.29)\\
\boldsymbol{\sigma}_{\Omega\backslash S},\ \dot{\boldsymbol{\sigma}}_{\Omega\backslash S} &\to \text{bounded}, & (6.30)\\
\boldsymbol{\sigma}_S,\ \dot{\boldsymbol{\sigma}}_S &\to \text{bounded}, & (6.31)\\
[[\boldsymbol{\sigma}]] = \boldsymbol{\sigma}_S - \boldsymbol{\sigma}_{\Omega\backslash S} &\to \text{bounded}, & (6.32)\\
\boldsymbol{\tau}_{\Omega\backslash S} = \boldsymbol{\sigma}_{\Omega\backslash S}\,\boldsymbol{n} &\to \text{bounded}, & (6.33)\\
\boldsymbol{\tau}_S = \boldsymbol{\sigma}_S\,\boldsymbol{n} &\to \text{bounded}. & (6.34)
\end{aligned}
$$

6.3.2. Strong discontinuity equation

6.3.2.1. Displacement jump

Let us recall the following general form for the K-hypoplastic constitutive equations (see eq. (3.31)):

$$\overset{\circ}{\boldsymbol{\sigma}} = \boldsymbol{H}(\boldsymbol{\sigma}, \dot{\boldsymbol{\epsilon}}, e) = \boldsymbol{H}(\boldsymbol{\sigma}, \boldsymbol{D}, e) = \boldsymbol{\mathcal{L}}(\boldsymbol{\sigma}, e) : \boldsymbol{D} + \boldsymbol{N}(\boldsymbol{\sigma}, e) \, \|\boldsymbol{D}\|\,, \tag{6.35}$$

where the objective co-rotational (Jaumann) stress rate $\overset{\circ}{\boldsymbol{\sigma}}$ defined by (3.32)

$$\overset{\circ}{\boldsymbol{\sigma}} = \dot{\boldsymbol{\sigma}} + \boldsymbol{\sigma}\boldsymbol{W} - \boldsymbol{W}\boldsymbol{\sigma}. \tag{6.36}$$

By using eqs. (6.35), (6.12) and (6.18) the jump of $\overset{\circ}{\boldsymbol{\sigma}}$ may be taken in the following form

$$\left[\!\left[\overset{\circ}{\boldsymbol{\sigma}}\right]\!\right] = \overset{\circ}{\boldsymbol{\sigma}}_S - \overset{\circ}{\boldsymbol{\sigma}}_{\Omega\backslash S} = \boldsymbol{\mathcal{L}} : [\![\boldsymbol{D}]\!] + \boldsymbol{N}\lambda_0. \tag{6.37}$$

From eq. (6.27) the rate of the traction vector reads

$$[\![\dot{\boldsymbol{\tau}}]\!] = [\![\dot{\boldsymbol{\sigma}}]\!]\,\boldsymbol{n} = \boldsymbol{0}, \tag{6.38}$$

where

$$[\![\dot{\boldsymbol{\sigma}}]\!] = \dot{\boldsymbol{\sigma}}_S - \dot{\boldsymbol{\sigma}}_{\Omega\backslash S}. \tag{6.39}$$

Substituting (6.36) and (6.39) into (6.38) we have

$$\left[\!\left[\overset{\circ}{\boldsymbol{\sigma}}\right]\!\right]\boldsymbol{n} + \left\{-\boldsymbol{\sigma}_S\boldsymbol{W}_S + \boldsymbol{\sigma}_{\Omega\backslash S}\boldsymbol{W}_{\Omega\backslash S}\right)\boldsymbol{n} + \left(\boldsymbol{W}_S\boldsymbol{\sigma}_S - \boldsymbol{W}_{\Omega\backslash S}\boldsymbol{\sigma}_{\Omega\backslash S}\right\}\boldsymbol{n} = \boldsymbol{0}. \tag{6.40}$$

Introducing the following relations

$$\boldsymbol{\sigma}_S\boldsymbol{W}_S - \boldsymbol{\sigma}_{\Omega\backslash S}\boldsymbol{W}_{\Omega\backslash S} = \boldsymbol{\sigma}_S\,[\![\boldsymbol{W}]\!] + [\![\boldsymbol{\sigma}]\!]\,\boldsymbol{W}_{\Omega\backslash S}, \tag{6.41}$$

$$\boldsymbol{W}_S\boldsymbol{\sigma}_S - \boldsymbol{W}_{\Omega\backslash S}\boldsymbol{\sigma}_{\Omega\backslash S} = [\![\boldsymbol{W}]\!]\,\boldsymbol{\sigma}_S + \boldsymbol{W}_{\Omega\backslash S}\,[\![\boldsymbol{\sigma}]\!]\,, \tag{6.42}$$

we can rewrite eq. (6.40) as

$$\left[\!\left[\overset{\circ}{\boldsymbol{\sigma}}\right]\!\right]\boldsymbol{n} - \boldsymbol{\sigma}_S\,[\![\boldsymbol{W}]\!]\,\boldsymbol{n} + [\![\boldsymbol{W}]\!]\,\boldsymbol{\sigma}_S\boldsymbol{n} + [\![\boldsymbol{\sigma}]\!]\,\boldsymbol{W}_{\Omega\backslash S}\boldsymbol{n} + \boldsymbol{W}_{\Omega\backslash S}\,[\![\boldsymbol{\sigma}]\!]\,\boldsymbol{n} = \boldsymbol{0}, \tag{6.43}$$

where $[[\boldsymbol{\sigma}]]$ and $[[\boldsymbol{W}]]$ are defined by (6.28) and (6.13), respectively.

The last term in eq. (6.43) is vanished due to the traction continuity condition (6.27), thus, eq. (6.43) becomes

$$\left[\left[\overset{\circ}{\boldsymbol{\sigma}}\right]\right]\boldsymbol{n} - \boldsymbol{\sigma}_S\left[[\boldsymbol{W}]\right]\boldsymbol{n} + [[\boldsymbol{W}]]\boldsymbol{\sigma}_S\boldsymbol{n} + [[\boldsymbol{\sigma}]]\boldsymbol{W}_{\Omega\backslash S}\boldsymbol{n} = \mathbf{0}. \tag{6.44}$$

It is observed that the last term in eq. (6.44) is bounded because of eq. (6.9) as well as the conditions (6.29) and (6.32)

$$[[\boldsymbol{\sigma}]]\boldsymbol{W}_{\Omega\backslash S}\boldsymbol{n} \rightarrow \text{ bounded,} \tag{6.45}$$

and rather small as the bandwidth h tends to zero. Therefore, for strong discontinuity analysis eq. (6.44), in addition to eq. (6.37), can be rewritten as

$$\underline{(\boldsymbol{\mathcal{L}} : [[\boldsymbol{D}]])\boldsymbol{n} + \lambda_0\boldsymbol{Nn} - \boldsymbol{\sigma}_S[[\boldsymbol{W}]]\boldsymbol{n} + [[\boldsymbol{W}]]\boldsymbol{\sigma}_S\boldsymbol{n} = \mathbf{0},} \tag{6.46}$$

which is as identical as the equation for weak discontinuity analysis [9, 121].

Substituting (6.12) and (6.13) into (6.46) leads to

$$\frac{1}{h}\left\{\frac{1}{2}\left[\boldsymbol{\mathcal{L}} : ([[\dot{\boldsymbol{u}}]] \otimes \boldsymbol{n} + \boldsymbol{n} \otimes [[\dot{\boldsymbol{u}}]])\right]\boldsymbol{n} \quad - \quad \frac{1}{2}\left[\boldsymbol{\sigma}_S([[\dot{\boldsymbol{u}}]] \otimes \boldsymbol{n} - \boldsymbol{n} \otimes [[\dot{\boldsymbol{u}}]])\right]\boldsymbol{n}\right.$$
$$+ \quad \frac{1}{2}\left[([[\dot{\boldsymbol{u}}]] \otimes \boldsymbol{n} - \boldsymbol{n} \otimes [[\dot{\boldsymbol{u}}]])\boldsymbol{\sigma}_S\right]\boldsymbol{n}\Big\}$$
$$+ \quad \lambda_0\boldsymbol{Nn} = \mathbf{0}. \tag{6.47}$$

After rearrangment the terms we get the following system of equations

$$\frac{1}{h}\bar{\boldsymbol{A}}[[\dot{\boldsymbol{u}}]] = -\lambda_0\boldsymbol{Nn}, \tag{6.48}$$

where

$$\bar{\boldsymbol{A}}[[\dot{\boldsymbol{u}}]] = \frac{1}{2}\left[\boldsymbol{\mathcal{L}} : ([[\dot{\boldsymbol{u}}]] \otimes \boldsymbol{n} + \boldsymbol{n} \otimes [[\dot{\boldsymbol{u}}]])\right]\boldsymbol{n} - \frac{1}{2}\left[\boldsymbol{\sigma}_S([[\dot{\boldsymbol{u}}]] \otimes \boldsymbol{n} - \boldsymbol{n} \otimes [[\dot{\boldsymbol{u}}]])\right]\boldsymbol{n}$$
$$+ \quad \frac{1}{2}\left[([[\dot{\boldsymbol{u}}]] \otimes \boldsymbol{n} - \boldsymbol{n} \otimes [[\dot{\boldsymbol{u}}]])\boldsymbol{\sigma}_S\right]\boldsymbol{n}, \tag{6.49}$$

or under index

$$\bar{A}_{jk}[[\dot{u}]]_k = \left\{n_i\mathcal{L}_{ijkl}n_l - \frac{1}{2}\left[\sigma_{jk} + n_i\sigma_{ij}n_k\right] + \frac{1}{2}\left[n_r\sigma_{rm}n_m\delta_{jk} + n_i\sigma_{ik}n_j\right]\right\}[[\dot{u}]]_k. \tag{6.50}$$

Let us suppose that $\bar{\boldsymbol{A}}$ is nonsingular. The solution of the system of equations (6.48) gives

$$\frac{1}{h}\left[\!\left[\dot{\boldsymbol{u}}\right]\!\right] = -\lambda_0 \bar{\boldsymbol{A}}^{-1} \boldsymbol{N} \boldsymbol{n}. \tag{6.51}$$

Let us define $\boldsymbol{c}$ by

$$\boldsymbol{c}(\boldsymbol{n}, \boldsymbol{\sigma}, e) = -\bar{\boldsymbol{A}}^{-1}(\boldsymbol{n}, \boldsymbol{\sigma}, e)\boldsymbol{N}(\boldsymbol{\sigma}, e)\boldsymbol{n}, \tag{6.52}$$

which leads to the alternative form of eq. (6.51)

$$\frac{1}{h}\left[\!\left[\dot{\boldsymbol{u}}\right]\!\right] = \lambda_0 \boldsymbol{c}. \tag{6.53}$$

On inserting (6.19) into (6.53) we have

$$\frac{1}{h}\left[\!\left[\dot{\boldsymbol{u}}\right]\!\right] = \frac{1}{h}\left\|\left(\left[\!\left[\dot{\boldsymbol{u}}\right]\!\right] \otimes \boldsymbol{n}\right)^s\right\| \boldsymbol{c}. \tag{6.54}$$

Let us consider the term $\left\|\left(\left[\!\left[\dot{\boldsymbol{u}}\right]\!\right] \otimes \boldsymbol{n}\right)^s\right\|$

$$
\begin{aligned}
\left\|\left(\left[\!\left[\dot{\boldsymbol{u}}\right]\!\right] \otimes \boldsymbol{n}\right)^s\right\| &= \frac{1}{2}\left\|\left[\!\left[\dot{\boldsymbol{u}}\right]\!\right] \otimes \boldsymbol{n} + \boldsymbol{n} \otimes \left[\!\left[\dot{\boldsymbol{u}}\right]\!\right]\right\| \\
&= \frac{1}{2}\sqrt{2\left\|\left[\!\left[\dot{\boldsymbol{u}}\right]\!\right]\right\|^2 + 2\left(\left[\!\left[\dot{\boldsymbol{u}}\right]\!\right].\boldsymbol{n}\right)^2}.
\end{aligned}
\tag{6.55}
$$

According to the assumption that the normal movements are much smaller than those in the tangent direction within a shear band, we obtain

$$\left[\!\left[\dot{\boldsymbol{u}}\right]\!\right].\boldsymbol{n} = 0. \tag{6.56}$$

On inserting (6.56) into (6.55) we have

$$\left\|\left(\left[\!\left[\dot{\boldsymbol{u}}\right]\!\right] \otimes \boldsymbol{n}\right)^s\right\| = \frac{1}{\sqrt{2}}\left\|\left[\!\left[\dot{\boldsymbol{u}}\right]\!\right]\right\|. \tag{6.57}$$

Thus, eq. (6.54) can be rewritten as

$$\left[\!\left[\dot{\boldsymbol{u}}\right]\!\right] = -\frac{1}{\sqrt{2}}\boldsymbol{c}\left\|\left[\!\left[\dot{\boldsymbol{u}}\right]\!\right]\right\|. \tag{6.58}$$

Besides, we can obtain the following result from eq. (6.58)

$$\left\|\boldsymbol{c}\right\| = \sqrt{2}. \tag{6.59}$$

Substituting (6.58) into (6.56) yields

$$\underline{\boldsymbol{c}.\boldsymbol{n} = 0}. \tag{6.60}$$

Equations (6.58) and (6.60), in view of (6.52), provides the jump of $[[\dot{\boldsymbol{u}}]]$ in terms of the stress $\boldsymbol{\sigma}_S$, the void ratio e_S (see section 6.3.2.3) and the normal $\boldsymbol{n}$.

6.3.2.2. Void ratio

Let us recall the rate of the void ratio defined by (3.47)

$$\dot{e} = (1 + e)\mathrm{tr}\boldsymbol{D}. \tag{6.61}$$

The rate of the void ratio in the discontinuity surface S, in addition to eq. (6.10), can be expressed as

$$\dot{e} \;=\; (1 + e)\,\mathrm{tr}\boldsymbol{D}_S = (1 + e)\,\mathrm{tr}\left(\dot{\bar{\boldsymbol{\epsilon}}} + \frac{1}{h}\,([[\dot{\boldsymbol{u}}]] \otimes \boldsymbol{n})^s\right). \tag{6.62}$$

As h tends to zero, we have

$$\lim_{h \to 0} h\dot{e} \;=\; \lim_{h \to 0}(1 + e)\left[\mathrm{tr}h\dot{\bar{\boldsymbol{\epsilon}}} + \mathrm{tr}\left([[\dot{\boldsymbol{u}}]] \otimes \boldsymbol{n}\right)^s\right]. \tag{6.63}$$

If the void ratio in S is bounded, eq. (6.63) becomes

$$\underbrace{\lim_{h \to 0} h\dot{e}}_{0} = \underbrace{\lim_{h \to 0}(1 + e)\mathrm{tr}h\dot{\bar{\boldsymbol{\epsilon}}}}_{0} + \lim_{h \to 0}(1 + e)\mathrm{tr}\left([[\dot{\boldsymbol{u}}]] \otimes \boldsymbol{n}\right)^s, \tag{6.64}$$

which leads to

$$\mathrm{tr}\left([[\dot{\boldsymbol{u}}]] \otimes \boldsymbol{n}\right)^s = [[\dot{\boldsymbol{u}}]].\boldsymbol{n} = 0. \tag{6.65}$$

The condition (6.65) is actually the assumption (6.56). It means that the void ratio is bounded if only if eq. (6.65) is satisfied.

Substituting (6.65) into (6.62) we obtain

$$\dot{e} = (1 + e)\,\mathrm{tr}\dot{\bar{\boldsymbol{\epsilon}}}. \tag{6.66}$$

From eq. (6.66) it is observed that the void ratios within a shear band and at a neighbouring shear band are identical. Unfortunately, experimental observations show that the local void ratio within a shear band is larger than the void ratios on the left and right sides of a shear band. In addtion, it can be larger than the maximum void ratio determined by standard methods (Fig. 6 in *Oda and Kazama, 1998*[85] p.470). Thus, the open quesion is how to formulate the evolution equation to update the void ratio in the discontinuity surface.

6.3.2.3. Stress field

The objective stress rate $\overset{\circ}{\boldsymbol{\sigma}}$ in S can be obtained from eq. (6.35)

$$\overset{\circ}{\boldsymbol{\sigma}}_S = \boldsymbol{\mathcal{L}} : \boldsymbol{D}_S + \boldsymbol{N} \left\| \boldsymbol{D}_S \right\|. \tag{6.67}$$

Substituting eqs. (6.10) and (6.17) into (6.67) leads to

$$\overset{\circ}{\boldsymbol{\sigma}}_S = \boldsymbol{\mathcal{L}} : \dot{\bar{\boldsymbol{\epsilon}}} + \frac{1}{h} \boldsymbol{\mathcal{L}} : ([[\dot{\boldsymbol{u}}]] \otimes \boldsymbol{n})^s + \frac{1}{h} \boldsymbol{N} \left\| ([[\dot{\boldsymbol{u}}]] \otimes \boldsymbol{n})^s \right\|. \tag{6.68}$$

Multiplying both sides of eq. (6.68) by h and taking the limit as h tends to zero we have

$$\lim_{h \to 0} h \overset{\circ}{\boldsymbol{\sigma}}_S = \underbrace{\lim_{h \to 0} h(\boldsymbol{\mathcal{L}} : \dot{\bar{\boldsymbol{\epsilon}}})}_{0} + \lim_{h \to 0} \left[\boldsymbol{\mathcal{L}} : ([[\dot{\boldsymbol{u}}]] \otimes \boldsymbol{n})^s \right] + \lim_{h \to 0} \left[\boldsymbol{N} \left\| ([[\dot{\boldsymbol{u}}]] \otimes \boldsymbol{n})^s \right\| \right], \tag{6.69}$$

where $\overset{\circ}{\boldsymbol{\sigma}}_S$ defined by eq. (6.36)

$$\overset{\circ}{\boldsymbol{\sigma}}_S = \dot{\boldsymbol{\sigma}}_S + \boldsymbol{\sigma}_S \boldsymbol{W}_S - \boldsymbol{W}_S \boldsymbol{\sigma}_S. \tag{6.70}$$

Based on eqs. (6.11) and (6.70) as well as the condition (6.31), the left hand side of eq. (6.69) yields

$$\lim_{h \to 0} h \overset{\circ}{\boldsymbol{\sigma}}_S = \boldsymbol{\sigma}_S \left([[\dot{\boldsymbol{u}}]] \otimes \boldsymbol{n} \right)^{\text{skew}} - \left([[\dot{\boldsymbol{u}}]] \otimes \boldsymbol{n} \right)^{\text{skew}} \boldsymbol{\sigma}_S. \tag{6.71}$$

Combining eq. (6.71) and eq. (6.69) together, we have

$$\begin{aligned} &\boldsymbol{\sigma}_S \left([[\dot{\boldsymbol{u}}]] \otimes \boldsymbol{n} \right)^{\text{skew}} - \left([[\dot{\boldsymbol{u}}]] \otimes \boldsymbol{n} \right)^{\text{skew}} \boldsymbol{\sigma}_S \\ &= \boldsymbol{\mathcal{L}} : ([[\dot{\boldsymbol{u}}]] \otimes \boldsymbol{n})^s + \boldsymbol{N} \left\| ([[\dot{\boldsymbol{u}}]] \otimes \boldsymbol{n})^s \right\|, \end{aligned} \tag{6.72}$$

which provides a discrete non-linear stress-jump constitutive equation at the interface S. This equation allows the determination of the complete stress tensor $\boldsymbol{\sigma}_S$ on S in terms of the jump of $[[\dot{\boldsymbol{u}}]]$ and the unit normal $\boldsymbol{n}$.

6.4. Bifurcation analysis

In order to find the unit normal vector $\boldsymbol{n}$ to the discontinuity surface S as the discontinuity initiates, let us first find the condition whether localization occurs based on bifurcation condition. For weak discontinuities *Chambon, 2000*[17] and *Huang et al., 2005*[50] suggested

the inequality to check bifurcation condition in the CLOE models and the K-hypoplastic models, repectively. Here we can adopt their works to establish this condition for strong discontinuities.

Let us recall eq. (6.12)

$$\boldsymbol{D}_S = \boldsymbol{D}_{\Omega \backslash S} + \frac{1}{h} \left([[\dot{\boldsymbol{u}}]] \otimes \boldsymbol{n} \right)^s . \tag{6.73}$$

Substituting eq. (6.53) into eq. (6.73) yields

$$\boldsymbol{D}_S = \boldsymbol{D}_{\Omega \backslash S} + \lambda_0 \left(\boldsymbol{c} \otimes \boldsymbol{n} \right)^s . \tag{6.74}$$

Let us define $\Delta \boldsymbol{D}$ by

$$\left(\boldsymbol{c} \otimes \boldsymbol{n} \right)^s = \Delta \boldsymbol{D}. \tag{6.75}$$

On inserting eq. (6.75) into eq. (6.74) we have

$$\boldsymbol{D}_S = \boldsymbol{D}_{\Omega \backslash S} + \lambda_0 \Delta \boldsymbol{D}. \tag{6.76}$$

Let us recall eq. (6.18)

$$\lambda_0 = \|\boldsymbol{D}_S\| - \|\boldsymbol{D}_{\Omega \backslash S}\| . \tag{6.77}$$

By using the relation (6.76) eq. (6.77) becomes

$$\lambda_0 + \|\boldsymbol{D}_{\Omega \backslash S}\| = \|\boldsymbol{D}_{\Omega \backslash S} + \lambda_0 \Delta \boldsymbol{D}\| . \tag{6.78}$$

Square of both side in eq. (6.78) yields

$$\lambda_0^2 + 2\lambda_0 \|\boldsymbol{D}_{\Omega \backslash S}\| + \|\boldsymbol{D}_{\Omega \backslash S}\|^2 = \|\boldsymbol{D}_{\Omega \backslash S}\|^2 + 2\lambda_0 \boldsymbol{D}_{\Omega \backslash S} : \Delta \boldsymbol{D} + \lambda_0^2 \|\Delta \boldsymbol{D}\|^2 . \tag{6.79}$$

After rearrangement the terms we have

$$\lambda_0^2 (\|\Delta \boldsymbol{D}\|^2 - 1) + 2\lambda_0 (\boldsymbol{D}_{\Omega \backslash S} : \Delta \boldsymbol{D} - 2\lambda_0 \|\boldsymbol{D}_{\Omega \backslash S}\|). \tag{6.80}$$

The non-trivial solution ($\lambda_0 \neq 0$) gives

$$\lambda_0 = 2 \frac{\|\boldsymbol{D}_{\Omega \backslash S}\| - \boldsymbol{D}_{\Omega \backslash S} : \Delta \boldsymbol{D}}{\|\Delta \boldsymbol{D}\|^2 - 1} . \tag{6.81}$$

Let us define α by

$$\cos \alpha = \frac{\boldsymbol{D}_{\Omega \setminus S} : \Delta \boldsymbol{D}}{\left\| \boldsymbol{D}_{\Omega \setminus S} \right\| \left\| \Delta \boldsymbol{D} \right\|}. \tag{6.82}$$

On inserting (6.82) into eq. (6.81) we have

$$\lambda_0 = 2 \left\| \boldsymbol{D}_{\Omega \setminus S} \right\| \frac{1 - \left\| \Delta \boldsymbol{D} \right\| \cos \alpha}{\left\| \Delta \boldsymbol{D} \right\|^2 - 1}. \tag{6.83}$$

Based on the inequality $\lambda_0 = \left\| \boldsymbol{D}_S \right\| - \left\| \boldsymbol{D}_{\Omega \setminus S} \right\| \geq - \left\| \boldsymbol{D}_{\Omega \setminus S} \right\|$ we get

$$\lambda_0 = 2 \left\| \boldsymbol{D}_{\Omega \setminus S} \right\| \frac{1 - \left\| \Delta \boldsymbol{D} \right\| \cos \alpha}{\left\| \Delta \boldsymbol{D} \right\|^2 - 1} \geq - \left\| \boldsymbol{D}_{\Omega \setminus S} \right\|. \tag{6.84}$$

Two possible cases are:

- $\left\| \Delta \boldsymbol{D} \right\|^2 - 1 > 0$:

  The minimum value of λ_0 corresponding to $\cos \alpha = 1$ is

  $$(\lambda_0)_{\min} = 2 \left\| \boldsymbol{D}_{\Omega \setminus S} \right\| \frac{1 - \left\| \Delta \boldsymbol{D} \right\|}{\left\| \Delta \boldsymbol{D} \right\|^2 - 1} \geq - \left\| \boldsymbol{D}_{\Omega \setminus S} \right\|, \tag{6.85}$$

  or

  $$2(1 - \left\| \Delta \boldsymbol{D} \right\|) + \left\| \Delta \boldsymbol{D} \right\|^2 - 1 \geq 0, \tag{6.86}$$

  which can be written as

  $$(\left\| \Delta \boldsymbol{D} \right\| - 1)^2 \geq 0. \tag{6.87}$$

  This inequality is always met.

- $\left\| \Delta \boldsymbol{D} \right\|^2 - 1 = 0$: $\lambda_0 \to \infty$. This condition is met at the onset of localization.

  To prove it, let us consider the square norm of $\Delta \boldsymbol{D}$ from eq. (6.75)

  $$\left\| \Delta \boldsymbol{D} \right\|^2 = \frac{1}{4} \left(2 \left\| \boldsymbol{c} \right\| + 2 \boldsymbol{c}.\boldsymbol{n} \right). \tag{6.88}$$

  On inserting eqs. (6.59) and (6.60) into eq. (6.88) we have

  $$\left\| \Delta \boldsymbol{D} \right\|^2 = \frac{1}{2} \left\| \boldsymbol{c} \right\| = 1. \tag{6.89}$$

Therefore the bifurcation condition is then

$$\underline{\left\| \Delta \boldsymbol{D} \right\|^2 - 1 \geq 0}, \tag{6.90}$$

which is in agreement with the inequality proposed by *Chambon, 2000*[17] and *Huang et al., 2005*[50] for weak discontinuities.

Now the unit normal vector $\boldsymbol{n}$ can be identified based on (6.90). In general, the criterion (6.90) can be written in the form of a polynomial expression of degree 4 in term of $\tan^2 \theta$ (*Desrues and Chambon, 2002*[26], *Bauer, 1999*[9], see also *Ortiz et al., 1987*[91]).

$$a_0 + a_1 \tan^2 \theta + a_2 \tan^4 \theta + a_3 \tan^6 \theta + a_4 \tan^8 \theta \geq 0. \tag{6.91}$$

This criterion as a function of $\tan^2 \theta$, for example, for an elementary volume along a triaxial stress path can be depicted in Fig. 6.2 (*Desrues and Chambon, 2002*[26]).
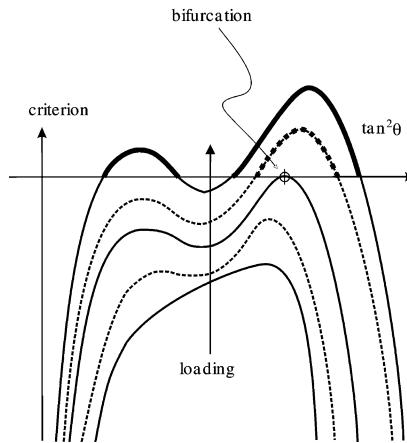
Figure 6.2.: The bifurcation condition is met as soon as one root exists for which the criterion is null [26].

6.5. Summary

Throughout the previous sections, the strong discontinuity analysis for hypoplastic models has been explored by neglecting the normal movements in the discontinuity surface S. Some of main ingredients of this analysis are summarized as follows:

- From the traction continuity (eqs. (6.24-6.26)), both the stress and the stress rate (not the objective stress rate) have to remain bounded at the discontinuity surface whereas the strain, the strain rate and the norm of the strain rate are unbounded. Then, the displacement jump is determined according to eqs. (6.58) and (6.60).

- Under the condition of the bounded stress field, a consistent discrete constitutive equation (6.72) emerges which relates the stress field at the discontinuity path to both the displacement jump and the normal.

- According to the assumption (6.56), the void ratios within a shear band and at a neighbouring shear band are bounded and identical based on eq. (6.66). However, the later result is not consistent with experimental observations. Consequently, it is necessary to propose the evolution equation to update the void ratio in the discontinuity surface. It should be noted that if the void ratio in S is unbounded, the density factor f_e (3.41) tends to zero and the density f_d (3.39) is unbounded. As a result, the constitutive tensor $\mathcal{L}$ (3.33) tends to zero. In this case, the general form for the K-hypoplastic models (6.35) cannot be employed to described the mechanical behaviour at a material point in the interface S.

- The bifurcation condition (6.90) is in agreement with the one proposed by *Chambon, 2000*[17] and *Huang et al., 2005*[50]. The normal to the discontinuity path can be determined by this condition.

Here the strong discontinuity approach is based on the discontinuous displacement field which induces the macroscopically unbounded strain. This approach is predicated upon the assumption of a zero thickness shear band. In the new theory developed in the next part of the thesis this assumption leads to the unbounded micro-strain of the inelastic phase inside the discontinuity. Moreover the shear band is formed naturally based on the energy minimization principles associated with micro-structure developments while it is necessary to determine the position of a shear band by tracking strong discontinuities in the strong discontinuity approach.

Part II.

Simulation of strain localization by means of energy relaxation

7. Relaxed energy analysis of shear bands for inelastic materials at small deformation

In this chapter a new approach to the problem of shear localization is proposed. It is based on energy minimization principles associated with micro-structure developments and the micro-shearing of a rank-one laminate which is aligned to a shear band. The thickness of the shear band represented by its volume fraction is assumed to tend to zero. The problem of the non-convex energy arising due to the formation of shear bands is solved by energy relaxation in order to ensure that the corresponding problem is well-posed. An application of the proposed formulation to isotropic material is presented. The capability of the proposed concept is demonstrated through numerical simulation of a shear test and a tension test.

7.1. Existence of solutions of non-linear boundary value problems

The existence of equilibrium solutions of non-linear boundary value problems can be proved based on the direct methods of calculus of variations. The basic idea of this method is the minimization of a energy functional.

Let us consider the following total potential energy

$$\Pi(\boldsymbol{u}) = \int_{\Omega} W(\boldsymbol{\epsilon}) \, d\Omega - \int_{\Omega} \boldsymbol{u}^{\mathrm{T}} \boldsymbol{f} \, d\Omega - \int_{\partial\Omega_{\sigma}} \boldsymbol{u}^{\mathrm{T}} \bar{\boldsymbol{t}} \, dA \tag{7.1}$$

where $\boldsymbol{u}$ is the displacement, $\boldsymbol{f}$ is the body force per unit volume, $\bar{\boldsymbol{t}}$ is the distributed load acting on the part $\partial\Omega_{\sigma}$ of the surface, and W is the non-linear elastic strain energy.

The strain field $\boldsymbol{\epsilon}$ is given as

$$\boldsymbol{\epsilon} = \nabla^{s} \boldsymbol{u}, \tag{7.2}$$

where $()^{s}$ is the symmetric part of $()$.

Now we look at solutions of minimization problems of the form

$$(\mathcal{P}) \quad \inf_{\boldsymbol{u}} \left\{ \Pi(\boldsymbol{u}) \, | \, \boldsymbol{u} = \bar{\boldsymbol{u}} \text{ on } \partial\Omega_{u} \right\}. \tag{7.3}$$

For elastic materials this corresponds to the well-known principle of minimum of the potential energy. But inelastic materials can be incorporated as well via a time-incremental formulation. In this case W denotes the so-called condensed energy [15, 41, 75].

For softening materials there exists an infinite number of possible solutions for $(\mathcal{P})$ due to the ill-posed boundary value problem. As a result of this, numerical solutions suffer from discretization sensitivity [21].

If the potential energy W is not quasiconvex in some region of the material body Ω, the functional I

$$I(\boldsymbol{u}) = \int_{\Omega} W(\boldsymbol{\epsilon}) \, d\Omega \tag{7.4}$$

is not sequentially weakly lower semicontinuous [20], thus the minimizer in problem $(\mathcal{P})$ may be unattained [20]. Following [20], the functional $I(\boldsymbol{u})$ is replaced by a *relaxed* functional $I_Q(\boldsymbol{u})$

$$I_Q(\boldsymbol{u}) = \int_{\Omega} QW(\boldsymbol{\epsilon}) \, d\Omega \,, \tag{7.5}$$

where the *quasiconvexified* functional $QW(\boldsymbol{\epsilon})$, also called *quasiconvex envelope* of W or *quasiconvex hull* of W, is defined by the minimization problem

$$QW(\boldsymbol{\epsilon}) = \inf_{\boldsymbol{\varphi}} \frac{1}{\omega} \int_{\omega} W\left(\boldsymbol{\epsilon} + \nabla\boldsymbol{\varphi}\right) d\Omega \tag{7.6}$$

for a fixed but arbitrary bounded domain ω and every $\boldsymbol{\varphi}$ with $\boldsymbol{\varphi} = \boldsymbol{0}$ on $\partial\omega$, herein $\boldsymbol{\varphi}$ is denoted as fluctuation field.

Let us introduce a scalar function [39] by

$$\psi(x) = \begin{cases} \dfrac{x}{\xi}, & 0 \leq x \leq \xi, \\ \dfrac{1-x}{1-\xi} & \xi \leq x \leq 1, \text{ periodically repeated,} \end{cases} \tag{7.7}$$

as can be seen in Fig. 7.1a.

The fluctuation field is defined by

$$\boldsymbol{\varphi}(\boldsymbol{x}) = \boldsymbol{a}\psi\left(\boldsymbol{n} \cdot \boldsymbol{x}\right), \quad \|\boldsymbol{n}\| = 1 \tag{7.8}$$

correponding to the laminate depicted in Fig. 7.1b, where $\boldsymbol{n}$ is the unit normal vector to laminates and $\boldsymbol{a}$ is a arbitrary vector. Then the gradient of the fluctuation field $\boldsymbol{\varphi}$ has the

a. Scalar function $\Psi(x)$

b. Laminates of first order and representative volume element (RVE)
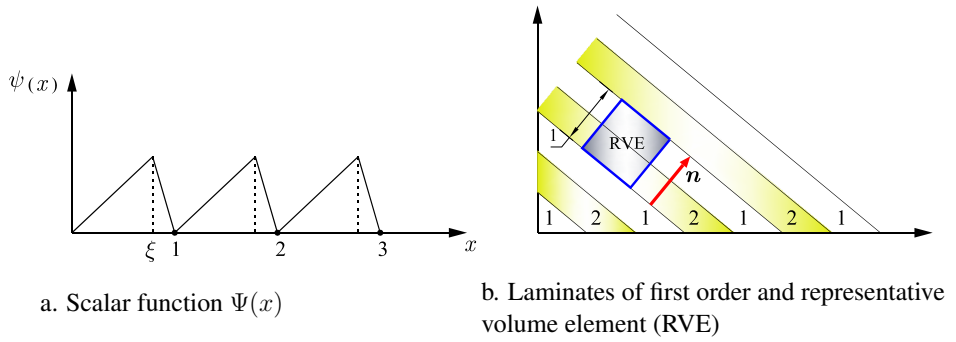
Figure 7.1.: Laminates as special fluctuation fields $\boldsymbol{\varphi}$ [39].

following values

$$\nabla\boldsymbol{\varphi}(\boldsymbol{x}) = \begin{cases} \dfrac{1}{\xi}\boldsymbol{a}\otimes\boldsymbol{n}, & \text{if } \boldsymbol{x} \text{ belongs to laminate 1,} \\[2mm] -\dfrac{1}{1-\xi}\boldsymbol{a}\otimes\boldsymbol{n} & \text{if } \boldsymbol{x} \text{ belongs to laminate 2.} \end{cases} \tag{7.9}$$

Without restriction we consider the representative volume element as shown in Fig. 7.1b. Then the definition of quasiconvexified functional (7.6) reduces to

$$W_R(\boldsymbol{\epsilon}) = \inf\{\, \xi W(\boldsymbol{\epsilon} + \frac{1}{\xi}\boldsymbol{a}\otimes\boldsymbol{n}) + (1-\xi)W(\boldsymbol{\epsilon} - \frac{1}{1-\xi}\boldsymbol{a}\otimes\boldsymbol{n})\,|\,\xi\,,\,\boldsymbol{a}\,,\,\boldsymbol{n}\,;$$
$$0 \le \xi \le 1\,,\,\|\boldsymbol{n}\| = 1\}, \quad (7.10)$$

which can be written in the alternative form

$$W_R(\boldsymbol{\epsilon}) = \inf\{\xi_1 W(\boldsymbol{\epsilon}_1) + \xi_2 W(\boldsymbol{\epsilon}_2)\,|\,\xi_1\,,\,\xi_2\,,\,\boldsymbol{\epsilon}_1\,,\,\boldsymbol{\epsilon}_2\,;\,0 \le \xi_i \le 1\,,$$
$$\xi_1 + \xi_2 = 1\,,\,\boldsymbol{\epsilon} = \xi_1\boldsymbol{\epsilon}_1 + \xi_2\boldsymbol{\epsilon}_2\,,\,\mathrm{rank}\,(\boldsymbol{\epsilon}_1 - \boldsymbol{\epsilon}_2) \le 1\}, \quad (7.11)$$

where ξ_1 and ξ_2, respectively, are two volume fractions of the laminates 1 and 2; $\boldsymbol{\epsilon}_1$ and $\boldsymbol{\epsilon}_2$, respectively, are strain fields of the laminates 1 and 2.

Eq. (7.10), or equivalently (7.11) is exactly the definition of the first order rank-one convexification [20, 55]. Therefore rank-one convexification is nothing more than quasiconvexification restricted to laminates as possible fluctuation fields. In the following considerations the proposed formulation in this thesis is developed based on a first-order rank-one convexification.

7.2. General assumptions

In this theory localization phenomena are regarded as micro-structure developments associated with nonconvex energy functions. The micro-structures consist of two domains: a low-strain domain and a high-strain one. Let us consider a so-called RVE (representative volume element) obtained by zooming on the region around the point A as shown in Fig. 7.2. The RVE is split into two volume fractions: the volume fraction ξ of a low-strain domain and the volume fraction $(1 - \xi)$ of a high-strain domain.
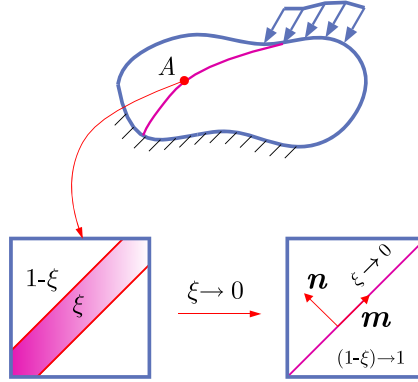
Figure 7.2.: Shear band is treated as the micro-shearing of a rank-one laminate.

When strain localization occurs, the following assumptions related to the volume fraction ξ are made

(1) After the onset of localization, the width of the shear band represented by the volume fraction ξ tends to zero

$$\xi \to 0. \tag{7.12}$$

(2) The energy inside the shear band W_2 is assumed to obey

$$W_2(\xi\boldsymbol{\epsilon}) = |\xi|\, W_2(\boldsymbol{\epsilon}). \tag{7.13}$$

where $W_2(\boldsymbol{\epsilon})$ may be taken in the following form

$$W_2(\boldsymbol{\epsilon}) \;=\; (\boldsymbol{\epsilon} : \boldsymbol{\mathcal{D}} : \boldsymbol{\epsilon})^{\frac{\alpha}{2}}. \tag{7.14}$$

where $\boldsymbol{\mathcal{D}}$ is symmetric fourth-order, positive definite tensor. For the special case $\boldsymbol{\mathcal{D}} = A^2\boldsymbol{\mathcal{I}}$, where $\boldsymbol{\mathcal{I}}$ is the fourth-order unit tensor (7.59), the general form (7.14) reduces to

$$W_2(\boldsymbol{\epsilon}) \;=\; A^\alpha \left(\boldsymbol{\epsilon} : \boldsymbol{\epsilon}\right)^{\frac{\alpha}{2}} = A^\alpha \left\|\boldsymbol{\epsilon}\right\|^\alpha. \tag{7.15}$$

The first assumption is based on the observations that the width of shear bands is normally very small relative to the dimension of structure [[85, 67]. This assumption is corresponds to the concept of the strong discontinuity proposed by *Simo et al., 1993*[98] and *Oliver, 1995*[88] among others.

According to the second assumption, the energy inside a shear band is positive homogeneous of first degree in the strain field (7.13). Only for the form of this energy as given in eqs. (7.14) and (7.15) corresponding to $\alpha = 1$, the energy has the desired property leading to strong discontinuities. If α is larger than 1, the material will exhibit only weak discontinuities. If α is smaller than 1, the relaxed energy does not exist because of lacking coercivity.

Based upon these assumptions, let us start with the consideration of a very simple one-dimensional model to discuss the physical implications of the proposed approach. Then it will be generalized to two-dimensional problem.

7.3. One-dimensional problem

7.3.1. Micro-strain

Let us denote by ϵ_1 and ϵ_2 two micro-strains present at initiation of a shear band (see Fig. 7.3a). A visualization given in Fig. 7.3a depicts the shape of a non-convex potential energy W and its convexification. Due to the finite volume fraction ξ ($\xi \neq 0$) the shear band is treated as *weak discontinuity*. The volume fraction ξ (Fig. 7.2) is frozen and assumed to be a priori determined by a given length scale parameter. This length scale parameter can be interpreted as the width of the micro-shear band on the micro-scale [74].

The potential energy W exhibiting *strong discontinuity* based on the assumption (7.12) shows in Fig. 7.3b. The width of the shear band now tends to zero ($\xi \to 0$) and the currently macroscopic strain decomposes into two micro-strains. The micro-strain ϵ_1 of the low-strain domain is bounded and the micro-strain ϵ_2 of the high-strain domain is unbounded.

To clarify why ϵ_2 is unbounded, let us start with the relation between the macro-strain ϵ and the two micro-strains ϵ_1, ϵ_2

$$\epsilon = (1 - \xi)\epsilon_1 + \xi \epsilon_2. \tag{7.16}$$

We assume that [63]:

$$\epsilon_1 = \epsilon - \xi d, \tag{7.17}$$
$$\epsilon_2 = \epsilon + (1 - \xi) d = \epsilon - \xi d + d, \tag{7.18}$$
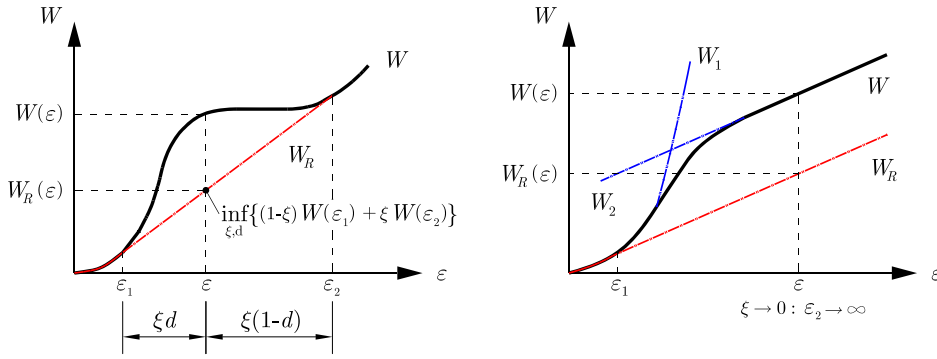
Figure 7.3.: Two micro-strains ϵ_1, ϵ_2 and relaxed energy W_R.

where $0 \leq \xi \leq 1$. Let us consider here the case $d \geq 0$ and $\epsilon \geq 0$. In the case $d \leq 0$ and $\epsilon \leq 0$, the procedure is completely similar. The case $\epsilon\, d < 0$ leading to $|\epsilon_2| < |\epsilon|$ does not exist.

Let us define s by

$$s = \xi d. \tag{7.19}$$

Substituting (7.19) into eqs. (7.17) and (7.18) yields

$$\epsilon_1 = \epsilon - s, \tag{7.20}$$
$$\epsilon_2 = \epsilon - s + \frac{s}{\xi}. \tag{7.21}$$

Let ξ tend to zero, $\dfrac{s}{\xi}$ will grow without bound and of course be extremely large in comparison with $(\epsilon - s)$. Thus, eq. (7.21) can be simplified as

$$\epsilon_2 \approx \frac{s}{\xi} \to \infty \quad \text{as } \xi \to 0\,. \tag{7.22}$$

The assumption of a zero width shear band immediately leads to an unbounded strain (7.22) of the high-strain domain at the discontinuity.

7.3.2. Relaxed energy

Based on the values of the two micro-strains ϵ_1 and ϵ_2 the potential energy W can be divided into three parts (see Fig. 7.3b). The quadratic part denoted as W_1 is the potential energy representing the behaviour at very small strains. The linear part W_2 is the potential energy

representing the behaviour at very large strains. The domain in strain space where $W(\epsilon) \neq W_1(\epsilon)$ and $W(\epsilon) \neq W_2(\epsilon)$ is of no importance since it does not influence the relaxed energy. Hence, the mixed energy of the two domains is defined by

$$W^{mix}(\epsilon) \quad = \quad (1 - \xi)W_1(\epsilon - s) + \xi W_2(\frac{s}{\xi}). \tag{7.23}$$

This mixed energy can be considered as an approximation of the potential energy W, which omits the energy between W_1 and W_2. Based on the assumptions (7.13) and (7.15) , the mixed energy can be simplified as

$$W^{mix}(\epsilon) \quad = \quad W_1(\epsilon - s) + A |s|. \tag{7.24}$$

The problem of the non-convex mixed energy arises due to the occurrence of shear bands. By introducing the concept of relaxation the problem can be resolved and becomes well-posed. The relaxed energy is obtained by the minimization procedure

$$W_R(\epsilon) = \inf \left\{ W^{mix}(\epsilon) \mid s \right\}. \tag{7.25}$$

As mentioning in Section 7.3.1 we consider here the case $d \geq 0$ and $\epsilon \leq 0$. Then the relaxed energy (7.25) can be rewritten as follows

$$W_R(\epsilon) = \inf \left\{ W^{mix}(\epsilon) \mid s, \, s \geq 0 \right\}. \tag{7.26}$$

The mixed stress is obtained by taking the derivative of the mixed energy (7.23) with respect to ϵ

$$\sigma(\epsilon) = (1 - \xi)\sigma(\epsilon_1) + \xi \sigma(\epsilon_2). \tag{7.27}$$

The stationary point of eq. (7.26) reads

$$\sigma(\epsilon) = \sigma(\epsilon_1) = \sigma(\epsilon_2) = A. \tag{7.28}$$

The slope of the relaxed energy represented by (7.28) is constant, consequently, the relaxed tangent modulus is equal to zero. Here the material parameter A can be interpreted as stress level inside the shear band. The relaxed energy W_R is depicted in Fig. 7.3b.

7.3.3. Example

The proposed formulation in the previous section is applied to an isotropic linear material. The mixed energy of the low-strain and high-strain domains obtained eq. (7.23) is given by

$$W^{mix}(\epsilon) = \frac{1}{2}E (\epsilon - s)^2 + A |s|. \tag{7.29}$$

where E is Young's modulus and A is a material parameter.

The relaxed energy is defined by

$$W_R(\epsilon) = \inf \left\{ W^{mix}(\epsilon) \mid s, s \geq 0 \right\}. \tag{7.30}$$

The local minimizer of the function (7.30) is

$$s = \begin{cases} 0 & \text{for } \epsilon < \dfrac{A}{E} \,. \\[3mm] \epsilon - \dfrac{A}{E} & \text{for } \epsilon \geq \dfrac{A}{E} \,. \end{cases} \tag{7.31}$$

Strain and stress can be calculated as below

- If $\epsilon < \dfrac{A}{E}$, we have $s = 0$. The relaxed energy is equal to the elastic strain energy

$$W_R(\epsilon) = W^{mix}(\epsilon) = \frac{1}{2} E \epsilon^2. \tag{7.32}$$

  The macroscopic strain ϵ is equal to ϵ_1 and ϵ_2 due to $\xi = 0$

$$\epsilon = \epsilon_1 = \epsilon_2. \tag{7.33}$$

  The material obeys Hooke's law

$$\sigma = \frac{\partial W^{mix}}{\partial \epsilon} = E\epsilon. \tag{7.34}$$

- If $\epsilon \geq \dfrac{A}{E}$, we obtain the micro-strains

$$\epsilon_1 = \epsilon - s = \frac{A}{E} \quad ; \quad \epsilon_2 \to \infty, \tag{7.35}$$

  The relaxed energy is the sum of the relaxed energy of the low-strain domain denoted by $[(1-\xi)W_1]_R$ and the relaxed energy of the high-strain domain denoted by $[\xi W_2]_R$

$$W_R(\epsilon) = \underbrace{\frac{A^2}{2E}}_{[(1-\xi)W_1]_R} + \underbrace{A\,|s|}_{[\xi W_2]_R}, \tag{7.36}$$

  The relaxed stress is given by

$$\sigma = \sigma_1 = \sigma_2 = \frac{\partial W_R}{\partial \epsilon} = A. \tag{7.37}$$

The relaxed energy as well as the relaxed stress are depicted in Fig. 7.4.
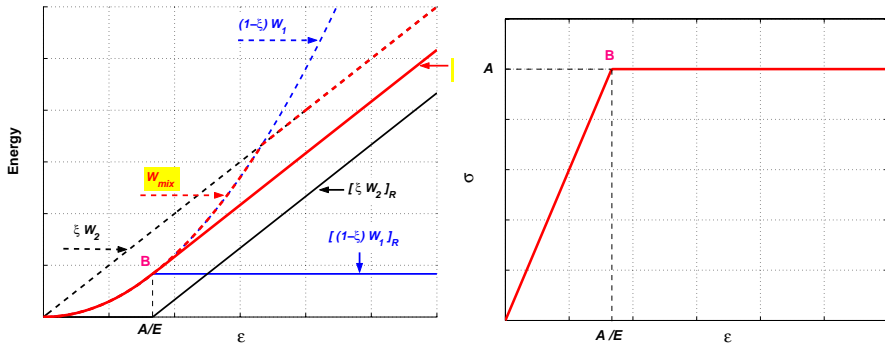
Figure 7.4.: Relaxed energy and stress in one-dimentional problem.

7.4. Two-dimensional problem

7.4.1. Micro-strain

In the two-dimensional problem the micro-strains ϵ_1 and ϵ_2 can be written as

$$\epsilon_1 \;=\; \epsilon - \xi(\boldsymbol{a} \otimes \boldsymbol{n})^{\mathrm{s}} \tag{7.38}$$

$$\epsilon_2 \;=\; \epsilon + (1 - \xi)(\boldsymbol{a} \otimes \boldsymbol{n})^{\mathrm{s}} = \epsilon - \xi(\boldsymbol{a} \otimes \boldsymbol{n})^{\mathrm{s}} + (\boldsymbol{a} \otimes \boldsymbol{n})^{\mathrm{s}} \tag{7.39}$$

where $(\boldsymbol{a} \otimes \boldsymbol{n})^{\mathrm{s}} = \frac{1}{2}(\boldsymbol{a} \otimes \boldsymbol{n} + \boldsymbol{n} \otimes \boldsymbol{a})$.

Let us define s by

$$\xi\boldsymbol{a} = s\boldsymbol{m}, \tag{7.40}$$

where $\|\boldsymbol{m}\| = 1$. Herein $\boldsymbol{m}$ and $\boldsymbol{n}$ are two unit vectors giving the direction of shear band evolution; s is a scaling parameter.

On inserting eq. (7.40) into eqs. (7.38) and (7.39), we have

$$\epsilon_1 = \epsilon - s(\boldsymbol{m} \otimes \boldsymbol{n})^{\mathrm{s}}, \tag{7.41}$$

$$\epsilon_2 = \epsilon - s(\boldsymbol{m} \otimes \boldsymbol{n})^{\mathrm{s}} + \frac{s}{\xi}(\boldsymbol{m} \otimes \boldsymbol{n})^{\mathrm{s}}. \tag{7.42}$$

As ξ tends to zero, $\dfrac{s}{\xi}$ will grow without bound. Thus, eq. (7.42) can be simplified as

$$\epsilon_2 \approx \frac{s}{\xi}(\boldsymbol{m} \otimes \boldsymbol{n})^{\mathrm{s}}. \tag{7.43}$$

7.4.2. Relaxed energy

The mixed energy of the two domains can be written in the following form

$$\boxed{W^{mix}(\epsilon) = W_1(\epsilon - s(\boldsymbol{m} \otimes \boldsymbol{n})^{\mathrm{s}}) + |s|\, W_2((\boldsymbol{m} \otimes \boldsymbol{n})^{\mathrm{s}}).} \tag{7.44}$$

As explained in section 7.3.2, the relaxed energy is computed in order to ensure the well-posed problem due to the emergence of a shear band. The relaxed energy is obtained by the minimization procedure

$$W_R(\epsilon) = \inf \left\{ W^{mix}(\epsilon) \mid s\,,\, \boldsymbol{m}\,,\boldsymbol{n}\,;\, \|\boldsymbol{m}\| = \|\boldsymbol{n}\| = 1 \right\}. \tag{7.45}$$

Let us consider the two potential energies representing the behaviour at very small and large strains, respectively

$$
\begin{aligned}
W_1(\epsilon) &= \frac{1}{2}\epsilon : \mathcal{C} : \epsilon & (7.46)\\
W_2(\gamma) &= (\gamma : \mathcal{D} : \gamma)^{\frac{1}{2}} & (7.47)
\end{aligned}
$$

where $\mathcal{C}$ and $\mathcal{D}$ are symmetric fourth-order, positive definite tensors; ϵ and γ are strain tensors. Substituting (7.46) and (7.47) into (7.44), one gets

$$
\begin{aligned}
W^{mix}(\epsilon) &= \frac{1}{2}(\epsilon - s\gamma) : \mathcal{C} : (\epsilon - s\gamma) + |s|\,(\gamma : \mathcal{D} : \gamma)^{\frac{1}{2}}\\
&= \frac{1}{2}\epsilon : \mathcal{C} : \epsilon + \frac{1}{2}s^2\gamma : \mathcal{C} : \gamma - s\,\epsilon : \mathcal{C} : \gamma + |s|\,(\gamma : \mathcal{D} : \gamma)^{\frac{1}{2}} & (7.48)
\end{aligned}
$$

where $\gamma = (m \otimes n)^{\mathrm{s}}$.

By use of the results in Box 7.1, minimization of (7.48) with respect to s yields

$$
s = \frac{\mathrm{sign}(\epsilon : \mathcal{C} : \gamma)}{(\gamma : \mathcal{C} : \gamma)^{\frac{1}{2}}}\left[\frac{|\epsilon : \mathcal{C} : \gamma|}{(\gamma : \mathcal{C} : \gamma)^{\frac{1}{2}}} - \left(\frac{\gamma : \mathcal{D} : \gamma}{\gamma : \mathcal{C} : \gamma}\right)^{\frac{1}{2}}\right]_{+} , \tag{7.49}
$$

and the corresponding energy with solution s (7.49)

$$
\inf_{s} W^{mix}(\epsilon) = \frac{1}{2}\epsilon : \mathcal{C} : \epsilon - \frac{1}{2}\left[\frac{|\epsilon : \mathcal{C} : \gamma|}{(\gamma : \mathcal{C} : \gamma)^{\frac{1}{2}}} - \left(\frac{\gamma : \mathcal{D} : \gamma}{\gamma : \mathcal{C} : \gamma}\right)^{\frac{1}{2}}\right]_{+}^{2}. \tag{7.50}
$$

Herein $a = \frac{1}{2}\gamma : \mathcal{C} : \gamma$, $b = -\epsilon : \mathcal{C} : \gamma$, $c = (\gamma : \mathcal{D} : \gamma)^{\frac{1}{2}}$. Easily one can recognise that a is positive due to the positive definiteness of the fourth-order tensor $\mathcal{C}$.

7.4.3. Computation of the relaxed stress and the tangent operator

The relaxed stress and the tangent operator are derived from the direct derivative of the relaxed energy (7.45). The first derivative of (7.45) reads

$$
\frac{\partial W_R}{\partial \epsilon} = \frac{\partial W^{mix}}{\partial \epsilon} + \frac{\partial W^{mix}}{\partial s}\frac{\partial s}{\partial \epsilon} + \frac{\partial W^{mix}}{\partial m}\frac{\partial m}{\partial \epsilon} + \frac{\partial W^{mix}}{\partial n}\frac{\partial n}{\partial \epsilon}. \tag{7.51}
$$

It is observed that the three last terms in eq. (7.51) vanish due to the necessary condition of

the minimization problem (7.45). Thus, the relaxed stress which is the average of the two micro-stresses has the form

$$\boxed{\boldsymbol{\sigma} = \frac{\partial W^{mix}}{\partial \boldsymbol{\epsilon}}.}$$

(7.52)

The relaxed stress by considering the form of the potential energy (7.50) yields

$$\boxed{\boldsymbol{\sigma} = \mathcal{C} : \boldsymbol{\epsilon} - s\,\mathcal{C} : \boldsymbol{\gamma}.}$$

(7.53)

The tangent operator is given by

$$\boxed{\mathcal{A} = \frac{\partial^2 W_R}{\partial \boldsymbol{\epsilon}^2} = \frac{\partial \boldsymbol{\sigma}}{\partial \boldsymbol{\epsilon}} = \mathcal{C} - (\mathcal{C} : \boldsymbol{\gamma}) \otimes \frac{\partial s}{\partial \boldsymbol{\epsilon}} - s \frac{\partial (\mathcal{C} : \boldsymbol{\gamma})}{\partial \boldsymbol{\epsilon}}.}$$

(7.54)

The theoretical developments are summarized in Box 7.2.

Box 7.1: Minimization problem: $\inf\limits_{s} W(s)$

$$\inf_{s} W(s).$$

$$W(s) = as^2 + bs + c\,|s| \quad \text{with } c > 0,\ a > 0.$$

Solution s

$$s = -\frac{1}{2a}(|b| - c)_+ \operatorname{sign}(b)$$

where

$$(|b| - c)_+ = \begin{cases} 0 & \text{for } |b| \le c. \\ |b| - c & \text{for } |b| > c. \end{cases}$$

$$\operatorname{sign}(b) = \frac{|b|}{b} \quad \text{for } b \neq 0.$$

Substituting (7.55) into (7.55) leads to

$$\inf_{s} W(s) = -\frac{1}{4a}(|b| - c)_+^2.$$

Box 7.2: Summary of some main formulations of the relaxed energy

Micro-strains

$$\epsilon_1 = \epsilon - s\gamma.$$
$$\epsilon_2 \approx \frac{s}{\xi}\gamma.$$

where $\gamma = (m \otimes n)^{\mathrm{s}}$

Mixed energy

$$W^{mix}(\epsilon) = \frac{1}{2}(\epsilon - s\gamma) : \mathcal{C} : (\epsilon - s\gamma) + |s|(\gamma : \mathcal{D} : \gamma)^{\frac{1}{2}}$$

Relaxed energy

$$W_R = \inf_{s,m,n} W^{mix}(\epsilon)$$

where

$$\inf_s W^{mix}(\epsilon) = \frac{1}{2}\epsilon : \mathcal{C} : \epsilon - \frac{1}{2}\left[\frac{|\epsilon : \mathcal{C} : \gamma|}{(\gamma : \mathcal{C} : \gamma)^{\frac{1}{2}}} - \left(\frac{\gamma : \mathcal{D} : \gamma}{\gamma : \mathcal{C} : \gamma}\right)^{\frac{1}{2}}\right]_+^2.$$

Solution s

$$s = \frac{\mathrm{sign}(\epsilon : \mathcal{C} : \gamma)}{(\gamma : \mathcal{C} : \gamma)^{\frac{1}{2}}}\left[\frac{|\epsilon : \mathcal{C} : \gamma|}{(\gamma : \mathcal{C} : \gamma)^{\frac{1}{2}}} - \left(\frac{\gamma : \mathcal{D} : \gamma}{\gamma : \mathcal{C} : \gamma}\right)^{\frac{1}{2}}\right]_+.$$

Relaxed stress

$$\sigma = \mathcal{C} : \epsilon - s\,\mathcal{C} : \gamma.$$

Tangent operator

$$\mathcal{A} = \frac{\partial^2 W_R}{\partial \epsilon^2} = \frac{\partial \sigma}{\partial \epsilon} = \mathcal{C} - (\mathcal{C} : \gamma) \otimes \frac{\partial s}{\partial \epsilon} - s\frac{\partial (\mathcal{C} : \gamma)}{\partial \epsilon}.$$

7.4.4. Variational formulation

The general total potential energy of an inelastic body can be written as

$$\Pi(u) = \int_\Omega W_R(\epsilon)\,dV - \int_\Omega u^{\mathrm{T}}f\,dV - \int_{\partial\Omega_\sigma} u^{\mathrm{T}}\bar{t}\,dA. \tag{7.55}$$

Let us denote

$$check = \left[\frac{|\epsilon : \mathcal{C} : \gamma|}{(\gamma : \mathcal{C} : \gamma)^{\frac{1}{2}}} - \left(\frac{\gamma : \mathcal{D} : \gamma}{\gamma : \mathcal{C} : \gamma}\right)^{\frac{1}{2}}\right]. \tag{7.56}$$

As the process of deformation progresses, $check$ may be negative, zero or positive. The positive value in turn signals the onset of localization.

    i. $check \leq 0: s = 0$ The relaxed energy $W_R(\epsilon)$ reduces to the elastic strain energy $W_1(\epsilon)$.

    ii. $check > 0: s \neq 0$ The shear band starts to develop. The homogeneous deformation ϵ decomposes into the two micro-strains ϵ_1 and ϵ_2. The nonconvex potential energy W^{mix} is replaced with the approximated rank-one convexification $W_R(\epsilon)$ to ensure the well-posedness of the problem.

7.5. Application of relaxation theory to isotropic materials

Let us recall the potential energy W_2 of high-strain domain

$$W_2(\boldsymbol{\gamma}) = (\boldsymbol{\gamma} : \boldsymbol{D} : \boldsymbol{\gamma})^{\frac{1}{2}}. \tag{7.57}$$

Softening behaviour is implicitly included in this linear function.

In what follows, we consider two possible cases. In the first case, $\boldsymbol{D}$ is equal to $\boldsymbol{C}$, where $\boldsymbol{C}$ is the fourth-order isotropic elastic tensor. In the second case, $\boldsymbol{D}$ is equal to $A\boldsymbol{I}$ as the special case defined by eq. (7.15).

7.5.1. Case 1: $\boldsymbol{D} = \boldsymbol{C}$

On inserting $\boldsymbol{D} = \boldsymbol{C}$ into (7.57) and (7.48) we obtain the mixed energy of two domains

$$W^{mix}(\epsilon) = \frac{1}{2}\epsilon : \boldsymbol{C} : \epsilon + \frac{1}{2}s^2\boldsymbol{\gamma} : \boldsymbol{C} : \boldsymbol{\gamma} - s\,\epsilon : \boldsymbol{C} : \boldsymbol{\gamma} + |s|\,(\boldsymbol{\gamma} : \boldsymbol{C} : \boldsymbol{\gamma})^{\frac{1}{2}}, \tag{7.58}$$

where $\boldsymbol{\gamma} = (\boldsymbol{m} \otimes \boldsymbol{n}^s)$; $\boldsymbol{C}$ is the fourth-order isotropic elastic tensor

$$\mathcal{C}_{ijkl} = \lambda\delta_{ij}\delta_{kl} + \mu\left(\delta_{ik}\delta_{jl} + \delta_{il}\delta_{jk}\right), \tag{7.59}$$

or in the tensor notation

$$\boldsymbol{C} = \lambda\,\boldsymbol{I} \otimes \boldsymbol{I} + \mu\left(\boldsymbol{\mathcal{I}} + \bar{\boldsymbol{\mathcal{I}}}\right), \tag{7.60}$$

where λ and μ are Lamé constants.

We consider the following relaxed energy

$$W_R(\epsilon) = \inf \left\{ W^{mix}(\epsilon) \mid s\,, \boldsymbol{m}\,, \boldsymbol{n}\,; \|\boldsymbol{m}\| = \|\boldsymbol{n}\| = 1 \right\}. \tag{7.61}$$

Let φ be the angle between two vectors $\boldsymbol{m}$ and $\boldsymbol{n}$ as depicted in Fig. 7.5, where the unit vector $\boldsymbol{t}$ is perpendicular to the vector $\boldsymbol{m}$. Then we write

$$\boldsymbol{n} = \boldsymbol{m} \cos\varphi + \boldsymbol{t} \sin\varphi, \tag{7.62}$$
$$\boldsymbol{m}.\boldsymbol{\epsilon}\,\boldsymbol{n} = (\boldsymbol{m}.\boldsymbol{\epsilon}\,\boldsymbol{m}) \cos\varphi + (\boldsymbol{m}.\boldsymbol{\epsilon}\,\boldsymbol{t}) \sin\varphi. \tag{7.63}$$
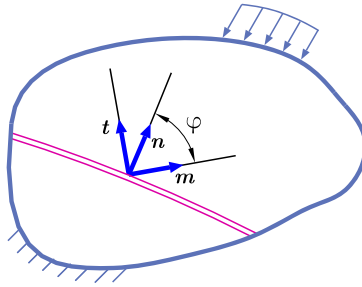
Figure 7.5.: Orientation of the shear band.
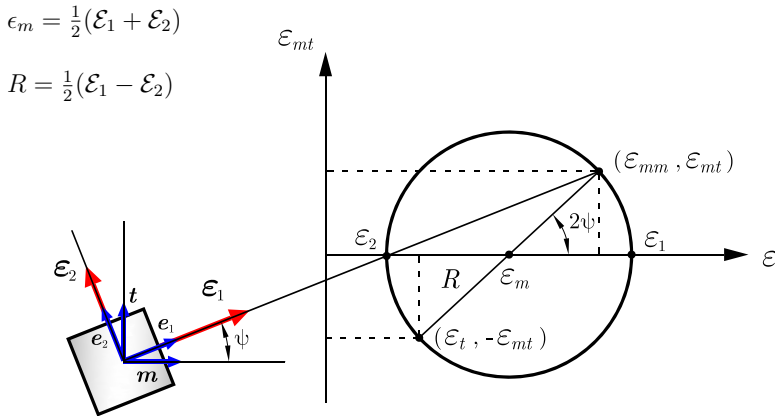
Figure 7.6.: Mohr strain circle.

Now we consider a plane which has $(\boldsymbol{m}, \boldsymbol{t})$ as the unit tangent and normal vectors. It is recognized that $(\boldsymbol{m}.\boldsymbol{\epsilon}\,\boldsymbol{m})$ is the normal strain whose direction is perpendicular to the plane

and $(\boldsymbol{m}.\boldsymbol{\epsilon}\,\boldsymbol{t})$ is the shear strain in this plane. Using Mohr's circle we can transform (7.63) into principal strains

$$
\begin{aligned}
\boldsymbol{m}.\boldsymbol{\epsilon}\,\boldsymbol{n} &= (\epsilon_m + R\cos 2\psi)\cos\varphi + R\sin 2\psi\,\sin\varphi \\
&= \epsilon_m \cos\varphi + R\cos(\varphi - 2\psi)
\end{aligned}
\tag{7.64}
$$

where R and ϵ_m are the maximum shear strain and the average strain; ψ is an angle between the vector $\boldsymbol{m}$ and the eigenvector $\boldsymbol{e}_1$ corresponding to the major principal strain $\mathcal{E}_1$ as denoted in Fig. 7.6.

Instead of minimizing (7.61) with respect to s, $\boldsymbol{m}$ and $\boldsymbol{n}$, now we minimize (7.65) with respect to s, ψ and φ based on eqs. (7.62-7.64)

$$
W_R(\boldsymbol{\epsilon}) = \inf\left\{ W^{mix}(\boldsymbol{\epsilon}) \mid s\,,\,\psi\,,\varphi\,;\, 0 \le \psi\,,\,\varphi \le \pi \right\}.
\tag{7.65}
$$

The results of the minimization problem (7.65) is given in Box 7.3. The algorithm is summarized in Box 7.4, 7.5 and 7.6.

7.5.2. Case 2: $\mathcal{D} = A^2\boldsymbol{\mathcal{I}}\ (A > 0)$

On inserting $\mathcal{D} = A^2\boldsymbol{\mathcal{I}}$ into (7.57) and (7.48) we obtain the mixed energy of the low-strain and high-strain domains

$$
W^{mix}(\boldsymbol{\epsilon}) = \frac{1}{2}\boldsymbol{\epsilon}:\boldsymbol{\mathcal{C}}:\boldsymbol{\epsilon} + \frac{1}{2}s^2\boldsymbol{\gamma}:\boldsymbol{\mathcal{C}}:\boldsymbol{\gamma} - s\,\boldsymbol{\epsilon}:\boldsymbol{\mathcal{C}}:\boldsymbol{\gamma} + A\,|s|\,\|\boldsymbol{\gamma}\|,
\tag{7.66}
$$

where $\boldsymbol{\gamma} = (\boldsymbol{m} \otimes \boldsymbol{n}^s)$.

Let us consider the following relaxed energy

$$
W_R(\boldsymbol{\epsilon}) = \inf\left\{ W^{mix}(\boldsymbol{\epsilon}) \mid s\,,\,\boldsymbol{m}\,,\boldsymbol{n}\,;\, \|\boldsymbol{m}\| = \|\boldsymbol{n}\| = 1 \right\}.
\tag{7.67}
$$

By substituting $\mathcal{D} = A^2\boldsymbol{\mathcal{I}}$ into (7.49) and (7.50) the minimization problem (7.67) with respect to s gives

$$
s = \frac{\operatorname{sign}(\boldsymbol{\epsilon}:\boldsymbol{\mathcal{C}}:\boldsymbol{\gamma})}{(\boldsymbol{\gamma}:\boldsymbol{\mathcal{C}}:\boldsymbol{\gamma})^{\frac{1}{2}}}\left[\frac{|\boldsymbol{\epsilon}:\boldsymbol{\mathcal{C}}:\boldsymbol{\gamma}| - A\,\|\boldsymbol{\gamma}\|}{(\boldsymbol{\gamma}:\boldsymbol{\mathcal{C}}:\boldsymbol{\gamma})^{\frac{1}{2}}}\right]_+,
\tag{7.68}
$$

where

$$
\begin{aligned}
\boldsymbol{\epsilon}:\boldsymbol{\mathcal{C}}:\boldsymbol{\gamma} &= \lambda(\operatorname{tr}\boldsymbol{\epsilon})(\boldsymbol{m}.\boldsymbol{n}) + 2\,\mu\,\boldsymbol{m}.\boldsymbol{\epsilon}\boldsymbol{n}, \tag{7.69} \\
\boldsymbol{\gamma}:\boldsymbol{\mathcal{C}}:\boldsymbol{\gamma} &= \mu + (\boldsymbol{m}.\boldsymbol{n})^2(\lambda + \mu). \tag{7.70}
\end{aligned}
$$

The energy (7.66) with s given by (7.68) takes the form

$$
\begin{aligned}
\inf_s W^{mix}(\boldsymbol{\epsilon}) &= \frac{1}{2}\boldsymbol{\epsilon} : \boldsymbol{C} : \boldsymbol{\epsilon} - \frac{1}{2}\left[\frac{|\boldsymbol{\epsilon} : \boldsymbol{C} : \boldsymbol{\gamma}| - A\,\|\boldsymbol{\gamma}\|}{(\boldsymbol{\gamma} : \boldsymbol{C} : \boldsymbol{\gamma})^{\frac{1}{2}}}\right]_+^2 \\
&= \frac{1}{2}\lambda(\mathrm{tr}\boldsymbol{\epsilon})^2 + \mu\,\|\boldsymbol{\epsilon}\|^2 - \frac{1}{2}\left[M(\boldsymbol{m},\boldsymbol{n})\right]_+^2,
\end{aligned}
\tag{7.71}
$$

where

$$
M(\boldsymbol{m},\boldsymbol{n}) = \frac{|\lambda(\mathrm{tr}\boldsymbol{\epsilon})(\boldsymbol{m}.\boldsymbol{n}) + 2\,\mu\,\boldsymbol{m}.\boldsymbol{\epsilon}\boldsymbol{n}| - \frac{A}{\sqrt{2}}\left[1 + (\boldsymbol{m}.\boldsymbol{n})^2\right]^{\frac{1}{2}}}{\left[\mu + (\boldsymbol{m}.\boldsymbol{n})^2(\lambda + \mu)\right]^{\frac{1}{2}}}.
\tag{7.72}
$$

Box 7.3: Summary of some main formulations of the relaxed energy ($\boldsymbol{D} = \boldsymbol{C}$)

Consider

$$
\boldsymbol{D} = \boldsymbol{C} = \lambda\,\boldsymbol{I} \otimes \boldsymbol{I} + \mu\left(\boldsymbol{\mathcal{I}} + \bar{\boldsymbol{\mathcal{I}}}\right).
$$

Mixed energy

$$
W^{mix}(\boldsymbol{\epsilon}) = \frac{1}{2}\left(\boldsymbol{\epsilon} - s\boldsymbol{\gamma}\right) : \boldsymbol{C} : \left(\boldsymbol{\epsilon} - s\boldsymbol{\gamma}\right) + |s|\left(\boldsymbol{\gamma} : \boldsymbol{C} : \boldsymbol{\gamma}\right)^{\frac{1}{2}}.
$$

Relaxed energy

$$
\inf_{s,\boldsymbol{m},\boldsymbol{n}} W^{mix}(\boldsymbol{\epsilon}) = \inf_{s,\varphi,\psi} W^{mix}(\boldsymbol{\epsilon}) = \frac{1}{2}\lambda(\mathrm{tr}\boldsymbol{\epsilon})^2 + \mu\,\|\boldsymbol{\epsilon}\|^2 - \frac{1}{2}\left[M(\varphi) - 1\right]_+^2.
$$

Solutions ψ, φ and s

$$
\psi = \frac{\varphi}{2}.
$$

$$
\sin\varphi = 0 \quad \text{or} \quad \cos\varphi = \frac{2\epsilon_m\mu + \lambda\mathrm{tr}\boldsymbol{\epsilon}}{2R\left(\lambda + \mu\right)}.
$$

$$
s = \frac{\mathrm{sign}\left[(\lambda\mathrm{tr}\boldsymbol{\epsilon} + 2\mu\epsilon_m)\cos\varphi + 2\mu R\right]}{\left[\mu + (\lambda + \mu)\cos^2\varphi\right]^{\frac{1}{2}}}\left[M(\varphi) - 1\right]_+.
$$

Relaxed stress

$$
\begin{aligned}
\boldsymbol{\sigma} &= \boldsymbol{C} : \boldsymbol{\epsilon} - s\,\boldsymbol{C} : \boldsymbol{\gamma} \\
&= \lambda\mathrm{tr}\boldsymbol{\epsilon}\,\boldsymbol{I} + 2\mu\boldsymbol{\epsilon} - s\left[\lambda\left(\boldsymbol{m}.\boldsymbol{n}\right)\boldsymbol{I} + 2\mu\left(\boldsymbol{m} \otimes \boldsymbol{n}\right)^s\right].
\end{aligned}
$$

Tangent operator

$$
\boldsymbol{\mathcal{A}} = \frac{\partial^2 W_R}{\partial\boldsymbol{\epsilon}^2} = \frac{\partial\boldsymbol{\sigma}}{\partial\boldsymbol{\epsilon}} = \boldsymbol{C} - \left(\boldsymbol{C} : \boldsymbol{\gamma}\right) \otimes \frac{\partial s}{\partial\boldsymbol{\epsilon}} - s\frac{\partial\left(\boldsymbol{C} : \boldsymbol{\gamma}\right)}{\partial\boldsymbol{\epsilon}}.
$$

Box 7.4: Two-dimensional relaxed energy algorithm

---

1. Compute two major and minor principle strains $\mathcal{E}_1$ and $\mathcal{E}_2$ as well as their eigen-vectors e_1 and e_2.
2. Find R and ϵ_m.
3. Check whether localization condition is met or not based on $check$.

  - If $check \leq 0$, $s = 0$ (see Box 7.6).

  - If $check > 0$, compute φ, s, m and n (see Box 7.5 and 7.6).

4. Compute relaxed energy $W_R(\epsilon)$.
5. Compute relaxed stress σ.
6. Compute tangent operator $\mathcal{A}$.

Box 7.5: Computing the orientation of the shear band evolution m and n

---

1. Compute rotation matrix

$$\boldsymbol{R} = \begin{pmatrix} \cos \psi & \sin \psi \\ -\sin \psi & \cos \psi \end{pmatrix}.$$

2. Find $\boldsymbol{m} = \boldsymbol{R}e_1$, $\boldsymbol{n} = \boldsymbol{R}e_2$, where e_1 and e_2 are two eigenvectors of the major and minor principal strains

$$\boldsymbol{\epsilon} = \mathcal{E}_1 e_1 \otimes e_1 + \mathcal{E}_2 e_2 \otimes e_2 \quad (\epsilon_1 \geq \epsilon_2).$$

3. Find $\boldsymbol{n}$.

$$\boldsymbol{n} = \boldsymbol{m} \cos \varphi + \boldsymbol{t} \sin \varphi.$$

Box 7.6: Checking localization condition

a. $R = 0$: implies $\sin \varphi = 0 \rightarrow \cos \varphi = 1$

$$M(\varphi) = \frac{|\lambda \text{tr}\boldsymbol{\epsilon} + 2\mu \epsilon_m|}{\sqrt{2\mu + \lambda}}.$$

Localization condition is checked based on *check*

$$check = M(\varphi) - 1 = \frac{|\lambda \text{tr}\boldsymbol{\epsilon} + 2\mu \epsilon_m|}{\sqrt{2\mu + \lambda}} - 1.$$

- $check \leq 0 : s = 0$.

- $check > 0 : s = \dfrac{\text{sign}\,(\lambda \text{tr}\boldsymbol{\epsilon} + 2\mu \epsilon_m)}{\sqrt{2\mu + \lambda}} check.$

b. $R \neq 0$: implies $\sin \varphi \neq 0$, then we have

$$\cos \varphi = \frac{2\epsilon_m \mu + \lambda \text{tr}\boldsymbol{\epsilon}}{2R\,(\lambda + \mu)}, \quad M = \sqrt{\frac{4\mu R^2\,(\lambda + \mu) + (2\mu \epsilon_m + \lambda \text{tr}\boldsymbol{\epsilon})^2}{\lambda + \mu}}.$$

Localization condition is checked based on *check* and $\cos \varphi$

$$check = M - 1.$$

- $check < 0$ or $\cos \varphi \notin [-1, 1] : s = 0.$

- $check > 0$ and $\cos \varphi \in [-1, 1] :$

$$\text{sign}\,[(\lambda \text{tr}\boldsymbol{\epsilon} + 2\mu \epsilon_m) \cos \varphi + 2\mu R] = 1.$$
$$s = \frac{check}{[\mu + (\lambda + \mu) \cos^2 \varphi]^{\frac{1}{2}}}.$$

Now two following cases are investigated. In the first case, $\boldsymbol{m}$ is assumed to be perpendicular to $\boldsymbol{n}$. In second one, $\boldsymbol{m}$ and $\boldsymbol{n}$ are arbitrary.

a. $\boldsymbol{m}.\boldsymbol{n} = cos\varphi = 0$

$\boldsymbol{m}.\boldsymbol{n} = 0$ implies that the normal displacements are much smaller than those in the tangent direction inside the shear band. This result had been observed in the experiment by *Finno et al, 1996* [35]. In the following considerations we develop a simple approach to the treatment of shear localization based on this assumption.

Substituting $\boldsymbol{m}.\boldsymbol{n} = 0$ into eq. (7.66) leads to the simplified form of the mixed energy

$$W^{mix}(\boldsymbol{\epsilon}) = \frac{\lambda}{2}(\text{tr}\boldsymbol{\epsilon})^2 + \mu \left(\|\boldsymbol{\epsilon}\|^2 - 2\,s\,\boldsymbol{m} \cdot \boldsymbol{\epsilon}\boldsymbol{n} + \frac{s^2}{2} \right) + \frac{A}{\sqrt{2}}\,|s| \qquad (7.73)$$

By use of (7.68) and (7.71) as well as (7.62) and (7.63) we can get the relaxed energy

$$W_R = \inf_{s,m,n} W^{mix} = \frac{\lambda}{2} tr(\epsilon)^2 + \mu \|\epsilon\|^2 - 2\mu \left[|\epsilon_{mn}| - \frac{\alpha}{2} \right]_+^2, \tag{7.74}$$

where $\alpha = \dfrac{A}{\sqrt{2}\mu}$, $|\epsilon_{mn}| = R$ is the maximum shear strain.

The minimization problem (7.74) with respect to s gives

$$s = (2|\epsilon_{mn}| - \alpha)_+ \text{sign}(\epsilon_{mn}) = \begin{cases} 0 & \text{if } |\epsilon_{mn}| < \alpha/2 \\ (2|\epsilon_{mn}| - \alpha)\,\text{sign}(\epsilon_{mn}) & \text{if } |\epsilon_{mn}| \ge \alpha/2 \end{cases} \tag{7.75}$$

The relaxed stress is obtained from eqs. (7.53) and (7.74)

$$\boldsymbol{\sigma} = \lambda tr\epsilon \, \boldsymbol{I} + 2\mu\epsilon - 2\mu s \, (\boldsymbol{m} \otimes \boldsymbol{n})^s. \tag{7.76}$$

On inserting (7.74) into (7.54) we get the tangent operator

$$\mathcal{A} = \lambda \boldsymbol{I} \otimes \boldsymbol{I} + \mu(\mathcal{I} + \bar{\mathcal{I}}) - 2\mu \left[(\boldsymbol{m} \otimes \boldsymbol{n})^s \otimes \frac{\partial s}{\partial \epsilon} + s \frac{\partial (\boldsymbol{m} \otimes \boldsymbol{n})^s}{\partial \epsilon} \right]. \tag{7.77}$$

Summary of some main formulations of this model is given in Box 7.7. The algorithm is similar to the algorithm in the case $\mathcal{D} = \mathcal{C}$ summarized in Box. 7.4, 7.5 and 7.6.

b. m and n are arbitrary

Based on Mohr strain circle as depicted in Fig. 7.6, eq. (7.72) can be rewritten as

$$M(\varphi, \psi) = \frac{\left| (\lambda tr\epsilon + 2\mu\epsilon_m) \cos\varphi + 2\mu R \cos(\varphi - 2\psi) \right| - \frac{A}{\sqrt{2}} (1 + \cos^2\varphi)^{\frac{1}{2}}}{\left[\mu + (\lambda + \mu) \cos^2\varphi \right]^{\frac{1}{2}}}. \tag{7.78}$$

Summary of some main formulations of this model is given in Box 7.8. The algorithm is similar to the algorithm in case $\mathcal{D} = \mathcal{C}$ summarized in Box. 7.4, 7.5 and 7.6.

Box 7.7: Summary of some main formulations of the relaxed energy
$$\mathcal{D} = A^2 \mathcal{I}, \, \boldsymbol{m}.\boldsymbol{n} = 0 \, .$$

Consider

$$\begin{aligned}
\mathcal{D} &= A^2 \mathcal{I}. \\
\mathcal{C} &= \lambda \, \boldsymbol{I} \otimes \boldsymbol{I} + \mu \left(\mathcal{I} + \bar{\mathcal{I}} \right). \\
\boldsymbol{m}.\boldsymbol{n} &= 0 \quad \rightarrow \quad \|\boldsymbol{\gamma}\| = \frac{1}{\sqrt{2}}.
\end{aligned}$$

Mixed energy

$$W^{mix}(\boldsymbol{\epsilon}) = \frac{\lambda}{2}(\mathrm{tr}\boldsymbol{\epsilon})^2 + \mu \left(\|\boldsymbol{\epsilon}\|^2 - 2\,s\,\boldsymbol{m}\cdot\boldsymbol{\epsilon n} + \frac{s^2}{2} \right) + \frac{A}{\sqrt{2}}\,|s| \, .$$

Relaxed energy

$$W_R = \inf_{s,\boldsymbol{m},\boldsymbol{n}} W^{mix} = \frac{\lambda}{2}\mathrm{tr}\,(\boldsymbol{\epsilon})^2 + \mu \|\boldsymbol{\epsilon}\|^2 - 2\mu \left[|\epsilon_{mn}| - \frac{\alpha}{2} \right]_+^2 \, .$$

Solutions φ, ψ, s

$$\begin{aligned}
\psi &= \frac{\varphi}{2} = \frac{\pi}{4} \\
s &= \left(2\,|\epsilon_{mn}| - \alpha \right)_+ \mathrm{sign}(\epsilon_{mn})
\end{aligned}$$

where $|\epsilon_{mn}| = R$.

The relaxed stress

$$\boldsymbol{\sigma} = \lambda \mathrm{tr}\boldsymbol{\epsilon}\,\boldsymbol{I} + 2\mu\boldsymbol{\epsilon} - 2\mu s \left(\boldsymbol{m} \otimes \boldsymbol{n} \right)^s .$$

Tangent operator

$$\mathcal{A} = \lambda \boldsymbol{I} \otimes \boldsymbol{I} + \mu(\mathcal{I} + \bar{\mathcal{I}}) - 2\mu \left[\left(\boldsymbol{m} \otimes \boldsymbol{n} \right)^s \otimes \frac{\partial s}{\partial \boldsymbol{\epsilon}} + s \frac{\partial \left(\boldsymbol{m} \otimes \boldsymbol{n} \right)^s}{\partial \boldsymbol{\epsilon}} \right] .$$

Box 7.8: Summary of some main formulations of the relaxed energy
$$\mathcal{D} = A^2 \mathcal{I}, \; -1 \le \boldsymbol{m}.\boldsymbol{n} \le 1 \, .$$

Consider

$$\begin{aligned}
\mathcal{D} &= A^2 \mathcal{I}. \\
\mathcal{C} &= \lambda \, \boldsymbol{I} \otimes \boldsymbol{I} + \mu \left(\mathcal{I} + \bar{\mathcal{I}} \right).
\end{aligned}$$

Mixed energy

$$W^{mix}(\boldsymbol{\epsilon}) \;=\; \frac{1}{2} \boldsymbol{\epsilon} : \mathcal{C} : \boldsymbol{\epsilon} + \frac{1}{2} s^2 \boldsymbol{\gamma} : \mathcal{C} : \boldsymbol{\gamma} - s \, \boldsymbol{\epsilon} : \mathcal{C} : \boldsymbol{\gamma} + A \, |s| \, \|\boldsymbol{\gamma}\| \, .$$

Relaxed energy

$$\inf_{s, \boldsymbol{m}, \boldsymbol{n}} W^{mix}(\boldsymbol{\epsilon}) = \inf_{s, \varphi, \psi} W^{mix}(\boldsymbol{\epsilon}),$$

where

$$\inf_{s} W^{mix}(\boldsymbol{\epsilon}) = \frac{1}{2} \lambda (\mathrm{tr}\boldsymbol{\epsilon})^2 + \mu \, \|\boldsymbol{\epsilon}\|^2 - \frac{1}{2} \left[M(\boldsymbol{m}, \boldsymbol{n}) \right]_+^2 \, ,$$

$$\sup_{\psi, \varphi} M(\psi, \varphi) \overset{\psi = \frac{\varphi}{2}}{\to} \sup_{\varphi} M(\varphi),$$

$$M(\varphi) = \frac{\left| (\lambda tr\boldsymbol{\epsilon} + 2\mu\epsilon_m) \cos \varphi + 2\mu R \right| - \frac{A}{\sqrt{2}} \left(1 + \cos^2 \varphi \right)^{\frac{1}{2}}}{\left[\mu + (\lambda + \mu) \cos^2 \varphi \right]^{\frac{1}{2}}}.$$

Solution s

$$s = \frac{\mathrm{sign}(\boldsymbol{\epsilon} : \mathcal{C} : \boldsymbol{\gamma})}{(\boldsymbol{\gamma} : \mathcal{C} : \boldsymbol{\gamma})^{\frac{1}{2}}} \left[M(\varphi) \right]_+ .$$

Relaxed stress

$$\begin{aligned}
\boldsymbol{\sigma} &= \mathcal{C} : \boldsymbol{\epsilon} - s \, \mathcal{C} : \boldsymbol{\gamma} \\
&= \lambda tr\boldsymbol{\epsilon} \, \boldsymbol{I} + 2\mu\boldsymbol{\epsilon} - s \left[\lambda \left(\boldsymbol{m}.\boldsymbol{n} \right) \boldsymbol{I} + 2\mu \left(\boldsymbol{m} \otimes \boldsymbol{n} \right)^s \right].
\end{aligned}$$

Tangent operator

$$\mathcal{A} = \frac{\partial^2 W_R}{\partial \boldsymbol{\epsilon}^2} = \frac{\partial \boldsymbol{\sigma}}{\partial \boldsymbol{\epsilon}} = \mathcal{C} - (\mathcal{C} : \boldsymbol{\gamma}) \otimes \frac{\partial s}{\partial \boldsymbol{\epsilon}} - s \frac{\partial (\mathcal{C} : \boldsymbol{\gamma})}{\partial \boldsymbol{\epsilon}}.$$

7.6. Numerical examples

In this section the proposed models presented in Section 7.5 are implemented in the non-linear finite element code FEAP [105]. In what follows we investigate two numerical examples: a shear test and a tension test under plane strain conditions. The main goal of the numerical investigations is the analysis of the developing shear bands and the demonstration of the mesh independence of the proposed relaxation technique. Different kinds of elements are used in this section. More details of these elements can be found in Chapter 4.

7.6.1. Shear test

The performance of the proposed model based on the assumption of $\mathcal{D} = A^2\mathcal{I}$ and $\boldsymbol{m}.\boldsymbol{n} = 0$ introduced in Section 7.5.2 and Box 7.7 is illustrated through numerical simulation of the following shear test.

A block, rectangular in profile, is subjected to simple shear under plane strain conditions as depicted in the Fig. 7.7. In order to trigger localization the material in the indicated middle left and right parts of the specimen is equipped with an initially lower value of $A = 27\ Nmm$.
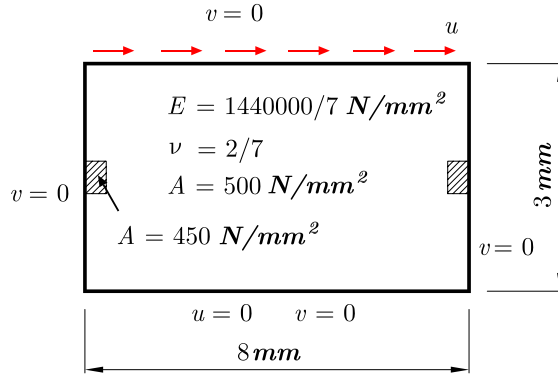
Figure 7.7.: Localization within shear test. Geometry and boundary conditions.

The test is performed with four different discretizations of the sample: 8x3, 18x7, 36x14, 54x21 elements. Relaxed analysis of this problem indicates that localization occurs simultaneously with the loss of convexity signaled by the shear strain $\gamma_{12} = 2\epsilon_{mn} = \alpha$ corresponding to the shear stress $\sigma_{xy} = \frac{A}{\sqrt{2}}$. Hence, this critical point marks the limit of convex analysis. The post-peak behaviour is now investigated.

The solution obtained by use of MES and Q4 elements with full quadrature is not coincident with mesh refinement. The MES method and the displacement method result in load-displacement curves widely different (Figs. 7.8a, 7.9a). Distribution of shear strains

at $u = 0.8\,mm$ (Figs. 7.8b, 7.9b) is only concentrated in the middle and in the boundary, and the shear strains of the two connected regions are small. Thus, the shear band does not completely form in the whole structure even though the prescribed displacement u is continuously increased.

a. Load-displacement response.

b. Distribution of shear strain at u=0.8 mm.
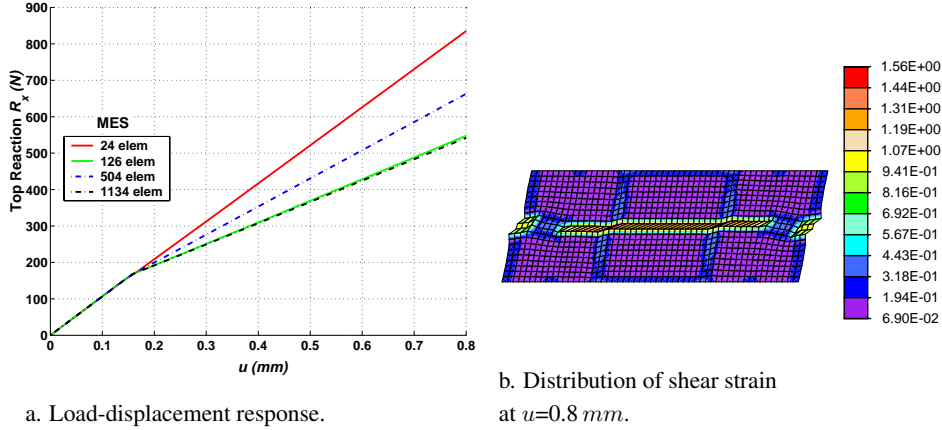
Figure 7.8.: Model based on the assumption of $\boldsymbol{D} = A^2\boldsymbol{\mathcal{I}}$ and $\boldsymbol{m}.\boldsymbol{n} = 0$: Localization within shear test by use of MES element (the mixed enhanced strain method).

a. Load-displacement response.

b. Distribution of shear strain at u=0.8 mm.
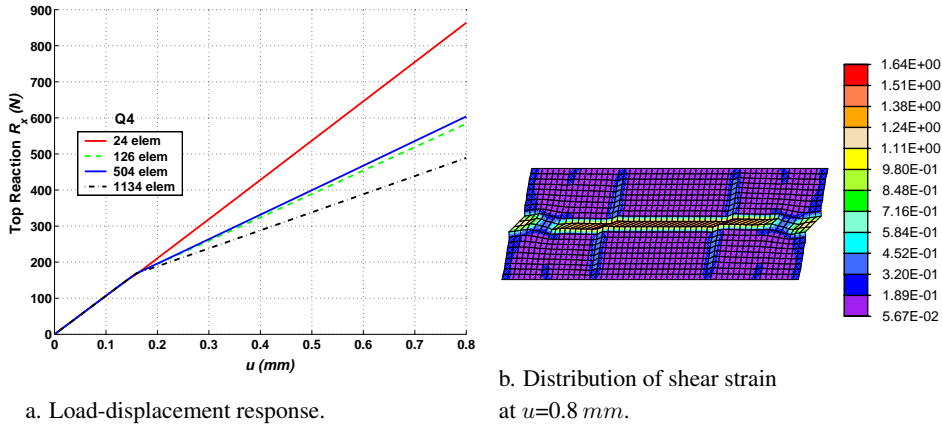
Figure 7.9.: Model based on the assumption of $\boldsymbol{D} = A^2\boldsymbol{\mathcal{I}}$ and $\boldsymbol{m}.\boldsymbol{n} = 0$: Localization within shear test by use of Q4 element (the displacement method with full quadrature).

Contrary to MES and Q4 elements, mesh-independent response is evident in the Q4-1Gauss element (the displacement method with one-point quadrature) in Fig. 7.10a. Once the shear band forms, the softening behaviour occurs along it (Fig. 7.10a, b). Material inside the shear band then decomposes into two domains: low-strain and high-strain domains whose relaxed energies are $[(1 - \xi)W_1]_R$ and $[\xi W_2]_R$, respectively (Fig. 7.10c). As can be seen,

the firstly relaxed energy is asymptotic to a constant whereas the latterly relaxed energy is concentrated inside the shear band and continuously increases significantly as the increase of the prescribed displacement u. The relaxed stress also approaches a constant.
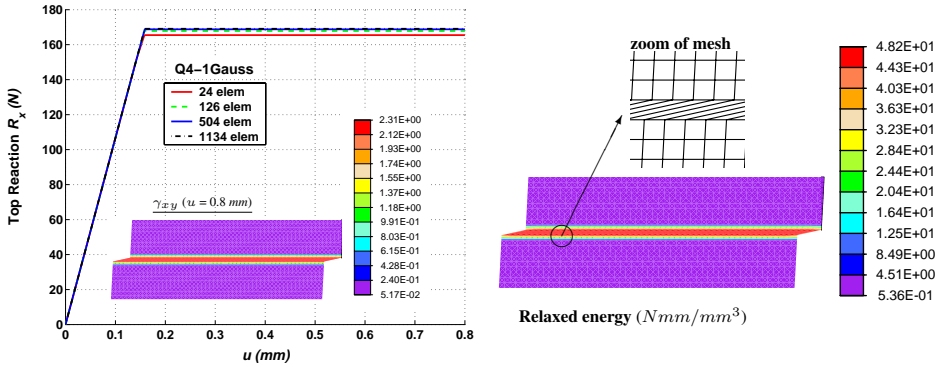
a. Load-displacement response and distribution of shear stress at $u{=}0.8\,mm$.

b. Distribution of relaxed energy at $u{=}0.8\,mm$.
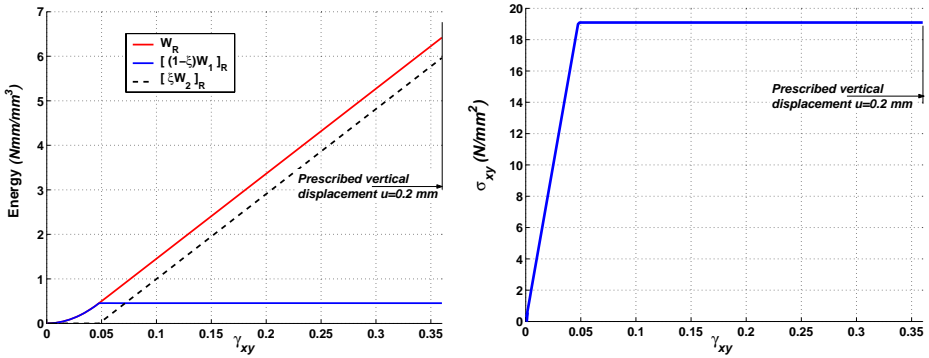
c. Relaxed energy and relaxed shear stress at the weak elements

Figure 7.10.: Model based on the assumption of $\boldsymbol{D} = A^2\boldsymbol{\mathcal{I}}$ and $\boldsymbol{m}.\boldsymbol{n} = 0$: Localization within shear test by use of Q4-1Gauss element (the displacement method with one-point quadrature).

The reduced integration such as Q4-1Gauss element has the property that a hourglass mode appears due to instabilities in the displacement field. Herein it is interesting that this element behaves better than MES, EAS and QM6 elements in this example. As observed in this example, no stress oscillation occurs. The band takes on the correct shape as a straight line in this case for all mesh densities. All of the deformation is eventually concentrated inside the shear band.

7.6.2. Tension test

A cubical sample is subjected to a prescribed vertical displacement under plane strain conditions. The geometry of the specimen and the boundary conditions imposed on displacements as well as material parameters are given in Fig. 7.11. In order to trigger the shear band formation the imperfection in geometry along the height of specimen is introduced.
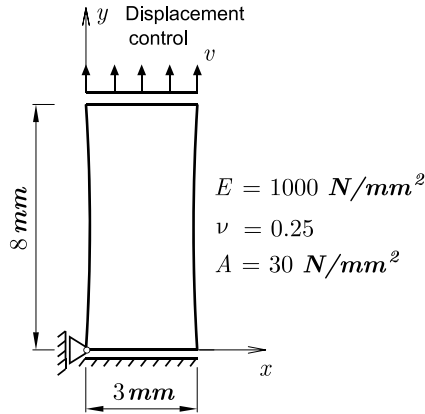
Figure 7.11.: Localization in tension. Geometry and boundary conditions.

We demonstrate the performance of the three different proposed models presented in Section 7.5 through this example.

7.6.2.1. Model based on the assumption of $\mathcal{D} = A^2 \mathcal{I}$, $\boldsymbol{m}.\boldsymbol{n} = 0$ (Section 7.5.2 and Box 7.7)

The sample is discretized with four different meshes: 3x8, 7x18, 14x36, 21x54 elements. The load-displacement curves behave identically for $v < 0.3126\,mm$ in Figs. 7.14a and 7.15a. The localization is delayed until the maximum shear strain is equal to $\frac{\alpha}{2}$ corresponding to $v \approx 0.3126\,mm$, then the performance of diverse finite element methods starts to differ. The localization band is straight, at $45°$ with the direction of principal strain.

Mesh-dependence response obtained by use of the Q4 element in Fig. 7.14 becomes evident in considering post-peak behaviour. Although the relaxed energy is concentrated inside the shear band, the deformation shape of the Q4 element is not reasonable.

As we expected in Fig. 7.15a, the solutions obtained by using MES, EAS, and QM6 elements are practically coincident in term of vertical reactions, thus showing the objective of the proposed relaxed theory. The distribution of the relaxed energy shown in Fig. 7.15b points out the localized elements and demonstrates the potential of the enhanced finite element method

in capturing localization.
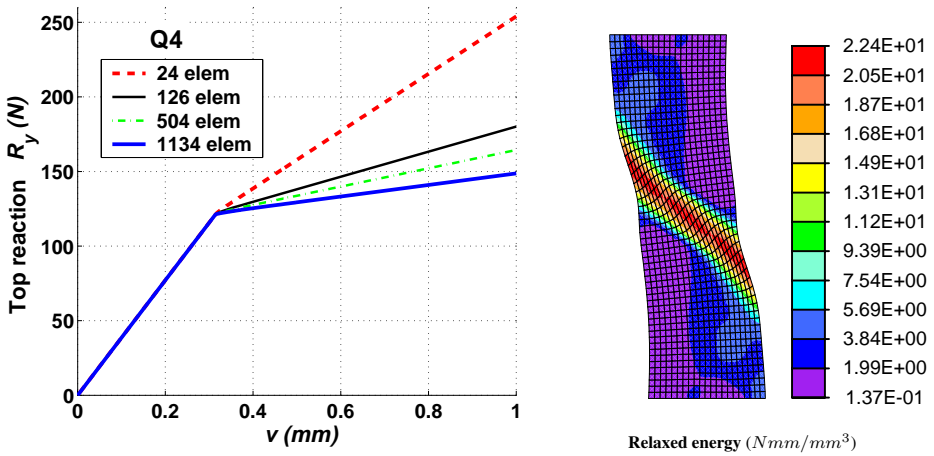
a. Load-displacement response.

b. Distribution of relaxed energy at v=1.0 mm.

Figure 7.12.: Model based on the assumption of $\boldsymbol{D} = A^2\boldsymbol{\mathcal{I}}$ and $\boldsymbol{m}.\boldsymbol{n} = 0$: Localization in tension by use of Q4 element (the displacement method).

The relaxed energy and normal stress σ_y presented in Fig. 7.16 are calculated in the element 356 at the first Gauss point. As observed, the relaxed stress softens on the discontinuity due to geometrical behaviour.

It is very interesting to see the performance of the different finite element formulations by considering the deformation shape of sample. As we observe in Fig. 7.17, the solution obtained by use of the Q4 element fails to capture effects of strain localization.

a. Load-displacement response.

b. Distribution of relaxed energy
at $v=1.0\,mm$.
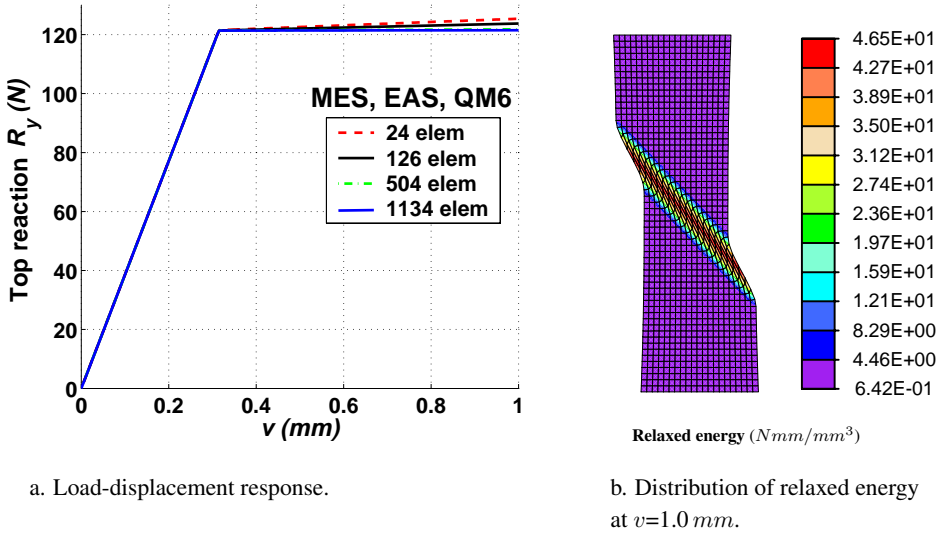
Figure 7.13.: Model based on the assumption of $\boldsymbol{D} = A^2\boldsymbol{\mathcal{I}}$ and $\boldsymbol{m}.\boldsymbol{n} = 0$: Localization
in tension by use of MES element (the mixed enhanced strain method), EAS
element (the enhanced assumed strain method) and QM6 element (the incompatible mode method).

a. Load-displacement response.

b. Distribution of relaxed energy
at $v=1.0\,mm$.
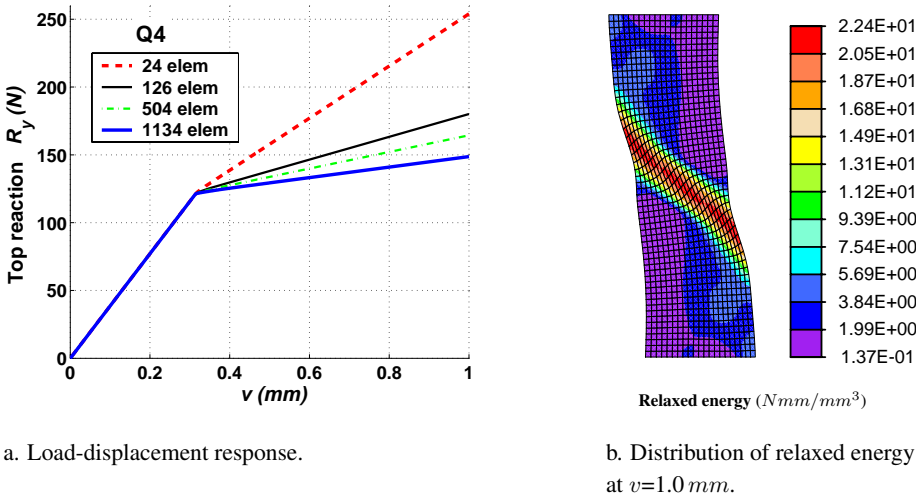
Figure 7.14.: Model based on the assumption of $\boldsymbol{D} = A^2\boldsymbol{\mathcal{I}}$ and $\boldsymbol{m}.\boldsymbol{n} = 0$: Localization in
tension by use of Q4 element (the displacement method).

a. Load-displacement response.

b. Distribution of relaxed energy at $v=1.0\,mm$.
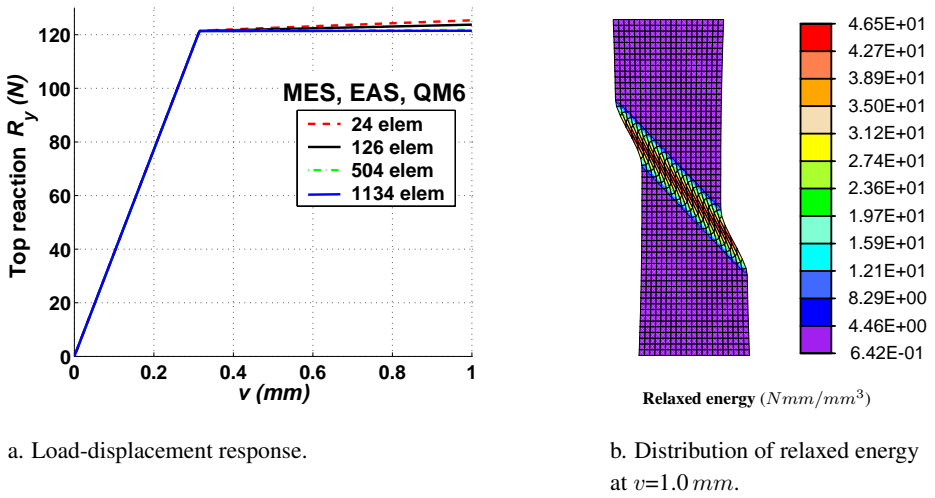
Figure 7.15.: Model based on the assumption of $\boldsymbol{D} = A^2\boldsymbol{\mathcal{I}}$ and $\boldsymbol{m}.\boldsymbol{n} = 0$: Localization in tension by use of MES element (the mixed enhanced strain method), EAS element (the enhanced assumed strain method) and QM6 element (the incompatible mode method).
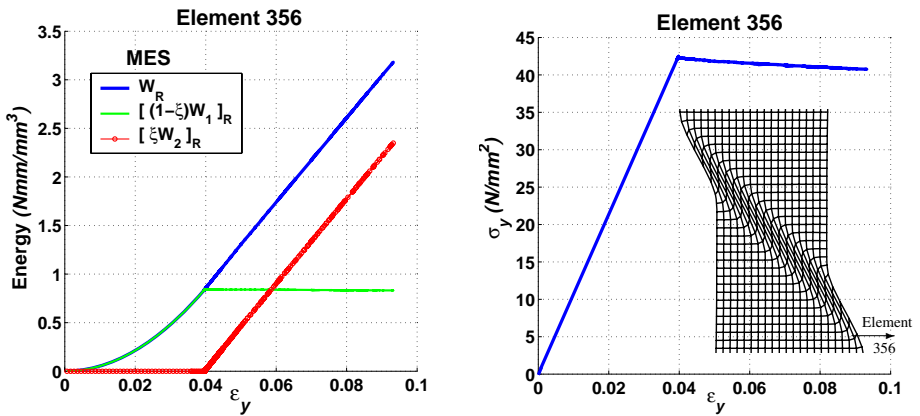
Figure 7.16.: Model based on the assumption of $\boldsymbol{D} = A^2\boldsymbol{\mathcal{I}}$ and $\boldsymbol{m}.\boldsymbol{n} = 0$: Relaxed energy and relaxed normal stress σ_y by use of MES element (the mixed enhanced strain method) at the first Gauss point of the element 356.
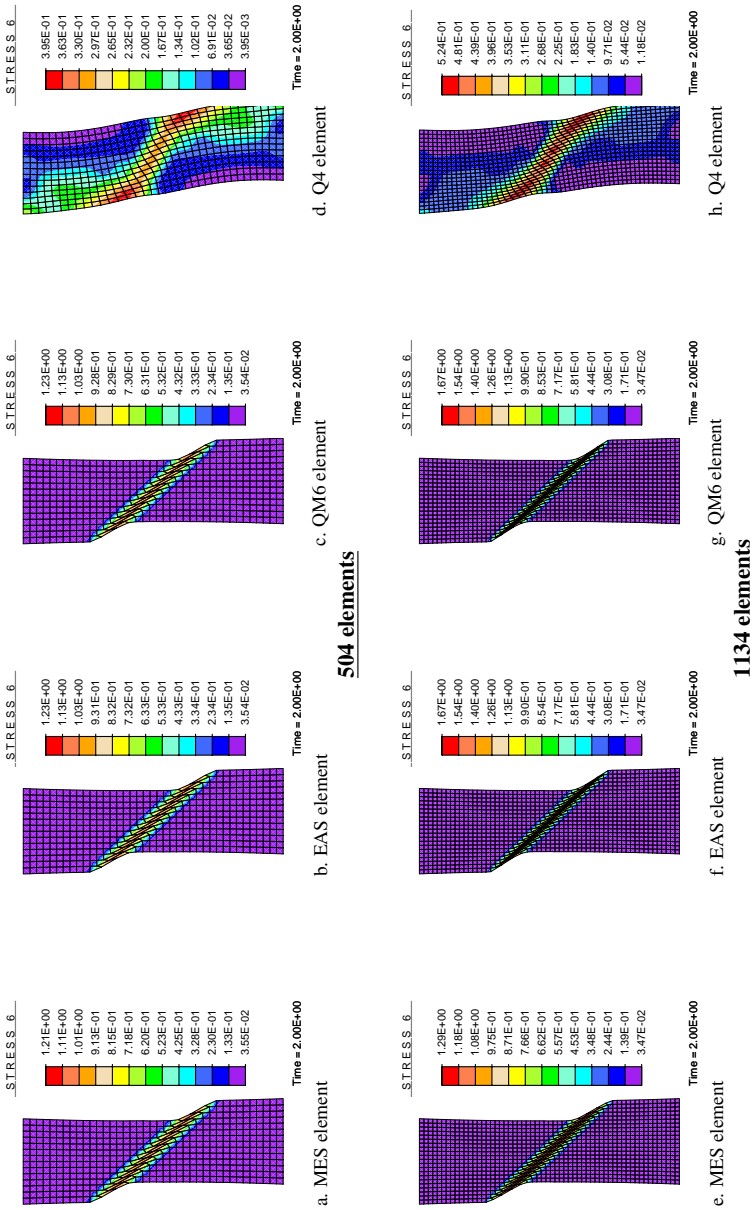
Figure 7.17.: Model based on the assumption of $\boldsymbol{D} = A^2\boldsymbol{\mathcal{I}}$ and $\boldsymbol{m}.\boldsymbol{n} = 0$: Localization in tension. Comparison of the different finite element methods: Distribution of shear strain at $v = 1.0\,mm$.

7.6.2.2. Model based on the assumption of $\mathcal{D} = A^2\mathcal{I}$ and $-1 \leq m.n \leq 1$ (Section 7.5.2 and Box 7.8)

The model used in previous section is predicated upon the assumption that m is perpendicular to n. In general, this assumption does not hold. Hence, the numerical results obtained from the model based on the assumption of $\mathcal{D} = A^2\mathcal{I}$ with $m.n \in [-1, 1]$, which is m and n being arbitrary, are discussed in this section.
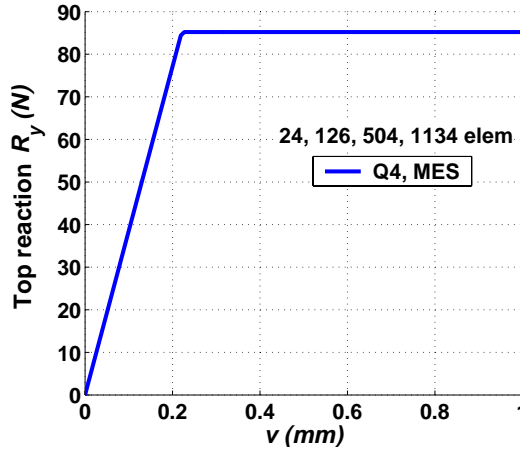

Figure 7.18.: Model based on the assumption of $D = A^2\mathcal{I}$ and $-1 \leq m.n \leq 1$: Localization in tension by use of MES element (the mixed enhanced strain method) and Q4 element (the displacement method): Load-displacement response.

The problem is analyzed by means of four discretizations of the domain, consisting of 3x8, 7x18, 14x36, 21x54 elements. The numerical results show that the solutions attained by use of Q4 and MES elements are identical as depicted in Fig. 7.18, thus confirming the objective of the proposed relaxed formulation. Relaxed analysis indicates that localization early occurs at $v \approx 0.2269\,mm$ by comparison with the one in the previous section ($v \approx 0.3126\,mm$).

The distribution of the relaxed energy depicted in Fig. 7.19 illustrates that the localization band is straight, parallel to the horizontal axis, and the relaxed energy is concentrated inside this band.

The behaviour of the relaxed energy and the vertical stress σ_y of the element 547 (Fig. 7.19) at the first Gauss point is shown in Fig. 7.20. As can be seen, the material within the shear band decomposes into low-strain and high-strain domains whose relaxed energies are $[(1 - \xi)W_1]_R$ and $[\xi W_2]_R$, respectively (Fig. 7.20b); outside the shear band the behaviour of material is elastic. The relaxed energy of the low-strain domain is asymptotic to a constant whereas the relaxed energy of the high-strain domain starts to increase linearly. As a result, the relaxed shear stress also approaches the material parameter A.

Relaxed energy (Nmm/mm^3)

a. 24 MES elements

b. 126 MES elements

c. 504 MES elements

Zoom

Element 547

d. 1134 MES elements
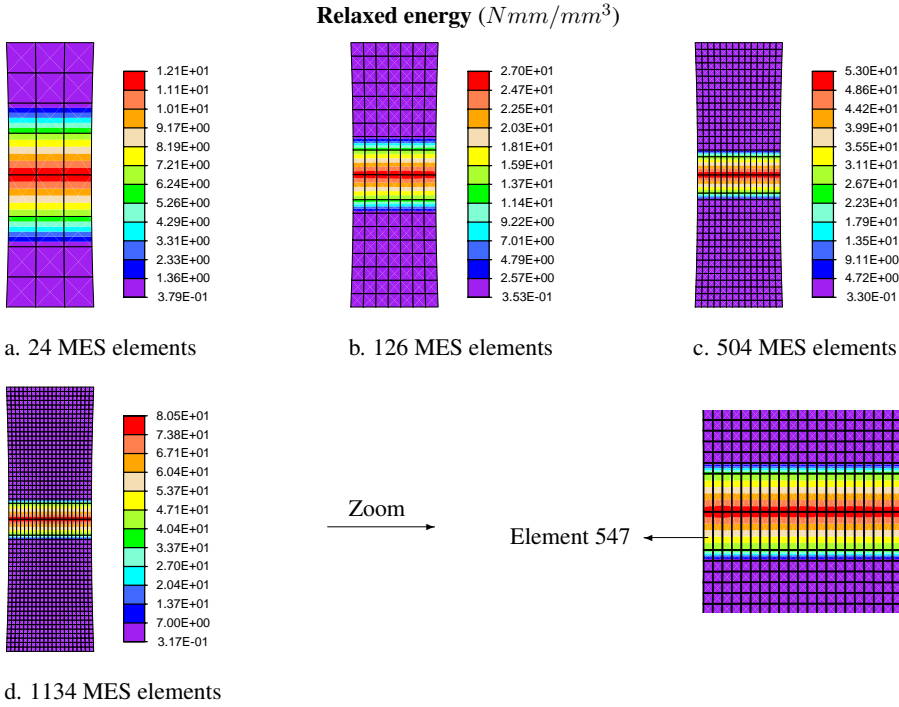
Figure 7.19.: Model based on the assumption of $\boldsymbol{D} = A^2 \boldsymbol{\mathcal{I}}$ and $-1 \leq \boldsymbol{m}.\boldsymbol{n} \leq 1$: Localization within tension test by use of MES element(the mixed enhanced strain method). Comparision of the different finite element meshes: Distribution of relaxed energy at $v = 1.0\, mm$.
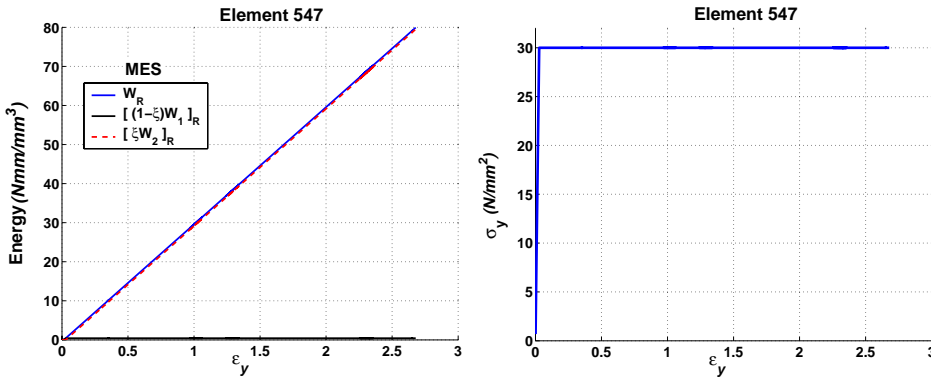
Figure 7.20.: Model based on the assumption of $\boldsymbol{D} = A^2 \boldsymbol{\mathcal{I}}$ and $-1 \leq \boldsymbol{m}.\boldsymbol{n} \leq 1$: Relaxed energy and relaxed normal stress σ_y by use of MES element (the mixed enhanced strain method) at the first Gauss point of the element 547.

7.6.2.3. Model based on the assumption of $\mathcal{D} = \mathcal{C}$ (Section 7.5.1 and Box 7.3-6)

We consider four discretizations of the domain: 3x8, 7x18, 14x36, 21x54 elements. The response obtained with four meshes is the same in load-displacement curves as shown in Fig. 7.21a, thus verifying again the lack of pathological mesh-dependence of the proposed formulation. As soon as the onset of localization is met at $v \approx 0.2427\,mm$ which signals the loss of convexity, the performance of the diverse finite element methods starts to differ.
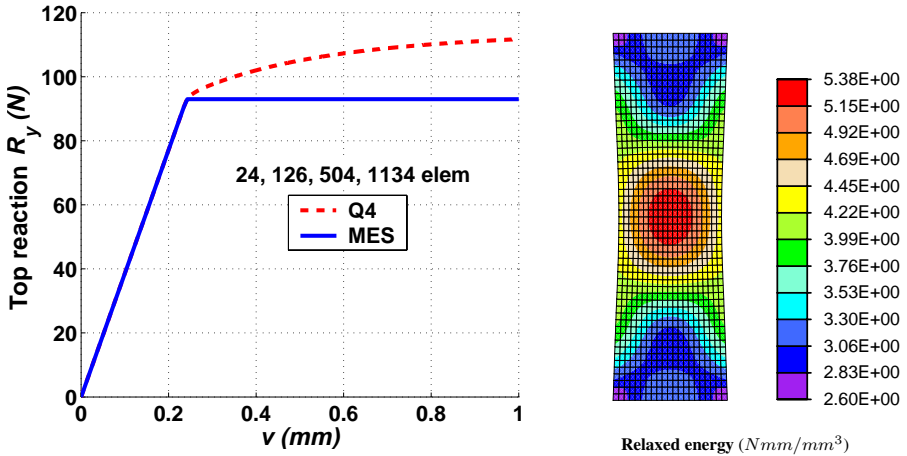
a. Load-displacement response.	b. Distribution of relaxed energy (Q4) at v=1.0 mm.

Figure 7.21.: Model based on the assumption of $\boldsymbol{D} = \boldsymbol{C}$: Localization in tension by use of MES element (the mixed enhanced strain method) and Q4 element (the displacement method).

The displacement method is unable to capture the localization and shows hardening behaviour as depicted in Fig. 7.21a and b.

Fig. 7.22 demonstrates that the enhanced formulation can resolve effect of strain localizations. In Fig. 7.22a and b, the mesh is too coarse to have the shear band. It is noted that the position of the discontinuity is coincident in the finer mesh of Fig. 7.22c and d., with element size being small enough for the geometry of the discontinuity to resolve into the expected shape. In comparison with the example of the tension test in Sections 7.6.2.2a and 7.6.2.2b, which have the formation of one shear band, there exists two symmetric shear bands in this example and their orientations are about $60°$ and $120°$ with the horizontal axis.

Fig. 7.23 shows the behaviour of the relaxed energy as well as the relaxed vertical stress σ_y of the element 465 (Fig. 7.22e) at the first gauss point inside the shear band. As can be seen, after the bifurcation point, the relaxed energy of the small-strain domain is asymptotic to a constant whereas the relaxed energy of the large-strain domain is concentrated inside the shear band and continuously increases significantly as the increase of the prescribed displacement v. As a result, the relaxed stress approaches a constant.

Relaxed energy (Nmm/mm^3)

a. 24 MES elements

b. 126 MES elements

c. 504 MES elements

d. 1134 MES elements

e. Orientation of shear bands at element 465 and element 481
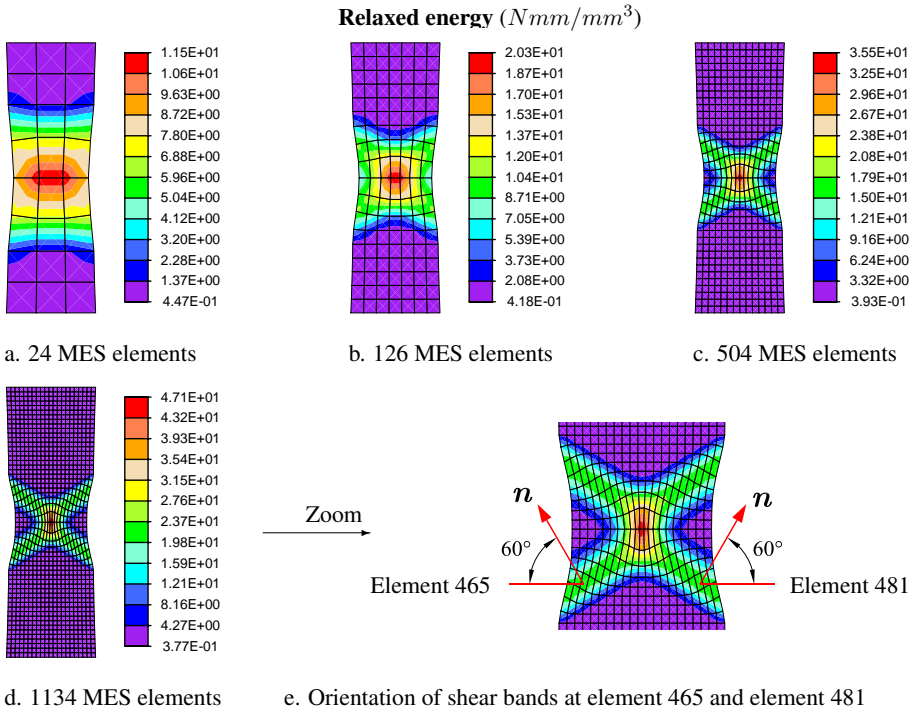
Figure 7.22.: Model based on the assumption of $D = C$: Localization within tension test by use of MES element (the mixed enhanced strain method). Comparison of the different finite element meshes: Distribution of relaxed energy at $v = 1.0\,mm$.
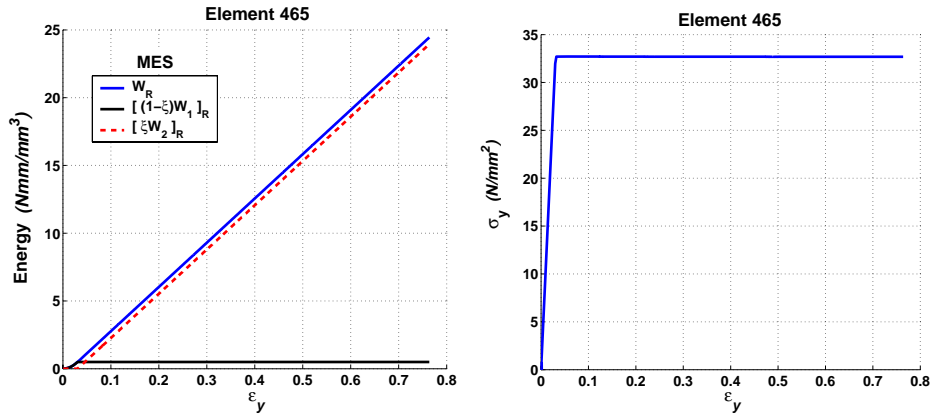

Figure 7.23.: Model based on the assumption of $D = C$: Relaxed energy and relaxed normal stress σ_y by use of MES element (the mixed enhanced strain method) at the first Gauss point of the element 465.

8. Relaxed energy analysis of shear bands for hyperelastic materials at large deformation

In this chapter the theory developed in the previous chapter for inelastic materials at small strains is extended to geometric and material non-linearities for hyperelastic material. The proposed theory is applied to both incompressible and compressible Neo-Hookean material models. The performance of the proposed energy relaxation is demonstrated through the numerical simulation of a simple shear test under plane strain condition. The presented numerical simulation shows that there is no mesh sensitivity.

8.1. General assumptions

Similar to Section 7.2 the theory developed below is based on the following assumptions

(1) After the onset of localization, the width of the shear band represented by the volume fraction ξ tends to zero (see Section 7.2 for explanation)

$$\xi \to 0. \tag{8.1}$$

(2) Most of the deformation is concentrated parallel to the band

$$\boldsymbol{Fm}.\boldsymbol{n} = 0. \tag{8.2}$$

where $\boldsymbol{F}$ is the deformation gradient, $\boldsymbol{Fm}$ and $\boldsymbol{n}$ are the oriented vectors of the shear band evolution.

(3) The energy inside a shear band is assumed in the form

$$
\begin{aligned}
W_2(\xi \boldsymbol{F}) &= |\xi|\, W_2(\boldsymbol{F}), & (8.3)\\
W_2(\boldsymbol{F}) &= A\,\|\boldsymbol{F}\|^{\alpha}\quad, \quad A > 0\,. & (8.4)
\end{aligned}
$$

The second assumption based on the results of the experiment by *Finno et al, 1996*[35] for soil. In their experiment, they showed that the normal movements are much smaller than those in the tangent direction inside the shear band. This assumption implies the two vectors $\boldsymbol{Fm}$ and $\boldsymbol{n}$ being orthogonal.

According to the third assumption, the energy inside a shear band is positive homogeneous of first degree in the strain field (8.3). Only for the form of this energy as given in eq. (8.4)

corresponding to $\alpha = 1$, the energy has the desired property leading to strong discontinuities. If α is larger than 1, the material will exhibit only weak discontinuities. If α is smaller than 1, the relaxed energy does not exist because of lacking coercivity.

8.2. Approximated rank-one convexification of potential energy

8.2.1. Micro-deformation gradient
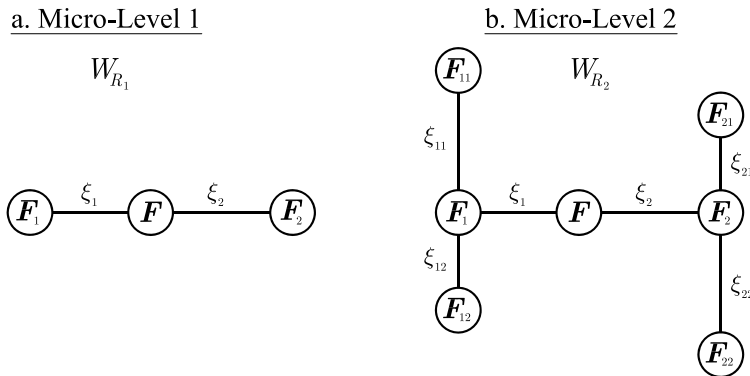
Figure 8.1.: Tree-diagram (*Hackl, 2005*[39])

As mentioned in Section 7.1, the exact rank-one convexification is approximated by taken into account the first micro-level (Fig. 8.1a). As a result, shear bands are treated as laminates of first order. Thus, deformation gradients $\boldsymbol{F}_1$ and $\boldsymbol{F}_2$ of low-strain and high-strain domains must satisfy the following conditions from eqs. (2.24) and (2.25)

$$\boldsymbol{F} = \xi \boldsymbol{F}_1 + (1 - \xi)\boldsymbol{F}_2, \tag{8.5}$$
$$\operatorname{rank}(\boldsymbol{F}_1 - \boldsymbol{F}_2) \le 1. \tag{8.6}$$

We introduce an appropriate ansazt for two domains as follows (see also eq. (2.26))

$$\boldsymbol{F}_1 = \boldsymbol{F} - d\xi(\boldsymbol{F}\boldsymbol{a} \otimes \boldsymbol{n}), \tag{8.7}$$
$$\boldsymbol{F}_2 = \boldsymbol{F} + d(1 - \xi)(\boldsymbol{F}\boldsymbol{a} \otimes \boldsymbol{n}) = \boldsymbol{F} - d\xi(\boldsymbol{F}\boldsymbol{a} \otimes \boldsymbol{n}) + d(\boldsymbol{F}\boldsymbol{a} \otimes \boldsymbol{n}). \tag{8.8}$$

Let us define s by

$$\xi \boldsymbol{F}\boldsymbol{a} = s\boldsymbol{F}\boldsymbol{m}, \tag{8.9}$$

where $\|\boldsymbol{Fm}\| = 1$. Herein $\boldsymbol{Fm}$ and $\boldsymbol{n}$ are the unit tangent and normal vectors of the shear band; s is a scaling parameter.

Substituting eq. (8.9) into eqs. (8.7) and (8.8) yields

$$\boldsymbol{F}_1 = \boldsymbol{F} - s(\boldsymbol{Fm} \otimes \boldsymbol{n}), \tag{8.10}$$

$$\boldsymbol{F}_2 = \boldsymbol{F} - s(\boldsymbol{Fm} \otimes \boldsymbol{n}) + \frac{s}{\xi}(\boldsymbol{Fm} \otimes \boldsymbol{n}). \tag{8.11}$$

As ξ tends to zero, $\frac{s}{\xi}$ will grow without bound. Thus, $\boldsymbol{F}_2$ can be simplified as

$$\boldsymbol{F}_2 \approx \frac{s}{\xi}(\boldsymbol{Fm} \otimes \boldsymbol{n}). \tag{8.12}$$

8.2.2. Relaxed energy

Similar to Section 7.3.2 the mixed energy of the two domains can be defined by

$$
\begin{aligned}
W^{mix}(\boldsymbol{F}) &= (1 - \xi)W_1(\boldsymbol{F} - s(\boldsymbol{Fm} \otimes \boldsymbol{n})) + \xi W_2(\frac{s}{\xi}(\boldsymbol{Fm} \otimes \boldsymbol{n})), \\
&= W_1(\boldsymbol{F} - s(\boldsymbol{Fm} \otimes \boldsymbol{n})) + |s|\, W_2(\boldsymbol{Fm} \otimes \boldsymbol{n}), \\
&= W_1(\boldsymbol{F} - s(\boldsymbol{Fm} \otimes \boldsymbol{n})) + A\,|s|\,\|\boldsymbol{Fm} \otimes \boldsymbol{n}\|.
\end{aligned}
\tag{8.13}
$$

According to the second assumption, $\boldsymbol{Fm}$ and $\boldsymbol{n}$ are orthogonal. The general formulation resulting from (8.13) may be taken in the following form

$$\boxed{W^{mix}(\boldsymbol{F}) = W_1(\boldsymbol{F} - s(\boldsymbol{Fm} \otimes \boldsymbol{n})) + A\,|s|\,.} \tag{8.14}$$

The problem of the non-convex mixed energy arises due to the occurrence of shear bands. By introducing the concept of relaxation the problem can be resolved and becomes well-posed. In general, if $\boldsymbol{Fm}$ is not perpendicular to $\boldsymbol{n}$, the relaxed energy is obtained by the minimization procedure

$$\boxed{W_R(\boldsymbol{F}) = \inf\,\{W^{mix}(\boldsymbol{F})\,|\,s\,,\,\boldsymbol{m}\,,\,\boldsymbol{n}\,;\,\|\boldsymbol{Fm}\| = \|\boldsymbol{n}\| = 1\,\}\,.} \tag{8.15}$$

By inserting eq. (8.13) into eq. (8.15) we obtain the relaxed energy as the sum of the relaxed energy of the low-strain domain denoted by $[(1 - \xi)W_1]_R$ and the relaxed energy of the high-strain domain denoted by $[\xi W_2]_R$

$$W_R(\boldsymbol{F}) = [(1 - \xi)W_1]_R + [\xi W_2]_R. \tag{8.16}$$

8.2.3. Computation of the relaxed stress and the tangent operator

The relaxed stress and the tangent operator are derived from the direct derivative of (8.15). The first derivative of (8.15) reads

$$\frac{\partial W_R}{\partial \boldsymbol{F}} = \frac{\partial W^{mix}}{\partial \boldsymbol{F}} + \frac{\partial W^{mix}}{\partial s}\frac{\partial s}{\partial \boldsymbol{F}} + \frac{\partial W^{mix}}{\partial \boldsymbol{m}}\frac{\partial \boldsymbol{m}}{\partial \boldsymbol{F}} + \frac{\partial W^{mix}}{\partial \boldsymbol{n}}\frac{\partial \boldsymbol{n}}{\partial \boldsymbol{F}}. \tag{8.17}$$

It is observed that the three last terms in eq. (8.17) vanish due to the necessary condition of the minimization problem (8.15). Thus, the relaxed first Piola Kirchhoff stress which is the average of the two micro-stresses has the form

$$\boxed{\boldsymbol{P} = \frac{\partial W^{mix}}{\partial \boldsymbol{F}}.} \tag{8.18}$$

Taking the derivative of (8.18) we obtain the tangent operator with respect to the reference configuration

$$\boxed{\mathcal{A} = \frac{\partial^2 W_R}{\partial \boldsymbol{F}^2} = \frac{\partial \boldsymbol{P}}{\partial \boldsymbol{F}}.} \tag{8.19}$$

8.3. Variational formulation

The general total potential energy functional in finite elasticity may be written in the reference configuration as

$$\Pi(\boldsymbol{u}) = \int_\Omega W_R(\boldsymbol{F}(\boldsymbol{u}))\, d\Omega - \int_\Omega \boldsymbol{u}^{\mathrm{T}}\boldsymbol{f}\, d\Omega - \int_{\partial\Omega_\sigma} \boldsymbol{u}^{\mathrm{T}}\bar{\boldsymbol{T}}\, dA\,, \tag{8.20}$$

where $\boldsymbol{f}$ and $\bar{\boldsymbol{T}}$ denote respectively the body force and the specified traction in the reference configuration, and $\partial\Omega_\sigma$ is the traction boundary for the reference configuration.

As the process of deformation progresses, s may be negative, zero or positive. The non-zero value in turn signals the onset of localization.

i. $\underline{s = 0}$: The relaxed energy $W_R(\boldsymbol{F})$ is equal to the elastic strain energy density function $W_1(\boldsymbol{F})$.

ii. $\underline{s \neq 0}$: The shear band starts to develop. The homogeneous deformation decomposes into the two micro-deformation gradients and the non-convex potential energy $W^{mix}(\boldsymbol{F})$ is replaced with the approximated rank-one convexification $W_R(\boldsymbol{F})$ defined by (8.15) to ensure the well-posedness of the problem.

8.4. Application of relaxation theory to Neo-Hookean material

8.4.1. Incompressible Neo-Hookean model

Using the incompressible Neo-Hookean model, the potential energy of the low-strain domain has the form

$$W_1(\boldsymbol{F}) = \frac{\mu}{2} \left[\text{tr}(\boldsymbol{F}\boldsymbol{F}^{\text{T}}) - 3 \right]. \tag{8.21}$$

Substituting eq. (8.21) into eq. (8.14) leads to

$$
\begin{aligned}
W^{mix}(\boldsymbol{F}) &= \frac{\mu}{2} \left[\text{tr}(\boldsymbol{F}\boldsymbol{F}^{\text{T}}) - 3 \right] + \frac{\mu s^2}{2} \\
&\quad - \mu s \, \text{tr} \left\{ \boldsymbol{F}(\boldsymbol{F}\boldsymbol{m} \otimes \boldsymbol{n})^{\text{T}} \right\} + A \, |s|.
\end{aligned}
\tag{8.22}
$$

Let us consider the following relaxed energy

$$W_R(\boldsymbol{F}) = \inf \left\{ W^{mix}(\boldsymbol{F}) \,|\, s, \, \boldsymbol{m}, \, \boldsymbol{n} \,;\, \|\boldsymbol{F}\boldsymbol{m}\| = \|\boldsymbol{n}\| = 1 \right\}. \tag{8.23}$$

By use of the results in Box 7.1 (see Section 7.4.2), the minimization problem (8.23) with respect to s yields

$$s = \frac{1}{\mu} \left[\mu \left| \text{tr} \left\{ \boldsymbol{F}(\boldsymbol{F}\boldsymbol{m} \otimes \boldsymbol{n})^{\text{T}} \right\} \right| - A \right]_{+} \text{sign} \left(\text{tr} \left[\boldsymbol{F}(\boldsymbol{F}\boldsymbol{m} \otimes \boldsymbol{n})^{\text{T}} \right] \right), \tag{8.24}$$

and the corresponding energy with solution s (8.24)

$$
\begin{aligned}
\inf_s W^{mix}(\boldsymbol{F}) &= \frac{\mu}{2} \left[\text{tr}(\boldsymbol{F}\boldsymbol{F}^{\text{T}}) - 3 \right] \\
&\quad - \frac{1}{2\mu} \left[\mu \left| \text{tr} \left\{ \boldsymbol{F}(\boldsymbol{F}\boldsymbol{m} \otimes \boldsymbol{n})^{\text{T}} \right\} \right| - A \right]_{+}^{2}.
\end{aligned}
\tag{8.25}
$$

Let us define M by

$$M(\boldsymbol{m}, \boldsymbol{n}) = \left| \text{tr} \left\{ \boldsymbol{F}(\boldsymbol{F}\boldsymbol{m} \otimes \boldsymbol{n})^{\text{T}} \right\} \right|. \tag{8.26}$$

In order to find the relaxed energy (8.23), we must minimize (8.25) with respect to the rest of the variables $\boldsymbol{m}$ and $\boldsymbol{n}$. It is observed that the first term of (8.25) is indenpedent of $\boldsymbol{m}$ and $\boldsymbol{n}$. Hence, instead of minimizing (8.25), now we maximize $M(\boldsymbol{m}, \boldsymbol{n})$ with respect to $\boldsymbol{m}$ and $\boldsymbol{n}$

$$\sup_{\boldsymbol{m}, \boldsymbol{n}} M(\boldsymbol{m}, \boldsymbol{n}). \tag{8.27}$$

In plane strain problem, the deformation gradient has the form

$$
\boldsymbol{F} = \begin{bmatrix} F_{11} & F_{12} & 0 \\ F_{21} & F_{22} & 0 \\ 0 & 0 & 1 \end{bmatrix}. \tag{8.28}
$$

Let m_1 and m_2 the components of the vector $\boldsymbol{m}$, n_1 and n_2 the components of the vector $\boldsymbol{n}$. Due to the orthogonality of the two unit vectors $\boldsymbol{Fm}$ and $\boldsymbol{n}$, we have

$$
m_1 = \frac{F_{12}n_1 + F_{22}n_2}{J}, \tag{8.29}
$$

$$
m_2 = -\frac{F_{11}n_1 + F_{21}n_2}{J}, \tag{8.30}
$$

where $J = \det \boldsymbol{F} = 1$ is the determinant of the deformation gradient $\boldsymbol{F}$ corresponding to the incompressible state.

On inserting (8.29) and (8.30) into (8.26) we have

$$
M(\boldsymbol{n}) = \left| n_1 n_2 (F_{11} - F_{22}) + F_{12} n_2^2 - F_{21} n_1^2 \right|. \tag{8.31}
$$

Thus, the maximization of (8.27) with respect to $\boldsymbol{m}$ and $\boldsymbol{n}$ may be reduced as

$$
\sup_{\boldsymbol{m},\boldsymbol{n}} M(\boldsymbol{m},\boldsymbol{n}) \overset{\boldsymbol{Fm}.\boldsymbol{n}=0}{\to} \sup_{\boldsymbol{n}} M(\boldsymbol{n}). \tag{8.32}
$$

The necessary condition of the maximization problem (8.32) with respect to the unit vector $\boldsymbol{n}$ leads to the solution $\boldsymbol{n}$

$$
2n_1 F_{21} = n_2 (F_{11} - F_{22}), \tag{8.33}
$$

$$
n_1 (F_{11} - F_{22}) = -2n_2 F_{12}. \tag{8.34}
$$

Eqs. (8.33) and (8.34) give the following constraint condition for the deformation gradient $\boldsymbol{F}$ as a shear band occurs

$$
(F_{11} - F_{22})^2 + 4F_{12}F_{21} = 0. \tag{8.35}
$$

The relaxed first Piola Kirchhoff stress tensor by use of eq. (8.22) may be taken in the following form

$$
\boldsymbol{P} = \frac{\partial W^{mix}(\boldsymbol{F})}{\boldsymbol{F}} = \mu \boldsymbol{F} - \mu s \left[\boldsymbol{Fm} \otimes \boldsymbol{n} + \boldsymbol{Fn} \otimes \boldsymbol{m} \right]. \tag{8.36}
$$

The relaxed Cauchy stress tensor can be written as

$$\boldsymbol{\sigma} = J^{-1}\mu \boldsymbol{F}\boldsymbol{F}^{\mathrm{T}} - \mu s J^{-1}\boldsymbol{F}\left[\boldsymbol{F}\boldsymbol{m} \otimes \boldsymbol{n}\boldsymbol{F}^{\mathrm{T}} + \boldsymbol{F}\boldsymbol{n} \otimes \boldsymbol{m}\boldsymbol{F}^{\mathrm{T}}\right]\boldsymbol{F}^{\mathrm{T}}, \tag{8.37}$$

where $J = 1$.

The theoretical developments are summarized in Box 8.1.

Box 8.1: Summary of some main formulations of the relaxed energy for the incompressible Neo-Hookean model

---

Micro-deformation gradient

$$\boldsymbol{F}_1 = \boldsymbol{F} - s(\boldsymbol{F}\boldsymbol{m} \otimes \boldsymbol{n}), \tag{8.38}$$
$$\boldsymbol{F}_2 \approx \frac{s}{\xi}(\boldsymbol{F}\boldsymbol{m} \otimes \boldsymbol{n}). \tag{8.39}$$

Mixed energy

$$\begin{aligned} W^{mix}(\boldsymbol{F}) &= \frac{\mu}{2}\left[\mathrm{tr}(\boldsymbol{F}\boldsymbol{F}^{\mathrm{T}}) - 3\right] + \frac{\mu s^2}{2} - \mu s\,\mathrm{tr}\left\{\boldsymbol{F}(\boldsymbol{F}\boldsymbol{m} \otimes \boldsymbol{n})^{\mathrm{T}}\right\} \\ &+ A\left|s\right|. \end{aligned} \tag{8.40}$$

Relaxed energy

$$W_R = \inf_{s,\boldsymbol{m},\boldsymbol{n}} W^{mix}(\boldsymbol{\epsilon}) = \frac{\mu}{2}\left[\mathrm{tr}(\boldsymbol{F}\boldsymbol{F}^{\mathrm{T}}) - 3\right] - \frac{1}{2\mu}\left[\mu M(\boldsymbol{n}) - A\right]_+^2, \tag{8.41}$$

where

$$M(\boldsymbol{n}) = \left|n_1 n_2(F_{11} - F_{22}) + F_{12}n_2^2 - F_{21}n_1^2\right|. \tag{8.42}$$

Solutions $\boldsymbol{n} = (n_1, n_2)$, $\boldsymbol{m} = (m_1, m_2)$ and s

- Solution $\boldsymbol{n} = (n_1, n_2)$

$$\begin{cases} 2n_1 F_{21} = n_2(F_{11} - F_{22}) \\ n_1^2 + n_2^2 = 1 \end{cases} \Rightarrow n_1\,,\,n_2 \tag{8.43}$$

 where $\boldsymbol{F}$ must be satisfied the following condition if *check* is positive

$$(F_{11} - F_{22})^2 + 4F_{12}F_{21} = 0. \tag{8.44}$$

Box 8.1: (continue)

- Solution $\boldsymbol{m} = (m_1, m_2)$

$$m_1 \quad = \quad \frac{F_{12}n_1 + F_{22}n_2}{J}\,, \tag{8.45}$$

$$m_2 \quad = \quad -\frac{F_{11}n_1 + F_{21}n_2}{J}. \tag{8.46}$$

- Solution s

$$s = \frac{1}{\mu}\left[\mu M(\boldsymbol{n}) - A\right]_+ \mathrm{sign}\left(\mathrm{tr}\left[\boldsymbol{F}(\boldsymbol{Fm} \otimes \boldsymbol{n})^T\right]\right), \tag{8.47}$$

where $J = \det \boldsymbol{F} = 1$.

First Piola Kichhoff stress tensor

$$\boldsymbol{P} = \mu\boldsymbol{F} - \mu s\left[\boldsymbol{Fm} \otimes \boldsymbol{n} + \boldsymbol{Fn} \otimes \boldsymbol{m}\right]. \tag{8.48}$$

Cauchy stress tensor

$$\boldsymbol{\sigma} = J^{-1}\mu\boldsymbol{F}\boldsymbol{F}^{\mathrm{T}} - \mu s J^{-1}\boldsymbol{F}\left[\boldsymbol{Fm} \otimes \boldsymbol{n}\boldsymbol{F}^{\mathrm{T}} + \boldsymbol{Fn} \otimes \boldsymbol{m}\boldsymbol{F}^{\mathrm{T}}\right]\boldsymbol{F}^{T}. \tag{8.49}$$

Tangent operator

$$\mathcal{A} = \frac{\partial\boldsymbol{P}}{\partial\boldsymbol{F}}. \tag{8.50}$$

The onset of bifurcation is detected based on $check$

$$check = \mu M(\boldsymbol{n}) - A. \tag{8.51}$$

- If $check \leq 0$, $s = 0$.

- If $check > 0$,

$$s = \frac{1}{\mu}check\,\mathrm{sign}\left(\mathrm{tr}\left[\boldsymbol{F}(\boldsymbol{Fm} \otimes \boldsymbol{n})^T\right]\right). \tag{8.52}$$

8.4.2. Compressible Neo-Hookean model

Using the compressible Neo-Hookean model, the potential energy of the low-strain domain has the form [104]

$$W_1(\boldsymbol{F}) = \frac{\mu}{2}\left[\mathrm{tr}(\boldsymbol{F}\boldsymbol{F}^{\mathrm{T}}) - 3 - 2\ln(\det\boldsymbol{F})\right] + \frac{\lambda}{2}(\det\boldsymbol{F} - 1)^2. \tag{8.53}$$

By substituting eq. (8.53) into eq. (8.14) the mixed energy has the following form

$$
\begin{aligned}
W^{mix}(\boldsymbol{F}) \;=\; & \frac{\mu}{2}\left[\operatorname{tr}(\boldsymbol{F}\boldsymbol{F}^{\mathrm{T}}) - 3\right] - \mu s\, tr\left[\boldsymbol{F}(\boldsymbol{F}\boldsymbol{m}\otimes\boldsymbol{n})^{\mathrm{T}}\right] \\
& + \frac{\mu s^2}{2} + A\,|s| + \lambda U(J) - \mu\ln J\,,
\end{aligned}
\tag{8.54}
$$

where

$$
U(J) = \frac{1}{2}\,(J-1)^2\,,
\tag{8.55}
$$

and

$$
J = \det\boldsymbol{F}_1 = \det\left[\boldsymbol{F} - s(\boldsymbol{F}\boldsymbol{m}\otimes\boldsymbol{n})\right] = \det\boldsymbol{F}\,\det\left[\boldsymbol{I} - s(\boldsymbol{m}\otimes\boldsymbol{n})\right].
\tag{8.56}
$$

In two-dimensional problem, by use of eq. (8.28), eq. (8.56) can be taken in the following form

$$
J = \det\boldsymbol{F} + as,
\tag{8.57}
$$

where

$$
a = -F_{12}n_1^2 + F_{21}n_2^2 + n_1 n_2(F_{11} - F_{22}).
\tag{8.58}
$$

For convenience to find the derivative of W^{mix} with respect to s and $\boldsymbol{n}$, the mixed energy (8.54) may be rewritten as

$$
\begin{aligned}
W^{mix}(\boldsymbol{F}) \;=\; & \frac{\mu}{2}\left[\operatorname{tr}(\boldsymbol{F}\boldsymbol{F}^{T}) - 3\right] + \frac{\lambda}{2}\,(\det\boldsymbol{F} - 1)^2 \\
& + \frac{1}{2}(\mu + \lambda\,a^2)s^2 + bs + A\,|s| - \mu\ln(\det\boldsymbol{F} + as),
\end{aligned}
\tag{8.59}
$$

where

$$
\begin{aligned}
b \;=\; & \lambda\,a(\det\boldsymbol{F} - 1) - \mu\, tr\left[\boldsymbol{F}(\boldsymbol{F}\boldsymbol{m}\otimes\boldsymbol{n})^{T}\right], \\
\;=\; & c\,n_1^2 + d\,n_2^2 + e\,n_1 n_2,
\end{aligned}
\tag{8.60}
$$

$$
c \;=\; -\lambda F_{12}\,(\det\boldsymbol{F} - 1) + \mu F_{21},
\tag{8.61}
$$

$$
d \;=\; \lambda F_{21}\,(\det\boldsymbol{F} - 1) - \mu F_{12},
\tag{8.62}
$$

$$
e \;=\; [\lambda(\det\boldsymbol{F} - 1) - \mu]\,(F_{11} - F_{22}).
\tag{8.63}
$$

As explained in Section 7.3.2, the relaxed energy is computed in order to ensure the well-posed problem due to the emergence of a shear band. It is obtained by the minimization procedure

$$
W_R(\boldsymbol{F}) = \inf\left\{W^{mix}(\boldsymbol{F})\,|\,s\,,\,\boldsymbol{n}\,;\,\|\boldsymbol{n}\| = 1\,\right\}.
\tag{8.64}
$$

The relaxed first Piola Kirchhoff stress tensor resulting from (8.54) gives

$$
\begin{aligned}
\boldsymbol{P} &= \frac{\partial W^{mix}(\boldsymbol{F})}{\boldsymbol{F}} , \\
&= \mu(\boldsymbol{F} - \boldsymbol{F}^{-T}) - 2\mu s \boldsymbol{F}(\boldsymbol{m} \otimes \boldsymbol{n})^s + \lambda(J-1)J\boldsymbol{F}^{-\mathrm{T}}.
\end{aligned}
\tag{8.65}
$$

The relaxed second Piola Kirchhoff stress tensor reads

$$
\boldsymbol{S} = \mu(\boldsymbol{I} - \boldsymbol{C}^{-1}) + \lambda(J-1)J\boldsymbol{C}^{-1} - 2\mu s(\boldsymbol{m} \otimes \boldsymbol{n})^s,
\tag{8.66}
$$

where the right Cauchy-Green deformation tensor $\boldsymbol{C} = \boldsymbol{F}^{\mathrm{T}}\boldsymbol{F}$.

The relaxed Cauchy stress tensor yields

$$
\boldsymbol{\sigma} = \frac{\mu}{\det \boldsymbol{F}} \left[\boldsymbol{F}\boldsymbol{F}^{\mathrm{T}} - \boldsymbol{I} \right] - \frac{2\mu\, s}{\det \boldsymbol{F}} \boldsymbol{F}(\boldsymbol{m} \otimes \boldsymbol{n})^s \boldsymbol{F}^{T} + \lambda(J-1)\boldsymbol{I}.
\tag{8.67}
$$

The tangent operator with respect to the reference configuration are deduced from

$$
\begin{aligned}
\mathcal{A}_{IJKL} &= \lambda J(2J-1)C_{IJ}^{-1}C_{KL}^{-1} + [-\lambda J(J-1) + \mu]\left(C_{IK}^{-1}C_{JL}^{-1} + C_{IL}^{-1}C_{JK}^{-1}\right) \\
&\quad - 2\mu \left[(\boldsymbol{m} \otimes \boldsymbol{n})^s \otimes \frac{\partial s}{\partial \boldsymbol{C}} + s\frac{\partial (\boldsymbol{m} \otimes \boldsymbol{n})^s}{\partial \boldsymbol{C}} \right].
\end{aligned}
\tag{8.68}
$$

The spatial tangent operator related to the Cauchy stress $\boldsymbol{\sigma}$ is obtained by the push forward

$$
\begin{aligned}
a_{ijkl} &= \frac{1}{\det \boldsymbol{F}} F_{iI} F_{jJ} F_{kK} F_{lL} \mathcal{A}_{IJKL} , \\
&= \frac{1}{\det \boldsymbol{F}} \left\{ \lambda J(2J-1)\delta_{ij}\delta_{kl} + [\mu - \lambda J(J-1)]\left(\delta_{ik}\delta_{jl} + \delta_{il}\delta_{jk}\right) \right\} \\
&\quad - \frac{\mu F_{iI} F_{jJ} F_{kK} F_{lL}}{\det \boldsymbol{F}} \left[(m_I n_J + m_J n_I)\frac{\partial s}{\partial C_{KL}} + s\frac{\partial (m_I n_J + m_J n_I)}{\partial C_{KL}} \right].
\end{aligned}
\tag{8.69}
$$

The theoretical developments are summarized in Box 8.2.

Box 8.2: Summary of some main formulations of the relaxed energy for the compressible Neo-Hookean model

Micro-deformation gradient

$$\boldsymbol{F}_1 = \boldsymbol{F} - s(\boldsymbol{F}\boldsymbol{m} \otimes \boldsymbol{n}), \tag{8.70}$$

$$\boldsymbol{F}_2 \approx \frac{s}{\xi}(\boldsymbol{F}\boldsymbol{m} \otimes \boldsymbol{n}). \tag{8.71}$$

Mixed energy

$$\begin{aligned} W^{mix}(\boldsymbol{F}) \;=\;& \frac{\mu}{2}\left[\operatorname{tr}(\boldsymbol{F}\boldsymbol{F}^T) - 3\right] + \frac{\lambda}{2}\left(\det \boldsymbol{F} - 1\right)^2 \\ &+\; \frac{1}{2}(\mu + \lambda\,a^2)s^2 + bs + A\,|s| - \mu\ln(\det \boldsymbol{F} + as). \end{aligned} \tag{8.72}$$

Relaxed energy

$$W_R(\boldsymbol{F}) = \inf\left\{W^{mix}(\boldsymbol{F})\,|\,s,\,\boldsymbol{n}\,;\,\|\boldsymbol{n}\| = 1\,\right\}. \tag{8.73}$$

Cauchy stress tensor

$$\boldsymbol{\sigma} = \frac{\mu}{\det \boldsymbol{F}}\left[\boldsymbol{F}\boldsymbol{F}^{\mathrm{T}} - \boldsymbol{I}\right] - \frac{2\mu\,s}{\det \boldsymbol{F}}\boldsymbol{F}(\boldsymbol{m} \otimes \boldsymbol{n})^s\boldsymbol{F}^T + \lambda(J - 1)\boldsymbol{I}. \tag{8.74}$$

The spatial tangent operator

$$\begin{aligned} a_{ijkl} \;=\;& \frac{1}{\det \boldsymbol{F}}\left\{\lambda J(2J - 1)\delta_{ij}\delta_{kl} + [\mu - \lambda J(J - 1)]\left(\delta_{ik}\delta_{jl} + \delta_{il}\delta_{jk}\right)\right\} \\ &-\; \frac{\mu F_{iI}F_{jJ}F_{kK}F_{lL}}{\det \boldsymbol{F}}\left[(m_I n_J + m_J n_I)\frac{\partial s}{\partial C_{KL}} + s\frac{\partial(m_I n_J + m_J n_I)}{\partial C_{KL}}\right]. \end{aligned}$$

where $J = \det \boldsymbol{F}_1$.

8.5. Numerical examples

8.5.1. Example 1: Incompressible Neo-Hookean model

To study some numerical aspects of the proposed formulation an example of a simple shear test is considered. The deformation gradient in the simple shear test defined by

$$\boldsymbol{F} = \begin{bmatrix} 1 & F_{12} \\ 0 & 1 \end{bmatrix}. \tag{8.75}$$

Material parameters are the elastic modulus $E = 1000\ N/mm^2$, the Poisson's ratio $\nu = 0.25$ and $A = 30\ N/mm^2$.

8.5.1.1. Analytical solution

On inserting (8.75) into (8.31) we have

$$M(\boldsymbol{n}) = \left| F_{12} n_2^2 \right|. \tag{8.76}$$

We consider the maximization problem

$$\sup_{\boldsymbol{n}} M(\boldsymbol{n}) = \sup_{\boldsymbol{n}} \left| F_{12} n_2^2 \right|. \tag{8.77}$$

The minimization problem (8.77) with respect to $\boldsymbol{n}$ gives

$$\boldsymbol{n} = (0, \pm 1). \tag{8.78}$$

Thus,

$$\sup_{\boldsymbol{n}} M(\boldsymbol{n}) = |F_{12}|. \tag{8.79}$$

Substituting (8.78) into (8.29), (8.30) and (8.24) leads to

$$s = \left[|F_{12}| - \frac{A}{\mu} \right]_+ \text{sign}(F_{12}). \tag{8.80}$$

It is recognized that localization occurs if $|F_{12}| > \dfrac{A}{\mu} = 0.075$.

The Cauchy shear stress σ_{12} from eq. (8.37) reads

$$\sigma_{12} = \mu(F_{12} - s). \tag{8.81}$$

Two possible cases are:

- $|F_{12}| \leq \dfrac{A}{\mu} = 0.075 \;\rightarrow\; s = 0 : \sigma_{12} = \mu F_{12}.$

- $|F_{12}| > \dfrac{A}{\mu} = 0.075 \;\rightarrow\; s = F_{12} - \dfrac{A}{\mu}\text{sign}(F_{12}) : \sigma_{12} = A\,\text{sign}(F_{12}).$

8.5.1.2. Numerical solution by use of *Mathematica* [114]

Let us select $0 \leq F_{12} \leq 0.3$. The minimization of (8.22) with two variables s and $\boldsymbol{n}$ can be obtained by using the command "NMinimize" in *Mathematica* [114]. The numerical results of the energy relaxation and the relaxed shear stress σ_{12} are shown in Fig. 8.2. At

$F_{12} = 0.075$ a shear band has begun to form and the corresponding normal vector is $\boldsymbol{n} = (0, 1)$. Material inside the shear band then decomposes into two domains: low-strain and high-strain domains whose relaxed energies are $[(1-\xi)W_1]_R$ and $[\xi W_2]_R$, respectively (Fig. 8.2). As can be seen, the relaxed energy of the low-strain domain is asymptotic to a constant whereas the relaxed energy of the high-strain domain starts to increase linearly. As a result, the relaxed shear stress also approaches the material parameter A. Thus A can be interpreted as the stress level in the shear band.
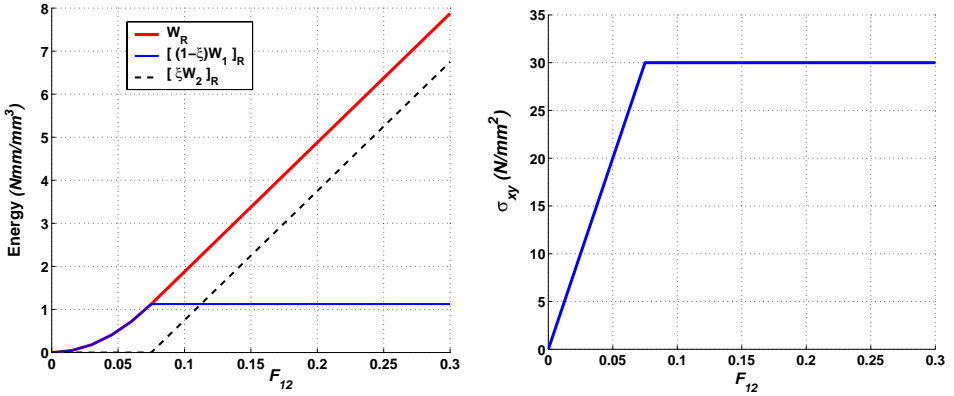
Figure 8.2.: Incompressible Neo-Hookean model: Relaxed energy and relaxed shear stress σ_{xy}.

## 8.5.2. Example 2: Compressible Neo-Hookean model
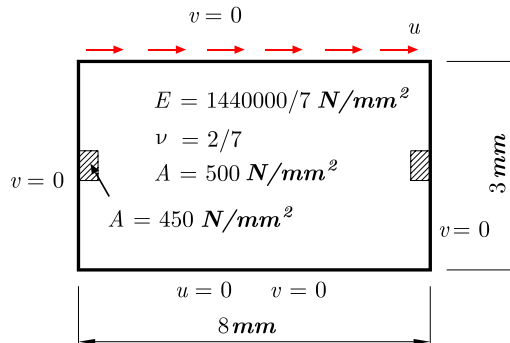
Figure 8.3.: Localization within shear test. Geometry and boundary conditions.

The geometry, the loading and boundary conditions of a specimen under plane strain condition as well as material parameters are shown in Fig. 8.3. The material in the indicated

middle left and right parts of the specimen is given an initially lower value of $A = 450\,Nmm$ in order to trigger the shear band formation. Four-node quadrilateral elements based on the displacement method (Q4-element) and three-field-mixed formulation (Mixed-Q4 element) are employed. The minimization problem (8.64) is carried out in *NAG* [95]. The model is implemented in the general code FEAP [103].

The sample is discretized with four different meshes: 8x3, 18x7, 36x14, 54x21 elements. The solutions are practically coincident in terms of vertical reactions in Fig. 8.4a, thus confirming again the lack of mesh sensitivity of the proposed formulation. Relaxed analysis of this problem shows that localization occurs at $u = 0.01734\,mm$ simultaneously with the loss of convexity. The fact that the Cauchy shear stress σ_{xy} approaches the material parameter A (Fig. 8.5b) is in good agreement with the analytical result in the incompressible Neo-Hookean model presented in the first example because the deformation gradient at Gauss point has the form (8.75). The distribution of the relaxed energy of high-strain domain depicted in Fig. 8.4b demonstrates that the energy is concentrated inside the shear band. Relaxation indicates that the material decomposes into low-strain and high-strain domains inside the shear band; outside the shear band the behaviour of material is elastic. More details can be seen in Fig. 8.5 for the behaviour of the relaxed energy as well as the relaxed shear stress at the first Gauss point of the weak elements.

a. Load-displacement response.

b. Distribution of relaxed energy $[\xi W_2]_R$ at u=0.1 mm.
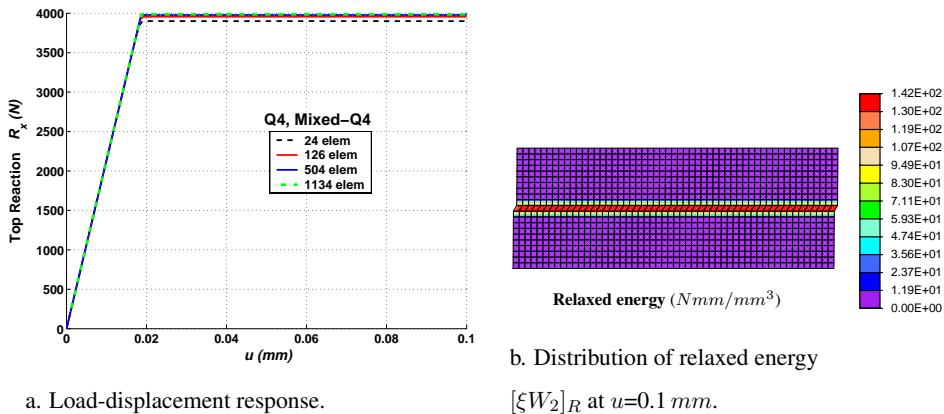
Figure 8.4.: Compressible Neo-Hookean model: Localization within shear test by use of Q4 element (the displacement method) and Mixed-Q4 element (the three-field mixed formulation).

Fig. 8.6 illustrates the distribution of the Almansi shear strain at $u = 0.1\,mm$. As can be seen, most of deformation is concentrated in the band. It is very interesting that the relaxed analysis by using Q4 and Mixed-Q4 elements yields the identical post-critical branches for all mesh densities.
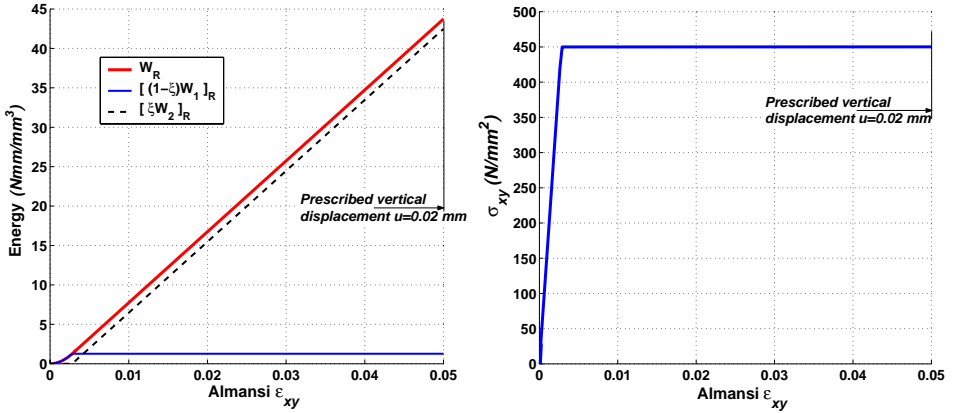
Figure 8.5.: Compressible Neo-Hookean model: Localization within shear test by use of Q4 element (the displacement method) and Mixed-Q4 element (the three-field mixed formulation): Relaxed energy and shear stress in weak elements at the first Gauss point.

a. 24 Q4 and Mixed-Q4 elements

b. 126 Q4 and Mixed-Q4 elements

c. 504 Q4 and Mixed-Q4 elements

d. 1134 Q4 and Mixed-Q4 elements
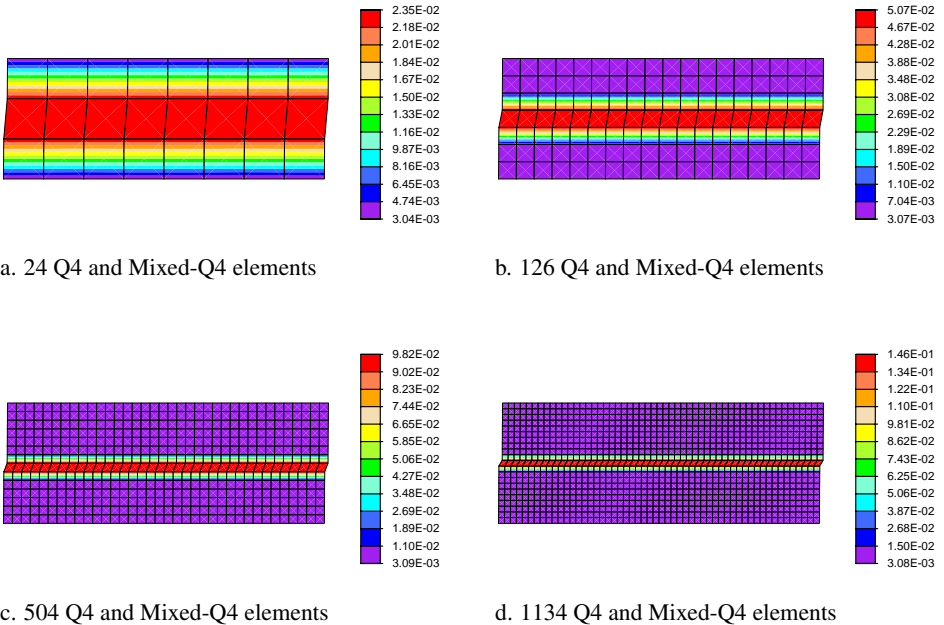
Figure 8.6.: Compressible Neo-Hookean model: Localization within shear test by use of Q4 element (the displacement method) and Mixed-Q4 element (the three-field mixed formulation): Distribution of Almansi shear strain at $u = 0.1mm$.

9. Relaxed energy analysis of shear bands for fluid-saturated inelastic porous media at small deformation

In this chapter the proposed energy relaxation for shear localization in fluid-saturated inelastic porous media is presented. The theory is predicated upon the assumption that strain field and variation in water content inside the shear band are assumed to tend to infinity. Throughout this chapter compressive stress and strain are negative as in the sign convention of continuum mechanics, the compressible fluid is positive.

9.1. Saturated one-phase flow in porous medium

9.1.1. Governing equations

Soils composed of solids, liquids and gases are multiphase materials. If all the voids are filled by liquids, for example water, the soil is saturated. For fully saturated conditions, the governing equations based upon Biot theory are derived from the following equations under the assumptions of small-strain theory, isothermal equilibrium (*Lewis and Schrefler, 1993* [68], *Zienkiewicz, 1982*[124], *Zienkiewicz et al, 1999*[125]):

1. The linear momentum balance equation of the solid-fluid mixture

$$\text{div}\,\boldsymbol{\sigma} + \rho\,\boldsymbol{b} - \rho\ddot{\boldsymbol{u}} = \boldsymbol{0}. \tag{9.1}$$

Herein $\boldsymbol{\sigma}$ is the total Cauchy stress in the combined solid and fluid mix, $\boldsymbol{b}$ is the body force per unit mass, $\ddot{\boldsymbol{u}}$ is the acceleration of the solid skeleton and ρ is the total density of the mixture, i.e.

$$\rho = n\rho_{\text{w}} + (1-n)\rho_s \tag{9.2}$$

where ρ_s and ρ_w are the intrinsic densities of the solid and water phases, repectively and n is the porosity, i.e.

$$n = \frac{dv^{\text{w}}}{dv}, \tag{9.3}$$

where dv and dv^{w} are the volume elements of the mixture and the water phase, respectively.

The relation between the total stress $\boldsymbol{\sigma}$ and the effective stress $\boldsymbol{\sigma}^{''}$ with the hydrostatic stress due to the pore pressure p reads [68, 125]

$$\boldsymbol{\sigma}^{''} = \boldsymbol{\sigma} + \alpha\,\boldsymbol{I}p, \tag{9.4}$$

where α is Biot's constant defined by (9.11), $\boldsymbol{I}$ is the second order unit tensor.

2. The momentum balance of the fluid

$$-\nabla p - \boldsymbol{F}_R - \rho_w\ddot{\boldsymbol{u}} + \rho_w\boldsymbol{b} = \boldsymbol{0}, \tag{9.5}$$

where $\boldsymbol{F}_R$ represents the viscous drag forces which, assuming the Darcy seepage law, can be written as

$$\boldsymbol{k}\boldsymbol{F}_R = \dot{\boldsymbol{w}}. \tag{9.6}$$

Here $\dot{\boldsymbol{w}}$ denotes the velocity of the fluid flow. The displacement $\boldsymbol{w}$ of the pore fluid relative to the solid skeleton is defined by

$$\boldsymbol{w} = n\,(\boldsymbol{U} - \boldsymbol{u}), \tag{9.7}$$

where $\boldsymbol{U}$ is the total displacement of the fluid measured from the same datum as $\boldsymbol{u}$, the division by the porosity n is introduced to convert the average fluid displacement to the true ones in the pores.

The permeability matrix $\boldsymbol{k}$ has the dimension of [length]^3[time]/[mass]. The link between each value of $\boldsymbol{k}$ and the soil mechanics convention k', which is used with the dimension of [length]/[time], is defined by

$$k = \frac{k'}{\rho_w g}, \tag{9.8}$$

where g is the graviational acceleration at which the permeability is measured.

3. The mass balance of the flow

$$\nabla^T\dot{\boldsymbol{w}} + \dot{\zeta} = 0, \tag{9.9}$$

where ζ is the variation in water content; $\dot{\zeta}$ is the rate at which the volume of water changes per unit total volume of mixture. The change of the water volume is due to

- (a) the increased volume due to a change in strain i.e.: $d\epsilon_{ii}$;

- (b) the additional volume stored by compression of void fluid caused by the fluid pressure increase: $\dfrac{ndp}{K_w}$;

- (c) the additional volume stored by compression of grains by the fluid pressure increase: $\dfrac{(1-n)dp}{K_s}$;

- (d) the change in volume of the solid phase caused by a change in the intergranular effective contact stress: $-\dfrac{K_T}{K_s}\left(d\epsilon_{ii} + \dfrac{dp}{K_s}\right)$,

where K_T, K_s and K_w are the bulk modulus of the solid skeleton, the grain material and the water, respectively; ϵ_{ii} is the total volumetric strain.

The rate of the variation in water content is obtained by adding all the above contributions together (a)-(d)

$$\dot{\zeta} = \alpha\dot{\epsilon}_{ii} + \frac{\dot{p}}{Q}, \tag{9.10}$$

where α and Q are the Biot's constant defined by

$$1 \quad - \quad \alpha = \frac{K_T}{K_s}, \tag{9.11}$$

$$\frac{1}{Q} \quad = \quad \frac{n}{K_w} + \frac{\alpha - n}{K_s}. \tag{9.12}$$

Equations (9.1), (9.5) and (9.9) are suplemented by the following boundary conditions:

- Boundary conditions on the parts $\partial\Omega_u$ and $\partial\Omega_\sigma$:

$$\boldsymbol{u} \quad = \quad \bar{\boldsymbol{u}} \quad \text{on } \partial\Omega_u, \tag{9.13}$$

$$\bar{\boldsymbol{t}} \quad = \quad \boldsymbol{\sigma}\boldsymbol{\nu} \quad \text{on } \partial\Omega_\sigma, \tag{9.14}$$

where $\boldsymbol{\nu}$ is the outward normal unit vector on the boundary $\partial\Omega_\sigma$, $\bar{\boldsymbol{u}}$ and $\bar{\boldsymbol{t}}$ are the imposed displacement and the traction force on the boundaries $\partial\Omega_u$ and $\partial\Omega_\sigma$, respectively;

- Boundary conditions on the parts $\partial\Omega_p$ and $\partial\Omega_u$ for the fluid phase :

$$p \quad = \quad \bar{p} \quad \text{on } \partial\Omega_p, \tag{9.15}$$

$$(\boldsymbol{\nu}')^T\boldsymbol{w} \quad = \quad w_n \quad \text{on } \partial\Omega_w, \tag{9.16}$$

where $\boldsymbol{\nu}'$ is the outward normal unit vector on the boundary $\partial\Omega_w$, $\bar{p}$ and w_n are the imposed pore pressure and the normal outflow on the boundaries $\partial\Omega_p$ and $\partial\Omega_w$, respectively.

Equations (9.1), (9.5) and (9.9) together with the boundary contions (9.13-9.16) and the constitutive equation provide the system of equations in three unknown variables (u, p, w).

In quasi-static, the motion is so slow that all dynamic force terms can be neglected. Now the displacement of the fluid flow w can be determined in terms of u and p. Consequently, the system of equations (9.1), (9.5) and (9.9) is reduced to

$$\mathrm{div}\boldsymbol{\sigma} + \rho\,\boldsymbol{b} = \boldsymbol{0}. \tag{9.17}$$

$$\nabla^T \left[\boldsymbol{k} \left(-\nabla p - \rho_w \boldsymbol{b} \right) \right] + \alpha \dot{\epsilon}_{ii} + \frac{\dot{p}}{Q} = 0. \tag{9.18}$$

Disretization of the governing equations (9.17) and (9.18) based on the displacement-based finite element formulation and the enhanced assumed strain method can be found in Section 4.2, 4.4 as well as *Lewis and Schrefler, 1993* [68], *Zienkiewicz et al, 1999*[125] and *Mira et al., 2003*[76].

9.1.2. Numerical example

A strip foundation on a saturated soil is subjected to a prescribed vertical displacement. The geometry of the considered domain and the imposed boundary conditions on displacements and pore pressure are given in Fig. 9.1. The material parameters are given in Table 9.1.

E	ν	n	ρ_s	ρ_w	K_s	K_w	$k'_x = k'_y$
KN/m^2	-	-	kg/m^3	kg/m^3	KN/m^2	KN/m^2	m/s
2x10^4	0.2	0.3	2x10^3	1x10^3	1x10^{10}	1x10^{10}	1x10^{-8}

Table 9.1.: Material parameters.

The displacement-based finite element formulation with eight-node displacement and four-node pressure interpolations (Q8P4) and the enhanced assumed strain method with four-node displacement and seven enhanced modes for pressure interpolations (EAS) are used in this example. The constitutive equation for solid skeleton is based on the model with the assumption of $\mathcal{D} = A^2\mathcal{D}$ and $\boldsymbol{m}.\boldsymbol{n} = 0$ introduced in Section 7.5.2 and Box 7.7.

We consider two different discretizations of the domain in this numerical example: 10x10 and 40x40 elements. The relaxed energy at the element under the corner of foundation as well as the distribution of the relaxed energy of the high-strain domain $[\xi W_2]_R$ are depicted in Figs. 9.3, 9.4 by use of 1600 Q8P4 and EAS elements, respectively, corresponding to the first case $a = 10\,B$ (Fig. 9.1). Figs. 9.5 and 9.6 report the results of 1600 EAS elements for the second case $a = 5\,B$ (Fig. 9.1). It can be seen in Figs. 9.3c, 9.4c and 9.5c that there
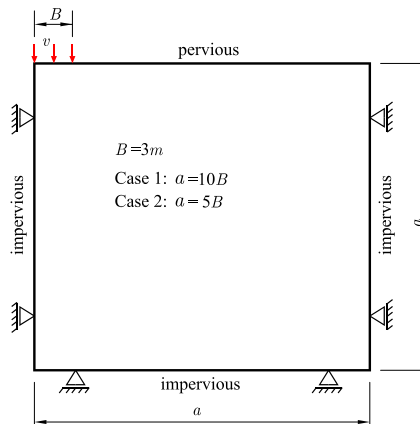
Figure 9.1.: Saturated soil foundation problem: Geometry and boundary conditions.

exists an inelastic region indicating the formation of shear bands under the foundation.

However, the results in terms of load and displacement (Fig. 9.2) show mesh-dependence response caused by the lack of the relaxed pore pressure in the relaxed energy presented in Section 7.5.2. To assure mesh independent results, the relaxed stress as well as the relaxed pore pressure is introduced through the proposed energy relaxation in the next parts of this chapter.
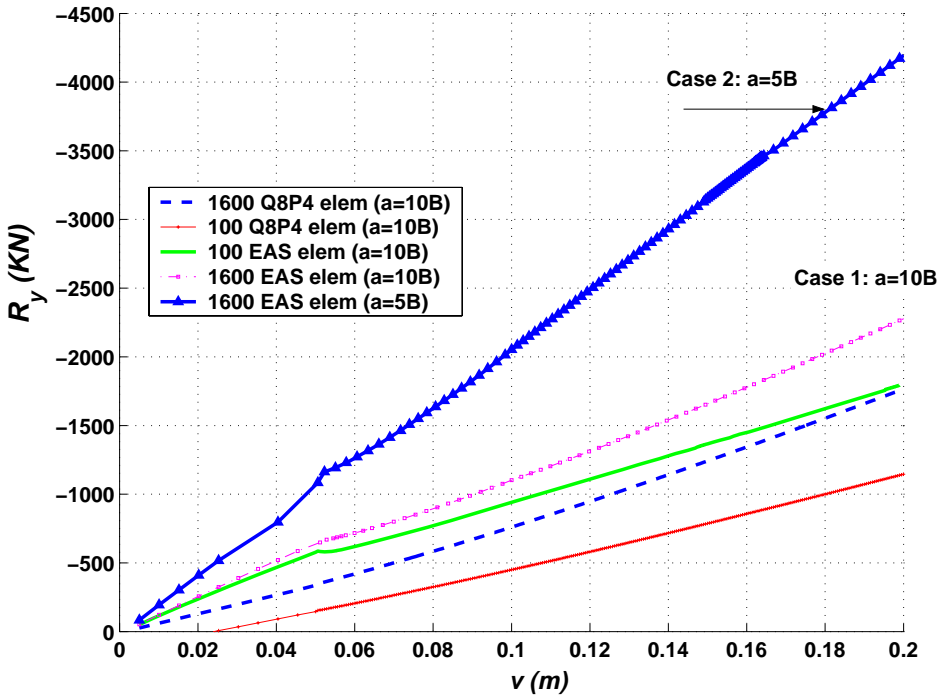
Figure 9.2.: Load-displacement response.
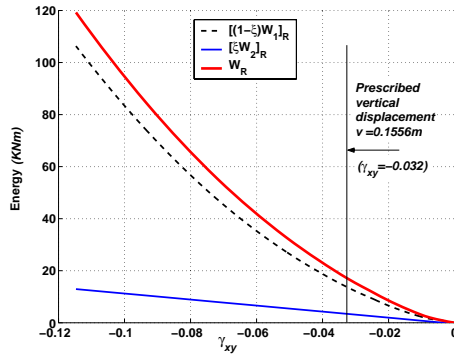
a. Relaxed energy-shear strain at the first
Gauss point of the element 121.
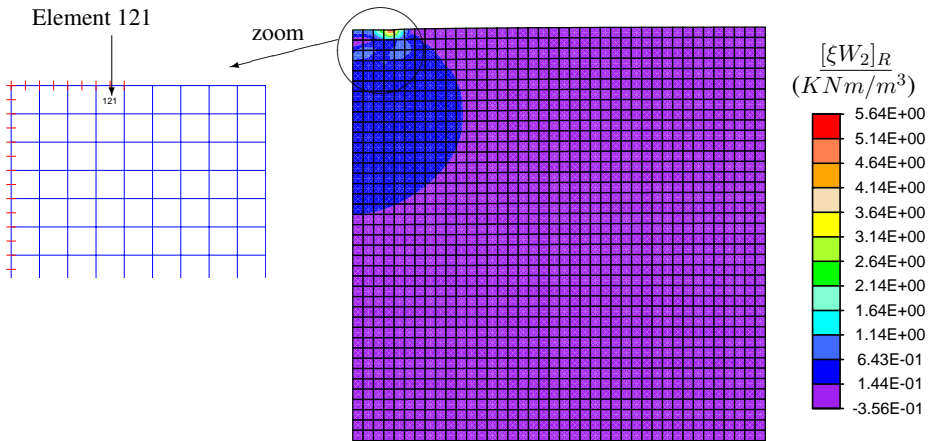
b. Distribution of relaxed energy at the first Gauss point at $v = 0.1556\,m$.

Figure 9.3.: Case 1 ($a = 10\,B$): Soil foundation problem by use of 1600 Q8P4 elements
(The displacement-based finite element formulation with eight-node displace-
ment and four-node pressure interpolations).
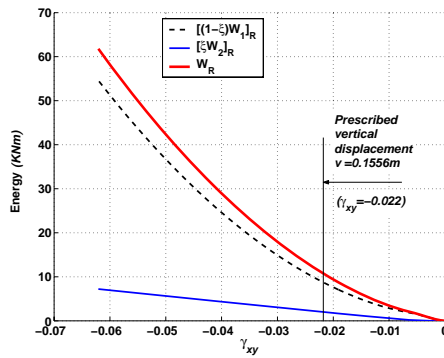
a. Relaxed energy-shear strain at the first
Gauss point of the element 121.
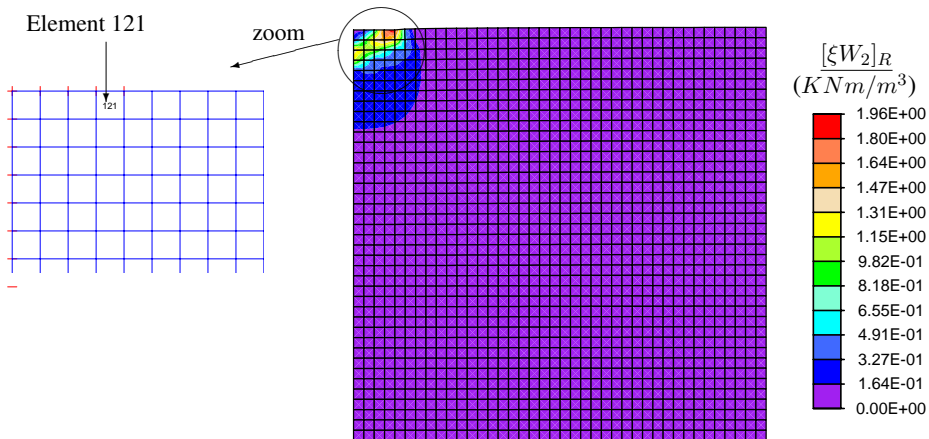
b. Distribution of relaxed energy at the first Gauss point at $v = 0.1556\,m$.

Figure 9.4.: Case 1 ($a = 10\,B$): Soil foundation problem by use of 1600 EAS elements
(The enhanced assumed strain method with four-node displacement and seven
enhanced modes for pressure interpolations).
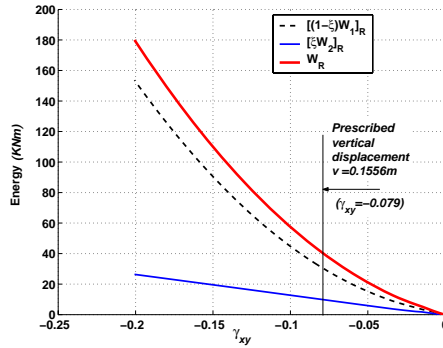
a. Relaxed energy-shear strain at the first
Gauss point of the element 281.
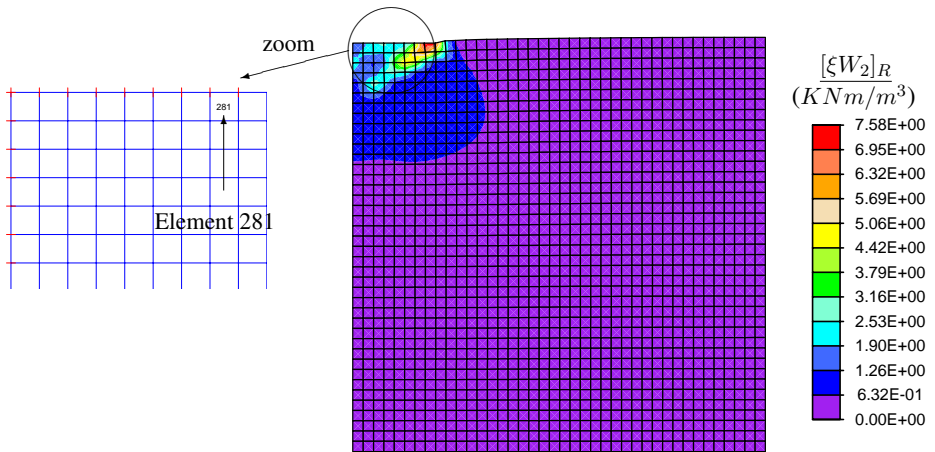
b. Distribution of relaxed energy at the first Gauss point at $v = 0.1556\,m$.

Figure 9.5.: Case 2 ($a = 5\,B$): Soil foundation problem by use of 1600 EAS elements (The enhanced assumed strain method with four-node displacement and seven enhanced modes for pressure interpolations).
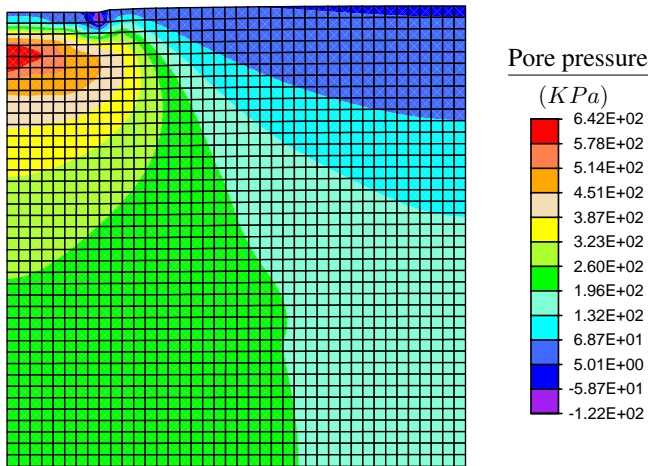
Figure 9.6.: Case 2 ($a = 5\,B$): Soil foundation problem by use of 1600 EAS elements (The enhanced assumed strain method with four-node displacement and seven enhanced modes for pressure interpolations): Distribution of pore pressure at the first Gauss point at $v = 0.1556\,m$.

9.2. Micro-strain and micro-variation in water content

In this part, the micro-strain and the micro-variation in water content can be determined based on the following assumption:

> **First assumption:** The width of a shear band tends to zero, $\xi \to 0$.

According to this assumption,

- the micro-strains of the low-strain and high-strain domains in solid derived from eqs. (7.41) and (7.43) in Section 7.4.1 can be expressed as

$$\epsilon_1 = \epsilon - s(\boldsymbol{m} \otimes \boldsymbol{n})^{\mathrm{s}}, \tag{9.19}$$

$$\epsilon_2 \approx \frac{s}{\xi}(\boldsymbol{m} \otimes \boldsymbol{n})^{\mathrm{s}} \to \infty \quad \text{as } \xi \to 0, \tag{9.20}$$

 where the unit vectors $\boldsymbol{m}$ and $\boldsymbol{n}$ are the oriented vectors of the shear band evolution.

- the micro-variations in water content have the following forms based on eqs. (7.20) and (7.22) in Section 7.3.1

$$\zeta_1 = \zeta - r, \tag{9.21}$$

$$\zeta_2 \approx \frac{r}{\xi} \to \infty \quad \text{as } \xi \to 0. \tag{9.22}$$

Herein r and s defined by eqs.(7.19) and (7.40), repectively, are the scaling parameters.

9.3. Relaxed energy of porous inelastic medium

According to *Biot, 1962*[12], the strain energy of a porous elastic medium has the following form

$$W_1(\epsilon, \zeta) = \frac{1}{2}\lambda_c(\mathrm{tr}\epsilon)^2 + \mu \, \|\epsilon\|^2 - \alpha \, Q(\mathrm{tr}\epsilon)\zeta + \frac{1}{2}Q\zeta^2, \tag{9.23}$$

where ϵ is the strain field for the solid; μ is the shear modulus; α and Q are the Biot's constants defined by (9.11) and (9.12), respectively; ζ is the variation in water content determined by eq. (9.10).

The coefficient λ_c links the Biot's constants α and Q with the Lamé constant λ:

$$\lambda_c = \lambda + \alpha^2 Q. \tag{9.24}$$

By use of eq. (9.23) the total stress and pore pressure are given by

$$\boldsymbol{\sigma} \;=\; \frac{\partial W_1}{\partial \boldsymbol{\epsilon}} = \lambda_c(\mathrm{tr}\boldsymbol{\epsilon})\boldsymbol{I} + 2\mu\boldsymbol{\epsilon} - \alpha\,Q\zeta\boldsymbol{I}. \tag{9.25}$$

$$p \;=\; \frac{\partial W_1}{\partial \zeta} = -\alpha Q\mathrm{tr}\boldsymbol{\epsilon} + Q\zeta. \tag{9.26}$$

It should be noticed that if the fluid (water in this case) is compressible, that is, when $Q \neq \infty$, we also obtain eq. (9.26) by taking the integration with respect to time of eq. (9.10).

Let us consider the second assumption

> **Second assumption:** The energy of the high-strain domain inside a shear band has the following form
>
> $$W_2(\boldsymbol{\epsilon}, \zeta) = \left[\frac{1}{2}\bar{\lambda}_c(\mathrm{tr}\boldsymbol{\epsilon})^2 + \bar{\mu}\,\|\boldsymbol{\epsilon}\|^2 - \bar{\alpha}\,\bar{Q}(\mathrm{tr}\boldsymbol{\epsilon})\zeta + \frac{1}{2}\bar{Q}\zeta^2\right]^{\frac{1}{2}} \tag{9.27}$$
>
> which satisfies the positive homogeneity of the first degree in $\boldsymbol{\epsilon}$ and ζ
>
> $$W_2(a\boldsymbol{\epsilon}, a\zeta) = |a|\,W_2(\boldsymbol{\epsilon}, \zeta) \tag{9.28}$$
>
> where $\bar{\lambda}_c$, $\bar{\mu}$, $\bar{\alpha}$ and $\bar{Q}$ are material paramters whose values determine the stress level in the shear band.

Similar to Chapters 7 and 8 the mixed energy of the porous inelastic medium can be taken in the following form

$$W^{mix}(\boldsymbol{\epsilon}, \zeta) = (1 - \xi)W_1(\boldsymbol{\epsilon} - s(\boldsymbol{m} \otimes \boldsymbol{n})^s, \zeta - r) + \xi W_2(\frac{s}{\xi}(\boldsymbol{m} \otimes \boldsymbol{n})^s, \frac{r}{\xi}). \tag{9.29}$$

Let ξ tend to zero and substituting (9.23) into the first term of eq.(9.29) we obtain

$$
\begin{aligned}
W_1(\boldsymbol{\epsilon} - s(\boldsymbol{m} \otimes \boldsymbol{n})^s, \zeta - r) \;=\;& \frac{1}{2}\lambda_c(\mathrm{tr}\boldsymbol{\epsilon})^2 + \mu\,\|\boldsymbol{\epsilon}\|^2 + \frac{s^2}{2}\left[\mu + (\lambda_c + \mu)(\boldsymbol{m}.\boldsymbol{n})^2\right] \\
&-\; s\left[\lambda_c(\boldsymbol{m}.\boldsymbol{n})\mathrm{tr}\boldsymbol{\epsilon} + 2\mu\,\boldsymbol{m}.\boldsymbol{\epsilon}\boldsymbol{n}\right] \\
&-\; \alpha\,Q\left[\mathrm{tr}\boldsymbol{\epsilon} - s(\boldsymbol{m}.\boldsymbol{n})\right](\zeta - r) \\
&+\; \frac{1}{2}Q(\zeta - r)^2. \tag{9.30}
\end{aligned}
$$

According to the second assumption, the second term of eq.(9.29) can be written as

$$\xi W_2(\frac{s}{\xi}(\boldsymbol{m} \otimes \boldsymbol{n})^s, \frac{r}{\xi}) = W_2(s(\boldsymbol{m} \otimes \boldsymbol{n})^s, r). \tag{9.31}$$

On inserting (9.27) into eq.(9.31) we get

$$W_2(s(\boldsymbol{m} \otimes \boldsymbol{n})^s, r) = \left[\frac{s^2}{2}\left(\bar{\mu} + (\bar{\lambda}_c + \bar{\mu})(\boldsymbol{m}.\boldsymbol{n})^2\right) - \bar{\alpha}\,\bar{Q}(\boldsymbol{m}.\boldsymbol{n})sr + \frac{1}{2}\bar{Q}r^2\right]^{\frac{1}{2}}. \tag{9.32}$$

Addition of all components (9.30) and (9.32), the mixed energy (9.29) yields

$$
\begin{aligned}
W^{mix}(\boldsymbol{\epsilon}, \zeta) \;=\; & W_1(\boldsymbol{\epsilon} - s(\boldsymbol{m} \otimes \boldsymbol{n})^s, \zeta - r) + W_2(s(\boldsymbol{m} \otimes \boldsymbol{n})^s, r), \\
=\; & \frac{1}{2}\lambda_c(\mathrm{tr}\boldsymbol{\epsilon})^2 + \mu \,\|\boldsymbol{\epsilon}\|^2 + \frac{s^2}{2}\left[\mu + (\lambda_c + \mu)(\boldsymbol{m}.\boldsymbol{n})^2\right] \\
& -\; s\left[\lambda_c(\boldsymbol{m}.\boldsymbol{n})\mathrm{tr}\boldsymbol{\epsilon} + 2\mu\,\boldsymbol{m}.\boldsymbol{\epsilon}\boldsymbol{n}\right] \\
& -\; \alpha\,Q\left[\mathrm{tr}\boldsymbol{\epsilon} - s(\boldsymbol{m}.\boldsymbol{n})\right](\zeta - r) + \frac{1}{2}Q(\zeta - r)^2 \\
& +\; \left[\frac{s^2}{2}\left(\bar{\mu} + (\bar{\lambda}_c + \bar{\mu})(\boldsymbol{m}.\boldsymbol{n})^2\right) - \bar{\alpha}\,\bar{Q}(\boldsymbol{m}.\boldsymbol{n})sr + \frac{1}{2}\bar{Q}r^2\right]^{\frac{1}{2}}.
\end{aligned}
\tag{9.33}
$$

The problem of the non-convex energy (9.33) arizing due to the formation of shear bands is solved by energy relaxation in order to ensure that the corresponding problem is well-posed. The relaxed energy is obtained by the minimization procedure

$$
W_R(\boldsymbol{\epsilon}) = \inf\left\{W^{mix}(\boldsymbol{\epsilon}) \mid s\,,\,r\,,\,\boldsymbol{m}\,,\,\boldsymbol{n}\,;\,\|\boldsymbol{m}\| = \|\boldsymbol{n}\| = 1\right\}.
\tag{9.34}
$$

Let us recall eq. (7.64)

$$
\begin{aligned}
\boldsymbol{m}.\boldsymbol{\epsilon}\,\boldsymbol{n} \;=\; & (\epsilon_m + R\cos 2\psi)\cos\varphi + R\sin 2\psi\,\sin\varphi\,, \\
=\; & \epsilon_m \cos\varphi + R\cos(\varphi - 2\psi),
\end{aligned}
\tag{9.35}
$$

where R and ϵ_m are the maximum shear strain and the average strain; ψ is an angle between the vector $\boldsymbol{m}$ and the eigenvector $\boldsymbol{e}_1$ corresponding to the major principal strain $\mathcal{E}_1$ as denoted in Fig. 7.6; φ is the angle between two unit vectors $\boldsymbol{m}$ and $\boldsymbol{n}$:

$$
\boldsymbol{m}.\boldsymbol{n} = \cos\varphi.
\tag{9.36}
$$

The mixed energy (9.33) can be rewritten as an alternative form by inserting eqs. (9.35) and (9.36)

$$
\begin{aligned}
W^{mix} \;=\; & \frac{1}{2}\lambda_c(\mathrm{tr}\boldsymbol{\epsilon})^2 + \mu \,\|\boldsymbol{\epsilon}\|^2 + \frac{s^2}{2}\left[\mu + (\lambda_c + \mu)(\cos\varphi)^2\right] \\
& -\; s\left[\lambda_c\boldsymbol{\epsilon}\cos\varphi + 2\mu\left(\epsilon_m \cos\varphi + R\cos(\varphi - 2\psi)\right)\right] \\
& -\; \alpha\,Q\left[\mathrm{tr}\boldsymbol{\epsilon} - s\cos\varphi\right](\zeta - r) + \frac{1}{2}Q(\zeta - r)^2 \\
& +\; \left[\frac{s^2}{2}\left[\bar{\mu} + (\bar{\lambda}_c + \bar{\mu})(\cos\varphi)^2\right] - \bar{\alpha}\,\bar{Q}(\cos\varphi)sr + \frac{1}{2}\bar{Q}r^2\right]^{\frac{1}{2}}.
\end{aligned}
\tag{9.37}
$$

Therefore, the relaxed energy (9.34) can be expressed as the following minimization problem by considering the mixed energy (9.37)

$$
W_R(\boldsymbol{\epsilon}) = \inf\left\{W^{mix}(\boldsymbol{\epsilon}) \mid s\,,\,r\,,\,\varphi\,,\psi\,;\,0 \leq \varphi\,,\,\psi \leq \pi\right\}.
\tag{9.38}
$$

The necessary condition of the maximization problem (9.34) with respect to ψ leads to two possible solutions

$$\psi \;=\; \frac{\varphi}{2}\,, \tag{9.39}$$

$$\text{or} \quad \psi \;=\; \frac{\varphi}{2} + \frac{\pi}{2}\,, \tag{9.40}$$

where $0 \le \varphi \le \pi$. Herein we consider first case $\psi = \dfrac{\varphi}{2}$. The procedure for second case is similar and is not considered here.

In order to find the relaxed energy (9.38) we can use the following mixed energy by substituting (9.39) into (9.37)

$$
\begin{aligned}
W^{mix} \;=\;& \frac{1}{2}\lambda_c(\mathrm{tr}\boldsymbol{\epsilon})^2 + \frac{1}{2}Q\zeta^2 - \alpha\,Q\,\zeta\,\mathrm{tr}\boldsymbol{\epsilon} \\
& + \; s^2(a + bx^2) + csx + ds + er + fsxr + gr^2 \\
& + \; \sqrt{s^2(a + bx^2) + fsxr + gr^2}\,.
\end{aligned} \tag{9.41}
$$

Here

$$a \;=\; \frac{\mu}{2}\,, \tag{9.42}$$

$$b \;=\; \frac{\lambda_c + \mu}{2}\,, \tag{9.43}$$

$$c \;=\; -\left(\lambda_c\mathrm{tr}\boldsymbol{\epsilon} + 2\mu\,\epsilon_m\right) + \alpha\,Q\,\zeta, \tag{9.44}$$

$$d \;=\; -2\mu R, \tag{9.45}$$

$$e \;=\; \alpha\,Q\,\mathrm{tr}\boldsymbol{\epsilon} - Q\,\zeta, \tag{9.46}$$

$$f \;=\; -\alpha\,Q, \tag{9.47}$$

$$g \;=\; \frac{1}{2}Q, \tag{9.48}$$

$$x \;=\; \cos\varphi. \tag{9.49}$$

It should be noticed that the solutions s, r and φ of the minimization problem (9.34) can be found directly by *Mathematica* [114].

The relaxed stress and the relaxed pore pressure by using eq. (9.37) are given by

$$
\begin{aligned}
\boldsymbol{\sigma} \;=\;& \frac{\partial W^{mix}}{\partial\boldsymbol{\epsilon}}\,, \\
=\;& \lambda_c(\mathrm{tr}\boldsymbol{\epsilon})\boldsymbol{I} + 2\mu\boldsymbol{\epsilon} - s\left[\lambda_c(\boldsymbol{m}.\boldsymbol{n})\mathrm{tr}\boldsymbol{\epsilon} + 2\mu\,(\boldsymbol{m}\otimes\boldsymbol{n})^s\right] - \alpha\,Q(\zeta - r)\boldsymbol{I}.
\end{aligned} \tag{9.50}
$$

$$p \;=\; \frac{\partial W^{mix}}{\partial\zeta} = -\alpha Q\left(\mathrm{tr}\boldsymbol{\epsilon} - s\boldsymbol{m}.\boldsymbol{n}\right) + Q(\zeta - r). \tag{9.51}$$

The relaxed effective stress links the relaxed stress and relaxed pore pressure based on eq. (9.4)

$$
\begin{aligned}
\boldsymbol{\sigma}^{''} &= \boldsymbol{\sigma} + \alpha\,\boldsymbol{I}p\,, \\
&= \lambda(\mathrm{tr}\boldsymbol{\epsilon})\boldsymbol{I} + 2\mu\boldsymbol{\epsilon} - s\left[\lambda(\boldsymbol{m}.\boldsymbol{n})\boldsymbol{I} + 2\mu\left(\boldsymbol{m}\otimes\boldsymbol{n}\right)^{s}\right].
\end{aligned}
\tag{9.52}
$$

It is very interesting that the relaxed effective stress (9.52) has the identical form of eq.(7.73).

9.4. Summary

Throughout this chapter, the relaxed energy analysis of shear bands for fluid-saturated inelastic porous media at small deformation is presented. The peformance of the energy relaxation presented in Section 7.5.2 incorporating the Biot theory is demonstrated through the numerical simulation of a soil foundation problem. The numerical results show that mesh sensitivity cannot be removed. Hence, the relaxed energy of porous inelastic media is suggested. The main features of the proposed formulation may be summarized as follows:

- The assumption of a zero thickness shear band induces the unbounded micro-strain and the unbounded micro-variation in water content of the high-strain domain according to eqs. (9.20) and (9.22).

- The assumption of the positive homegeneity of the first degree in strain and variation in water content leads to the bounded mixed energy of the high-strain domain. This potential energy can be identified from one of the equations (9.33), (9.37) and (9.41).

- By use of Mohr strain circle the relaxed energy determined by the minimization problem for the mixed energy with three variables instead of four variables.

- The relaxed effective stress (9.52) obtained from the relaxed total stress and the relaxed pore pressure is as identical as the one presented in Section 7.5.1.

10. Conclusions and outlook

The simulation of localization phenomena has become of considerable interest due to its importance in predicting material failure. The presented thesis deals with three issues:

(1) Simulation of shear band formation in hypoplastic models by the multi-field finite element method.

(2) Analysis of strong discontinuities in hypoplastic models.

(3) Simulation of shear localization by energy relaxation.

In the first issue, the multi-field finite element formulations of shear localization in materials are presented to decrease the mesh dependence for shear bands's simulation. The formulations are based upon hypoplastic constitutive laws for soils and the variational formulation involving three independent variables: displacement, stress and strain rates. Included in these formulations are the standard displacement method, the three-field mixed formulation, the enhanced assumed strain method and the mixed enhanced strain method. Several numerical examples, which demonstrate the capability and performance of the different finite element formulations, are compared with available experimental data for Hostun RF sand and numerical results for Karlsruhe sand on biaxial tests. The numerical results obtained from the multi-field finite element formulations based on the Wolffersdorff hypoplastic model reveal a pathological dependence on the discretization. The resulting problem is not purely numerical, because the mesh dependence is the direct consequence of the ill-posedness of the boundary value problem, which indicates an underlying mathematical problem.

An analysis for strong discontinuity in hypoplasticity is presented in the second issue of the thesis as an alternative approach to eliminate the mesh dependence. In order to make the constitutive equation compatible with the appearence of strong discontinuities, several requirements on the stress field are imposed. Then this results in a set of equations which may be solved for the additional unknowns appearing in the problem: the displacement jump, the stress field at the discontinuity path and the normal vector. It is found that by void ratios of areas inside a shear band and at a neighbouring shear band are identical when one neglects the normal movements in the discontinuity surface. However, this result is in conflict with the experimental observations by *Oda and Kamaza, 1998*[85]. This gives rise to a need to derive the new evolution equation to update the void ratio in the discontinuity surface. The form of this evolution equation is still an open question.

The last issue focuses on a theorical framework for the treatment of shear localizations in solid materials. The theory is based on energy minimization principles associated with micro-structure developments under the assumptions of a shear band of a zero thickness and of the mixed energy inside a shear band. The first assumption immediately leads to unbounded strain of the high-strain domain at the discontinuity. According to the second assumption the proposed mixed energy in inelastic materials consists of the energy involving the behaviour at very small strain and the energy representing the behaviour at very large strain, which is a linear function and implicitly takes into account softening behaviour. The fact that the energy representing the behaviour in very large strain is a function of the inelastic strain is in close agreement with the experiment by *Wei et al., 2002*[112].

Localization phenomena are interpreted as micro-structure developments associated with the nonconvex mixed energy. The problem of the non-convex energy arizing due to the formation of shear bands is solved by energy relaxation in order to ensure that the corresponding problem is well-posed. The relaxed energy, which is approximated by a first order rank-one convexification, is defined by a local minimization problem for the mixed potential energy with three variables. The onset of localization is detected through the proposed optimization process. The relaxed results link locally averaged stresses with strains in a heterogeneous material. The mesh dependence can be handled by convexification of the potential energy, while the emergence of shear bands can continuously evolve in a well defined and physically meaningful manner.

The theory is also extended to geometric and material non-linear theory for hyperelastic materials. The numerical results closely match the analytical result, verifying again the lack of pathological mesh dependence of the proposed relaxed energy.

Finally, the above energy relaxation is applied to porous inelastic media based on Biot theory. The presented numerical results manifest mesh sensitivity in case of a soil foundation problem. Thus, the energy relaxation taking into account the relaxed pore pressure is introduced. To determine the relaxed fields of stress and pore pressure, the minization problem for the mixed energy, which is a function of strain and variation in water content, is settled. In high-strain domain the strain and the variation in water content become unbounded.

It should be noted that the theory developed in the last issue indeed belongs to a subclass of the approach suggested by *Carstensen, Hackl and Mielke, 2002*. In their approach the general formulation of inelasticity is governed by the stored energy function and the dissipation function. However, the dissipation function in the proposed theory here cannot be derived explicitly.

On the basis of the results obtained in this thesis, several directions for future work are suggested

- Evolution equation to update the void ratio in the discontinuity surface for strong dis-

coninuity approach incorporating hypoplasticity.

- Numerical simulation of shear localization in inelastic porous media based on the proposed theory in Chapter 9.

- An exact treatment of a rank-one convexification analysis of shear bands.

- Comparison between numerical results obtained from the proposed energy relaxation and experiment.

Bibliography

[1] K.A. Alshibli and S. Sture. Shear band formation in plane strain experiments of sand. *J. Geotech. Geoen-viron. Engng. (ASCE)*, 126:4951–503, 2000.

[2] F. Armero and K. Garikipati. An analysis of strong discontinuities in multiplicative finite strain plasticity and their relation with the numerical simulation of strain localization in solids. *Int. J. Solids Structures*, 33:2863–2885, 1996.

[3] R.J. Asaro. Material modelling and failure modes in metal plasticity. *Mech. Mat.*, 4:343–373, 1985.

[4] Z.P. Bažant, T.B. Belytschko, and T.P. Chang. Continuum model for strain softening. *J. Engng. Mech., ASCE*, 110:1666–1692, 1984.

[5] J.M. Ball. Convexity conditions and existence theorems in nonlinear elasticity. *Arch. Rat. Mech. Anal.*, 63:337–403, 1977.

[6] S. Bartel, C. Carstensen, K. Hackl, and U. Hoppe. Effective relaxation for microstructure simulations: algorithms and applications. *Comput. Methods Appl. Mech. Engng.*, 193:5143–5175, 2004.

[7] T. Bartel and K. Hackl. A novel approach to the modelling of single-crystalline materials undergoing martensitic phase-transformations. *Mat. Sci. Engng. A - Structural materials properties microstructure and processing*, 481:371–375, 2008.

[8] E. Bauer. Calibration of a comprehensive hypoplastic model for granular materials. *Soils and Foundations*, 36:13–26, 1996.

[9] E. Bauer. Analysis of shear band bifurcation with a hypoplastic model for a pressure and density sensitive granular material. *Mech. Mat.*, 31:597–609, 1999.

[10] E. Bauer and I. Herle. Stationary states in hypoplastic. In D. Kolymbas, editor, *Constitutive Modelling of Granular Materials*, pages 167–192. Springer, 2000.

[11] A. Benallal, R. Billardon, and G. Geymonat. Localization phenomena at the boundaries and interfaces of solids. In C.S Desai, editor, *Proc. Third Int. Conf. Constitutive Laws for Engineering Materials: Theory and Applications*, pages 387–390. Tucson, Arizona, 1991.

[12] M.A. Biot. Mechanics of deformation and acoustic propagation in porous media. *J.

Appl. Mech., 33:1482–1498, 1962.

[13] M. Bischoff, E. Ramm, and D. Braess. A class of equivalent enhanced assumed strain and hybrid stress finite elements. *Comput. Mech.*, 22:443–449, 1999.

[14] R.I. Borja. A finite element model for strain localization analysis of strongly discontinuous fields based on standard galerkin approximation. *Comput. Methods Appl. Mech. Engng.*, 190:1529–1549, 2000.

[15] C. Carstensen, K. Hackl, and A. Mielke. Non-convex potentials and microstructures in finite-strain plasticity. *Proc. R. Soc. Lond. A*, 458:299–317, 2002.

[16] R. Chambon. Localization criteria for non-linear constitutive equations of geomaterials. *Mech. Cohe. Fric. Mat.*, 5:61–82, 2000.

[17] R. Chambon. Uniqueness, second order work and bifurcation in hypoplasticity. In D. Kolymbas, editor, *Constitutive Modelling of Granular Materials*, pages 147–165. Springer, 2000.

[18] R. Chambon, J. Desrues, W. Hammad, and R. Charlier. Cloe, a new rate-type constitutive model for geomaterials. theoretical and implementation. 18:253–278, 1994.

[19] A. Cherkaev. Approaches to nonconvex variational problems of mechanics. In P. P. Casta, J.J. Telega, and B. Gambin, editors, *Nonlinear Homogenization and its Applications to Composites, Polycrystals and Smart Materials*, pages 65–105. Springer Netherlands, 2005.

[20] B. Dacorogna. *Direct methods in the calculus of variations*. Springer-Verlag, Berlin, 1989.

[21] R. de Borst. Damage, material instabilities, and failure, chapter 10. In E. Stein, R. de Borst, and T.J.R. Hughes, editors, *Encyclopedia of Computational Mechanics*, volume 2, pages 335–373. Wiley, Chichester, 2004.

[22] R. de Borst and H.B. Mühlhaus. Gradient-dependent plasticity: Formulation and algorithmic aspects. *Int. J. Num. Meth. Eng.*, 35:521–539, 1992.

[23] R. de Borst, J. Pamin, J.C.J Schellekens, and L.J. Sluys. Instability in materials - computational aspects. In H.J. Siriwardane and M.M. Zaman, editors, *Computers Methods and Advances in Geomechanics*, volume 2, pages 91–102. Balkema, Rotterdam, 1994.

[24] R. de Borst and L.J. Sluys. Localization in a cosserat continuum under static and dynamics loading conditions. *Comput. Methods Appl. Mech. Engng.*, 90:805–827, 1991.

[25] A. DeSimone and G. Dolzmann. Material instabilities in nematic elastomers. *Phys. D.*, 136:175–191, 2000.

[26] J. Desrues and R. Chambon. Shear band analysis and shear moduli calibration. *Int. J. Solids Structures*, 39:3757–3776, 2002.

[27] J. Desrues and G. Viggianin. Strain localization in sand: an overview of the experimental results obtained in grenoble using stereophotogrammetry. 28:279–321, 2004.

[28] J. Desrues, B. Zweschper, and P.A. Vermeer. Database for tests on hostun rf sand. In *Institutsbericht 13, Institut für Geotechnik, Universität Stuttgart*, 2000.

[29] H.E. Déve and R.J. Asaro. The development of plastic failure modes in crystalline materials: shear bands in fcc polycrystals. *Metall. Trans. A*, 20:579–593, 1989.

[30] H.E. Déve and R.J. Asaro. The influence of hydrogen on the development of localized plastic deformation in internally nitrided single crystals of iron. *Scripta Metall.*, 23:389–395, 1989.

[31] L. Drăguşin. A hypoelastic model for soils: Part i-iv. *Int. J. Eng. Sci.*, 19:511–552, 1981.

[32] R.A.B Engelen, M.G.D. Geers, and F.P.T. Baaijens. Nonlocal implicit gradient-enhanced elasto-plasticity for the modelling of softening behaviour. *Int. J. Plast.*, 19:403–433, 2003.

[33] A.C. Eringen. Theory of miropolar elasticity. In H. Leibowitz, editor, *Fracture, an Advanced Treatise*, pages 621–729. Academic Press, New York, 1968.

[34] W. Fellin and A. Ostermann. Consistent tangent operators for constitutive rate equations. *Int. J. Numer. Anal. Meth. Geomech.*, 26:1213–1233, 2002.

[35] R.J. Finno, W.W. Harris, M.A. Mooney, and G. Viggiani. Strain localization und undrained steady state of sand. *J. Geotech. Engng*, 122:462–473, 1996.

[36] R.K. Garikipati. *On strong discontinuities in inelastic solids and their numerical simulation*. PhD thesis, Stanford University, 1996.

[37] D. Gudehus. A comparison of some constitutive laws for soils under radially symmetric loading and unloading. In Wittke, editor, *Third International Conference on Numerical Methods in Geomechanic*, pages 1309–1323. Balkema, Rotterdam, Aachen, 1979.

[38] G. Gudehus. A comprehensive constitutive equation for granular materials. *Soils and Foundations*, 36:1–12, 1996.

[39] K. Hackl. *Micromechanics of materials*. Lecture note, International Summer School on Continuum Mechanical Modelling of Materials, 2000.

[40] K. Hackl and F.R. Fischer. On the relation between the principle of maximum dissi-

pation and inelastic evolution given by dissipation potentials. *Proc. R. Soc. Lond. A*, 464:117–132, 2008.

[41] K. Hackl and R. Heinen. An upper bound to the free energy of n-variant polycrystalline shape memory alloys. *J. Mech. Phys. Solids*, 56:2832–2843, 2008.

[42] K. Hackl and U. Hoppe. On the calculation of microstructures for inelastic materials using relaxed enegies. In C. Miehe, editor, *Proceedings of IUTAM Symposium on Computational Mechanics of Solid Material at Large Strains*, pages 77–86. Boston, 2001.

[43] W.I. Hammad. *Modélisation non linéaire et étude éxperimentale des bandes de cisaillement dans les sables*. PhD thesis, UJF Grenoble, 1991.

[44] O.M. Heeres and R. de Borst. Implicit integration of hypoplastic models. In D. Kolymbas, editor, *Constitutive Modelling of Granular Materials*, pages 457–470. Springer, 2000.

[45] I. Herle. *Hypoplastizität und Granulometrie einfacher Korngerüste*. PhD thesis, Veröffentlichung des Institutes für Bodenmechanik und Felsmechanik der Universität Fridericiana in Karlsruhe, Heft 142, 1997.

[46] I. Herle and Gudehus G. Determination of parameters of a hypoplastic constitutive model from properties of grain assemblies. *Mech. Cohe. Fric. Mat.*, 4:461–486, 1999.

[47] R. Hill. A general theory of uniqueness and stability in elastic-plastic solids. *J. Mech. Phys. Solids*, 6:236–249, 1958.

[48] G. A. Holzapfel. *Nonlinear solid mechanics: a continuum approach for engineering*. John Wiley & Sons Ltd, 2000.

[49] W. Huang and E. Bauer. Numerical investigations of shear localization in a micropolar hypoplastic material. *Int. J. Numer. Anal. Meth. Geomech.*, 27:325–352, 2003.

[50] W. Huang, M. Hjiaj, and W. S. Sloan. Bifurcation analysis for shear localization in non-polar and micro-polar hypoplastic continua. *J. Engng. Math.*, 52:167–184, 2005.

[51] H. Hügel. *Prognose von Bodenverformungen*. PhD thesis, Veröffentlichung des Institutes für Bodenmechanik und Felsmechanik der Universität Fridericiana in Karlsruhe, Heft 136, 1995.

[52] M. Jirásek. Objective modeling of strain localization. *Revue française de génie civil*, 6:1119–1132, 2002.

[53] M. Karakouzian, N. Huydma, and B. Avar. Observations and nomenclature of shear bands formed in granular soils. *Electronic, J. Geotech. Engng. (EJGE), paper ID# 0103*, 2001.

[54] P. Kasper Eric and L. Taylor Robert. A mixed-enhanced strain method: Linear problems. In *No. UCB/SEMM-97/02*, 1997.

[55] R.V. Kohn and G. Strang. Optimal design and relaxation of variational problems i, ii, iii. *Comm. Pure Appl. Math.*, 39:113–137, 1986.

[56] D. Kolymbas. Introduction to hypoplasticity, advances in geotechnical engineering and tunnelling. volume 1. Batkema Press, 2000.

[57] D. Kolymbas and I. Herle. Hypoplasticity as a constitutive framework for granular soils. In J. A. Yamamuro and V. N. Kaliakin, editors, *Soil Constitutive Models: Evaluation, Selection and Calibration*, pages 257–289. VA: American Society of Civil Engineers (= ASCE Geotechnical Special Publication 128), 2005.

[58] K. Kolymbas. An outline of hypoplasticity. *Arch. Appl. Mech.*, 61:143–151, 1991.

[59] K. Kolymbas. Hypoplasticity as a constitutive framework for granular materials. In H.J Siriwardane and M.M. Zaman, editors, *Proc. Computer Methods and Advances in Geomechanics*, pages 197–208. Balkema, 1994.

[60] K. Kolymbas and I. Herle. Hypoplasticity: a framework to model granular materials. In B. Cambou, editor, *Behaviour of Granular Materials*, pages 239–268. Springer, 1997.

[61] K. Kolymbas and I. Herle. Shear and objective stress rates in hypoplasticity. *Int. J. Numer. Anal. Meth. Geomech.*, 27:733–744, 2003.

[62] Y.T. Lai, I.R. Borja, G.B. Duvernay, and L.R. Meehan. Capturing strain localization behind a geosynthetic-reinforced soil wall. 27:425–451, 2003.

[63] C. Lambrecht, C. Miehe, and J. Dettmar. Energy relaxation of non-convex incremental stress potentials in a strain-softening elastic-plastic bar. *Int. J. Solids Structures*, 40:1369–1391, 2003.

[64] R. Larsson, P. Steinmann, and K. Runesson. Finite element embedded localization band for finite strain plasticity based on a regularized strong discontinuity. *Mech. Cohe. Fric. Mat.*, 4:171–194, 1998.

[65] P. W. Leech. Observations of adiabatic shear band formation in 7039 aluminum alloy. *Metall. Mat. Trans. A*, 16(10):900–1903, 1985.

[66] J. Lemonds, R.J. Asaro, and A. Needleman. A numerical study of localized deformation in bi-crystals. *Mech. Mat.*, 4:417–435, 1985.

[67] J.J. Lewandowski and A.L. Greer. Temperature rise at shear bands in metallic glasses. *Nature Materials*, 5:15–18, 2006.

[68] R.W. Lewis and B.A. Schrefler. The finite element method in the static and dynamic deformation and consolidation of porous media. Edition 2th, John Wiley & Sons Ltd, 1998.

[69] L.L. Lisiecki, D.Q. Nelson, and R.J. Asaro. Lattice rotations, necking and localized deformation in fcc single crystals. *Scripta Metall.*, 16:441–448, 1982.

[70] G. Maier and T. Hueckel. Nonassociated and coupled flow rules of elastoplasticity for rock like materials. *Int. J. Rock Mech. Min. Sci. & Geomech*, 16:77–92, 1979.

[71] Th. Maier. Comparison of non-local and polar modelling of softening in hypoplasticity. *Int. J. Numer. Anal. Meth. Geomech.*, 28:251–268, 2004.

[72] C. Miehe. Strain-driven homogenization of inelastic microstructures and composites based on an incremental variational formulation. *Int. J. Num. Meth. Eng.*, 55:1285–1322, 2002.

[73] C. Miehe and M. Lambrecht. Analysis of microstructure development in shear bands by energy relaxation of incremental stress potentials: large-strain theory for standard dissipative solids. *Int. J. Num. Meth. Eng.*, 58:1–41, 2003.

[74] C. Miehe and M. Lambrecht. A two-scale finite element relaxation analysis of shear bands in non-convex inelastic solids: small-strain theory for standard dissipative materials. *Comput. Methods Appl. Mech. Engng.*, 192:473–508, 2003.

[75] A. Mielke. Deriving new evolution equations for microstructures via relaxation of variational incremental problems. *Comput. Methods Appl. Mech. Engng.*, 193:5095–5127, 2004.

[76] P. Mira, M. Pastor, T. Li, and X. Liu. A new stabilized enhanced strain element with equal order of interpolation for soil consolidation problems. *Comput. Methods Appl. Mech. Engng.*, 192:4257–4277, 2003.

[77] C.B. Jr. Morrey. Quasi-convexity and the lower semicontinuity of multiple integrals. *Pacific, J. Math.*, 2:25–53, 1952.

[78] H.B Mühlhaus and E.C. Aifantis. A variational principle for gradient plasticity. *Int. J. Solids Structures*, 28:845–858, 1991.

[79] H.B Mühlhaus and I. Vardoulakis. The thickness of shear bands in granular materials. *Geotechnique*, 37:271–283, 1987.

[80] S. Müller. Variational models for microstructure and phase transitions. In S. Hilderbrandt and M. Struwe, editors, *Calculus of variation and geometric evolution problems, Lecture notes in mathematics*, pages 85–210. Springer, 1999.

[81] M.K. Neilsen and H.L. Schreyer. Bifurcations in elastic-plastic materials. *Int. J. Solids*

Structures, 30(4):521–544, 1993.

[82] A. Niemunis. *Extended hypoplastic models for soils*. Des Institutes für Grundbau und Bodenmechanik der Ruhr-Universität Bochum, Heft 34, 2003.

[83] K. Nübel, Danzig, and A. Niemunis. *Finite element implementation of hypoplasticity - UMAT for von Wolffersdorff hypoplastic model*. http://www.ibf.uni-karlsruhe.de/lbg/forschung/hypoplasticity/hyp-downloads.html, 1998.

[84] K. Nübel and W. Huang. A study of localized deformation pattern in granular media. *Comput. Methods Appl. Mech. Engng.*, 193:2719–2743, 2004.

[85] M. Oda and H. Kamaza. Microstructure of shear bands and its relation to the mechanisms of dilatancy and failure of dense sranular soils. *Géotechnique*, 48(4):465–481, 1998.

[86] J. Oliver. On the discrete constitutive models induced by strong discontinuity kinematics and continuum constitutive equations. *Int. J. Solids Structures*, 37:7207–7229, 2000.

[87] J. Oliver. Topics on failure mechanics. In *International Center for Numerical Methods in Engineering (CIMNE)*, 2002.

[88] J. Oliver. Modelling strong discontinuities in solid mechanics via strain softening constitutive equations: Fundamental and numerical simulation. In *Monograph CIMNE No. 28*, May 1995.

[89] J. Oliver, M. Cervera, and O. Manzoli. Strong discontinuities and continuum plasticity models: the strong discontinuity approach. *Int. J. Plast.*, 15:319–351, 1999.

[90] J. Oliver, A.E. Huespe, E. Samaniego, and E.W.V. Chaves. On strategies for tracking strong discontinuities in computational failure mechanics. In H. Mang, F. Rammerstorfer, and J. Eberhardsteiner, editors, *Proc. World Congress on Computational Mechanics, WCCM V*. Vienna University of Technology, Austria, 2002.

[91] M. Ortiz, Y. Leroy, and A. Needleman. A finite element method for localized failure analysis. *Comput. Methods Appl. Mech. Engng.*, 61:189–214, 1987.

[92] J. Pamin. *Gradient-dependent plasticity in numerical simulation of localization phenomena*. PhD thesis, Delft University of Technology,The Netherlands, 1994.

[93] R.H.J. Peerlings, R. de Borst, W.A.M. Brekelmans, and J.H.P. de Vree. Gradient enhanced damage for quasi-brittle materials. *Int. J. Num. Meth. Eng.*, 17:3391–3403, 1996.

[94] U. Perego. Variationally consistent stress recovery for enhanced strain finite elements. *Commun. Numer. Meth. Engng.*, 16:151–163, 2000.

[95] NAG Research. *The Numerical Algorithms Group (NAG) Fortran Libra-ry*. http://www.nag.co.uk/numeric/FL/fldescription.asp. The Numerical Algorithms Group Ltd, Oxford UK, 2001.

[96] D. Roddeman. *Finite element implementation of hypoplasticity - UMAT for von Wolffersdorff hypoplastic model*. http://www.uibk.ac.at/geotechnik/res/fehypo.html, 1997.

[97] G. Romano, S. F. Marotti de, and M. Diaco. Well-posedness and numerical performances of the strain gap method. *Int. J. Num. Meth. Eng.*, 51:103–126, 2001.

[98] J.C. Simo, J. Oliver, and F. Armero. A analysis of strong discontinuities induced by strain-softening in rate-independent inelastic solids. *Comput. Mech.*, 12:277–296, 1993.

[99] J.C. Simo and M.S. Rifai. A class of mixed assumed strain methods and the method of incompatible modes. *Int. J. Num. Meth. Eng.*, 29:1595–1638, 1990.

[100] P. Steinmann, R. Larsson, and K. Runesson. On the localization properties of multiplicative hyperelasto-plastic continua with strong discontinuities. *Int. J. Solids Structures*, 34:969–990, 1997.

[101] L. Strömberg and M. Ristinmaa. FE-formulation of a non-local plasticity theory. 136:127–144, 1996.

[102] C. Tamagnini, G. Viggiani, and R. Chambon. A review of two different approaches to hypoplasticity. In D. Kolymbas, editor, *Constitutive Modelling of Granular Materials*, pages 107–145. Springer, 2000.

[103] R.L. Taylor. *A finite element analysis program, programmer manual*. University of California at Berkeley, 2004.

[104] R.L. Taylor. *A finite element analysis program, theory manual*. University of California at Berkeley, 2004.

[105] R.L. Taylor. *A finite element analysis program, user manual*. University of California at Berkeley, 2004.

[106] J. Tejchman. Comparative FE-studies of shear localization in granular within polar and non-local hypoplasticity. *Mech. Res. Commun.*, 31:341–354, 2004.

[107] J. Tejchman. Influenece of a charecterestic length on shear zone formation in hypoplasticity with different enhancements. *Comp. Geotech.*, 31:594–611, 2004.

[108] J. Tejchman and E. Bauer. Numerical simulation of shear band formation with a polar hypoplastic constitutive model. *Comp. Geotech.*, 19(3):221–244, 1996.

[109] J. Tejchman and E. Bauer. Numerical simulation of shear band with a hypoplastic

constitutive model. *Comp. Geotech.*, 18(1):71–84, 1996.

[110] Maier Th. Nonlocal modeling of softening in hypoplasticity. *Comp. Geotech.*, 30:599–610, 2003.

[111] L. Vu-Quoc and X.G. Tan. Optimal solid shells for non-linear analyses of multilayer composites. *Comput. Methods Appl. Mech. Engng.*, 192:975–1016, 2003.

[112] Q. Wei, D. Jia, K.T. Ramesh, and E. MA. Evolution and microstructure of shear bands in nanostructured fe. *Appl. Phys. Lett.*, 81(7):1240–1242, 2002.

[113] P.-A. von Wolffersdorff. A hypoplastic relation for granular materials with a predefined limit state surface. *Mech. Cohe. Fric. Mat.*, 1:251–271, 1996.

[114] Inc. Wolfram Research. Mathematica edition: Version 5.0. Wolfram Research, Inc., Champaign, Illinois, 2003.

[115] W. Wu. *Hypoplastizitdt als mathematisches Modell zum mechanischen Verhalten granularer Stoffe*. PhD thesis, Veröffentlichung des Institutes für Bodenmechanik und Felsmechanik der Universität Fridericiana in Karlsruhe, Heft 129, 1992.

[116] W. Wu. Rational approach to anisotropy of sand. *Int. J. Numer. Anal. Meth. Geomech.*, 22:921–940, 1998.

[117] W. Wu and E. Bauer. A simple hypoplastic constitutive model for sand. *Int. J. Numer. Anal. Meth. Geomech.*, 8:833–862, 1994.

[118] W. Wu and E. Bauer. Hypoplastic constitutive model with critical state for granular materials. *Mech. Mat.*, 23:45–69, 1996.

[119] W. Wu and D. Kolymbas. Numerical testing of the stability criterion for hypoplastic constitutive equations. *Mech. Mat.*, 9:245–253, 1990.

[120] W. Wu and K. Kolymbas. Hypoplastic then and now. In D. Kolymbas, editor, *Constitutive Modelling of Granular Materials*, pages 57–105. Springer, 2000.

[121] W. Wu and Z. Sikora. Localized bifurcation in hypoplasticity. *Int. J. Eng. Sci.*, 29(2):195–201, 1991.

[122] S.T. Yeo and B.C. Lee. Equivalence between enhanced assumed strain method and assumed stress hybrid method based on the hellinger-reissner principle. *Int. J. Num. Meth. Eng.*, 39:3083–3099, 1996.

[123] H.M. Zbib and E.C. Aifantis. On the gradient-dependent theory of plasticity and shear banding. *Acta Mechanica*, 92:209–225, 1992.

[124] O.C. Zienkiewicz. Basic formulation of static and dynamic behaviour of soil and other porous media. In J.B. Martins, editor, *Numerical Methods in Geomechanics*, pages

39–55. D. Reidel Publishing Company, 1982.

[125] O.C. Zienkiewicz, A.H.C. Chan, and Schrefler B.A. Shiomi T. Pastor, M. Computational geomechanics. John Wiley & Sons Ltd, 1999.

[126] O.C. Zienkiewicz and R.L. Taylor. The finite element method - volume 1: The basis. Edition 5th. Butterworth-Heinmann, London, 2000.

[127] O.C. Zienkiewicz and R.L. Taylor. The finite element method - volume 2: Solid mechanics. Edition 5th. Butterworth-Heinmann, London, 2000.